

Micromachined Multifunctional Polyvinylidene Fluoride Tactile Sensor for Minimally Invasive Surgery Graspers

Saeed Sokhanvar

A Thesis
in
the Department
of
Mechanical and Industrial Engineering

Presented in Partial Fulfilment of the Requirements
for the Degree of Doctor of Philosophy
Concordia University
Montreal, Quebec, Canada

August 2007
© Saeed Sokhanvar, 2007



Library and
Archives Canada

Bibliothèque et
Archives Canada

Published Heritage
Branch

Direction du
Patrimoine de l'édition

395 Wellington Street
Ottawa ON K1A 0N4
Canada

395, rue Wellington
Ottawa ON K1A 0N4
Canada

Your file Votre référence

ISBN: 978-0-494-31153-0

Our file Notre référence

ISBN: 978-0-494-31153-0

NOTICE:

The author has granted a non-exclusive license allowing Library and Archives Canada to reproduce, publish, archive, preserve, conserve, communicate to the public by telecommunication or on the Internet, loan, distribute and sell theses worldwide, for commercial or non-commercial purposes, in microform, paper, electronic and/or any other formats.

The author retains copyright ownership and moral rights in this thesis. Neither the thesis nor substantial extracts from it may be printed or otherwise reproduced without the author's permission.

AVIS:

L'auteur a accordé une licence non exclusive permettant à la Bibliothèque et Archives Canada de reproduire, publier, archiver, sauvegarder, conserver, transmettre au public par télécommunication ou par l'Internet, prêter, distribuer et vendre des thèses partout dans le monde, à des fins commerciales ou autres, sur support microforme, papier, électronique et/ou autres formats.

L'auteur conserve la propriété du droit d'auteur et des droits moraux qui protègent cette thèse. Ni la thèse ni des extraits substantiels de celle-ci ne doivent être imprimés ou autrement reproduits sans son autorisation.

In compliance with the Canadian Privacy Act some supporting forms may have been removed from this thesis.

Conformément à la loi canadienne sur la protection de la vie privée, quelques formulaires secondaires ont été enlevés de cette thèse.

While these forms may be included in the document page count, their removal does not represent any loss of content from the thesis.

Bien que ces formulaires aient inclus dans la pagination, il n'y aura aucun contenu manquant.


Canada

Abstract

Promising results of Minimally Invasive Surgery, MIS, in the last two decades have been the main incentive of numerous researches in this area. However, despite numerous advantages of this relatively new technique, using of long tools inserted through small ports on the body deprive surgeons of the depth perception, dexterity, sense of touch, and straightforward hand-eye coordination that are accustomed to surgeons in open procedures. Many researches have been launched to rectify the mentioned shortcomings and some improvements, such as, excellent stereo visual feedback and satisfactory dexterity, have been made recently in robotic assisted surgical systems.

However, the current MIS tools whether in endoscopic surgery or in robotic assisted surgery are incapable of providing tactile feedback. The tactile information collected by the surgeons hand in an open surgery is vital for success in complex and delicate operations. For instance, the ability to distinguish between different types of tissue in the body is of vital importance to a surgeon. Before making an incision into tissue, the surgeon must identify what type of tissue is being incised. Failure to classify properly the tissue can cause severe consequences.

There have been some attempts to develop smart MIS graspers with integrated sensors. However, many of these integrated sensors are limited to force or softness sensing. From a functional point of view, integrating several sensors each of them is responsible for measuring a specific quantity is difficult. In contrast, a multi-functional tactile sensor which would be able to address several concerns such as force measurement, determining position of the force, assessing softness of the grasped object, detecting any hidden lumps in bulk soft tissue is highly desirable. The transduction techniques used in the relevant researches have been reported as capacitive and piezoelectric techniques. In this study, the piezoelectric polymer Polyvinylidene Fluoride (PVDF) has been used as the transducer due to its unique features and also bio-compatibility.

This study aimed at introducing a multi-functional tactile sensor which would be able to address many of the required information in a surgery procedure. A unit of the

proposed sensor is able to measure the applied force and its position along the length of the sensor system. In addition, it is also able to differentiate the softness of the contact objects. An array of sensor is able to locate the applied load or any hidden mass in a plane (i.e. xy plane). Integration of the sensors into both jaws of the grasper, enables the smart grasper to determine the depth of any hidden masses. Regardless of the type of the integrated sensor, the study of stress profile in the presence of a lump, at the contact surface of object-grasper is of importance. The behavior of the soft tissue highly influences the stress distribution at the contact surface of tissue and grasper. Although modeling all of the complex behavior of soft tissue is very difficult, in this study, the nonlinear characteristics of the tissue is considered. In the absence of the soft tissue the simulation and experiments are conducted on the elastomers which exhibit very similar behavior.

However, the ultimate objective is the integration of the proposed sensor with the existing MIS graspers. To do this, the sensor must be microfabricated. Therefore, in order to study the feasibility of micromachining of the proposed sensor, the microfabrication procedure for the tactile sensor was examined and the fabrication difficulties were identified. The conventional anisotropic wet etching has been used for micromachining the device.

Acknowledgments

I would like to take this opportunity to express my thanks to my advisors, Dr. Javad Dargahi, and Dr. Muthukumaran Packirisamy for their support and direction. I would also like to thank my committee members Dr. Mojtaba Kahrizi, Dr. Ion Stiharu and Dr. Ramin Sedaghati who have helped me throughout my PhD program. Particularly, I would like to thank Dr. Sedaghati for his help in finite element topics.

Nobody has given me, as much support and encouragement in the course of my doctoral program, as my wife, Mahmonir Pooladgar. Over the past four years, she has been with me in all the highs and lows, helping me to stay on the track when I became distracted by other pursuits. I am grateful to her for her loving care of our two sons, Sepehr and Parsa and her patience in living a student life in the past four years.

I appreciate FCAR and NSECR for their financial supports. I would like to thank all award committees for honoring me through their recognition and support. In particular, I am appreciative of an ASME Quebec Section Scholarship Award, Concordia J.W. O'Brien Fellowship, Power Corporation of Canada Fellowship, Precarn Graduate Scholarship, HydroQuebec Award and finally from NSERC for granting me an IRDF (Industrial Research and Development Fellowship).

I would also like to thank my labmates, Mohammad Reza Ramezanifard, Mohamad Amin Changizi, Ashkan Mirbagheri, Ali Bonakdar, Marjan Molavi, Rozbeh Ahmadi and Ali Shabram for their camaraderie and teamwork. In particular, I would like to thank Mr. Mohammad Reza Ramezanifard who helped me in electronics and computer interfacing.

In addition, I would like to thank Dr. Paula Wood-Adams and Dr. Suong Van Hoa for providing me test equipments, Danny Juras for assistance in experimental setups. This work was not possible without the efforts of many others in Concordia University. I would like to thank all of professors who have shared their information and insights with me, Concordia staff, Arlene Zimmerman, Leslie Hosein and Lee Harris among many others who helped me directly or indirectly to make this thesis a reality.

To
My Wife,
My Mother & My Father

Contents

List of Figures	xiii
List of Tables	xxii
1 Introduction	1
1.1 Motivation	3
1.2 Tactile Sensing: Previous Work	4
1.3 Human Tactile Sensing	6
1.4 Tactile Sensing in Surgery and Medicine	9
1.5 MIS and Tactile Sensing	11
1.5.1 Force Sensing	14
1.5.2 Force Position	14
1.5.3 Softness Sensing	14
1.5.4 Lump Detection	17
1.6 Piezoelectricity	18
Polyvinylidene Fluoride as a Piezoelectric Material	18
1.7 MicroElectroMechanical Systems (MEMS)	21
1.7.1 MEMS in Surgery	21
1.7.2 Micromachining	23
1.8 Objective of Research	25
1.9 Thesis Scope and Outline	26
2 Characterization of Piezoelectric Polyvinylidene Fluoride Film	28
2.1 Introduction	28

2.2	The Mechanical Properties of Piezoelectric PVDF Film: Uniaxial and Biaxial	29
2.3	The Piezoelectric Properties of the Uniaxial and Biaxial PVDF Films . . .	30
2.3.1	Measurement of d_{31} and d_{32}	31
2.3.2	The Anisotropic Property of Uniaxial PVDF film and its Influence on Sensor Application	33
	Uniaxial PVDF Film	35
	Biaxial PVDF Film	37
2.4	Characterization of Piezoelectric PVDF Film in Sandwich Configurations .	39
2.4.1	The Finite Element Analysis of Sandwiched PVDF for Different Surface Roughnesses	41
	Uniaxial PVDF Film	44
	Biaxial PVDF Film	49
2.5	Experiments	51
2.5.1	Surface Friction Measurement	51
2.5.2	The Experiments Performed on the Sandwiched PVDF for Different Surface Roughnesses	53
2.6	Discussion and Conclusions	55
3	Multifunctional Tactile Sensor: Design, Analysis, Fabrication and Test- ing	58
3.1	Specifications of Tactile Sensors for use in MIS	58
3.2	Design and Structure of the Sensor	60
3.3	Sensor Modeling	62
3.3.1	Analytical Model	62
3.3.2	Finite Element Model	67
3.3.3	Distributed Loads	68
3.3.4	Concentrated Loads	69
3.3.5	Softness Sensing	72
3.4	Sensor Fabrication	75

3.5	Experiments	76
3.5.1	Force Position	76
3.5.2	Softness Sensing	77
3.6	Discussion and Conclusions	81
4	Tissue-Grasper Interaction	83
4.1	Introduction	83
4.2	The Force Signature of MIS Graspers	84
4.2.1	Calibration	84
4.2.2	Force Signature	86
4.3	Hyperelasticity	88
4.4	Hyperelastic Relationships in Uniaxial Loading	89
4.5	Finite Element Modeling	93
4.5.1	The Parametric Study	96
	The Effect of Lump Size	98
	The Effect of Depth	98
	The Effect of Applied Load	101
	The Effect of Lump Stiffness	102
4.6	Experimental Validation	103
4.7	Discussion and Conclusions	108
5	Graphical Rendering of Localized Lumps for MIS Applications	110
5.1	Introduction	110
5.2	System Design	113
5.3	Sensor Structure	114
5.4	Rendering Algorithm	115
5.4.1	Graphical Representation of Localized Lump in One Dimension . .	117
5.4.2	Graphical Representation of Localized Lumps in Two Dimensions .	118
5.5	Finite Element Simulations	124

5.6	Experiments	125
5.7	Results and Discussion	126
5.8	Conclusions	131
6	Design, Analysis, Fabrication and Testing of MEMS Tactile Sensor	133
6.1	Introduction	133
6.2	Sensor Design	134
6.3	3D Finite Element Modeling	137
6.3.1	Simulation Results	139
6.4	Sensor Fabrication	141
6.4.1	Cleaning	143
	Precleaning	144
	Cleaning	145
6.4.2	Oxidation	145
6.4.3	Lithography	146
	Spin Coating	147
	Soft Baking	147
	Exposure	147
	Developing	148
	Hard Bake	148
6.4.4	Oxide layer etching	148
6.4.5	Tetramethylammonium Hydroxide, TMAH Etching	149
6.4.6	Sensor Assembly	152
6.5	Testing & Validation: Softness Characterization	153
6.6	Discussion and Conclusions	158
7	Summary, Conclusions, Contributions and Proposed Future Work	160
7.1	Summary and Conclusions	160
7.2	Contributions	163

7.3	Proposed Future Work	164
References		165
A	Piezoelectric governing equations	183
A-1	The IEEE Notations	190
B	Transverse Vibration of Beams	194
B-1	Distributed load	200
B-2	Concentrated Force	201
C	Large Deformation Mechanics	202
C-1	Measures of deformation in 1-D	202
C-2	Kinematics: Continuum Mechanics Approach	203
C-2.1	Configuration	203
C-2.2	Material and Spatial Descriptions	204
C-2.3	Displacement	205
C-2.4	Deformation Gradient Tensor and Jacobian of the motion	205
C-2.5	Polar Decomposition Theorem	206
C-3	Strain Tensor: Referential formulation	206
C-3.1	Dilation	206
C-3.2	Strain-Displacement Relations	207
C-4	Stress Tensor: Referential formulation	208
C-4.1	Alternative Stress Tensors	209
C-5	Constitutive Equation	209
C-5.1	Constitutive Equations in terms of Invariants	210
C-5.2	Incompressible isotropic hyperelasticity	211
D	Finite Element Formulations	213
D-1	Nonlinear Finite Element formulation	213
D-1.1	Fundamental Equations	214

D-1.2	Mixed Formulation Methods	216
	Mixed u-p Formulation	216
D-2	Piezoelectric formulation	217

List of Figures

1.1	Two typical MIS graspers used for the slippery tissues.	12
1.2	Endoscopic surgery using MIS tools.	12
1.3	The idea of artificial tactile sensing which must be able to extract all required information from the operation environment through a teletaction system and transmit them to the surgeon's hand.	13
1.4	The conventional notations of the principal directions of uniaxial (top) and biaxial (bottom) PVDF film. Uniaxial PVDF film can be classified into orthotropic materials, while biaxial films show behavior similar to the transversely isotropic materials.	20
1.5	Anisotropic etching of a (100)-silicon.	24
2.1	The material testing machine used for the characterization of mechanical properties of PVDF film.	30
2.2	Tested stress-strain characteristics for the uniaxial piezoelectric PVDF in 1-direction as well as 2-direction.	31
2.3	The experimental setup used for measurement of piezoelectric coefficients d_{31} and d_{32}	32
2.4	The results obtained for the piezoelectric coefficients d_{31} and d_{32} of uniaxial piezoelectric PVDF in 1-direction as well as 2-direction, respectively.	33
2.5	The PVDF material coordinate system (1, 2, 3) versus the global coordinate system (x, y, z).	34

2.6	The predicted variations of normalized output voltage of the uniaxial piezoelectric PVDF film for different applied loads. For this simulation load F was 10 N.	36
2.7	Variation of output voltage of the uniaxial piezoelectric PVDF film versus force amplitude for different PVDF deviation angles.	37
2.8	Variation of output voltage of the uniaxial piezoelectric PVDF film versus force amplitude for different PVDF deviation angles. The total voltage (V_{total}), as well as its components associated with coefficients d_{31} ($V_{d_{31}}$) and d_{32} ($V_{d_{32}}$) are separately plotted.	38
2.9	Variation of output voltage of the uniaxial piezoelectric PVDF film versus force amplitude for different PVDF deviation angles.	38
2.10	The geometry of the problem in which a PVDF film is sandwiched between two solid plates and a load is applied in the normal direction.	42
2.11	The total output voltage of a uniaxial PVDF film compressed between two blocks in the presence of the friction.	45
2.12	The output voltages of ten equal PVDF sensing elements are evenly positioned along its 1-axis. While the applied load is kept constant, the friction coefficient is varied between zero to one. The horizontal axis of the graph is normalized by half the length of the PVDF film.	47
2.13	The distribution of output voltage over the uniaxial PVDF film segments compressed between two plates in the presence of a friction of $\mu = 1$. The horizontal axis of the graph is normalized by half the length of the PVDF film.	48
2.14	The response of the PVDF film against applied pressure for different friction coefficients.	49
2.15	The total output voltage of a biaxial PVDF film compressed between two plates in the presence of the friction.	50

2.16	The output voltages of ten equal biaxial PVDF sensing elements evenly positioned along the x-axis. While the applied load is kept constant, the friction coefficient is varied between zero and one. The horizontal axis is normalized by half the length of PVDF film, and hence zero represents the center of the film and 1 denotes the PVDF edge at x=15 mm.	51
2.17	The experimental setup used to measure friction coefficients. PVDF films were adhered to both sides of mid-plate. The friction surfaces were attached to the internal surfaces of top and bottom plates.	52
2.18	In this part of the experimental setup the PVDF film is sandwiched between two plates. The internal surfaces of the plates are covered with the pre-characterized surfaces.	53
2.19	The configuration used for the experiment to measure the PVDF response to the friction material.	54
2.20	A view of experimental setup used to measure the PVDF response to the friction materials.	54
2.21	Comparison between theoretical data and experimental results. For both cases a 20 N force is applied (errorbar indicates the range of readings).	56
3.1	The scheme of a MIS grasper equipped with an array of the proposed sensor. . .	60
3.2	Cross section of a sensor unit (one tooth).	61
3.3	The basic scheme for the proposed softness sensing technique.	61
3.4	The cross section of the beam and contacted object. The initial composite beam is transformed to an equivalent beam with only one material.	64
3.5	The kinematics of deformed beam (Kirchhoff Theory).	65
3.6	Predicted variations of output charge for a given sinusoidal input force. . . .	66
3.7	The linear relation between the uniform distributed load and the output voltage of the middle PVDF film.	69

3.8	The outputs of the middle PVDF (V_{Mid}), support1 (V_{Sup1}) and support2 (V_{Sup2}) when point load is applied at different locations along the beam (The PVDF drawn direction at the supports, is aligned with the X-axis direction, while the drawn direction of the middle PVDF is rotated by 90 degrees so that it is perpendicular to the X-axis).	70
3.9	The outputs of the middle PVDF (V_{Mid}), support1 (V_{Sup1}) and support2 (V_{Sup2}) when point load is applied at different locations along the beam (The PVDF at the supports are rotated by 90 degree so that they are perpendicular to the X-axis direction, while the drawn direction of the film in the middle is aligned with the X-axis).	71
3.10	The total output of either supports when a point load ranged from 0.5 to 5 N is applied to the middle of the sensor.	73
3.11	The output of the PVDF films at the supports when distributed loads ranged from 0.75 to 4.5 N applied to the elastomeric objects with different Young's modulus.	74
3.12	The output of the middle PVDF film when distributed load ranged from 0.75 N to 4.5 N is applied on to the soft objects.	74
3.13	A picture of the manufactured sensor, with a known load applied at the mid point of the sensor.	75
3.14	Block diagram of the electrical components used for amplification, signal conditioning and recording the PVDF film output.	78
3.15	The output of middle PVDF film when a load was applied along the sensor at equal intervals (errorbar indicates the range of readings).	78
3.16	The picture of the Type A Test Block Kit used as standard soft material for softness sensing characterization. Under each color the softness number in Shore A scale is indicated.	79
3.17	The compressive stress-strain curve obtained for standard silicon rubbers. . . .	80

3.18	The relationship between the compressive Young's modulus of the silicon rubbers and their associated softness number in shore A scale (errorbar indicates the range of readings).	80
3.19	The output of middle PVDF film, when a 3 N load was applied to silicon rubbers with softness ranging from 32 to 89 shore A (errorbar indicates the range of readings).	81
4.1	The picture of endoscopic grasper, soft object and the sensor used for this experiment.	85
4.2	The experimental relationship between applied force and conductance of the sensor.	85
4.3	The relationship between applied force and sensor's output voltage.	86
4.4	The force profile experienced by a grasped soft object. V_0 is the output voltage of the sensor. The corresponding force, sensed by the sensor is also shown in the middle graph. The frequency content (Hz) of the force shows that the force waveform is very similar to sinusoidal or half-sinusoidal waveforms.	87
4.5	The force profile experienced by a grasped hard object.	88
4.6	Comparison between testing and 3-term Mooney-Rivlin strain energy function. The horizontal and vertical axes are engineering strain and engineering stress, respectively.	93
4.7	A half-model of soft tissue which contains a lump	97
4.8	The pressure distribution at the contact surface when the lump radius was increased from $R = 1 \text{ mm}$ to $R = 4 \text{ mm}$ and $P_{in} = 5 \text{ kPa}$	99
4.9	The pressure distribution at the contact surface when the lump radius was increased from $R = 1 \text{ mm}$ to $R = 4 \text{ mm}$	99
4.10	The effect of lump depth on the stress distribution when $P_{in} \approx 10 \text{ kPa}$, $R = 2 \text{ mm}$ and the center of the lump is changed from 2 mm to 8 mm from the contact (bottom) surface.	100
4.11	Peak pressures for different lump depths when $P_{in} \approx 10 \text{ kPa}$, $R = 2 \text{ mm}$ and the center of the lump is changed from 2 mm to 8 mm from the contact surface.	101

4.12	The variation of stress profile due to the variations of applied load. The values are normalized based on the background pressure for $U = 1mm$. In these simulations the lump with the radius of $R = 2 mm$ was located in the middle of the tissue. .	102
4.13	The maximum pressures obtained from nonlinear analysis against those of linear analysis. Simulation conditions are similar to that of Figure 4.12.	103
4.14	The stress distribution for different E_L , the Young's modulus of the lump while the Young's modulus of tissue was kept constant at $E_T = 15 kPa$. The applied load was $U_y = 1 mm$ and the lump was considered to be in the middle of the tissue.	104
4.15	The pressure ratio for different E_L/E_T . The similar values for the parameters that of Figure 4.14.	104
4.16	The sensor with seven sensing elements is connected to DAQ.	106
4.17	Soft object with embedded lumps under the test. Top plate was to replicate the upper jaw of grasper to apply compressive loads.	106
4.18	The experimental data versus finite element results (error bar indicates the range of readings). The simulation conditions for Test1: $U_y = 2.5 mm$, $R = 3 mm$, Depth= $5 mm$ and for Test2 : $U_y = 1 mm$, $R = 2 mm$, Depth= $4 mm$	107
5.1	Components of the proposed system.	114
5.2	A view of the grasper with one active jaw equipped with an array of the seven sensing elements.	115
5.3	Locating the lump in one direction and its graphical rendering.	119
5.4	The second design of grasper in which both upper and lower jaws are equipped with sensing elements.	120
5.5	The flowchart of the algorithm implemented in LabView and used for the graphical rendering.	121

5.6	The graphical rendering of the characterized lump in two dimensions. (a) A lump located in a soft material with the upper and lower sensor arrays, (b) 2D intensity graph associated with the sensor array outputs, (c) A 7x7 matrix showing the location of the lump, (d) A 60x100 matrix that gives a better information on location and size of the lump.	122
5.7	The relationship between grasped object and intensity matrix.	122
5.8	A view of the sectioned and meshed finite element model of soft object and the embedded lump.	125
5.9	Photographs of the sensors under the test. (a) The sensor with one active jaw used for construction of one dimension graphical images. (b) The sensor with two active jaws used for two-dimension graphical rendering of detected lumps. .	127
5.10	Photograph of the experimental setup.	128
5.11	The experimental and analytical results of four case study.	129
5.12	The experimental and analytical results for two dimensional localization. Each row illustrates the information of the studied case. In the right column, the dashed line represents the output voltages of the lower array of the sensors, while the solid line is associated with the upper jaw.	130
6.1	A proposed design of the smart grasper in which the incorporation of microfabricated sensor is presented.	135
6.2	Backside view of the sensor's top part. The positions of the PVDF films and the electrodes configurations are illustrated in this view.	135
6.3	The scheme of top and bottom parts,(dimensions are in mm).	137
6.4	The meshed FEM model of the MEMS tactile sensor.	137
6.5	The deflected structure when a distributed load of 111 kPa was applied to the first beam and its two supports.	139
6.6	The deflection curve of first beam when a distributed load of 111 kPa is applied to the beam and its two end supports. Solid line illustrates the result obtained from Equation 6.1, while the squares indicate the FEM results.	139

6.7	(a) The actual cross section after anisotropic etching, (b) the equivalent rectangular cross section used in closed form formula and finite element analysis. In both cases the thickness was 180 μm	140
6.8	The finite element model of the sensor when a soft material is placed on the first tooth and a uniform compressive load is applied.	141
6.9	The output of the middle PVDF film at constant pressure 111 kPa when the Young's modulus of the contact object is varied between 0.01 MPa and 1 MPa. .	142
6.10	Process flow of micromachining process used for top and bottom parts.	143
6.11	The sequence of micromachining process summarized.	144
6.12	The mask patterns used for the lithography process. While the bottom left pattern is the the one that was used for bottom part (supports), the other three patterns were used to fabricate top parts with 1,3 and 4 hanging beams.	147
6.13	The samples after development process.	148
6.14	The TMAH etching setup used for micromachining.	150
6.15	Some samples of micromachined silicones are shown.	151
6.16	A micromachined beam and a support. (The (100) plane, which is parallel to the paper is shown. The {111} planes which make two sides of the beam are also illustrated).	151
6.17	The void space between two adjacent beams.	151
6.18	The top part of the sensor. PVDF film at the supports and attached to the beams are shown. The direction of the PVDF films are also shown.	152
6.19	The macromachined tactile sensor.	153
6.20	A picture of durometer used in this study.	154
6.21	Durometer type OO.	155
6.22	Durometer dial reading scale OO versus Young's modulus of soft objects are plotted.	156
6.23	MEMS sensor being tested using a electrodynamic shaker.	156

6.24 Durometer dial reading scale OO versus Young's modulus of soft objects are plotted.	157
6.25 Durometer dial reading scale OO versus Young's modulus of soft objects are plotted.	158
A.1 The relations between mechanical, electrical and thermal properties of a crystal. The names of the effects are shown. The tensor rank of each variable is shown in round brackets and the rank of the properties in square brackets [89].	184
A.2 The relations between mechanical, electrical and thermal properties of a crystal. The symbols corresponding to each variable and properties are illustrated [89].	185
A.3 The number of independent variables for $mm2$ class. The darker circles show non-zero components.	189
B.1 Schematic of the prismatic bar and its free body diagram.	194
C.1 The undeformed and deformed length of a bar.	202
C.2 Displacement field of a typical particle.	205

List of Tables

2.1	PVDF properties reported by manufacturers. Piezoelectric and Elastic coefficients are given in pC/N and GPa respectively. The symbol d_{3h} , represents the hydrostatic piezoelectric coefficient.	34
2.2	List of abrasive materials and their corresponding friction coefficients.	53
3.1	The specification of Type A Test Block Kit.	77
4.1	The constants of 2 and 3 terms Mooney-Rivlin Model (kPa).	93
6.1	The maximum beam deflection at the center, Y_{max} , corresponding stress in x-direction, σ_x , and the output voltage of the middle PVDF film, V_{mid} when Young's modulus of the contact object, E_{obj} is varied between 0.01 MPa to 1 MPa.142	
6.2	General specifications of durometers type A and OO.	154
A.1	Conversion table for replacing tensor indices with matrix indices.	191
D.1	Description of terms in equations D-13	220

Abbreviations

ALE	: Lagrangian-Eulerian formulation
ASTM	: American society for testing and materials
DAQ	: data acquisition card
DC	: direct current
DMF	: dimethylformamide
EC	: European community
ESP	: electro spray
FDA	: food and drug administration
FEM	: finite element modeling
FSR	: force sensitive resistor
IRDH	: industrial rubber hardness degrees
LVDT	: linear variable differential transformer
MEMS	: microelectromechanical system
MIS	: minimally invasive surgery
PC	: Pacinian corpuscles
PVDF	: polyvinylidene fluoride
RA	: rapid adaptor
SA	: slow adaptor
TL	: total Lagrangian method
TMAH	: tetramethylammonium hydroxide
TPDT	: two-point discrimination threshold
UL	: updated Lagrangian method
UV	: ultra violet

Chapter 1

Introduction

Surgery is the treatment of diseases or other ailments through manual and instrumental means. In the past, this involved cutting and swing of tissues. However, advances in surgery have helped reducing or eliminating the invasiveness of surgical procedures. In *open surgery* referred to as first-generation technique, a large incision would be made in the body allowing the surgeon to have full access to the surgical area. In open surgery, surgeon is able to come into contact with organs and tissues and to manipulate them freely. While a large incision allows the surgeon to have a wide range of motion as well as tissue assessment through palpation, it causes a lot of trauma to the patient. Increasingly, surgeons begin to realize the limitations they encounter in the operating theaters [1]. For instance, in a conventional open-heart cardiac operation , the rib cage must be cracked and split, exposing the heart muscle. The invasiveness of the procedure causes a long hospital stay, increasing costs and pain to the patient. In many surgical procedures, the majority of trauma to the patient is caused by the surgeon's incisions to gain access to the surgical site rather than the procedure itself. For instance, for cholecystectomies (or gall bladder removal surgery), as 59% of the postoperative hospital stay is the result of trauma caused by incisions in the abdomen to gain access to the gall bladder instead of the actual removal of the gall bladder [2].

To overcome many of the shortcomings and complications of open surgery, the minimally invasive surgery, referred to as the second generation surgical procedure, uses a

few small holes, access points, or ports that are punctured into the body and trocars are inserted through them. A trocar consists of a guiding canula or tube with a valve/seal system to allow the body to be inflated with carbon dioxide. An endoscope is inserted into one of the trocar ports to allow the surgeon to have a view of the surgical site. Various other surgical instruments such as clippers, scissors, graspers, shears, cauterizes, dissectors, and irrigators are mounted on long poles and can be inserted and removed from the other trocar ports to allow the surgeon to perform the necessary tasks. Using a monitor to watch the operation is not very intuitive and it disrupts the natural hand-eye coordination. In addition the 2-D image eliminates the surgeon's depth perception [3]. As the images from the camera are magnified, small motion such as the tremor in camera or even the heartbeat can cause the surgical team to experience motion-induced nausea. Another difficulty in MIS is caused by the trocars that act as pivot points in order to amplify surgeon's movement. In addition, there is no tactile feedback, so the surgeon has no sense of how hard he is pulling or cutting or twisting or suturing, etc. These factors cause a number of adjustments to be made by the surgeon, which require significant retraining on how to do the procedures in a minimally invasive surgery. These hardships also limits surgeons to perform only simpler surgical procedures. Nowadays, modern surgical procedures are far more complex than that of the past and the surgeons knowledge and skill alone may not guarantee the success of an operation [4]. To rectify some of these problems the third-generation of surgical procedures, robotic surgery, was developed. Robotic surgery can bring about various benefits, such as: reducing the stress on the surgeons, decreasing the surgery duration, and reducing the time required for a patient to recover from an operation [5, 6]. However, the current medical robots have not eliminated all above mentioned shortcomings in MIS. As an example, Da Vinci and Zeus medical robots have rectified a number of MIS shortcomings, nevertheless surgeons still suffer from lack of tactile sensing and its associated capabilities [7, 8].

The ability to distinguish between different types of tissue in the body is of vital importance to a surgeon. Before making an incision into tissue, the surgeon must identify

what type of tissue is being incised, such as fatty, muscular, vascular, or nerve tissue. Failure to properly classify tissue can cause severe consequences. For example, if a surgeon fails to properly classify a nerve and cuts it, then the patient can suffer effects ranging from a loss of feeling to loss of motor control. The identification and classification of different types of tissue during surgery, and more importantly during cutting operation, will lead to the creation of *smart surgical tools*. One major approach in developing smart surgical tools is retrofitting of the existing surgical tools instead of developing new and revolutionary tools due to its advantages. Surgical tools are subject to many regulatory controls, such as Food and Drug Administration (FDA) and European Community (EC), that normally takes 5 to 15 years long [9]. Therefore, retrofitting current surgical tools is preferred as it is the fastest path to the market. In addition, the modified tools have already been accepted by surgeons who are familiar with their applications and use. Furthermore, the costly clinical trials can be avoided or reduced for retrofitted tools.

To sum up, smart endoscopic tools are highly required to enhance the current state of MIS and surgical robots performance. To do this, using of the existing MIS tools as host and developing smart compartment to the host structure would be highly beneficial and desirable.

1.1 Motivation

Minimally invasive procedures are growing rapidly, with 40% of surgeries being performed in this manner and in the next decade 80% of all surgeries will be done using MIS [10]. However, despite many advantages of MIS to the traditional surgery, almost complete lack of a sense of touch is one of the principal shortcomings in today's MIS procedures. Using of long slender MIS tools has imposed sever restrictions on surgeon's tactile capabilities when compared with the traditional open surgery. Restoring the lost tactile perception has been the motivation of several recent research works including the present research. In addition to the introduction of an innovative multifunctional tactile sensor which can

be integrated into the conventional MIS tools, exploring of potential capabilities of such sensors in terms of force measurement, force position sensing, softness sensing is of high importance. Another challenging problem in this area is the development of methodologies for interpreting and converting the data gathered by tactile sensors into a useful format for surgeons. In this regard, several attempts have been made to develop different kinds of tactile display. However, none of them has found practical application due to the difficulties in using them. This provided the motivation for introducing a graphical scheme in which the tactile information is graphically presented to the surgeon.

1.2 Tactile Sensing: Previous Work

Tactile sensing can be defined as a form of sensing that can measure given properties of an object through physical contact between the sensor and the object. Tactile sensors, therefore, are used for measuring the parameters of a contact between the sensor and an object. In other words, they detect and measure the spatial distribution of forces on a sensory area. The processes of slip and touch sensing can also be related to tactile sensing. Slip, in effect, is the measurement and detection of the movement of an object relative to the sensor. Touch sensing can be correlated with the detection and measurement of a contact force at a specified point. The spectrum of stimuli that can be covered by tactile sensing ranges from providing information about the status of contact, such as presence or absence of an object in contact with the sensor, to a thorough mapping or imaging of the tactile state and the object surface texture [11].

There are two determining factors in the design of a variety of tactile sensors. The first one is the type of application and the second is the type of object to be contacted [12]. For instance, unlike hard objects, when the tactile sensor is targeted towards soft objects (e.g. most biological tissues), more complexities arise and there is a need for more sophisticated designs. In general, tactile sensors can be divided into the following categories: mechanical (binary touch mechanism), capacitive, magnetic, optical, piezoelectric,

piezoresistive (strain gauges), and silicon-based (micro-electromechanical).

One of the most exciting and relatively new application areas for tactile sensor is in robotics, minimally invasive surgery and robotic minimally invasive surgery [13]. Numerous research work in design and manufacturing of variety of tactile sensing has been reported. For instance, the development of a 8×8 silicon pressure tactile sensor array with on-chip signal readout circuits has been implemented by Wen *et al.* [14]. The integrated sensor array was fabricated using a combination of microelectromechanical systems (MEMS) and microelectronics. The prototype device was characterized in the pressure range of 0-150 kPa, in which the sensors exhibited a linear response with a mean sensitivity of 30.1 mV/kPa. Another tactile sensor chip has been developed for measuring distribution of forces on its surface [15]. The chip has eight force-sensitive areas, called taxel, with a pitch of $240 \mu m$. Surface micromachining techniques are used to produce small cavities that work as pressure-sensitive capacitors. To enable transduction of normal forces to the sensitive areas, the sensor chip surface was covered with silicone rubber. The radius of the sphere and the load working on it can be estimated with high precision from the tactile sensor output data. An integrated three-dimensional tactile sensor with robust MEMS structure and soft contact surface suitable for robotic applications has been developed by Mei *et. al* [16]. The sensor has a maximum force range of 50N in the vertical direction and $\pm 10N$ in the x and y horizontal directions. The tactile sensor includes 4×8 sensing cells each exhibiting an independent, linear response to the three components of forces applied on the cells. With neural network training, the tactile sensor produced reliable three-dimensional force measurements and repeatable response on tactile images. Another study describes the development of a new type of tactile sensor, which is designed to operate with a PZT element employed as the sensor [17]. Most researchers have attempted to design tactile sensors with a number of discrete sensing elements arranged in a matrix form [18]. The main problem with this type of design is cross talk [19]. Although the force is actually exerted on a single element of the matrix, an undesirable response from the adjacent sensing elements often occurs. This, in turn, leads

to error in measurement. In cases where polyvinylidene fluoride (PVDF) film has been used as the basis for the design of a matrix of high spatial resolution tactile sensors, the same crosstalk problems have often been reported [18]. A further problem with the matrix array of PVDF sensing elements is that, it requires one coaxial cable for each sensing element. The more the number of sensing elements the more the number of connection points. Consequently, this leads to sensor fragility and causes the design to be a bulky one, which is highly disadvantageous in various robotic applications. Therefore, to avoid mentioned difficulties, development of tactile sensors with minimal sensing elements has also been taken into account by researchers.

1.3 Human Tactile Sensing

Prior to any attempt for development of a suitable tactile sensor that can replace a human hand, a very concise review of structure, mechanisms and capabilities of human hand is helpful. Generally speaking, human tactile sensing has a complex nature and to find suitable technological analogies in science or engineering is not an easy task [20, 21]. The nature of tactile sensing through the skin is not simply the transduction of one physical property into an electronic signal. This is mainly because the sense of touch assumes many forms [22]. These forms include the detection of temperature, texture, shape, force, friction, pain, and other related physical properties [23, 24]. In addition, unlike the visual and auditory senses, the touch signal is not a well-defined quantity and the researchers of this field are still dealing with the basics of collecting the most relevant data [25, 26].

Contact sensing in human normally is divided into *kinesthetic sensing* and *cutaneous sensing* [27]. The kinesthetic information refers to geometric, kinetic and force data of the limbs, such as position and velocity of joints, actuation forces etc., which is mainly mediated by sensory receptors in muscles, articular capsulae and tendons. These (kinesthetic) receptors include muscle spindles, which respond to changes in muscle length, and tendon organs, which sense muscle tension [28]. The cutaneous sensing is the perception

of contact information with receptors in the skin such as pressure and deformation, both in space and in time. Considerable research has been devoted to detailing the function of human cutaneous sensing [29, 21]. There are about 17000 mechanoreceptor in the grasping surfaces of the human hand, comprising Meissner's Corpuscles, Merkel Disks, Ruffini Organs, and Pacinian Corpuscles (PC), differentiated into classes depending on their receptive fields, speed and intensity with which they adapt to static stimuli [30]. In addition to these specialized mechanoreceptors, there are many free nerve endings in the finger tip skin which respond to local mechanical deformation [31]. Some free nerve endings are sensitive to thermal and pain stimuli. Thus, our tactile sensory experience is built from a variety of sensors responding to a number of physical parameters.

In general, human sensing and motor control bandwidths range from a few Hz to several hundred Hz [32](which is slow in comparison with robotic manipulators). Nerve conduction velocities are usually less than about 60 *m/s*. Latencies are at least 20 – 30 *m/s* for the fastest reflexes and much longer for other reflexes and voluntary responses. Generally speaking these sensors are hysteretic, nonlinear, time varying, and slow.

Tactile receptors are located in clusters around the human skin and they look like jelly material. When they are stimulated or squeezed in some way, the layers rub against each other causing an electrical nerve to be generated. Then, these nerve signals flash to the brain, where an overall touch picture from these nerve signals is assembled [33]. Sense of touch involves arrays of different nerve types and sensing elements to relay a whole body experience [30]. This is contrary to other senses, which are localized in the eyes, nose, mouth, and ears. These receptors, or tactile units, are all located in the various layers of the skin, which provides support and protection from the external environment. The skin of the hand, in particular, is highly specialized to provide detailed tactile feedback [34]. The glabrous (hairless) skin on the front of the hand contains the most nerve endings. They peak in density on the central whorl of the fingertips. Various types of mechanoreceptors can be categorized as: Type I with small receptive fields; Type II with large fields; rapid adaptors (RA) which have no static response; and slow adaptors

(SA) which do not stop firing in response to a constant stimulus. One of the important features of skin mechanoreceptors is their spatial resolution [18, 35]. For example, when two different places on human skin are touched simultaneously by two sharp objects, it can be shown that there is a minimum resolvable spacing between the contact points. Additionally, it can be proven that this minimum resolvable separation is different in various parts of the human anatomy [36].

When a force is applied to the tip of the finger, the large receptive, rapidly adapting PC units located all over the finger and palm will fire indicating a stimulation occurring somewhere. As a result, the small receptor of RA (e.g., Meissner's Corpuscle) units around the location of the application of the force will also fire. If, however, the stimuli are held stationary, the SA I (e.g., Merkel Disk) and SA II (e.g., Ruffini Endings) will consequently exhibit afferent responses. It has been suggested that the SA II units are very sensitive to tangential forces [20], while the SA I units might code both normal and shear forces [35]. With regard to the individual receptors, the Merkel Disks are reported to respond to both compression and shear forces, and free nerve endings are sensitive to slight pressures. With regard of the position of the load, the rapidly adapting RA units will provide information about to the position, while slowly adapting units of SA I will indicate the size of the stimuli [37]. However, the PC units and SA II units will also be active, indicating that something is happening somewhere.

It has been speculated that the sensation of softness may correlate with activity in the SA I fibers because their rate of firing is determined by the amount of sustained deformation. However, softness/hardness perception requires vertical motion [37], thus the rapidly adapting units might contribute to the perception of softness, indicating local stimulation. The PC units will also be active for the same reason as discussed in the case of position and size stimuli.

If a sensor is to mimic the human hand tactile capabilities, then a set of finger-like criteria extracted from analysis of human sensing can be defined and used as (sometimes minimum) desired conditions. Having said that, an artificial tactile sensor would require

an array of sensors with spatial resolution of about 1-2 mm [26], which translates to an approximately 10-15 element grid on a fingertip-sized area. In terms of force sensitivity if the analogy is considered appropriate, then a sensitivity range of 0.01-10 Newton would be required to be delivered in a tactile sensor and a dynamic range of 1000:1 would be considered satisfactory [18]. In summary, the sensor should demonstrate high sensitivity and broad dynamic range. With regard to human capabilities, the vibration bandwidth reported at the fingertips is a few Hz for separate touches and several hundreds Hz for merely sensing vibration [32]. However, this is another parameter, which cannot be readily considered in terms of human fingertip analogue. The potential complexity of a data processing system coupled with a tactile sensor and, in particular, the continued need to update the information coming from the sensor, necessitate the fastest response time possible. In summary, the response time of the touch-transducer should be small compared to the time of an overall control-loop cycle. In addition to the above factors, tactile sensors should ideally be capable of withstanding harsh environments, for example, temperature, humidity, radiation, and chemical stresses. In other words, they should remain robust and unaffected in terms of physical properties despite continued usage and have minimal tactile cross-talk. Additionally, they should not be affected by electric field effects.

1.4 Tactile Sensing in Surgery and Medicine

There are a considerable number of interesting applications for tactile sensors in the industries such as, health care, service robotics, agriculture, and food processing [18, 22]. However, their applications in surgery and medicine are highly unique [38]. Surgery is essentially a visual and tactile experience and any limitations on the surgeon's sensory abilities are most undesirable. From the biomedical engineering point of view, minimally invasive surgery (MIS) is probably the fastest developing area of research in which the use of tactile and visual sensing is actually of critical importance [39, 40]. Despite the fact that MIS is about two decades old, it is now being used routinely as one of the most preferred

choices for various types of operations. Here, in spite of its many advantages such as, less pain, reduction of trauma, faster recovery time, smaller injuries, and reduction of post-operation complications, MIS reduces the tactile sensory perception of the surgeon during grasping or manipulation of biological tissues. It has been reported that measuring the magnitude and location of the applied forces exerted by the endoscopic grasper during MIS is the fundamental requirement for the safe handling of biological tissues [41]. In effect, to perform MIS more efficiently, a surgeon should be able to feel the tissues and detect the presence of blood vessels and ducts during the procedures. The ability of sensing the soft tissues is especially important during controlled manipulation tasks, for example, grasping of internal organs, gentle load transferring during lifting, removing tissues (e.g., gallbladder in laparoscopic surgery and loose bodies in knee arthroscopy), and suturing tissues together. The necessity of tactile sensing becomes more evident, when the surgeons need to manipulate soft tissues (e.g., palpation) using MIS procedures [42]. Here, to identify and examine various properties of soft tissues, such as, softness and texture are very difficult, since the surgeon is mostly relying on his/her visual abilities. This, in turn, means that locating hidden anatomical features such as tumors, or sensing the abnormal stiffness of organs can be adversely affected [43].

Another interesting application of artificial tactile sensing is in telemedicine procedures [44, 45]. Telemedicine allows health care professionals to use connected medical devices in the evaluation, diagnosis, and treatment of patients in other locations, including space ships. Using medical robotics, telecommunications technology, network computing, and videoconferencing systems, the performance of these devices can be enhanced [46]. One of the most important aspects of using telemedicine is to enable surgeons to perform various procedures at remote locations. These procedures include minor surgeries, consultation, or palpation. For instance, during the human missions to the lunar surface, astronauts are thousands of miles away from definitive medical care. Because of this great distance from the Earth, new systems and procedures should be developed to support in-flight medical operations. To achieve these goals, telesurgical methods can be employed. Telesurgery

uses the technological advances acquired in both robots and telemetry [47]. Surgical telemanipulation or teletaction, using the advantages of tactile sensing, is possibly one of the future applications of telemedicine-based telesurgical procedures.

1.5 MIS and Tactile Sensing

The minimally invasive idea emerged around 25 years ago with the re-emergence of laparoscopy - a procedure that passes a telescope-like instrument with a built-in light source into the abdomen through tiny incisions in the belly. Through this telescope, the surgeon is able to directly view organs inside the abdomen, and even perform operations on them. Laparoscopy suddenly caught the imagination of general surgeons who saw great potential for use in other situations. Thoracic surgeons (who operate upon the lungs and other organs inside the chest) were quick to see the potential in their field as well. Using a modified laparoscope (promptly re-named a "Thorascope") the pioneers examined diseases of the lungs and food pipe, and carried out minor operations. As they gained experience and confidence, and as technological developments helped create better and versatile instruments, more and more complex operations became possible. Although the first use of the minimally invasive surgery backs to many years ago, MIS began its victory train through the operation rooms in recent years. Indeed the penetration speed was breathtaking and today numerous types of operations are done by this technique. The minimally invasive surgery, also called endoscopic surgery, is regarded as a powerful technique that gives a patient's fast recovery as minimizing tissue damage [1, 48]. MIS uses long tools (see Figure 1.1) and tiny cameras inserted through small incisions in the body to access the organ. According to the operation fields, MIS is classified into thoracoscopy, arthroscopy, pelviscopy, angioscopy, laparoscopy, etc. For instance, Figure 1.2 shows a knee surgery utilizing endoscopic tools. The representative field of MIS is the laparoscopy surgery (abdominal and pelvic organs) that has a larger workspace than the others of MIS.

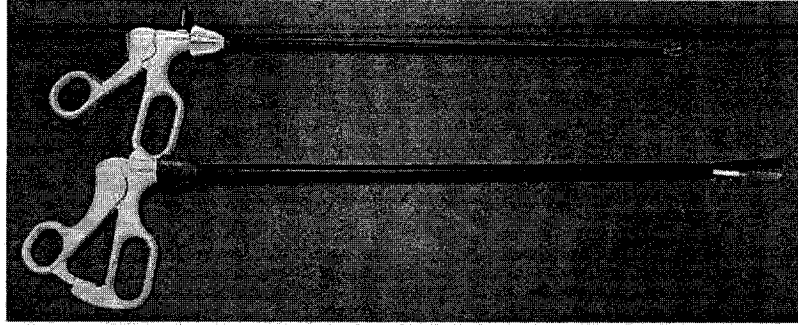


Figure 1.1: Two typical MIS graspers used for the slippery tissues.

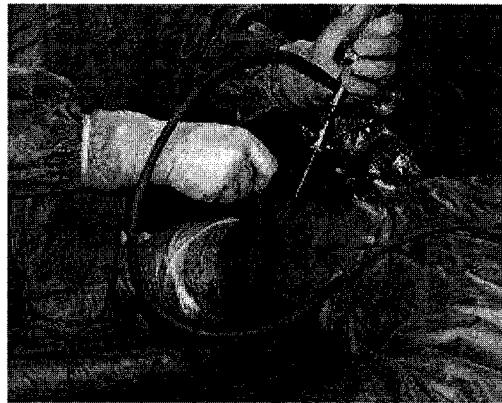


Figure 1.2: Endoscopic surgery using MIS tools.

The minimally invasive surgical approach offers several advantages over traditional open surgery. First of all, the cosmetic result is almost always superior to that achieved with an open operation. For many operations, post-operative pain is significantly reduced. Earlier return to routine, faster discharge from the hospital, and a more rapid return to full activities are additional benefits. Surgeons skilled in minimally invasive surgical procedures regularly perform them as rapidly as they perform the equivalent open operations. Furthermore, the reduction in patient hospital stay results in an actual lowering of total hospital costs for many of the procedures performed. Since the advantages and disadvantages of MIS are normally compared with open surgery, the ideal tactile sensing capability of an ideal MIS tool is assumed to replicate the human tactile perceptions. Figure 1.3 [49]

shows that surgical instruments should ideally substitute human finger tactile capabilities.

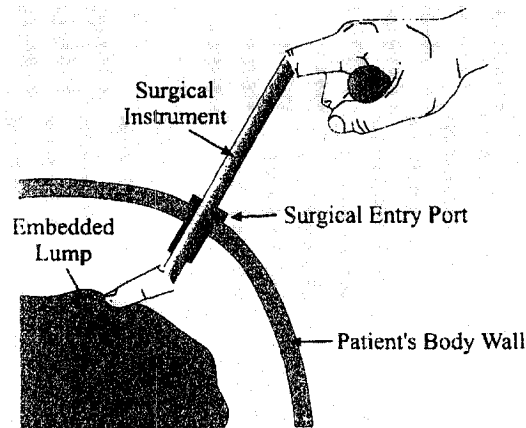


Figure 1.3: The idea of artificial tactile sensing which must be able to extract all required information from the operation environment through a teletaction system and transmit them to the surgeon's hand.

Human finger is able to detect softness, texture, temperature, vibration, friction, object shape, and moisture content of the contact object. For surgeons, softness sensing, texture and palpation are the most important and functional ones. However, an ideal endoscope must measure all parameters that a human hand are able to detect and transmit them to the surgeon by means of a tactile display. Tactile display, in turn, should be able to reconstruct all these information for the surgeon. Ideally, surgeons must be able to obtain comprehensive knowledge of the operation field through an intelligent endoscopic tool. Particularly, they must be informed of the magnitude of the applying forces and the threshold not to damage tissue. Gregory [50] *et al.* emphasize on the importance of the force feedback on performance of MIS. Their results show that subjects are more comfortable and more accurate at characterizing tissues with simultaneous vision and force feedback compared to vision feedback alone. The advancement of MIS techniques is also helpful for the development of Robotic Assisted Minimally Invasive Surgery as well as Tele-Robotic Minimally Invasive Surgery and in general for teleoperation procedures. Since MIS is a kind of teleoperation, as hands of surgeon are not in the site of operation,

minimally invasive tools can readily be integrated into teleoperation systems.

1.5.1 Force Sensing

Force sensing, is a basic and necessary capability of tactile sensors that has been investigated for a long time. Today very sophisticated force sensors for both concentrated and distributed force/pressure are available in the market. The majority of tactile sensors are working based on piezoelectric, piezoresistive and capacitive techniques or a combination of these properties [12, 21, 22, 51].

1.5.2 Force Position

The capability of finding the position of applied load is believed to be very useful in MIS procedures. A homogenous soft object compressed between two jaws of MIS grasper experiences a uniform distributed load. However, as shown in Chapter 4, the presence of an embedded lump in a grasped soft object appears as a point load superimposed on a uniform distributed load. Therefore, one of the immediate and most interesting applications of force position sensitivity as shown in this research is in locating any hidden features in bulky soft object. Nevertheless, the application of force position sensitivity is not only limited to lump detection.

1.5.3 Softness Sensing

Softness/hardness of the soft objects is defined as resistance of material to deformation (or indentation) [52, 53]. Hardness sensing is already in use in industry. There are specific procedures to measure the hardness of the hard objects. However to measure the softness of the soft objects generally and the soft tissues particularly, one must consider the behavior of the contact object. Soft tissues are nonlinear and viscoelastic materials. In addition they show hysteresis in loading and unloading. Variation in characteristics of the different soft tissues adds even more complexity to the problem. Characterization of

the soft tissues has been restricted by the fact that the behavior of the soft tissues differs *in vivo* from *ex vivo* conditions.

The softness testing of soft objects is most commonly measured by the shore (Durometer) test. This method measures the resistance of the object toward indentation and provides an empirical hardness value that does not have explicit relation to the other properties or fundamental characteristics. Shore hardness, using either the shore A or shore D or shore OO scale, is the preferred method for rubbers/elastomers. While shore OO is used to measure the softness of very soft materials, shore A scale is used for soft rubbers and the shore D scale is used for harder ones. The shore A softness is the relative softness of elastic materials such as rubber or soft plastics and can be determined with an instrument called a shore A durometer [53]. International Rubber Hardness Degrees (IRHD) also introduces a measurement scale for this purpose. Young's modulus can be related to the softness of soft objects by a nonlinear relationship and can represent how much spring force, a rubber component will exert when subjected to a deformation. Several researchers have attempted to measure the softness of soft objects in different ways. One method is using piezoelectric material in their natural frequency and differentiating contact objects due to shift in natural frequency. Reported shift in natural frequency for wooden plate to silicone gum is about 750 Hz [54]. Using mechanical torsional step and then measuring the transient response to this stimuli is reported by Yamamoto [55]. They used a rotational step motor to create a screw-like motion in soft tissue. At this moment, viscoelasticity of the epidermis is evaluated from analyzing the inducting coil of the step motor. The waveform of the voltage of inducing coil can be characterized by overshoot, damping ratio and undamped natural frequency. Hardness evaluation was carried out by Bajcsy [56], by pressing a robotic finger, sensorized with a low spatial resolution tactile sensor, against the object. This was performed in small incremental displacement steps, and by reading the sensor output during the loading and subsequent unloading processes. Material hardness was ranked according to the slopes of the linear parts of the loading and unloading sensor outputs. Work along similar lines was reported by Bardelli *et al*

[57], using a single element sensor made of a piezoelectric polymer pressed against flat sheets of rubbery materials of different compliance and backed by a reference load cell. Hardness ranking was associated with the slope of the straight line obtained in the sensor out-put reference cell signal plane under loading. De Rossi *et al* [58] proposed the use of charged polymer hydrogels as materials useful in tactile sensing, in particular for softness perception, because of their ideal compliance matching with human skin. Softness sensing has been applied as a diagnostic tool. For example in diabetic neuropathic subjects, the hardness of foot sole soft tissue increases in different foot sole areas [59]. Using an active palpation sensor for detecting prostate cancer and hypertrophy is reported by Tanaka [60].

Although a number of tactile sensors have already been designed, analyzed and manufactured [11, 60, 61, 62, 63], some of them for MIS applications, most of the developed tactile sensors are confined to force sensing. In addition, the proposed tactile sensors, either are very complex in structure and operation or difficult to microfabricate. For instance, Shikida *et.al.* [62], reports an active tactile sensor able to detect both contact force and hardness of an object. Their system consists of a diaphragm with a mesa at the center, a piezoresistance displacement sensor at the periphery, and a chamber for pneumatic actuation. To detect the hardness-distribution, the contacted mesa element is pneumatically driven towards the object. The contacted region of the object is deformed according to the driving force of the mesa element and the hardness of the object. Then from the relationship between the resultant deformation and the driving force generated by pneumatic pressure, the hardness of the contact object can be evaluated. The proposed tactile sensor is microfabricable which makes it attractive. However, precise pneumatic drive and control of a matrix of these sensors could be a formidable task.

Dargahi *et.al.* [11], proposed a softness sensor which consists of two coaxial cylinders. The outer cylinder is compliant and the inner one is rigid. The cylinders are attached to a base plate in such a way that two circular PVDF films are also inserted between the cylinders and base plate. When the tactile sensor is in contact with an object, depending

to the softness of the object, the ratio of the PVDF films outputs would be different. Although the proposed idea of softness measurement is novel, it is difficult to fabricate the sensor through the conventional micromachining procedures due to use of compliant material. In addition, in order to change the working range of the sensor (the range of the objects Young's modulus that the sensor is capable of measuring) the Young's modulus of the compliant cylinder must be changed which potentially is very difficult.

Another approach by Lindahl *et. al.* [64] to detect the physical properties, stiffness and elasticity of human skin, utilizes a piezoelectric sensor oscillated at resonance frequency. A vibration pick up electronics and a PC with software for measurement of the change in frequency when the sensor is attached to an object are other parts of this sensor. The sensor was essentially developed to be used in a hand-held device and there is no report on sensor microfabrication. In addition, no experiments associated with MIS application were conducted, therefore, the capability of the sensor in detecting the applied load, softness of the object and detecting any embedded lump within the tissue is not examined.

1.5.4 Lump Detection

Among the missing information in MIS, Palpation is of special importance. Palpation, is routinely being used in open surgery by surgeons to differentiate the abnormal tissues from the normal tissues, or detecting the tumors as the biological tissue composition and consistency often vary from one tissue to another by various diseases [65]. The localization of hidden anatomical features has been the subject of some researches [66]-[70]. However, these studies have largely been focused on breast cancers. Hence their findings cannot be directly used for MIS applications. Kattavenos [71] reported the development of a tactile sensor for recording data when the sensor is swept over the phantom with simulated tumors. However, no information regarding the size and depth of the lump is extracted from the data.

1.6 Piezoelectricity

The *piezoelectric effect* is a reversible electromechanical effect where the mechanical strain ϵ and stress σ are coupled to the electric field E and displacement D (or charge density) as follows:

$$D = d \sigma \quad \epsilon = d^T E \quad (1.1)$$

where d^T is the transpose of matrix d . The first equation describes the charge density when stress is applied to the crystal and is called *direct* piezoelectric effect. Alternately, the second equation describes the *converse* piezoelectric effect in which the crystal becomes strained when an electric field E is applied.

Polyvinylidene Fluoride as a Piezoelectric Material

Since 1970's, when the enhanced piezoelectricity of polyVinylidene fluoride, PVDF, was achieved [72], due to its combined merits of high elasticity, high processing capacity, and high piezoelectricity, the investigation on its properties and applications has been increasingly grown. The successful applications of PVDF in beams, plates, and membranes for the vibration control [73, 74], damage detection or structure health monitoring [75, 76], shape and motion control [77], force and pulse sensing applications [78], among many others are increasingly reported in the literature. In this study, PVDF as a highly sensitive polymeric piezoelectric material is selected because of its linearity, biocompatibility [79], MEMS compatibility, and wide range of frequency, which starts almost from zero. As a piezoelectric material it is capable to transform mechanical forces or displacements directly to the charge without any driving supply voltage, this can be counted as an advantage of piezoelectric materials over several other techniques such as resistive, capacitive, and conductive. In addition PVDF films can be used in a number of situations such as axial and normal tension and compression, which makes them superior to many other transduction methods such as piezoresistive, and capacitive techniques.

The piezoelectric PVDF, which is commonly prepared in the form of thin films, is a semi crystalline polymer with a crystal volume fraction of about 50-60 % after melt

extrusion. Having quenched at a temperature below 150 °C, PVDF crystallizes in phase α (or form II). As a result of a mechanical stretching normally up to four times of initial length [80] at about 60 °C, the α -phase film undergoes transition to the β -phase (or form I), which exhibits highly piezoelectric sensitivity [81]. Among four stable crystal structures at room temperature, a PVDF film in β phase, polarized at elevated temperatures, shows very strong piezoelectric and pyroelectric properties. The mechanical stretch tends to align the 1-axis of the crystals parallel to the stretching direction, giving the crystals the desired orientation. Then an induced electric field above 100V/ μm under controlled temperature aligns the dipoles [82]. It seems that the field is more effective in aligning the dipoles during the mechanical processing stage in which the crystals are reformed into oriented lamellae [83]. Although the above PVDF manufacturing method is popular, it is not the only way of preparing this piezoelectric polymer. Some other techniques such as spin coating, and types of deposition methods are also investigated [84, 85], particularly in conjugation with the Micro-Electro Mechanical Systems (MEMS) technology. However, due to the complexity of the in-house PVDF depositions, the pre-manufactured PVDF in different applications including MEMS devices are frequently reported [86, 87, 88].

The anisotropic behavior of the uniaxial PVDF film, indeed originates from the aforementioned process history, as the large degree of microscopic order resulting from the orientation reduces the in plane 1-axis randomness and make the macroscopic piezoelectric behavior more consistent with that of the mm_2 point group crystal symmetry. Of the thirty-two crystal classes, PVDF with mm_2 symmetry is known to exhibit direct piezoelectricity with the permittivity, ϵ (a 3×3 matrix with nonzero component on diagonal), piezoelectric coefficient matrix, d (a 3×6 matrix with nonzero d_{15} , d_{24} , d_{31} , d_{32} , d_{33}), and the stiffness matrix, C (given for orthotropic material) [89].

The uniaxial film is the result of mechanical drawing of the film in one direction. This direction is called *drawn direction* or referred to as 1-axis which has the highest piezoelectric coefficient. Alternatively, stretching the film in two in-plane axes yields the biaxial PVDF film with lower but laterally isotropic piezoelectric properties.

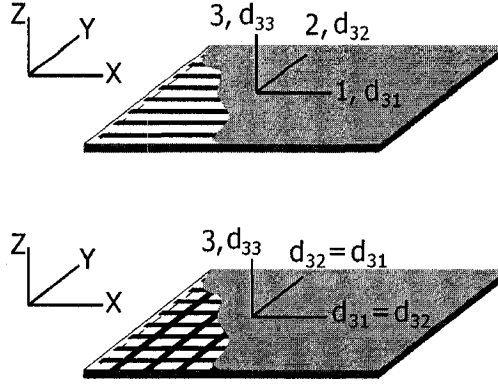


Figure 1.4: The conventional notations of the principal directions of uniaxial (top) and biaxial (bottom) PVDF film. Uniaxial PVDF film can be classified into orthotropic materials, while biaxial films show behavior similar to the transversely isotropic materials.

Figure 1.4 illustrates the metalized uniaxial and biaxial PVDF films along with their principal directions and their associated piezoelectric coefficients. In the uniaxial PVDF film (top picture) the *drawn direction* which also exhibits the highest sensitivity is labeled as 1-axis, whereas the perpendicular direction with a sensitivity of about one tenth of that of drawn direction, is referred to as *transverse*. The *thickness direction*, 3-axis, is normal to the plane of 1 and 2-axes. In thickness mode, normal load is applied to the surface of the PVDF and the resultant output charge is collected from the surface. In this case, d_{33} relates the magnitude of the applied load F to the produced charge Q .

The biaxial film shows isotropic behavior in the plane of the film. In addition, the piezoelectric coefficients for the directions 1 and 2, d_{31} and d_{32} , respectively, are equal. In dealing with piezoelectric coefficients, d_{ij} , the first and second subscripts represent the electrical and mechanical direction, respectively. For instance, d_{31} is the piezoelectric coefficient that relates the charge collected from the area of film, i.e. 3-axis, to the force applied in the 1-axis direction.

As it can be concluded from Figure 1.4, due to thinness of the film, practically the only sides of the PVDF that electrodes can be deposited are the surfaces that are perpendicular to the 3-axis. However, force can be applied in all three directions. This is the reason

why d_{31} , d_{32} and d_{33} are the most common coefficients that are used. The PVDF film can generally be attached to the host structure in a rotated state in which the drawn direction (1-axis) is not necessarily aligned with the global coordinate system. In this case, for example for a force applied in X – *direction*, both d_{31} and d_{32} will contribute in the output charge.

Due to the remarkable difference between d_{31} , the piezoelectric coefficient in the 1–axis direction, and d_{32} , the coefficient in the 2–axis direction, ($d_{32} \approx d_{31}/10$), the uniaxial PVDF film is used in *extensional mode* (1-axis) in over 90% of the practical applications [90]. Although extensional mode can be attributed to both directions 1 and 2, in which the film can extend, normally direction 1 is intended.

1.7 MicroElectroMechanical Systems (MEMS)

1.7.1 MEMS in Surgery

Microelectromechanical systems (MEMS) is a technology developed from the integrated circuit (IC) industry to create miniature sensors and actuators. MEMS devices were used in medical applications in the early 1970s with the advent of the silicon micromachined disposable blood pressure sensors [91]. Since then MEMS devices have expended into other medical areas including surgery. Today, the incorporation of MEMS devices on surgical tools represents one of the greatest growth areas [9]. MEMS technology has the potential to improve surgical outcomes and lower the risk, at a reduced cost by providing data about instrument force, force position, tissue softness, detection of any hidden anatomical features among many others. MEMS devices are able to offer competitive advantages because of their low cost due to batch fabrication, small size, and improved functionality. On the other hand, one of the fastest growth in surgery is owned by minimally invasive surgery. It is estimated that by end of next decade, 80% of all surgeries will be done by MIS [9]. Recent researches in this area have mainly revolved around design and fabrication of MEMS based tactile sensors. Special attention has been paid to develop smart endoscopic

tools through integration of miniaturized sensors into MIS graspers.

Biocompatibility, is a requirement for MEMS devices that come into contact with the human body. The level of required biocompatibility, of course is case dependent. Although no cellular toxicity with conventional MEMS materials has been reported [92], isolating MEMS devices from the body by packaging them in biocompatible polymers is a conventional procedure. Sterilization is another concern in using medical MEMS devices. Packaging must be of a compatible material with the designated sterilization methods. There are a number of techniques for sterilization such as using high temperature and moisture in autoclaves, or using gas such as ethylene oxide or irradiation.

Any medical MEMS device should meet many regulatory controls such as those enforced by the Food and Drug Administration (FDA) or European Community (EC). Design cycle for BioMEMS generally takes between 5 to 15 years. The approval process for disruptive technology can be substantially longer. Lengthy sets of clinical trials can be avoided if MEMS sensors are applied to existing surgical tools. For instance, retrofitting existing surgical tools is the preferred method of entry for MEMS products due to its faster path to market. In addition, retrofitted tools have already been accepted by surgeons who are familiar with their applications and use.

MEMS devices which come into contact with the body must be biocompatible. Fortunately, preliminary results indicate that there are no cellular toxicity effects and no increase in clotting with conventional MEMS materials [92]. However, the current approach in using MEMS *in vivo* relies on isolating MEMS devices from the body by packaging them in biocompatible polymers. These polymers, however, can add to the size of MEMS devices as well as reduce their accuracy. To overcome these issues, nano-particle coatings and bio-compatible polymer micro-machining need to be investigated further [92].

The design of the intended sensor must be such that it is possible to adapt for MEMS technology. The MEMS techniques are considered for the microfabrication of the sensor. Many techniques such as anisotropic etching now are routinely used in MEMS and can be applied for the silicon etching. Integrating PVDF film into silicon can be performed mono-

lithically or through hybrid integration. Monolithic integration utilizes microfabrication techniques such as spin coating to integrate the piezoelectric film.

This study uses hybrid integration in which pre-polarized factory made PVDF film is used. Since deposition techniques of PVDF are currently being researched at this department, full monolithic integration would be possible in future works.

1.7.2 Micromachining

Micromachining is a way of fabricating MEMS devices. This includes thin film deposition, photolithography and etching. Micromachining can be categorized into *bulk micromachining* and *surface micromachining*. Bulk micromachining involves removal of significant regions of the substrate (e.g. etching cavities in a silicon substrate) and can thus be thought of as a subtractive process. Surface micromachining, on the other hand, involves building up and patterning thin-film layers to realize the desired structures on the surface of the wafer (an additive process) [93]. Micromachining efforts, to date, have primarily focused on silicon, partly for historical reasons, and partly for practical ones. In fact, most of the techniques developed for the integrated circuit industry are well characterized for silicon. Etching is widely used for silicon bulk micro-machining and can be categorized into *dry* and *wet* or *isotropic* and *anisotropic* etching. Dry etching utilizes gaseous phase etchant for both sacrificial and bulk micro-machining.

Anisotropic wet etching, on other hand, uses chemical etchant in the form of the liquid and the etch rate is crystallographic orientation dependent. For instance, three planes (100), (110), and (111) are of particular importance in silicon crystals. A 400:1 ratio of etching rates between $\langle 100 \rangle$ to $\langle 111 \rangle$ orientations is possible [94]. Due to the difference in etch rates, when a (100) wafer is exposed to etchant, a pyramid with sidewall slope at 54.74° appears. This feature is used to fabricate many micromachined devices. Etch front for isotropic and anisotropic silicon etching is introduced in Figure 1.5. Due to difference in etch rate for various orientations mask window opening must be designed accordingly.

Popular wet anisotropic etchant for silicon include potassium hydroxide (KOH), ethylene-

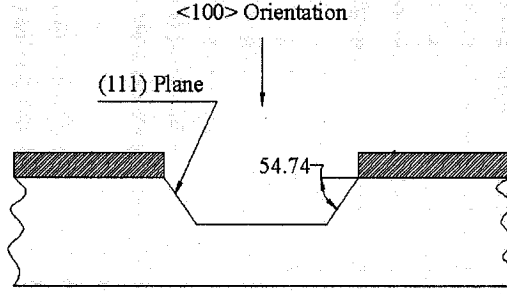


Figure 1.5: Anisotropic etching of a (100)-silicon.

diamine and pyrocatechol (EDP), and the one used in this work, tetramethyl ammonium hydroxide (TMAH). To transfer a pattern to a silicon substrate, photolithography is the popular technique. This method uses several steps including applying photoresist; expose the photoresist to UV light through a mask. The final steps are development, etching and resist removal. Spinning is the common method of applying photoresist on a silicon substrate. Masks, which consist of opaque and transparent regions to block and transmit UV light in that order, are often made of quartz. This work used standard positive photolithography in conjugation with TMAH etching for the sensor microfabrication. After making the desired silicon structure using bulk micromachining, PVDF layer must be integrated with the device. In recent years, the interest in integrating PVDF or its copolymers on silicon base has strongly grown [86, 95]. There are two principal methods to integrate the PVDF film into a MEMS device namely monolithic and hybrid. Sakata [84], and Asahi et al, [85] used electrospray method to deposit PVDF on silicon substrate. Fujitsuka [96] reports deposition of PVDF by ESP technique in a pyroelectric array sensor. A PVDF solution of 0.2 wt% in an organic solvent such as dimethylformamide (DMF) was charged by applying an electric voltage of 8-15 kV between the needle and the electrode of the substrate. The charged droplets of the PVDF solution were transported from the needle to the substrate by the electric field. On the way to the substrate, most solvent is vaporized by N_2 . Subsequently, polymers of the PVDF along with the residual solvent are deposited on the electrode of the substrate, and simultaneously dipoles in the PVDF

were arranged perpendicularly to the substrate due to the electric field. Kohler et al, used spin coating technique to deposit PVDF on a 3-inch silicon wafer. The achieved film thickness was $1.3\ \mu m$. They used capacitance poling at room temperature with satisfactory results. Deposition of PVDF and its copolymers utilizing spin coating method have been reported by Schellin *et. al.* [97]. Vacuum deposition is also used for deposition of PVDF on a substrate by Hoon, [98]. Physical vapor deposition or spray-assisted vapor deposition methods are used by Park [99] and Choy [100]. Chatrathi [101] also reports the microfabrication of PVDF films using spin coating technique. On the other hand, Binnie *et. al.* [86] tried a number of methods and believe using hybrid method is the most reliable technique. They used a UV curing acrylic to adhere a $9\ \mu m$ poled PVDF film to the silicon substrate. The sample was then placed under a strong UV lamp at a slightly raised temperature to cure the adhesive. This method is introduced as a simple and low cost process. Weller, [87] also have used pre-polarized $9\ \mu m$ thick PVDF film on a silicon substrate by means of UV curing epoxy to develop a pyroelectric sensor array.

1.8 Objective of Research

The objective of this research revolves around introducing a system for registering and demonstrating the tactile information in MIS. This system requires an integrated tactile sensor for extracting tactile information from the grasped object, interpretation of the obtained data and presenting the data in a functional way. The whole task is divided into smaller objectives, which are stated as below.

- Proposing a design for a multifunctional tactile sensor, appropriate for MIS tools.
- Characterization of the proposed sensor.
- Characterizing the utilized transduction element (i.e., PVDF) and investigating the influence of different boundary conditions on PVDF output in the sandwich structures, which is used in the sensor.

- Studying the applicability of the position sensitivity in locating the lump in bulk soft object.
- Developing a reasonable model for the grasped soft object (e.g., Hyperelastic model).
- Micromachining of the proposed sensor.
- Performance testing of the proposed sensor to differentiate soft objects as well as its capability in locating lumps.

1.9 Thesis Scope and Outline

Due to multidisciplinary nature of the work the scope of this research is limited to some key aspects of the haptic sensing, such as, force, force position and softness sensing, and a general class of MIS tools, which are suitable for tissue grasping. The transduction element is chosen to be uniaxial piezoelectric PVDF film. A brief characterization of PVDF has been taken into account in order to be used in design, analysis, fabrication and testing of the proposed sensor. To model the grasped soft tissue, a simple model of the soft tissue such as linear elastic model (or hyperelastic model) is considered. Due to the difficulties in using real soft tissue elastomeric materials which exhibit very similar behavior, are used. The anisotropic silicon wet etching of MEMS technology is considered for micromachining.

This thesis is divided into seven chapters and four appendices. To be self contained, the fundamental formulations used in this study are gathered and in order to avoid interruption of flow in chapters, presented in appendices. Therefore, each chapter is self-contained, however, the reader can consult the corresponding appendix when needed.

The motivation, objectives and scope of this research along with an introduction to tactile sensing, minimally invasive surgery, piezoelectricity and micromachining are presented in Chapter 1.

The next chapter is dedicated to PVDF characterization. In this chapter, mechanical

and piezoelectric characteristics of both uniaxial and biaxial piezoelectric PVDF film are examined. The influence of anisotropic property of PVDF film in its performance is also taken into consideration. Finally, this chapter reports on the influence of the surface friction in sandwich configurations. The theoretical and experimental knowledge gained from Chapter 2, is used throughout the research.

Chapter 3, introduces the fundamental working concept of the proposed sensor in softness sensing as well as position sensing. In addition to analytical and numerical (FEM) approaches, experiments are also conducted to validate the obtained results.

As soft tissue exhibits nonlinearity (among many other complexities), Chapter 4 focuses on hyperelastic characteristics of soft objects. Particularly the effect of existence of a lump on surface stress distribution is emphasized. This chapter is confined to the uniaxial compression state which is the case in the grasped tissues by MIS graspers.

Alternatively, Chapter 5 proposes a graphical method for presentation of gathered tactile information by any typical smart MIS grasper.

Chapter 6 describes the design, analysis, fabrication and testing of microtactile sensor. Finally Chapter 7, contains a summary, some suggestions for future work and points out the contributions of the present research.

Chapter 2

Characterization of Piezoelectric Polyvinylidene Fluoride Film

2.1 Introduction

Piezoelectric polymer Polyvinylidene Fluoride (PVDF) film exhibits extremely large piezoelectric and pyroelectric response, making it attractive for the design of highly sensitive sensors for use in robotics and endoscopes sensors [1, 11, 22, 61, 102]. The piezoelectric applications of the PVDF film vary from robotic (e.g., matrix sensors, displacement measuring transducers), medical instruments (e.g., blood flow detectors and ultrasonic echography) to military applications (e.g., hydrophones and IR detectors). The application of PVDF extends to transportation, sports, acoustical sensors, optical, and electrical sensors. It is believed that piezoelectric principles have been the most attractive amongst research in the field of tactile sensors [18]. PVDF film exhibits many advantages; it is light, rugged, and potentially low cost. It is skin-like, can be prepared between $6\text{ }\mu\text{m}$ to 2 mm in thickness and due to its flexibility, could be formed into complex surfaces [103]. In addition, PVDF has bandwidth ranging from near D.C. up to the megahertz range. Due to numerous advantages of the piezoelectric PVDF it has been used as the transducer (sensing element) in the proposed tactile sensor in this study. Prior to any discussion on the tactile sensor principle or its structure, an elaborate investigation on PVDF itself

including its mechanical and electromechanical (piezoelectricity) properties are required. Although several investigators have reported measurements of the piezoelectric and pyroelectric properties of PVDF film [104]-[111], some in-depth theoretical and experimental knowledge about the PVDF characteristics and the parameters that affects its application in different structures are still required.

In this section (in conjunction with Appendix A), the detail of theoretical and experimental knowledge that was required to understand the fundamentals of using PVDF in a piezoelectric sensor is elaborated. Furthermore, basic measurements of material properties, which was required to allow interpretation of the results obtained in any PVDF sensing devices, are conducted. Tests are carried out on the commercial film supplied by Goodfellow [112], which serve two purposes: To allow one to ascertain the adequacy of the PVDF test procedures in comparison with the nominal values provided by the manufacturer, and to provide base measurements for any sensor systems using PVDF film. Section 2.2 reports the characterization of mechanical properties of PVDF film for both uniaxial and biaxial films, while Section 2.3 is devoted to the measurements of piezoelectric coefficients of piezoelectric PVDF films. In addition, the effect of anisotropic PVDF film on its output is discussed in this section. In Section 2.4, details of the characterization of PVDF in sandwich configuration, including the effect of friction are reported.

2.2 The Mechanical Properties of Piezoelectric PVDF Film: Uniaxial and Biaxial

A precise mechanical testing machine (Bose, 3200 Series) was used to attain the stress strain characteristics of the uniaxial PVDF film in 1 and 2-axes. The peak force of the system is $\pm 225\text{ N}$ in a 12.5 mm range of displacement. The apparatus is shown in Figure 2.1. The extension of the film was measured using a calibrated Linear Variable Differential Transformer (LVDT). Three specimens of $110\text{ }\mu\text{m}$ film were cut into a dumbbell shape. The gauge length of the specimens was 26 mm and the width was 8 mm .

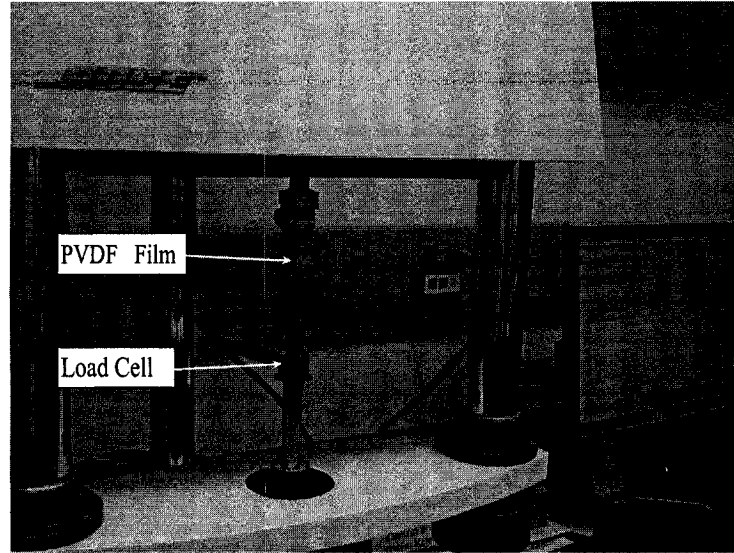


Figure 2.1: The material testing machine used for the characterization of mechanical properties of PVDF film.

Tensile stress-strain characteristics were obtained for specimens oriented in the 1-direction and in the 2-direction. These averaged results are shown in Figure 2.2. The load (displacement) was applied in a ramp fashion (0.1 mm/sec), and the extension and load was measured during the test. These measurements showed that the Young's modulus parallel to the drawn direction was 2.3 GPa while perpendicular to the drawn direction the modulus was 1.85 GPa . These compare with the modulus range given by Goodfellow, which are $1.8\text{--}2.7 \text{ GPa}$ for the longitudinal and $1.7\text{--}2.7 \text{ GPa}$ for the transverse directions, respectively. Similar experiments were conducted to measure the mechanical property of biaxial film. The calculated Young's modulus from the obtained results was 1.95 GPa which is comparable with value 2 GPa provided by manufacturer.

2.3 The Piezoelectric Properties of the Uniaxial and Biaxial PVDF Films

The three piezoelectric coefficients, d_{31} , d_{32} and d_{33} are of special interest in sensor applications. The measurement of piezoelectric coefficients d_{31} and d_{32} compared to that of

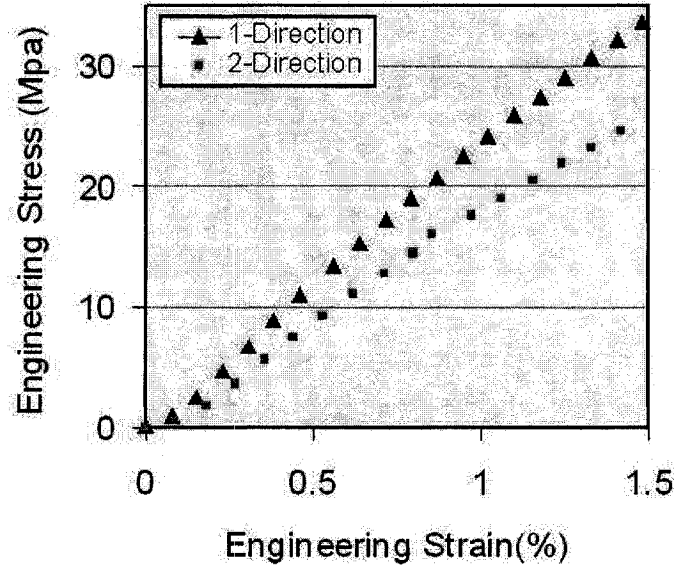


Figure 2.2: Tested stress-strain characteristics for the uniaxial piezoelectric PVDF in 1-direction as well as 2-direction.

d_{33} , is straightforward and is explained below. Measurement of d_{33} is challenging and is discussed separately in Section 2.4.

2.3.1 Measurement of d_{31} and d_{32}

Since there is no electrical (charge) output for piezoelectric materials in response to the applied DC loads, applying periodic loads is the conventional method of measuring the piezoelectric coefficients. A sinusoidal force is the simplest waveform for this purpose. The frequency of the sinusoidal load has to be determined and preferably must be higher than cut off frequency¹. A picture of experimental setup is shown in Figure 2.3.

In order to measure d_{31} , the piezoelectric coefficient of (Goodfellow) PVDF film in

¹Piezoelectric PVDF can simply be modeled as a voltage source in serial with a capacitor C. On the other hand the input impedance of amplifier can be modeled as a resistor R. The combination of R and C acts as a high-pass filter. For a given resistance R and capacitance C, at a certain frequency the output amplitude will be attenuated to 0.707 of the input amplitude. This frequency is called cut-off frequency. To avoid attenuation, working frequency must be enough above this frequency.

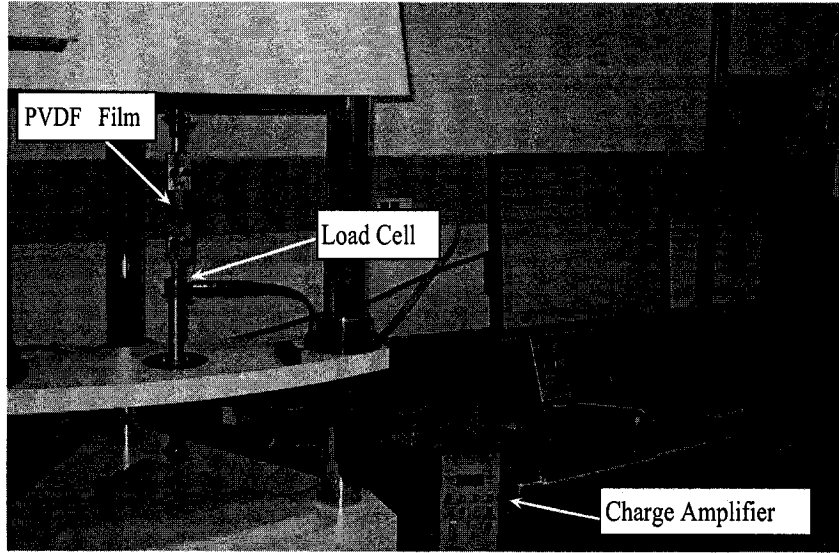


Figure 2.3: The experimental setup used for measurement of piezoelectric coefficients d_{31} and d_{32} .

drawn direction, samples were cut in such a way that drawn direction of the film was parallel with the length of the samples. Alternatively, to measure d_{32} the samples were cut out from the film in such a way that their drawn directions were perpendicular to the length of the samples. The effective length and width of the $110\text{ }\mu\text{m}$ thick sample were 20 mm and 8 mm, respectively. The results for coefficient d_{31} and d_{32} are illustrated in Figure 2.4. To calculate d_{31} and d_{32} , stress and charge density are required. The tensile stress was calculated from the applied force and cross section of the film. By knowing the amount of charge and also the surface area of the film (metalized area), charge density was calculated. The coefficient d_{31} is the ratio of charge density to the tensile stress. These measurements gave results in good agreement with the nominal values quoted by Goodfellow [112], with $d_{31} = 19.0 \pm 0.3\text{ pC/N}$ and $d_{32} = 2.0 \pm 0.1\text{ pC/N}$. (The values quoted by Goodfellow were $18 - 20\text{ pC/N}$ and 2 pC/N for d_{31} and d_{32} , respectively).

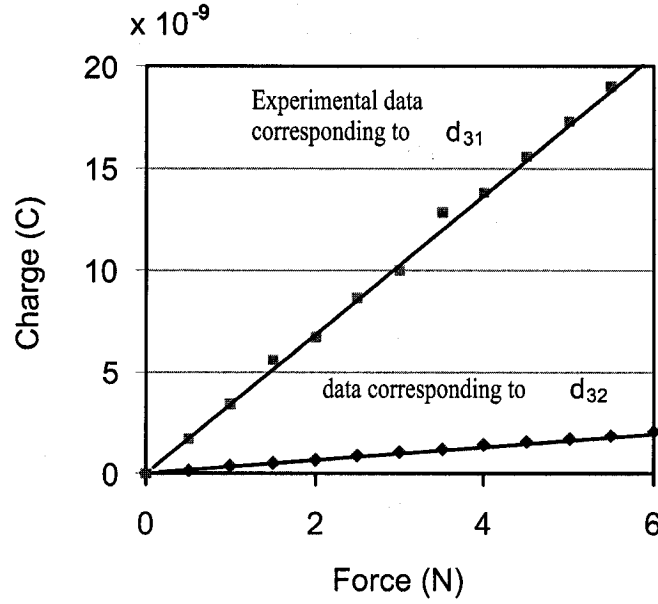


Figure 2.4: The results obtained for the piezoelectric coefficients d_{31} and d_{32} of uniaxial piezoelectric PVDF in 1-direction as well as 2-direction, respectively.

2.3.2 The Anisotropic Property of Uniaxial PVDF film and its Influence on Sensor Application

As mentioned earlier, the mechanical process on uniaxial and biaxial PVDF films are different. The uniaxial PVDF film behavior is quite similar to the orthotropic materials, while biaxial PVDF film exhibits the properties of transversely isotropic materials. In addition, there is no standard process for preparation of the PVDF film which causes parity in its mechanical and electrical properties. The discrepancy observed between few reported values for the material properties of the orthotropic PVDF, which has root in dissimilar mechanical and electrical production process, is one of the obstacles in considering the anisotropic properties of the piezoelectric PVDF in the studies. Various electrical and mechanical properties for the uniaxial and biaxial PVDF film are reported by different manufacturers [112, 113, 114] and are given in Table 2.1.

This section aims at the elaborating the effects of anisotropic behavior of both the uniaxial and biaxial PVDF film on the output voltage in the sensory mode. The behavior

Table 2.1: PVDF properties reported by manufacturers. Piezoelectric and Elastic coefficients are given in pC/N and GPa respectively. The symbol d_{3h} , represents the hydrostatic piezoelectric coefficient.

	Uniaxial PVDF							Biaxial PVDF		
	d_{31}	d_{32}	d_{33}	d_{3h}	E_{11}	E_{22}	E_{33}	$d_{31} = d_{32}$	d_{33}	$E_{11} = E_{22}$
Piezoflex	14	2	-34	-18	2.5	2.1	0.9	-	-	-
Goodfellow	18/20	2	-20	-6	1.8/2.7	1.7/2.7	-	8	15/16	2
Piezotech	18	3	-20	-	-	-	-	7	-24	-

of the PVDF film can be attributed to the mechanical anisotropic characteristic, which affects the stress-strain relation as well as non-equality of d_{31} and d_{32} in the electro-mechanical relations. The response of the sensation and actuation modes varies as a function of deviation angle θ , which is the angle between the material coordinate system in which all material properties are defined and the global coordinate system. In order to show the differences between these two types of PVDF films, a simple cantilever beam was selected as the host structure.

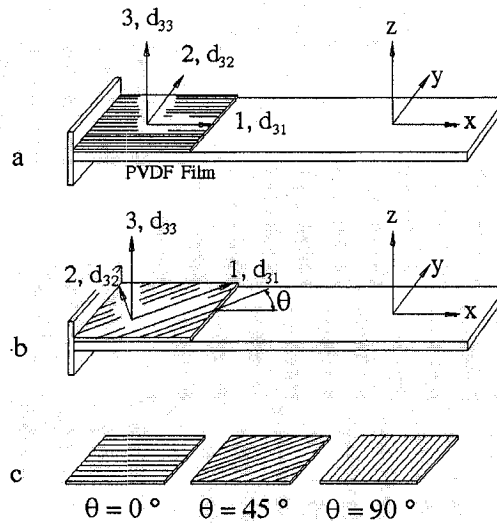


Figure 2.5: The PVDF material coordinate system (1, 2, 3) versus the global coordinate system (x, y, z).

Figure 2.5-a, shows the case where the PVDF film is adhered to the beam in such a way that the material coordinate system and the global coordinate system have the same orientations, while Figure 2.5-b, represents the case that the PVDF 1-axis is rotated with the amount of θ with respect to the global coordinate system (x, y, z). As it is emphasized in Figure 2.5-c, the edges of the piezoelectric patches remain parallel with the global axes, however, the drawn direction, i.e. 1-axis, rotates with respect to the global axis. When the developed stress due to the applied load is in the x-axis direction, the best sensing and actuation response will be achieved from a piezoelectric, which its 1-axis is oriented in the global x direction. However, in some cases the orientation of the applied load might result in a two-dimensional stress profile and thus finding the best orientation to attach the piezoelectric film is important. The rotation between the material property and the global coordinate system can also occur inadvertently during the manufacturing phase of a sensor. Obviously by simply considering PVDF as an isotropic material, no alterations in the responses in terms of deviation angle would be observed.

Uniaxial PVDF Film

As mentioned earlier, the behavior of the uniaxial PVDF film under the similar condition is different from that of the biaxial PVDF film. Figure 2.6 shows the predicted variations of normalized total output voltages in terms of the deviation angles of the uniaxial PVDF subjected to a set of forces, F , $2F$ and $3F$, in which F is a downward point load of 10 N applied at the tip of the cantilever. The length, width and thickness of the cantilever are 24 cm, 2.4 cm and 2 mm, respectively. In Figure 2.6, the curve corresponding to $3F$ is normalized and was used as a reference for the other force values. Even though the results are shown for a force $F=10$ N, the trend is identical for any force F in the linear range. The results show that for each force state, the variation of the voltage due to the orientation angle is nonlinear and significant (the voltage output at $\theta = 90$ is dropped to 4% of its initial value at zero degree). This remarkable decrease is not only due to the difference between piezoelectric coefficients in 1 & 2-directions, but also because of

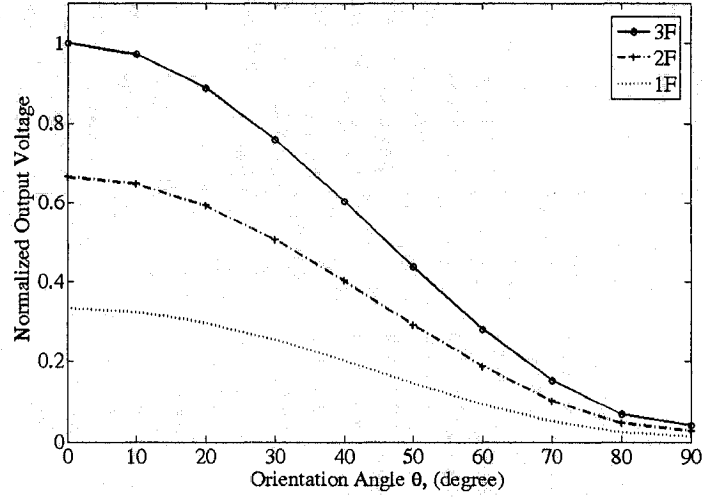


Figure 2.6: The predicted variations of normalized output voltage of the uniaxial piezoelectric PVDF film for different applied loads. For this simulation load F was 10 N.

difference in Young's modulus of PVDF in these two principal directions. Although the piezoelectric output voltage decreases nonlinearly with increasing the deviation angle, for each specific angle the output voltage increases linearly with increasing the applied force. This is shown in Figure 2.7. The contribution of each piezoelectric coefficient in the total response when the deviation angle varies between $\theta = 0^\circ$ and $\theta = 90^\circ$ is investigated and the results are shown in Figure 2.8. It can be realized that the total output voltage is mainly comprised of the voltage associated with d_{31} . For instance, at $\theta = 0^\circ$, only 1.5% of the total voltage is due to d_{32} . The significant reduction of d_{32} contribution in the output voltage can be attributed to the combined effect of both mechanical anisotropic properties of the uniaxial PVDF film, as well as the significant difference between d_{31} and d_{32} values in the uniaxial PVDF. The lower Young's modulus in the transverse direction yields the lower stress, hence the lower charge output for the same strain value compared with the biaxial film. It is seen that the maximum difference between the total output voltage and the voltage induced by d_{31} is at $\theta = 90^\circ$ and is equal to 4.5%. Similar to the biaxial case the voltage component resulted from d_{33} coefficient is close to zero. In many applications in which the uniaxial PVDF film experiences merely a uniaxial tension, it is

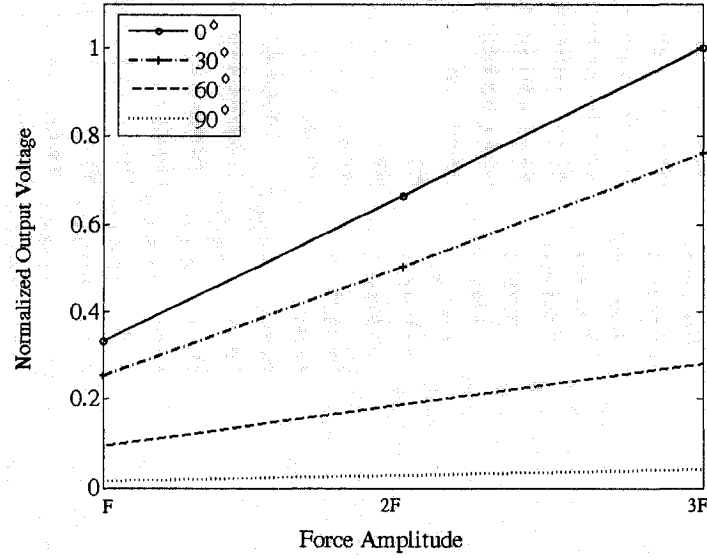


Figure 2.7: Variation of output voltage of the uniaxial piezoelectric PVDF film versus force amplitude for different PVDF deviation angles.

preferred to adhere the film in such a way that its material coordinate system coincides with the global coordinate system, where the deviation angle is zero.

Biaxial PVDF Film

The piezoelectric coefficients of the biaxial PVDF are equal in the 1-axis and the transverse direction, 2-axis. In other words, the ratio of d_{31}/d_{32} , for the biaxial PVDF film is unit. This equality of the piezoelectric coefficients is in compliance with the isotropic mechanical property of the biaxial PVDF film (i.e., $E_1 = E_2$). Figure 2.9 shows the result for the output voltage versus orientation angle of the biaxial PVDF film. The output voltage is normalized with respect to the total output voltage, V_{total} . The variations of the contributing components in the total output voltage, namely $V_{d_{31}}$ and $V_{d_{32}}$ which are due to the piezoelectric coefficients d_{31} and d_{32} respectively, are clearly shown in this figure. It is noted that in order to compute the voltage component associated with each piezoelectric coefficient, the other coefficients are set in turn to be zero. It can be realized that in the biaxial PVDF film, the total output voltage is constant, hence independent of

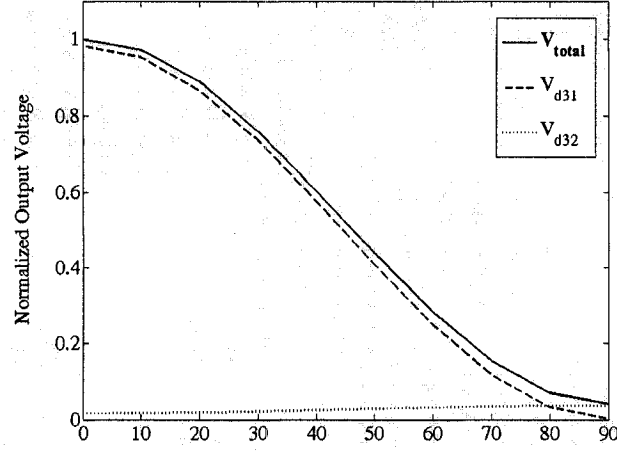


Figure 2.8: Variation of output voltage of the uniaxial piezoelectric PVDF film versus force amplitude for different PVDF deviation angles. The total voltage (V_{total}), as well as its components associated with coefficients d_{31} (V_{d31}) and d_{32} (V_{d32}) are separately plotted.

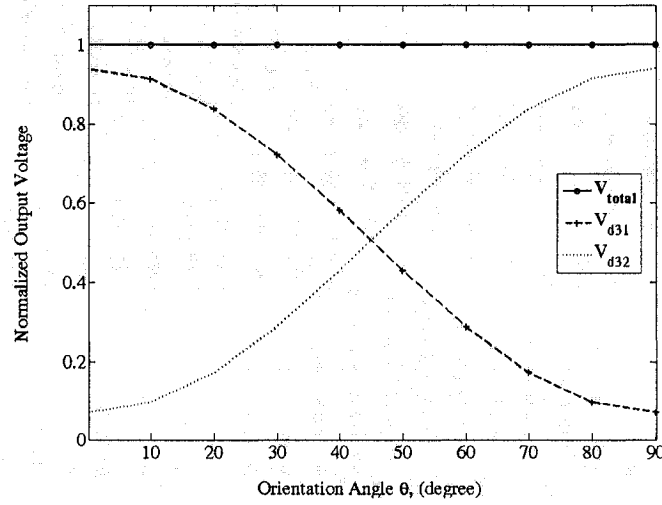


Figure 2.9: Variation of output voltage of the uniaxial piezoelectric PVDF film versus force amplitude for different PVDF deviation angles.

the deviation angle. The symmetry observed in Figure 2.9 is due to the equality of the d_{31} and d_{32} in the two perpendicular directions along with the isotropic material properties of the biaxial PVDF film. It is seen that in the zero degree deviation, the contribution of d_{32} in the total output is about 7%.

It should be noted that the contribution of the d_{33} in total output voltage depends on the boundary conditions and when there is no constraint in the Z-axis, no stress would be developed in this direction, hence no contribution due to d_{33} in the total output would be seen.

2.4 Characterization of Piezoelectric PVDF Film in Sandwich Configurations

Although the application of the PVDF films in extensional mode is dominant, there are some situations that the PVDF must be placed between two surfaces. For instance, in the traditional piezoelectric force sensors, it is customary to place the piezoelectric sensing element between two plates also acting as electrodes. These plates transmit the normal force to the surface of the PVDF, so that they transform the applied point load to a distributed load over the piezoelectric surface. Traditionally to avoid the complexity of considering friction forces, the sensor package is treated as a black box and just the relation between input and output is considered. Therefore, for a given set of piezoelectric element and surfaces, the output of the sensor is empirically calibrated in terms of the input load. Fortunately, the force sensors which are calibrated in this way perform well. However, in this case, the output charge of the PVDF is a combination of the thickness mode charge and another component which is caused by the friction force. Nonetheless, the response of piezoelectric sensor is highly sensitive to the surface condition and varies with any changes in manufacturing line that affects the surface condition.

As we see in this section, the results of this study is helpful in modification and optimization of the commercial piezoelectric force sensors. This research is performed

on the piezoelectric PVDF film, nevertheless, the results could be applied to any other piezoelectric force sensor in which the friction force is considerable. This study also has another fundamental application in the measurement of d_{33} , the piezoelectric coefficient in the thickness mode. The piezoelectric coefficient d_{33} is the most difficult coefficient to measure, as it is extremely difficult to apply a normal force to the film, yet not to constrain the lateral movement of the film hence inducing other stresses within the film. The output can thus have contributions from both the applied normal stress and the induced friction stresses. In order to avoid difficulties associated with the direct measurement of d_{33} , most researchers have used two indirect ways to calculate this value [108]-[111]. In one method d_{33} is determined using converse piezoelectric effect. In this method one measures the change in thickness of a small sample that results from the application of a known electric field. The problem with this approach is the mounting of the sample in a way that does not restrict its lateral motion [111]. This restriction could affect the accuracy of measurement. In the second method, d_{33} is measured indirectly by measuring the hydrostatic piezoelectric coefficient, d_{3h} . Using this value and knowing the values of d_{31} and d_{32} the value of d_{33} can be calculated. For a hydrostatic pressure P , the amount of charge is related to all three coefficients by [111]: $\Delta Q/A = -(d_{31} + d_{32} + d_{33})P$, in which $-(d_{31} + d_{32} + d_{33}) = d_{3h}$.

The present study, introduces a new approach for this problem. The effect of friction on PVDF output can be characterized by finding the trend of variations for some known friction coefficients, then it is possible to calculate d_{33} for the case that friction approaches zero. Therefore, a finite element contact analysis was performed in which piezoelectric PVDF was considered as an orthotropic material and the coefficient of friction was varied between zero to one and the output was recorded. The results are validated by performing an experiment on a similar geometry using pre-characterized surfaces. It is found that the inverse procedure can also be used in determining the friction coefficient of surfaces. The later method offers many advantages over the traditional friction measurement methods, such as *in situ* friction measurement, being non-invasive and low weight and cost.

From Equation A-18 (Appendix A), the output charge along the thickness direction per unit area, Q_3 , due to the stress in the film can be expressed as:

$$Q_3 = d_{31}\sigma_1 + d_{32}\sigma_2 + d_{33}\sigma_3 \quad (2.1)$$

When a PVDF film is compressed between two rigid flat surfaces, assuming, that there is no friction between the surfaces and the PVDF films, the film is free to expand laterally, i.e., in the directions of the 1 and 2 – *axes*. The output charge can thus be deduced from Equation 2.1 as:

$$Q = d_{33}F_n \quad (2.2)$$

where F_n is the applied normal load. This assumption, however, is difficult to use in practice. Friction force always exists and develops unwanted charge components. In general, therefore, the total output charge is different from above Q_3 by the magnitude of the friction induced component. Some authors have defined a new symbol, d_{33}^* [114], which relates the applied normal load to the output charge and is not necessarily equal to the d_{33} except in the frictionless state. The contribution of the friction component to the total output depends on several factors including the magnitude of the applied normal load, the friction coefficient between contact surfaces and the contact area of the PVDF film.

In order to obtain the output of the sandwiched PVDF film in the presence of friction, a contact finite element model was developed in Ansys 10. To validate the theoretical results of the FE analysis, similar experiments were also performed. In the following sections, the details of the modeling as well as the experimental work are explained.

2.4.1 The Finite Element Analysis of Sandwiched PVDF for Different Surface Roughnesses

Since contact problems involving friction produce non-symmetric stiffness, it is preferred to use a symmetrization algorithm which is less computationally expensive. Here the

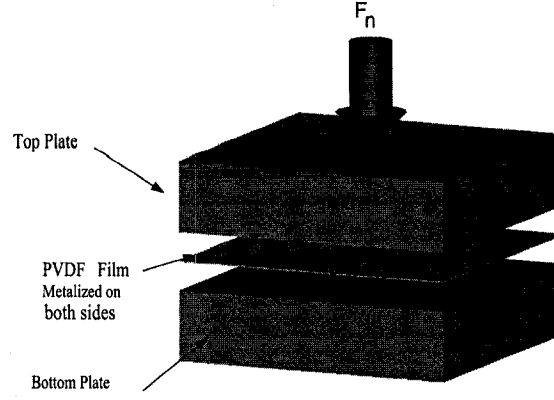


Figure 2.10: The geometry of the problem in which a PVDF film is sandwiched between two solid plates and a load is applied in the normal direction.

algorithm developed by Laursen and Simo [115] is used [116]. There are a couple of approaches used to solve the contact problems. The Pure Penalty method is the one that was used to solve this problem. This method requires both contact normal and tangential stiffness. Higher stiffness values decrease the amount of penetration but can lead to ill-conditioning of the global stiffness matrix and to convergence difficulties. The stiffness should be high enough so that contact penetration is acceptably small, but low enough so that the problem will be well-behaved in terms of convergence. The contact traction vector is:

$$\begin{Bmatrix} P \\ \tau_x \\ \tau_y \end{Bmatrix}$$

where:

P : normal contact pressure

τ_x : tangential contact stress in x direction

τ_y : tangential contact stress in y direction

The contact pressure is:

$$P = \begin{cases} 0 & \text{if } u_n > 0 \\ K_n u_n & \text{if } u_n \leq 0 \end{cases}$$

where K_n and u_n are contact normal stiffness and contact gap size, respectively. The frictional stress is obtained by Coulomb's law:

$$\tau_x = \begin{cases} K_s u_x & \text{if } \tau = \sqrt{\tau_x^2 + \tau_y^2} - \mu P < 0 \\ \mu K_n u_n & \text{if } \tau = \sqrt{\tau_x^2 + \tau_y^2} - \mu P = 0 \end{cases}$$

K_s : tangential contact stiffness

u_x : contact slip distance in x direction

μ : frictional coefficient

It can be seen that the isotropic Coulomb friction model is used for this analysis. In this model, two contacting surfaces can carry shear stresses up to a certain magnitude across their interface before they start sliding relative to each other. This state is known as sticking. The developed shear stress τ is the function of friction coefficient μ and contact normal pressure P , so that $\tau = \mu P$. In addition, there could be an initial cohesion sliding resistance b , which is referred to as COHE in Ansys, that can be added to the equivalent shear stress. Therefore, the Coulomb friction model can be defined as: $\tau = \mu P + b$. The contact cohesion provides sliding resistance even with zero normal pressure. On the other hand, normally there is a maximum contact friction stress τ_{lim} , in which regardless of the magnitude of normal contact pressure, sliding will occur if the friction stress reaches this value.

The geometry of the modeled problem can be seen in Figure 2.10. The computational time for this model can be reduced by taking advantage of the symmetry of the problem and only modeling half of the geometry. For the structural part, i.e. the top and bottom plates, the PLANE42 element, was used. This element is defined by four nodes having two degrees of freedom U_x and U_y , at each node. In order to model the piezoelectric PVDF film, the PLANE223, which is a 8-node coupled-field solid element was used. For the piezoelectric analyses, this element has three degrees of freedom at each node including U_x , U_y and $Volt$. The contacts between the PVDF film and the top and bottom surfaces were modeled using TARGET169 which is used to represent various *target* surfaces associated with the contact elements, CONTA171. The latter element is a 2-D, 2-node

surface-to-surface contact element that represents the deformable surface of a contact pair and is applicable to 2-D structural and coupled field contact analysis. This element is associated with the 2-D target segment element(TARGE169) defined with a set of shared Real Constants. Using the Real Constants, various controlling parameters such as COHE (b), the cohesion sliding resistance, TAUMAX (τ_{lim}), the maximum contact friction can be set. The coefficient of friction between the contact surfaces can be introduced as the material property of the contact element, CONTA171.

Uniaxial PVDF Film

The uniaxial PVDF film exhibits orthotropic properties which originate from the mechanical processing it undergoes. This orientation dependency exists in both mechanical and electrical domains. In other words, not only are the piezoelectric coefficients in the directions 1 and 2 different, but the Young's modulus of the uniaxial PVDF film in the directions 1 and 2 (E_1 and E_2 , respectively) also differ.

The PVDF film was considered to be a square of 30 *mm* by 30 *mm*. In this simulation, the PVDF bottom surface was grounded and the total area of the top surface was electrically coupled together to create an equipotential electrode area. In this case the whole PVDF film acted as one sensing element. Then a distributed load of 100 *kPa* was applied through the top plate. The coefficient of friction between the contact surfaces, i.e., the top and bottom surfaces of the PVDF film on the one hand and the inner surfaces of the top and bottom plates on the other hand, was incrementally increased. The results of this simulation are shown in Figure 2.11. For a better understanding, the negative output voltage is inverted and is shown in the positive Y-axis. Although the magnitude of the μ can theoretically reach very large values, a practical range of $\mu < 1$ is selected for the simulations. It is seen that the maximum output voltage is obtained at frictionless state of $\mu = 0$. The output voltage decreases nonlinearly with the increase of the friction coefficient. When the coefficient of friction is equal to 0.4, the maximum voltage drops by more than 70% . This remarkable attenuation is associated with the friction induced

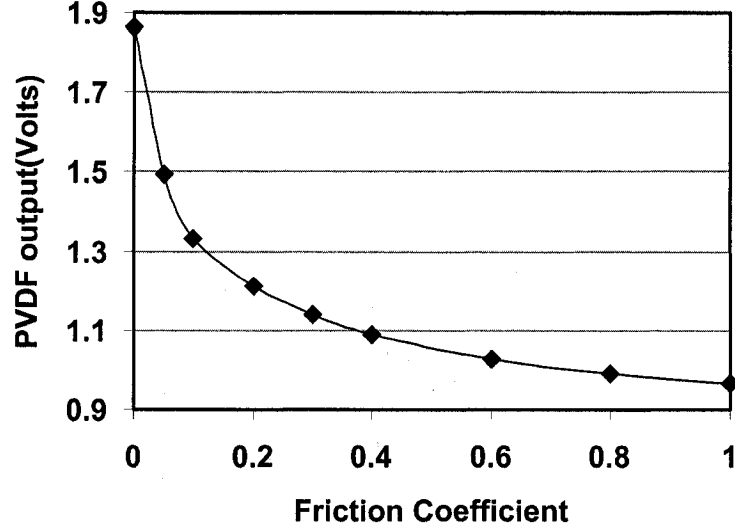


Figure 2.11: The total output voltage of a uniaxial PVDF film compressed between two blocks in the presence of the friction.

voltage component. In other words, for the frictionless state the PVDF film can freely expand so that the only non-zero stress component would be σ_3 and the other principal stresses would be zero ($\sigma_1 = \sigma_2 = 0$). However, when $\mu \neq 0$, friction force reduces the lateral expansion of the PVDF film and as a result stress in (1 - axis) and (2 - axis) directions will be developed. The reason that the inclusion of the x and y components causes the reduction in the total output voltage is due to the fact that d_{31} and $d_{32} > 0$ while $d_{33} < 0$. The results of the simulation for $\mu > 1$ shows that the variation in the output voltage is negligible. It is important to note that the maximum gain can be obtained at low friction for the uniaxial PVDF film in the sandwich configuration. Figure 2.11 also reveals the dependency of maximum output voltage on the friction coefficient particularly for $\mu < 0.1$. This explains why the accurate measurement of the d_{33} using the direct method is so difficult. This behavior, on the other hand could be beneficial for the accurate measurement of low friction forces and coefficients.

For the frictionless state $\mu = 0$, the results illustrated in Figure 2.11, can be compared with the classical theories. Since the metalized piezoelectric PVDF film can be modeled

as a capacitor, the relationship between the generated charge Q and the potential across its electrodes V can be written as: $Q = CV$ in which C is the capacitance of the PVDF specimen. On the other hand, the capacitance of the PVDF film with the area of A and thickness of t can be calculated from the known relationship : $C = \epsilon_0 \epsilon_r A/t$ in which $\epsilon_0 = 8.854 \times 10^{-12} F/m$ is the permittivity of free space and ϵ_r , the relative permittivity of PVDF, is 12. Substitution of the above relations into equation 2.2 reads:

$$V = \frac{d_{33}t}{\epsilon_0 \epsilon_r} P \quad (2.3)$$

in which $P = F_n/A$ is the applied pressure on the PVDF film. The numerical value of voltage in Equation 2.3 for the data given for the present case is 1.864, which agrees with result in Figure 2.11 obtained for $\mu = 0$.

In order to elaborate the results obtained in the previous analysis, a second simulation was performed in which the top surface of PVDF film was covered with ten electrodes of equal width that were evenly positioned on the surface. The bottom surface of the PVDF film is considered as the common ground for all the electrodes. The results of this model under a constant load are depicted in the Figure 2.12. This figure shows the relationship between the output voltage of each segment and different friction coefficients. It must be emphasized that each point in this figure represents a constant voltage over the area of a sensing element. To clarify this point, Figure 2.13 shows the details of voltage distribution of each sensing elements (for $\mu = 1$) as well as the variations of these voltages from one to the other. From this figure it is clear that the output voltage of each sensing element is a constant value over its area. The horizontal axis shows the normalized length of the PVDF film. Since half of the PVDF is modeled, zero is related to the center of the film and one is related to the half length of PVDF which here is 15 mm. For the frictionless case, i.e, $\mu = 0$, the voltage of all PVDF sensing elements are equal and at their maximum value. However, with an increase of the friction coefficient, the voltage output of each sensing elements begins to reduce. For a given friction coefficient, μ , the voltage attenuation of those elements that are closer to the edges is lower. This is because, the outer sensing elements carry less frictional load than those of the middle sensing elements.

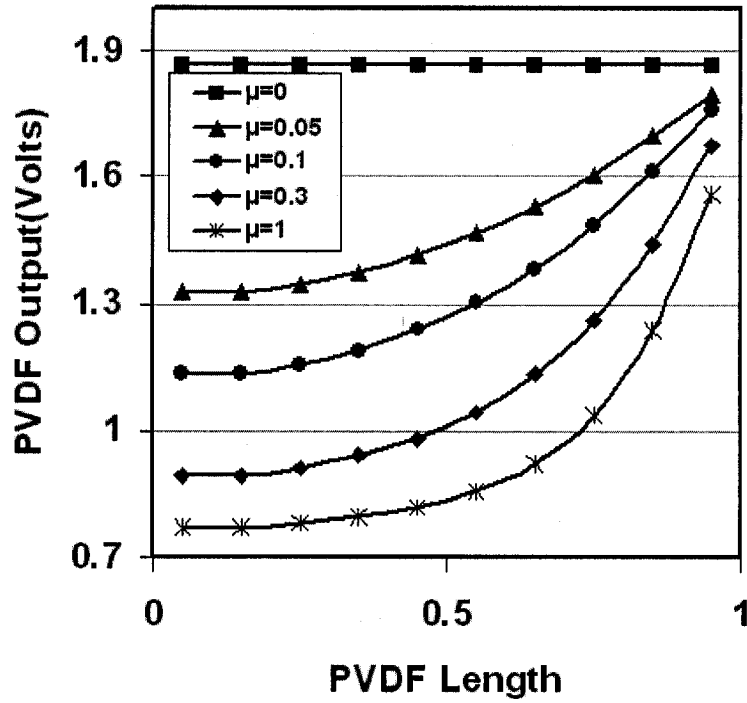


Figure 2.12: The output voltages of ten equal PVDF sensing elements are evenly positioned along its 1-axis. While the applied load is kept constant, the friction coefficient is varied between zero to one. The horizontal axis of the graph is normalized by half the length of the PVDF film.

Therefore, the frictional voltage component of the outer sensing elements is lower, and hence the total output is higher. The trend observed in Figure 2.12 is exactly the same as trend of variation of σ_x along the length of the PVDF film at the contact surface. It is now clear that Figure 2.11 represents the average voltage of a charge distribution over the whole PVDF film. On the other hand, the data shown in Figure 2.12, which is the result of segmentation of PVDF into ten separate sensing elements, are especially helpful to elaborate the study of the distribution of the frictional forces over the contact area.

Having observed the nonlinear behavior of output voltage of the PVDF against the friction coefficient, the relationship between the amplitude of the applied normal forces and the total output should also be examined. In this simulation, similar to the first

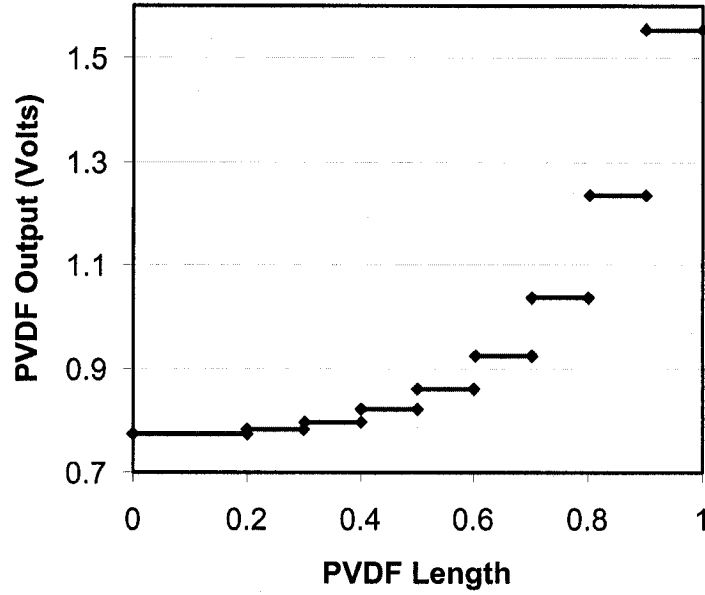


Figure 2.13: The distribution of output voltage over the uniaxial PVDF film segments compressed between two plates in the presence of a friction of $\mu = 1$. The horizontal axis of the graph is normalized by half the length of the PVDF film.

test, the electrical boundary conditions are defined in such a way that the whole PVDF film form only one sensing element. Therefore, for each given load, there exists only one voltage output. The applied load is ranged from 1 *kPa* to 200 *kPa* and the results for three typical friction coefficients, $\mu : 0, 0.3, 1$, are plotted. As demonstrated in Figure 2.14, for a constant friction coefficient, there is a linear relationship between the normal applied load and the sensor voltage output. This justifies why the industrial sensors are performing well and linear, even though the frictional forces have not been taken into consideration. These results also show that the output of identical sensors are the same if the friction coefficient of the sensor surfaces are exactly the same. This could be one of the main reasons for discrepancy in output voltage of sensors that are similar in structure but different in contact friction which is quite probable in manufacturing phase. This figure also shows that if, for any reason, the uniformity of manufactured sensors cannot be attained, it is better to work in the high friction region. In this way,

the dependency of the sensors with respect to the surface friction will be reduced to a minimum. However, if the contact surface is too rough, then the projections of the surface might cause unexpected results and might even damage the PVDF film.

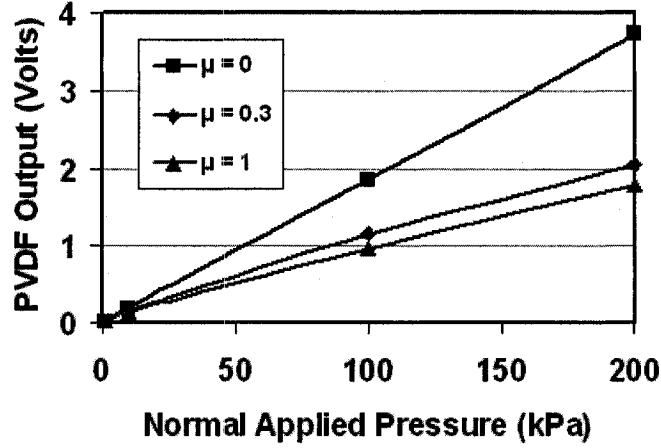


Figure 2.14: The response of the PVDF film against applied pressure for different friction coefficients.

Biaxial PVDF Film

As mentioned earlier, there are some differences between the biaxial and uniaxial piezoelectric PVDF films. For instance, biaxial film exhibits isotropic properties in terms of both mechanical($E_1 = E_2$) and electrical($d_{31} = d_{32}$) performance. Another important factor is the opposite polarity of d_{33} in uniaxial and biaxial PVDF films. The manufacturer [112], reports the values of d_{33} for the uniaxial and biaxial PVDF films as -20 pC/N , $+15 \text{ pC/N}$, respectively.

Since in the biaxial PVDF film all the piezoelectric coefficients have the same polarity, compared with the results of the previous simulations, it is expected that the friction induced components increase the total output. Figure 2.15 demonstrates the relationship between the output voltage of the biaxial piezoelectric PVDF film and the friction coefficient for a constant normal load. It is seen that this behavior is different from that of

uniaxial film. For the biaxial film the friction induced components increase the total output voltage. These results could provide some guidance for the proper selection of PVDF film type (between uniaxial and biaxial) for a particular application. The extreme sensitivity of the output voltage in the low friction coefficient range is again evident. Similar

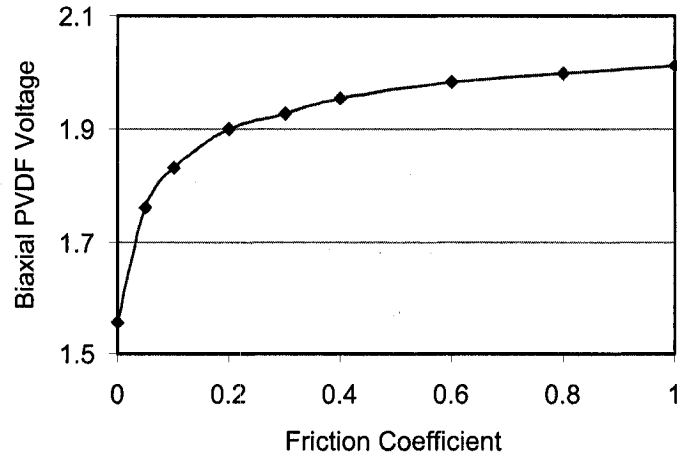


Figure 2.15: The total output voltage of a biaxial PVDF film compressed between two plates in the presence of the friction.

to the analysis of the uniaxial film, the whole length of the PVDF film is discretized into ten side-by-side electrodes which make ten independent sensors. As shown in Figure 2.16, voltage of each segment depends on the location of the sensing element as well as the friction coefficient. In this simulation, the PVDF bottom surface was taken as common ground of all the sensing elements. In accordance with the classical theories and also with the results obtained for the uniaxial PVDF film, the performance of all ten sensing elements is similar for $\mu = 0$. However, in the presence of friction, the outputs of sensing elements are different and depend on the friction coefficient as well as the location of the elements.

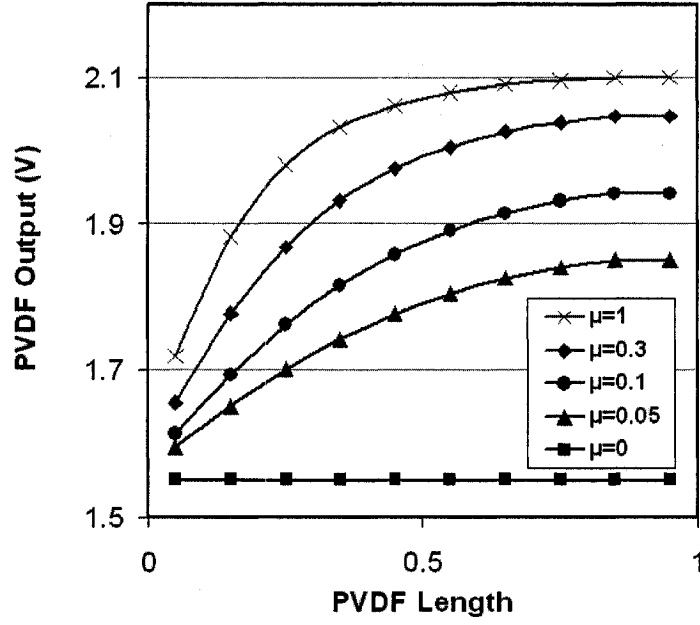


Figure 2.16: The output voltages of ten equal biaxial PVDF sensing elements evenly positioned along the x-axis. While the applied load is kept constant, the friction coefficient is varied between zero and one. The horizontal axis is normalized by half the length of PVDF film, and hence zero represents the center of the film and 1 denotes the PVDF edge at $x=15$ mm.

2.5 Experiments

In order to validate the results from the simulations of the influence of surface friction on the output of the PVDF compressed between two plates, a set of experiments were performed. Prior to conducting the main experiment, the friction coefficient of sample surfaces had to be estimated. Once the friction coefficient of the surfaces on both sides of PVDF film are experimentally determined, the characterized surfaces were used in another experimental set up to record the output voltage of the PVDF film.

2.5.1 Surface Friction Measurement

In order to measure the static friction coefficient of test surfaces, as shown in Figure 2.17, a conventional experimental setup was designed and implemented. Extreme care

was taken to reduce the unwanted friction forces. The minimum force increment steps were $0.01N$ and the force applied to the surfaces was in the range of 2 to $10N$. Some of

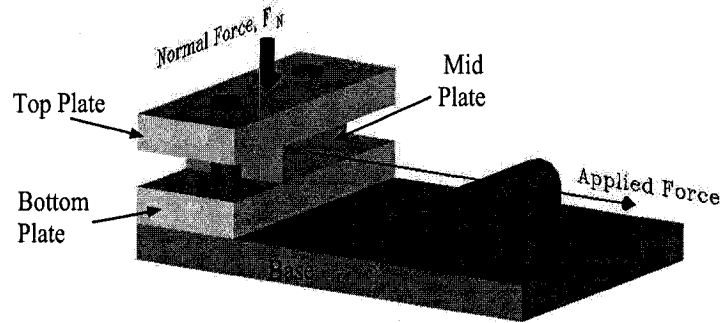


Figure 2.17: The experimental setup used to measure friction coefficients. PVDF films were adhered to both sides of mid-plate. The friction surfaces were attached to the internal surfaces of top and bottom plates.

the selected surfaces were made of standard abrasive papers. In addition, other available surfaces such as stationary paper or Plexiglass were also tested. To achieve low friction surfaces, lubricants were used. However, because of different problems, the application of oils did not yield satisfactory results. The first difficulty was the stiction of the smooth surfaces in the presence of the oil. The second difficulty was maintaining the uniformity of the lubrication conditions such as the thickness of the oil film in presence of different applied loads. To eliminate the mentioned difficulties, a couple of readily available dry lubricants were tested. Normally these materials can be sprayed on to the target surfaces. Alternatively, low friction materials such as Teflon tape which can be cut and pasted on the surface, can be used. For the present study a 555 Silicon Dry Film Lubricant and a molykote 321 Dry Film Lubricant from Dow Corning were used. In addition, a PTFE adhesive tape from Nitto Denko was tested. The data recorded for silicon dry film was not repeatable, as silicon film peeled off easily during the experiments. The selected abrasive papers include from very soft (grade 2000) to very rough (grade 240) grades. Since one of the surfaces in the tests was PVDF, one surface was tested against the PVDF film. However, the tested PVDF film was metalized with aluminum, hence the

aluminum coating was the real contact surface in the tests. Table 2.2 shows the tested materials and their corresponding, static coefficient friction established through testing.

Table 2.2: List of abrasive materials and their corresponding friction coefficients.

Surface	Black Dry Film	PTFE Tape	Stationary Paper	Abrasive 2000	Abrasive 1200	Abrasive 800	Abrasive 240
μ	0.11	0.19	0.29	0.35	0.40	0.44	0.55

2.5.2 The Experiments Performed on the Sandwiched PVDF for Different Surface Roughnesses

An experimental setup as illustrated in Figure 2.18 was used to apply the known load to the PVDF pressed between two friction surfaces. A square shaped $110\mu m$ -thick PVDF

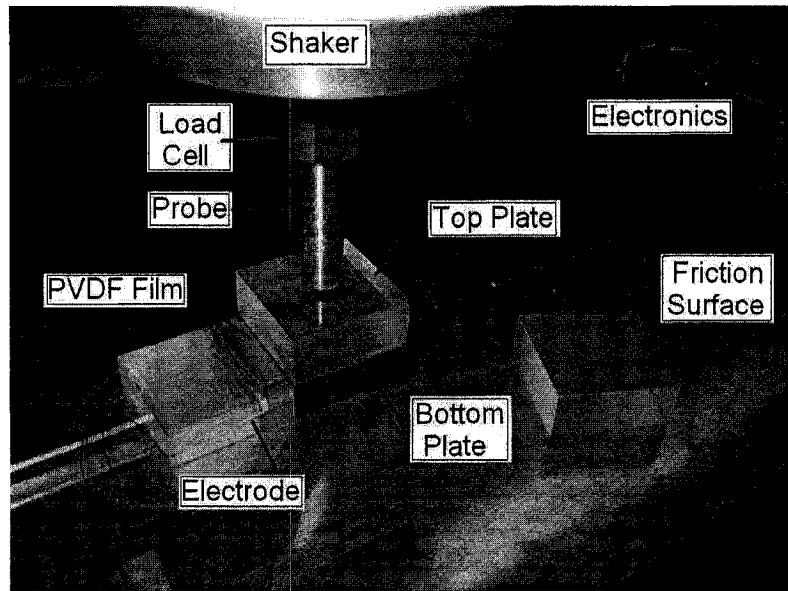


Figure 2.18: In this part of the experimental setup the PVDF film is sandwiched between two plates. The internal surfaces of the plates are covered with the pre-characterized surfaces.

film is placed between two Plexiglas thick plates and the mentioned pre-characterized surfaces were applied one by one between the plates and the top and bottom surfaces of the PVDF film as shown in Figure 2.19. A 20 Newtons load at the frequency of 20 Hz was

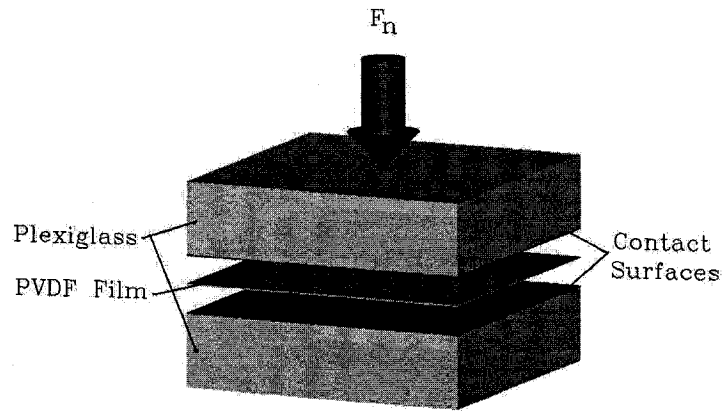


Figure 2.19: The configuration used for the experiment to measure the PVDF response to the friction material.

applied to the top plexiglas. Considering the area of $30\text{mm} \times 30\text{mm}$ of the PVDF film, the maximum pressure exerted to the film was about 22 kPa. A picture of experimental setup is shown in Figure 2.20. To apply a repetitive load, a signal generator with sinusoidal

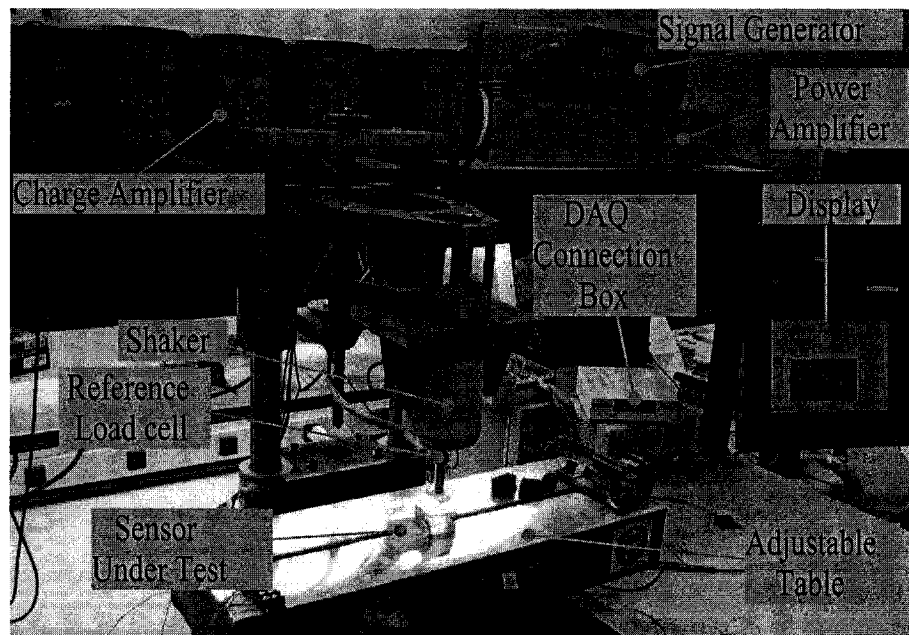


Figure 2.20: A view of experimental setup used to measure the PVDF response to the friction materials.

output was used. Before connecting this signal to the shaker, the signals were amplified

using a power amplifier (V203, PA25E-CE, Ling Dynamic Systems). To characterize the output voltage of the PVDF film sandwiched between two surfaces, a calibrated load sensor (Kistler 9712B50) was used to record the amplitude of the applied load. To record and analyze the output of the PVDF film when the friction coefficient of the surfaces were changed, a data acquisition system (National Instrument, NI PCI-6225) running Labview software (Version 7.1) was used. To connect the piezoelectric charge output to the DAQ, a charge amplifier, in which an operational amplifier converts the charge into the voltage, was used. In contrast to the voltage-mode amplifiers in which the output voltage depends on the input impedance, the output voltage in charge-mode amplifiers depends on the feedback capacitor, C_f and the charge developed on the piezoelectric film, Q . Therefore, the output voltage of the charge amplifier is independent of the cable capacitance. This is one of the main advantages of using charge amplifiers in piezoelectric applications. The voltage gain can be determined by the ratio Q/C_f . Using a Labview built-in Butterworth low pass filter, the 60 Hz line noise was filtered out. The peak-to-peak of the output and the corresponding input was recorded. The data was then saved in a file and plotted against the theoretical results as shown in Figure 2.21. The theoretical curve in Figure 2.21 is the result of a finite element model for the uniaxial PVDF film executed for an applied load of 22 kPa.

As shown in this figure, the experimental data also reveals a decaying trend when the friction coefficient is increased. However, for friction coefficients greater than 0.5 the projections of the abrasive papers would have caused permanent and local scratches leading to an increase in output. Therefore, for $\mu > 0.6$, no consistent data was obtained.

2.6 Discussion and Conclusions

This chapter addresses the fundamental theoretical and experimental knowledge necessitated for the development of the proposed tactile sensor. Characterization of mechanical

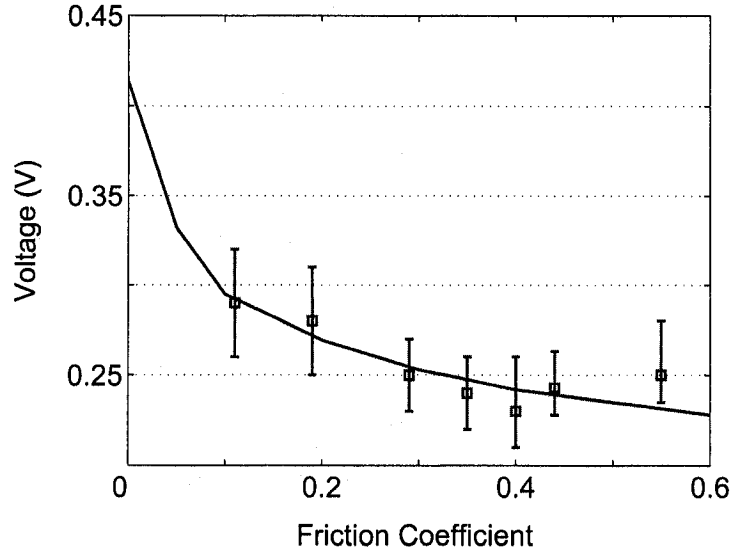


Figure 2.21: Comparison between theoretical data and experimental results. For both cases a 20 N force is applied (errorbar indicates the range of readings).

and electromechanical properties of piezoelectric PVDF, considering anisotropic behavior of PVDF has been the main focus of this study. The result of this study has provided not only a sound ground for development of the proposed sensor, but also a contribution in exploring piezoelectricity of PVDF in different configurations that could be used in variety of applications.

In theoretical approach, the effect of deviation angle, angle between material coordinate system and global coordinate system, which appears due to anisotropic behavior of PVDF film is analyzed using finite element method. In addition, the difference between uniaxial and biaxial PVDF film is also elaborated. Then the performance of PVDF film in thickness mode in which normally film is sandwiched between two plates, is considered. The main concern in this case was the effect of friction on the output of the PVDF. Using Ansys, a finite element contact analysis associated with the modeling of the PVDF piezoelectric is developed and the results for both uniaxial and biaxial PVDF for a range of friction coefficients are obtained. It is shown that the PVDF response is highly influenced by the contact friction. Hence, one of the key reasons for observing dissimilar outputs

from structurally similar manufacture sensor could be attributed to the difference in contact friction. Therefore, an extreme care should be paid to the uniformity of the contact surfaces during the manufacturing process. Simulations show that firm gluing of PVDF film to a surface is equivalent to have infinite friction between PVDF and the surface.

On the other hand, as a by product, the results of this study open a new window for measuring the roughness of the surfaces. The outcome of this study suggests that it is possible to measure the coefficient of friction of the contact surfaces using the proposed method. This technique is particularly appropriate for low friction range where accurate measurement is difficult and other available friction measurement methods are inadequate.

In experimental approach, the Young's modulus of PVDF film in 1 and 2-directions have been obtained. To investigate the dependency of PVDF output to friction a number of surfaces has been tested in order to determine their coefficients of friction. Then these characterized surfaces are used in another experimental setup in which PVDF film is sandwiched between the characterized surfaces.

Chapter 3

Multifunctional Tactile Sensor: Design, Analysis, Fabrication and Testing

3.1 Specifications of Tactile Sensors for use in MIS

If human tactile perception is considered to be a standard for artificial tactile sensing [21], an ideal tactile sensor must mimic all capabilities of human hand. Human tactile system is capable of responding to the applied force, position and size of stimuli, softness/hardness of object as well as roughness and texture of the contact object. In addition, human skin is capable of sensing temperature, vibration and humidity. At this time, design and development of a sensor replicating all of these capabilities is a very difficult task. Many researchers have developed tactile sensors that are able to detect one of the mentioned quantities. Development of multifunctional tactile sensors would enable the detection and measurement of some of important quantities required for specific tasks, such as, endoscopic surgery. Future surgical tools are anticipated to have sensors capable of distinguishing different kinds of tissues using tactile properties such as elasticity and be able to locate tumors, or abnormal stiffness of organs [23].

Surgeons must also be informed of any slippage when they are grasping tissues by MIS tools. Detecting the presence of blood vessels is also of prime importance to avoid bleeding from undesired cutting through an artery [117]. They must also know how much of the grasper is in contact with the tissues. The latter information is required for a safe grasping. Since the sensor must work in human body environment some restriction must also be complied. For instance the sensor must use the least possible wiring and the minimum current passing through the body. Many of the possible softness sensing methods, therefore are questionable when considered to be applied to the body. The sensitivity of the sensor must also be appropriate for low forces. And obviously, complexity of the sensor can be considered as a disadvantage. Miniaturization of such a sensor is another challenge for a candidate suitable for MIS.

The structure of the sensor is also important. Since the sensor must be accommodated into a grasper, the structure of the sensor must be compatible with the structure of the grasper. This multidisciplinary problem necessitates considering many of above-mentioned aspects in design, analyze, manufacturing and testing of the device. However considering all different aspects of this problem is not practical.

Softness and position sensing have been chosen among many abilities of the human tactile sensing. Grasping tools of MIS (for example rather than cutting tools) are considered in this study because of their frequent usage and complicated requirements.

In this chapter, design, analysis, fabrication and testing of a multifunctional tactile sensor for use in the MIS tools, are reported. Consistent with the existing MIS graspers, a tooth-like shape is considered for the sensor to ensure the ability of firm grasping. Due to the corrugated shape of the sensor system, it can be easily integrated within the traditional MIS graspers [78]. The design of the sensor is also adaptable to MEMS technology and able to be microfabricated. The materials proposed for the sensor system including silicon and PVDF film are biocompatible [79, 118]. It is worth to note that although this sensor is primarily designed for MIS applications, the concept employed for the softness sensing could be used in other areas, particularly in robotic applications.

It is shown that proposed sensor is able to measure the magnitude of the applied load and differentiate the softness of touched objects. The location of the applied load can also be found from the sensor output. Moreover, an array of the sensor could report the location of the concentrated load in a 2-D space. The status of grasping, i.e. position of the grasped tissue/object, and also any slippage during the operation could potentially be detected by the sensor array. As mentioned earlier, the piezoelectric PVDF film is chosen as transduction element in this design due to its unique features ,such as, linearity, high sensitivity, mechanical flexibility, and MEMS compatibility [72, 89, 119, 120, 121]. For detailed description of piezoelectric PVDF films see Chapter 2.

3.2 Design and Structure of the Sensor

Prior to describing the structure of the proposed sensor, introduction of host device, which is a complete grasper, is helpful. Figure 3.1 shows the proposed grasper in which one of the jaws (for example, the lower jaw) is equipped with an array of the sensor unit. The number of teeth may vary in different graspers and/or applications. This modular design assures that the performance of all sensor units are similar. Therefore, the operation of this array can substantially be studied by considering a sensor unit and thereafter in this paper, one tooth of the grasper is analyzed. Cross section of the sensor unit subjected to time dependent force $F(t)$ is shown in Figure 3.2. In Figures 3.1 and 3.2, the X and Y directions are selected similar to the traditional notation in the classical mechanics.

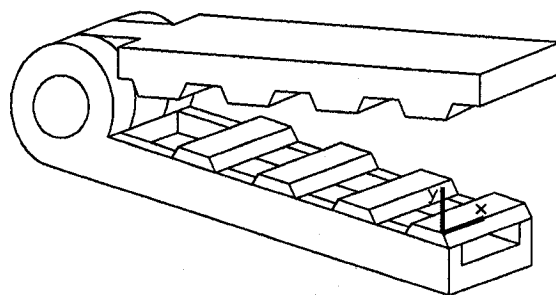


Figure 3.1: The scheme of a MIS grasper equipped with an array of the proposed sensor.

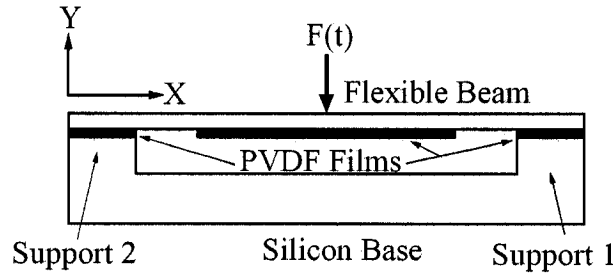


Figure 3.2: Cross section of a sensor unit (one tooth).

In order to find the softness of object, both the amplitude of the applied load and the resultant deflection are simultaneously required. Sensing mechanism utilizes PVDF films both in the thickness mode at end supports to measure the applied load, and in extensional mode attached to the flexible beam to measure the bending stresses. Knowing the applied load from the PVDF films at the supports and the amount of deflection or equivalently the developed bending stresses from the middle PVDF film, softness characterization of the objects is feasible. The concept of the sensor operation is depicted in Figure 3.3. As is

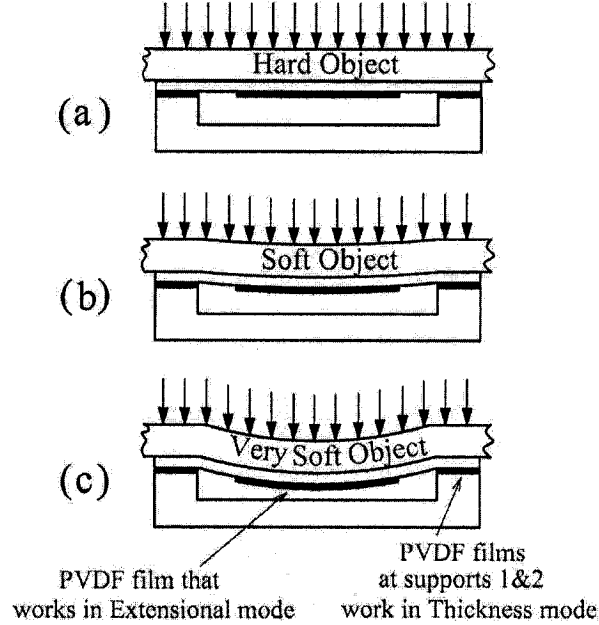


Figure 3.3: The basic scheme for the proposed softness sensing technique.

seen in Figure 3.3-a, when a rigid object is used as target, no deformation will be resulted in the beam. Although the PVDF films at the supports respond to the applied force, no output from the middle PVDF film (extensional mode) is expected.

However, a soft object under the load F will bend the beam. As it can be seen from Figures 3.3-b and 3.3-c, larger beam deflection is resulted for softer contact objects. Therefore, the PVDF film, which is firmly adhered to the beam, elongates and develops charge. The output charge is proportional to the bending stress, which itself is dependent on the extent of bending. The maximum amount of the bending can be controlled in the design stage by selecting the material of the flexible beam as well as its thickness and length for a maximum given load. A beam with higher Young's modulus or thickness shows less deflection but can sustain higher applied load. Conversely, a soft beam deflects easily and produces high output charge but may not be a good choice for high load applications since it can not develop enough gripping load. Thus with such a design, a delicate balance between the softness, load and the design output charge have to be established. For a given sensor, the thickness and material property of the beam are known, thus the deflection of the beam will only be a function of flexural rigidity of the contact object.

3.3 Sensor Modeling

In order to investigate the performance of the system in differentiating the softness of the contact objects, both the analytical approach and the finite element method are examined.

3.3.1 Analytical Model

The suspended part of the beam can be modeled using closed-form relationships. For the modeling, combination of the object and beam is considered as an isotropic composite beam. Cross section of the composite beam in bending can be transformed into a cross section of one material. Consider the case that the beam is composed of two materials,

namely the object with modulus E_1 and the beam with modulus E_2 , where $E_1 < E_2$. Let the equivalent single-material cross section be entirely made of the material of modulus E_1 . In order for the equivalent cross section to have the same bending rigidity as the true composite, it is necessary that more E_1 material replace the E_2 material. However, since the strains of the equivalent cross section are to be identical to the composite, the depth of the section relative to the bending axis cannot be altered, as strains depend on the position relative to this axis. Hence, the width of the beam can be increased without affecting the strains (see Figure 3.4). It can be seen that the relation between equivalent width b_e and the original width b is: $b_e = (E_2/E_1)b$, where b and b_e are the width of the beam before and after the transformation, respectively. The centroid of the transformed cross-section, d , is obtained by

$$d = \frac{\sum \tilde{y}A}{A} = \frac{b_e h_2^2 + b h_1^2 + 2b h_1 h_2}{2(b h_1 + b_e h_2)} \quad (3.1)$$

The area moment of inertia of the transformed (total E_1) cross-section, I_e , can be determined using parallel-axis theorem:

$$I_e = \frac{1}{12}(b h_1^3 + b_e h_2^3) + b h_1(h_2 + h_1/2 - d)^2 + h_2 b_e(d - h_2/2)^2 \quad (3.2)$$

In the case of $E_2 < E_1$, the relation will be: $b_e = (E_1/E_2)b$, and the equivalent E , is equal to E_2 (Young's modulus of the beam). In the remainder of this section, the calculated values for the equivalent beam are used in the formulations, nevertheless, for the simplicity the indices are removed. It also should be noted that the following formulation is adopted for thin beams in which the ratio of beam length (L) to the beam thickness ($h_1 + h_2$) is very large. Although there is no clear border between thin and thick beams, normally the ratio of $L/(h_1 + h_2) \geq 10$, is considered to be thin. The equation of motion for the free transverse vibration of the (equivalent) beam can be written as:

$$\frac{\partial^4 y}{\partial x^4} = -\frac{1}{a^2} \frac{\partial^2 y}{\partial t^2} \quad (3.3)$$

in which $a = \sqrt{EI/\rho A}$. In this equation EI , ρ , A are the flexural rigidity, density and cross section of the beam, respectively. The deflection function can be considered as

$$y = X(A \cos \omega t + B \sin \omega t) \quad (3.4)$$

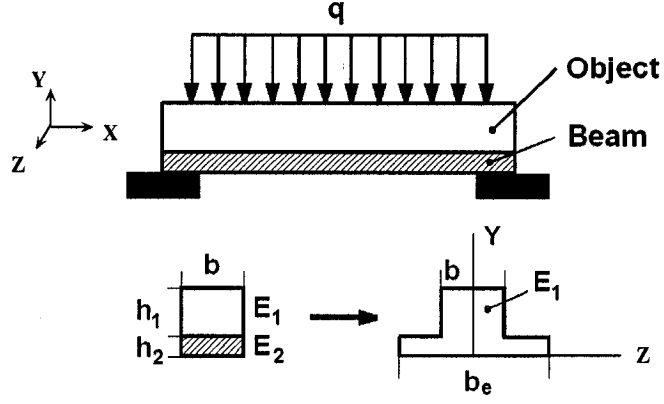


Figure 3.4: The cross section of the beam and contacted object. The initial composite beam is transformed to an equivalent beam with only one material.

Substitution of Equation 3.4 into Equation 3.3 results in

$$\frac{d^4 X}{dx^4} - K^4 X = 0 \quad (3.5)$$

where $\omega^2/a^2 = K^4$. The general solution of Equation 3.5 gives the typical normal functions for the transverse vibration of the beam [122, 123], which is:

$$X_n = C_1 \sin K_n X + C_2 \cos K_n X + C_3 \sinh K_n X + C_4 \cosh K_n X \quad (3.6)$$

where $K_n^4 = \omega_n^2/a^2$, and X_n , ω_n are the n^{th} normal-mode shape function of the beam and the natural undamped frequency of the n^{th} mode of the vibration, respectively. The constants C_1, C_2, C_3 and C_4 in Equation 3.6 must be determined from the boundary conditions at the ends of the beam. Since at a fixed end, the deflection and slope are equal to zero, boundary conditions are: $(X)_{x=0} = 0$, $(dX/dx)_{x=0} = 0$, $(X)_{x=L} = 0$, $(dX/dx)_{x=L} = 0$.

By applying the boundary conditions, the following frequency equation can be deduced as $\cos(K_n L) \cosh(K_n L) = 1$, in which $K_n L$, the roots of equation, can be calculated. Using orthogonality relationships for the eigenvalue problem of Equation 3.5, it is possible to transform the equation of motion to the modal coordinates. Eventually, applying a harmonic load leads to a similar eigenvalue problem from which the response for the dis-

tributed load and point load can be computed. For a distributed load $q(x, t) = Q(x, t)/m$, the displacement function will be (For more details see Appendix B)

$$W(x, t) = \sum_{n=1}^{\infty} \frac{X_n}{\omega_n} \int_0^L X_n \int_0^t q(x, \dot{t}) \sin \omega_n(t - \dot{t}) d\dot{t} dx \quad (3.7)$$

in which \dot{t} is a dummy variable. The out-of-plane displacement W , is the distance that the beam's neutral plane moves from its resting(unloaded) position at time t . For a concentrated load, $P_1(t) = P \sin \Omega t$ acting at the distance x_1 , the displacement W is calculated from:

$$W(x, t) = \frac{2P}{mL} \sum_{n=1}^{\infty} \frac{X_n X_{n1}}{\omega_n^2} \left(\sin \Omega t - \frac{\Omega}{\omega_n} \sin \omega_n t \right) \beta_n, \quad n = 1, 3, 5, \dots \quad (3.8)$$

where $\beta_n = (1 - \frac{\Omega^2}{\omega_n^2})^{-1}$, $\omega_n^2 = a^2 K_n^4$, and $ma^2 = EI$.

The result when the frequency of excitation approaches to zero can also be compared with the static deflection. Having computed W , the displacement in x-direction across a

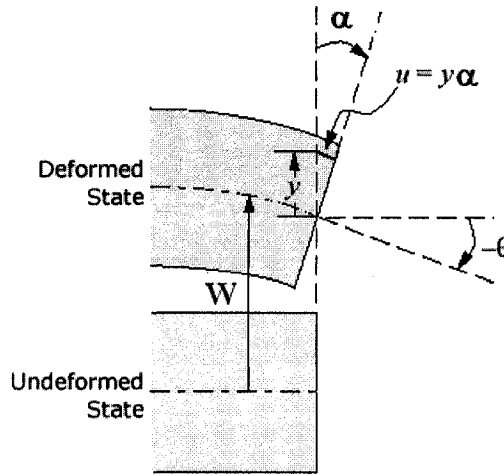


Figure 3.5: The kinematics of deformed beam (Kirchhoff Theory).

beam cross section, u , can be calculated. From the kinematics of beam shown in Figure 3.5, for small deformation, $u = \alpha y$ in which y is the distance of each point from neutral axis and α is the rotation of beam's cross section. Assuming that after bending, plane sections remain plane, normals to the cross sections remain normal and normal remains

unstretched, $\alpha = -\theta = -\frac{dW}{dx}$ in which θ is the rotation of the beam's neutral plane. Now the strain in x-direction is: $\epsilon_x = \frac{du}{dx} = -y\frac{d\alpha}{dx} = -y\frac{d^2W}{dx^2}$ and stress can be calculated from $\sigma_x = E\epsilon_x = -Ey\frac{d^2W}{dx^2}$.

The steady state response of this system to the harmonic input would be sinusoidal and the amplification factor is determined by β_n . As shown in Figure 3.6, the output response, charge Q is sinusoidal with a peak-to-peak amplitude proportional to the amplitude of the harmonic input force. Therefore, for each specific object the output of the sensor

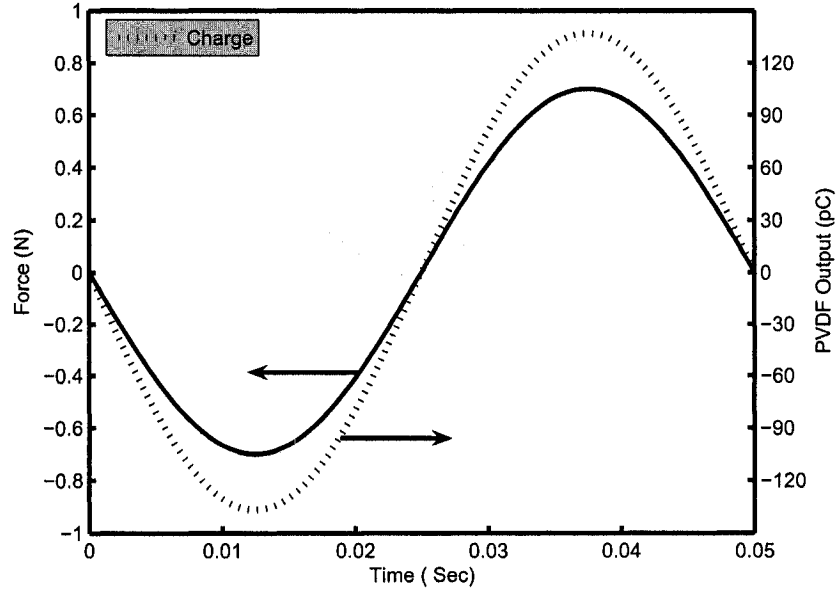


Figure 3.6: Predicted variations of output charge for a given sinusoidal input force.

would be a sinusoidal waveform with an amplitude, which is proportional to the softness of the contact object. The frequency of excitation is selected well above the cut off frequency of the system comprised of piezoelectric patch, electrical circuit and measurement equipments. It is possible to calculate the output voltage instead of output charge using the relation $Q = CV$, in which Q is the charge, V is the voltage and C is the capacitance of the film. The capacitance of the film can be calculated from $C = \epsilon_0\epsilon_r\frac{A}{d}$, where $\epsilon_0 = 8.85 \times 10^{-12}F/m$, is the permittivity of vacuum, ϵ_r is the relative permittivity of the PVDF film which is 12, A is the electrode area of the piezoelectric film and d is the

thickness of the film.

Although the analytical solution presented above is useful in studying the relationship between influential parameters, it has two major shortcomings. First, the derived formula is based on Euler beam theory, so that it cannot be used for thick beams. Second, no information about the stress state at the supports can be obtained based on this formulation. Therefore, to overcome these problems, a finite element analysis has been performed and is elaborated in the following section.

3.3.2 Finite Element Model

A coupled-field finite (FE) element analysis was used to obtain the response of the system including output charge at the supports. Using this method, the limitation on the thickness of the grasped objects imposed on the previous analytical approach is also removed, hence thicker objects can be studied as well. To perform the FE analysis, Ansys (Version 10.1.3) was used. The equations that were solved, are the linearized constitutive equations for a piezoelectric crystal when temperature difference and electrical field are negligible:

$$\{\sigma\}_{6 \times 1} = [C]_{6 \times 6} \{\epsilon\}_{6 \times 1} \quad (3.9)$$

$$\{D\}_{6 \times 1} = [e]_{6 \times 6}^T \{\epsilon\}_{6 \times 1} \quad (3.10)$$

where σ , ϵ , C and D are stress vector, strain vector, elasticity matrix and electric flux density vector, respectively. The piezoelectric matrix can be defined in $[e]$ form, the piezoelectric stress matrix, or in the $[d]$ form, the piezoelectric strain matrix (as it relates mechanical strain to the electric field), where the relationship between $[e]$ and $[d]$ can be found as: $[e] = [C] [d]$ and units normally are: $[e] : pC/m^2$, $[C] : N/m^2$ and $[d] : pC/N$. The geometry which is shown in Figure 3.2 was modeled. The piezoelectric PVDF was meshed using PLANE223, a 2-D 8-Node coupled-field solid element, suitable for piezoelectric modeling. In the piezoelectric mode, this element has three degrees of freedom at each node which are U_X , U_Y and $Volt$. In addition, the structural parts were meshed by PLANE183, a 2-D 8-Node structural solid element with only mechanical

degrees of freedom. Similar to the analytical method, both the PVDF film and the soft object are considered to be isotropic. The geometry and material properties used in the simulations are selected in such a way that they match the fabricated prototype. The free length of the beam and the length of the supports considered to be 22 *mm* and 4 *mm*, respectively. A 28 μm uniaxial PVDF film is modeled with $d_{31} = 20 \text{ pC/N}$, $d_{32} = 2 \text{ pC/N}$, and $d_{33} = -20 \text{ pC/N}$. The Young's modulus and Poisson ratio of the PVDF film are 10^9 Pa and 0.37, respectively. The flexible beam is made of a 0.8 *mm* thick Polystyrene sheet. The extensional PVDF patch assumed to be firmly attached to the beam. The other two patches of the PVDF films are sandwiched between the beam and the base. Even though only mechanical constraints are involved in finite element modeling of mechanical structures, electrical constraints are also very important in simulation of piezoelectric materials. The PVDF films that were used in the experiments were metalized at the both sides. This metal layer which also serves as electrode, creates an equipotential surface. Normally, one of these surfaces is connected to the ground and the voltage of the other surface is measured respect to the ground. Therefore, in all three piezoelectric sensing elements, the nodes at the bottom surface were electrically coupled together and considered as ground. In addition, the electrical degree of freedom of the nodes at the top surface were also considered to be electrically connected. In this way, potential were obtained for each PVDF film similar to the experimental setup. The response of the system to both distributed loads and concentrated loads are useful to be studied, as the distributed load naturally is applied when a soft material is pressed between two jaws of a grasper and the point load may be encountered when a lump is embedded in a bulky soft tissue.

3.3.3 Distributed Loads

For a given distributed load a symmetry is perceived. Therefore an equal output from both supports is expected to be proportional to the magnitude of the distributed load. The FE analysis has confirmed that the output of the middle PVDF film is proportional

to the beam deflection amplitude. The linear relationship between the magnitude of the uniformly distributed load and the voltage of the middle PVDF is demonstrated in Figure 3.7.

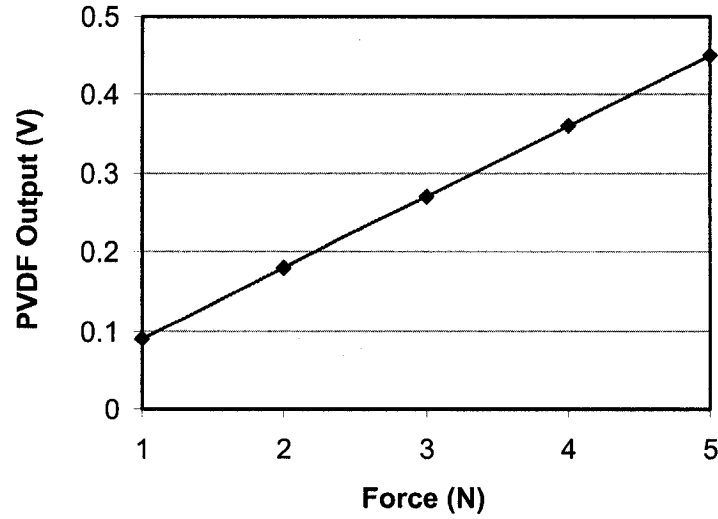


Figure 3.7: The linear relation between the uniform distributed load and the output voltage of the middle PVDF film.

The results also show that the output charge of the supports are equal and linear with respect to the magnitude of the applied load.

3.3.4 Concentrated Loads

As mentioned earlier, finding the location of a concentrated load potentially gives the sensor the ability of detecting lumps within the bulky soft tissue. Hence, the purpose of this test was to characterize the sensor output when a point load is applied at different locations of the beam. It is known that the maximum sensitivity for a given state of stress in a uniaxial PVDF film can be attained in the 1-axis direction associated with d_{31} , which is also called drawn direction (for more information regarding piezoelectric PVDF film see [119]). Initial simulations showed that the place and orientation of the PVDF films are very important. Hence a set of simulations was performed to achieve the optimum length,

place and orientation of the PVDF films. Of these simulations, two were performed to investigate the effect of orientation of the middle PVDF film (extensional mode). In the first simulation the orientation of the PVDF film is selected in such a way that the drawn direction, 1-axis is normal to the beam axis. While in the second one, the orientation is rotated by 90 degrees, hence the drawn direction is aligned with the X-axis. A point load with the intervals of 1.5 mm along the beam length, is applied to the beam and the output voltage of the three PVDF films are shown in Figures 3.8 and 3.9. When the PVDF drawn direction is aligned with the beam orientation, the output amplitude of the middle PVDF is about 0.5 volt (Figure 3.9), which for the same load is ten times more than the case in which the middle PVDF drawn direction is normal to the beam direction (Figure 3.8).

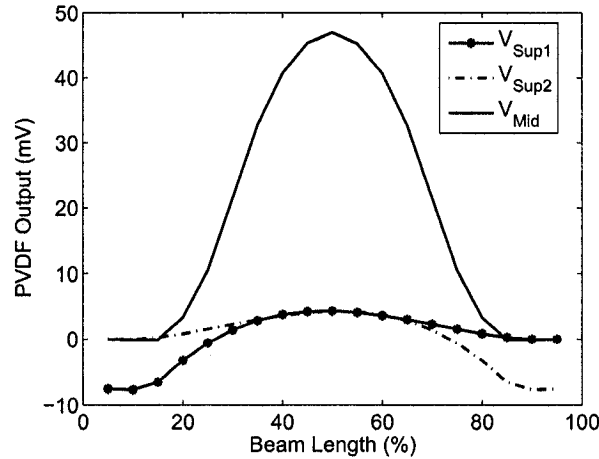


Figure 3.8: The outputs of the middle PVDF (V_{Mid}), support1 (V_{Sup1}) and support2 (V_{Sup2}) when point load is applied at different locations along the beam (The PVDF drawn direction at the supports, is aligned with the X-axis direction, while the drawn direction of the middle PVDF is rotated by 90 degrees so that it is perpendicular to the X-axis).

However the PVDF films at the supports showed a more complex behavior due to the existence of a compound state of the stress. The supports experience a combination of normal force along with component of stress in the X-direction. In addition, it is found that in the vicinity of the edges the complex state of stress might be encountered. In this

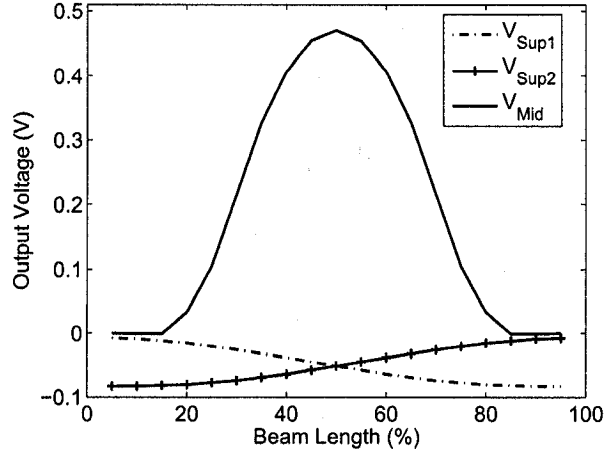


Figure 3.9: The outputs of the middle PVDF (V_{Mid}), support1 (V_{Sup1}) and support2 (V_{Sup2}) when point load is applied at different locations along the beam (The PVDF at the supports are rotated by 90 degree so that they are perpendicular to the X-axis direction, while the drawn direction of the film in the middle is aligned with the X-axis).

condition, even though the PVDF films at the central part of the supports experience uniform compressive stress, it is important to consider that close to the edges of the supports, non-uniformity in stress may occur. Due to this edge effect, undesired compressive stress and tensile stress occur at the inner and outer edges of the supports, respectively. This stress concentration affects the PVDF films output voltage and should be eliminated.

Figure 3.8 illustrates the output voltage of both supports when the PVDF drawn direction is aligned with the beam length, X-direction. The output of the PVDF film at each support is the combination of $\sigma_1 d_{31} + \sigma_3 d_{33}$, ($\sigma_2 \approx 0$). Since $d_{31} > 0$ and $d_{33} < 0$, it is possible that the algebraic sum of the output charge tends toward zero. This situation can be seen in Figure 3.8. In these points despite applying a load on the beam, the output of the PVDF films, positioned on the supports, is zero. This can be considered as a sort of uncertainty of the system, hence the location of the applied point load would be difficult to determine. To resolve this problem, the PVDF films at the supports are rotated in order to align the drawn direction perpendicular to the X-axis. Since $d_{32} \approx d_{31}/10$, the contribution of undesired mode, i.e. d_{32} is reduced to one tenth of the original state so

that, the dominant output charge is now associated with the thickness mode.

In addition, to avoid the edge effect, the metalized part of the PVDF film is reduced to the span of 0.2 to 0.8 of the support length. The result of these changes is shown in Figure 3.9. The output voltage at each support starts from a maximum negative value when the point load is applied exactly on that support and then the magnitude approaches to zero when the load moves toward the other support. Due to symmetric geometry, the responses of the supports also show similar but opposite trends. Using the output responses of both supports in the Figure 3.9, it is possible to find the position of the applied point load. In addition, the magnitude of the applied load can be measured from either supports. The determination of the magnitude and the position of a point load results in finding the location of any hard objects such as embedded small size bone or lump within a bulky soft tissue.

Therefore, in this study the arrangement used in Figure 3.9, is adopted. Note that in this figure the drawn direction of the middle PVDF film, 1-axis is aligned with x-direction, while the drawn direction of the PVDF films at the supports are rotated by 90 degrees. In order to obtain the relationship between the applied load and supports response, a set of point loads ranged from 0.5 to 5 N is applied at the center of the sensor and the resulted voltage from the supports is plotted in Figure 3.10. The linear relationship is observed. It should be noted that the effect of a point load which is applied exactly at the mid point of the beam is similar to the effect of a uniformly distributed load. Therefore, there could be some exceptional load combinations for which the outputs of the sensing elements are identical making the sensor unable to differentiate. Therefore, in order to differentiate these load conditions, the tissue has to be grasped from at least two different orientations or positions.

3.3.5 Softness Sensing

As previously mentioned, the primary feature of the proposed sensor is the ability to measure the compliance of the contact objects. These objects are assumed to be grasped

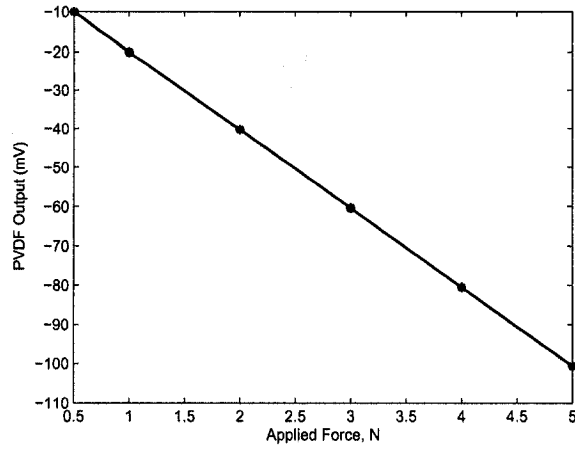


Figure 3.10: The total output of either supports when a point load ranged from 0.5 to 5 N is applied to the middle of the sensor.

and compressed with the MIS tool, causing the flexible part of the sensor to bend. In order to simulate a similar situation a distributed load is considered while soft objects are assumed to be isotropic with different Young's modulus. A wide range of soft objects are simulated and the outputs of the supports and middle PVDF films are recorded. The results are shown in Figures 3.11 and 3.12.

It can be seen in Figure 3.11 that the output of the PVDF films at the supports are substantially a function of applied force. On the other hand, Figure 3.12 shows that the output of the middle PVDF film is a function of both the applied force as well as the Young's modulus of the object. Therefore, knowing the applied force from the PVDF films at the supports (Figure 3.11), it is possible to distinguish the objects based on their compliance (Figure 3.12). The simulated tests covered a wide range of compliant objects corresponding to very soft materials having Young's modulus ranging from 10 kPa to 100 MPa. The sensor exhibits good sensitivity in this range. For instance, the output voltage of the sensor for $F=0.75$ N in Figure 3.12, varies from 12 mV for $E = 10^8 Pa$ to 110 mV for $E = 10^4 Pa$.

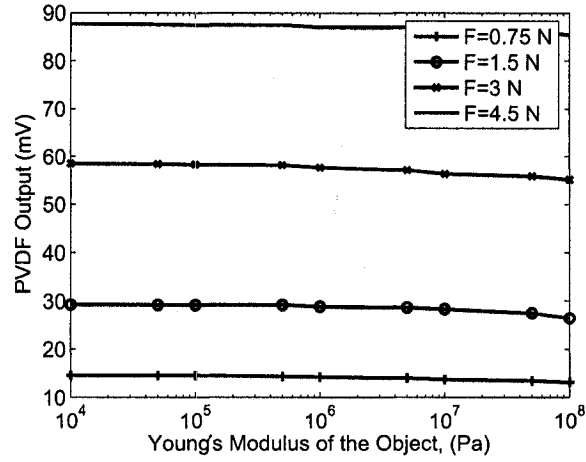


Figure 3.11: The output of the PVDF films at the supports when distributed loads ranged from 0.75 to 4.5 N applied to the elastomeric objects with different Young's modulus.

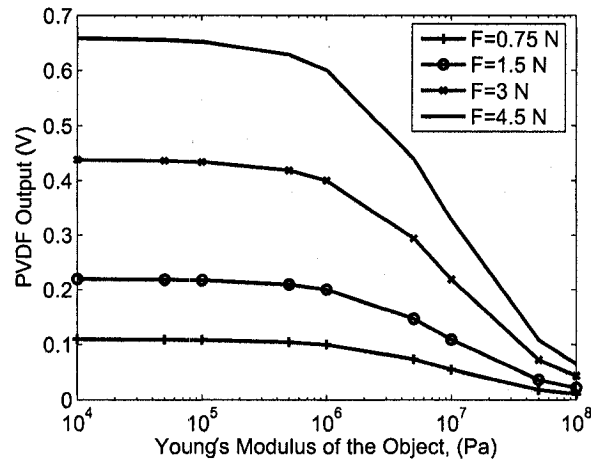


Figure 3.12: The output of the middle PVDF film when distributed load ranged from 0.75 N to 4.5 N is applied on to the soft objects.

3.4 Sensor Fabrication

A sensor unit, having uniaxial $28\text{-}\mu\text{m}$ PVDF film as sensing element and Polystyrene as flexible beam was fabricated. The beam and support lengths were 22 mm and 4 mm , respectively. In order to fabricate the sensor, the first three pieces of PVDF films were cut to the $4\text{ mm} \times 3\text{ mm}$ (two pieces) and $18\text{ mm} \times 4\text{ mm}$ (one piece). Having used the results of the finite element analysis, the middle PVDF film was cut along with the 1-axis, drawn direction, while the other two sensing elements were cut in 2-axis, transverse direction. Using conductive epoxy glue, thin copper electrodes were adhered to the top and bottom surfaces of the PVDF patches. The PVDF films, then were epoxy glued to the flexible beam. A firm adhesion guaranties that the strains developed in the PVDF film are equal to that of the beam. Finally the beam was placed on the solid platform. Figure 3.13 [124, 125] shows a photograph of the sensor, its wiring, the point load probe and the reference load sensor.

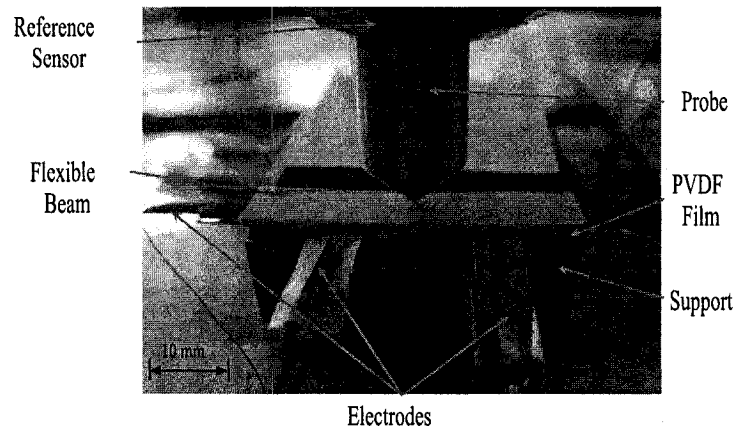


Figure 3.13: A picture of the manufactured sensor, with a known load applied at the mid point of the sensor.

3.5 Experiments

In order to validate the simulation results, an experimental set up was developed to test the fabricated sensor as well as its capability in discriminating objects based on their softness. A signal generator was used to apply sinusoidal waveform, which was fed into a set of a shaker and power amplifier (V203, PA25E-CE, Ling Dynamic Systems). To characterize the output voltage of the manufactured sensor unit, a calibrated load sensor (Kistler 9712B50) was used to record the amount of the applied load. To record the output of the middle PVDF of the sensor a data acquisition system, DAQ (National Instrument, NI PCI-6225) associated with Labview software (Version 7.1) was used. The 60 Hz line noise was filtered out using Labview built-in Butterworth low pass filter. The block diagram with a simplified electrical circuits are shown in Figure 3.14, in which the operational amplifier is used to convert the PVDF charge output into the voltage output. Since three PVDF films were used in this research, three channels similar to what is illustrated in Figure 3.14, were used.

In contrast to the voltage-mode amplifiers in which the output voltage depends on the input impedance, in charge-mode amplifiers the output voltage depends on the feedback capacitance, C_f and charge developed on the piezoelectric film, Q . Therefore, the output voltage of the charge amplifier is independent of the cable capacitance which is one of the main advantages of the charge amplifiers in piezoelectric applications. The voltage gain can be determined by the ratio Q/C_f .

3.5.1 Force Position

In order to test the performance of the sensor in detecting the position of applied force, a series of point loads was applied to the sensor (See Figure 3.13). With constant force, the position of the point load was moved along the length of the flexible beam of the sensor and data was recorded and plotted against the theoretical results as shown in Figure 3.15. This figure compares the results of the three approaches. The finite element results are taken from Figure 3.9. For the analytical part, the procedure presented in Section 3.3.1

was used. However, this time the load was applied to ten equally spaced points along the beam length and the peak values of the charge output were calculated. The charge values were then converted to the voltage values and plotted on the same graph. The experiments were also conducted with the conditions similar to those of the simulations. For each recording, a sinusoidal load was applied and peak-to-peak of about 20 samples were recorded in a file. For each loading condition, several reading was recorded. Then the average, maximum and minimum of the data were determined and plotted.

3.5.2 Softness Sensing

To characterize the sensor response when different soft materials are touched, a series of experiments using silicone rubbers (Test Kit) are conducted. The silicone rubber test kit (from Instron [126]) contains seven pieces of color-coded silicon rubber with different softness which is designed for calibration or verification purposes. The picture of type A test block kit which complies with the standard ASTM D2240 is shown in Figure 3.16. The softness of each piece in terms of Shore A and its corresponding color is shown in Table 3.1. To investigate the relationship between the elastic linear Young's modulus of the

Table 3.1: The specification of Type A Test Block Kit.

Color	Softness in Shore A
White	32.4 ± 2
Yellow	41.9 ± 2
Blue	52.0 ± 2
Green	61.3 ± 2
Red	71.7 ± 2
Brown	81.7 ± 2
Black	88.8 ± 2

pieces and their softness, a series of conventional compression tests were performed using

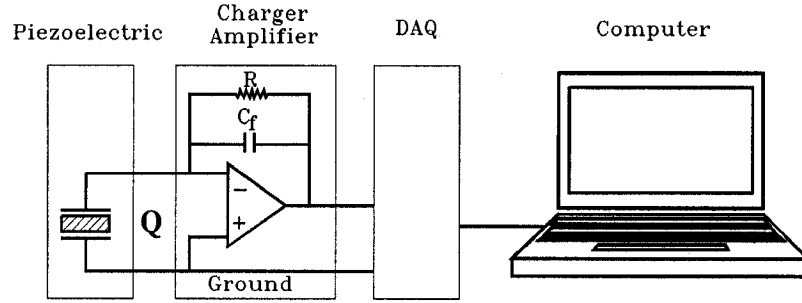


Figure 3.14: Block diagram of the electrical components used for amplification, signal conditioning and recording the PVDF film output.

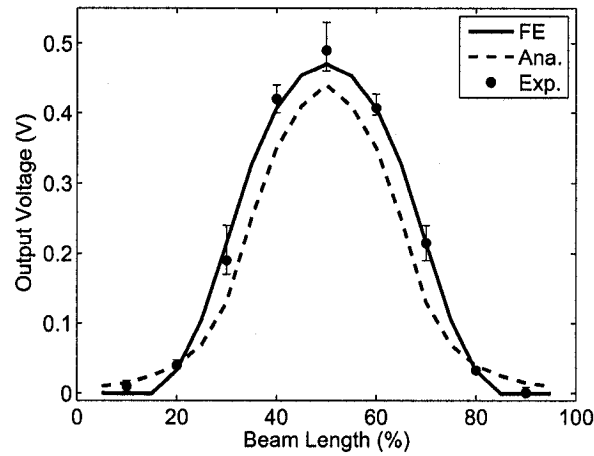


Figure 3.15: The output of middle PVDF film when a load was applied along the sensor at equal intervals (errorbar indicates the range of readings).

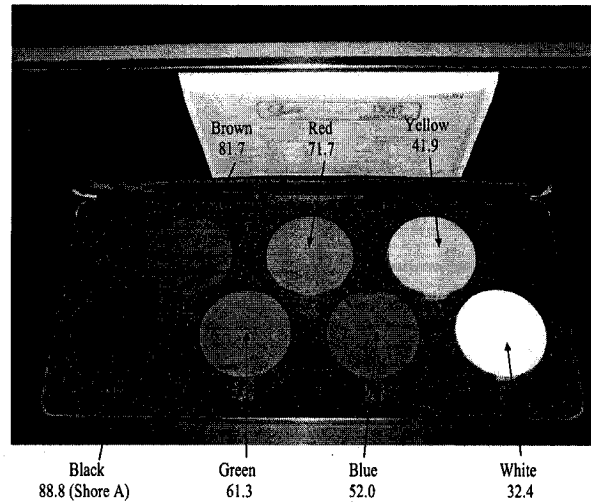


Figure 3.16: The picture of the Type A Test Block Kit used as standard soft material for softness sensing characterization. Under each color the softness number in Shore A scale is indicated.

Bose, 3200 Series. The stress-strain curve for four of these rubbers are shown in Figure 3.17. The nonlinear relationship between the Young's modulus of the silicon rubbers and their corresponding softness number is shown in Figure 3.18. For instance, for the two hardest rubber (Brown and Black), 22% difference in Young's modulus has produced a 8% difference in softness number. The characterized silicon samples were then used in soft sensing tests with the multifunctional sensor. The output of the middle PVDF when a load of 3 N was applied to a range of silicon rubbers from the softest to the hardest (i.e., from white to black) is shown in Figure 3.19. The output voltage drops significantly for the harder samples. It must be noted that the rate of this attenuation depends on the ratio of rigidity of contact objects to the rigidity of the beam. Repeating these tests for a wide range of standard soft materials and range of applied force, provides enough data for a look up table which can be used in a calibration procedure. Therefore, for a given force any output voltage can be attributed to a specific softness.

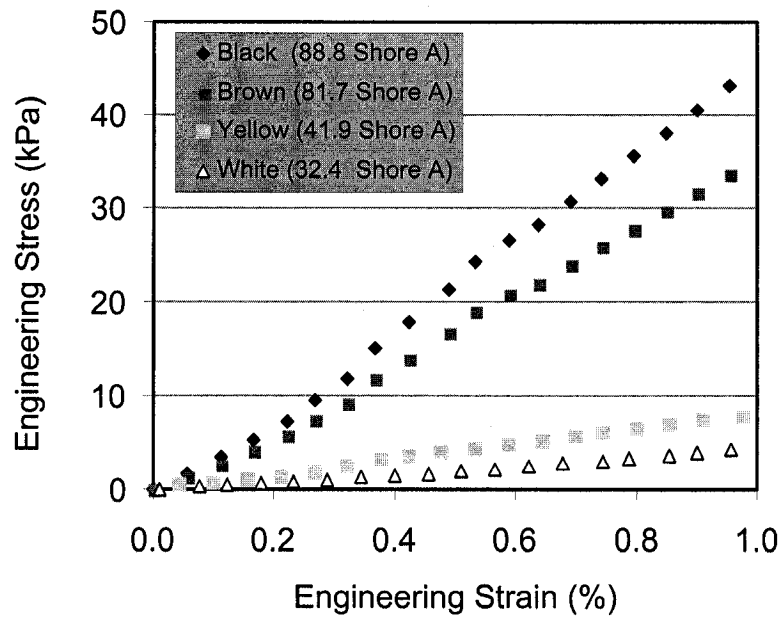


Figure 3.17: The compressive stress-strain curve obtained for standard silicon rubbers.

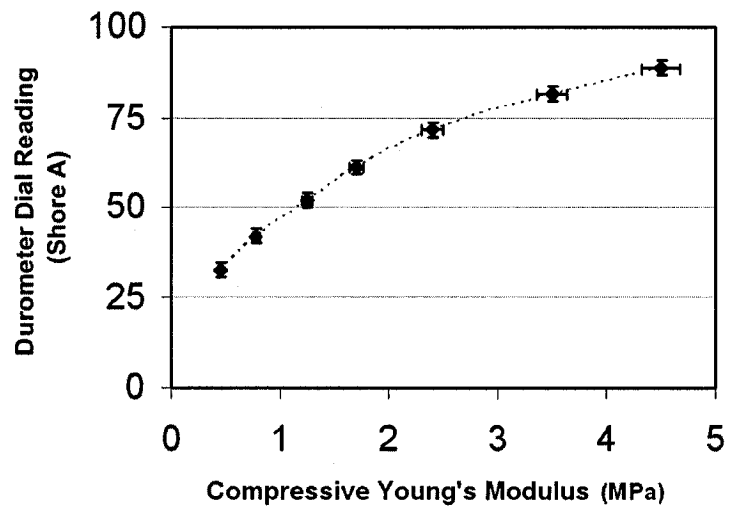


Figure 3.18: The relationship between the compressive Young's modulus of the silicon rubbers and their associated softness number in shore A scale (errorbar indicates the range of readings).

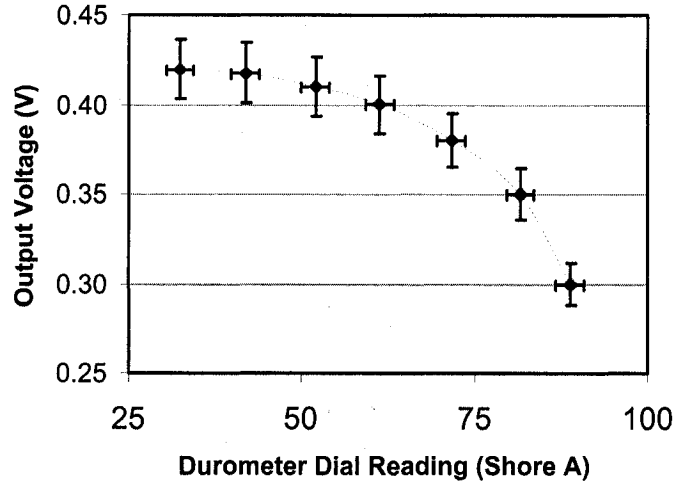


Figure 3.19: The output of middle PVDF film, when a 3 N load was applied to silicon rubbers with softness ranging from 32 to 89 shore A (errorbar indicates the range of readings).

3.6 Discussion and Conclusions

A PVDF based multi-functional tactile sensor for MIS applications is proposed. The operating concept, which is based on the combined flexural rigidity of the flexible beam and the soft object, is explained. One of the advantages of the sensor is that it can be microfabricated and hence can potentially be mass produced at a significantly reduced cost. It is also shown that the sensor is capable of measuring the magnitude and the position of the applied load on the object as well as the compliance of the contact object. The tooth-like structure of the sensor makes the sensor suitable for firm grasping of soft objects. This tooth-like shape can easily be obtained by using, for instance, anisotropic wet etching, which is a standard micromachining process. Another advantage of the sensor design is that one dimensional array or two dimensional matrix of the proposed sensor can easily be fabricated.

To evaluate these abilities, both analytical and numerical methods were used. In the analytical method, a simplified model for the thin beams and objects was used. The equivalent cross section of a composite beam was calculated and the responses of the beam for a harmonic point load as well as the distributed load were computed. It is

shown that for a given force, the peak amplitude of the PVDF output was proportional to the Young's modulus of the object. In addition, to model the PVDF films at the supports, a coupled-field finite element analysis using Ansys was performed. It was found that the best configuration for the PVDF films at the support was when the drawn direction, 1-axis was perpendicular to the beam orientation, X-axis. In this case the thickness mode was the dominant mode and the output was proportional to the total applied load. To validate the computed results, a sensor unit was prototyped and tested for position sensitivity. The obtained experimental results were in a close agreement with the theoretical data.

The Young's modulus encountered in MIS, depending on the type of surgery, may include a broad range of stiffness. The very soft tissues can have Young's modulus of several kPa. The rubber-like materials can have the Young's modulus ranged between several kPa to several MPa. The biopolymers show stiffer property up to several GPa. In this study, for the softness sensing, a broad range of soft materials ranged from 10 *kPa* to 100 *MPa* was simulated. However, the Young's modulus of the materials used in the experiments were less than 5 Mpa.

However, for the best result, the proposed sensor has to be optimized for a specific surgery with a given range of softness. A broader range of stiffness means less resolution. Therefore, to achieve the maximum sensitivity and resolution, not only the range of stiffness must be limited, but also the thickness, material and length of the flexible beam must be appropriately optimized.

To assess the capability of sensor in differentiating objects based on their softness, a couple of experiments were carried out. In addition to softness differentiation in a qualitative way, quantification of softness was presented using standard softness measurement used in the industries.

Chapter 4

Tissue-Grasper Interaction

4.1 Introduction

The interaction between grasper and tissue is important from several aspects. The information of how a grasper affects the force distribution within the grasped tissue, directly affects the grasper and tactile sensor design. In addition, for a given grasper, the existence of any anatomical features such as lumps or arteries affects the force distribution. The study of this distribution helps the optimization of the grasper and its tactile sensors to achieve, for instance, the desired spatial resolution. This study also responds to the question of how a smart endoscopic grasper should be tested.

Magnitude, frequency and shape of real forces that act at the interface of grasper and tissue is useful in testing the proposed multifunctional tactile sensor under a condition which is similar to the working conditions.

The first section of this chapter focuses on characterization of force applied to the object grasped by the endoscopic graspers. It is shown that the force profile applied to grasped object not only is related to force applied by the hand, but also depends on material properties of the grasped object. Experiments were conducted with several kinds of materials with different mechanical properties and profile of force in each case was recorded. The recorded force signature can be approximated by sinusoidal and pulse waveforms for soft and hard tissues, respectively. Although this section addresses general

characteristic of force experienced by tissue and grasper, it does not provide any information about the local distribution of force along grasper jaws. In addition, the capability of a smart endoscopic grasper in detecting hidden features such as lumps is of prime importance and hence the study of local force distribution in the presence of a lump is of particular interest. In characterizing lumps, a couple of parameters are involved. Therefore, a parametric study of lumps embedded in tissue after considering hyperelastic behavior of soft tissue is presented. The study of the effects of hidden lumps in soft tissue is crucial for the development of any smart endoscopic grasper. The response of any grasper equipped with tactile sensors depends on the real mechanical behavior of the grasped tissue.

4.2 The Force Signature of MIS Graspers

To characterize the load experienced by grasped soft object, two Force Sensitive Resistors, (FSR) are used. The one which is shown in Figure 4.1, is placed between two pieces of test materials. Once grasper is closed the resistance of the FSR is decreased and measured by a Data Acquisition Card (DAQ). The second FSR is attached to the handle of endoscopic grasper to measure the surgeon's applied force. The outputs of both sensors are connected to the DAQ through an electric circuit. A code is developed in LabView environment in which the forces are calculated from the measured resistance.

4.2.1 Calibration

Before any attempt to use the sensors, they had to be calibrated. Basically, when load is applied to the FSR sensor its resistance will change. Unfortunately, it was found that the relationship between applied force and resistance of the sensors was not linear. However, the relationship between the applied force and conductance of the sensor found to be linear. To obtain the force-conductance relationship of the sensors an experimental calibration procedure was conducted and the result is shown in Figure 4.2. For DAQ an

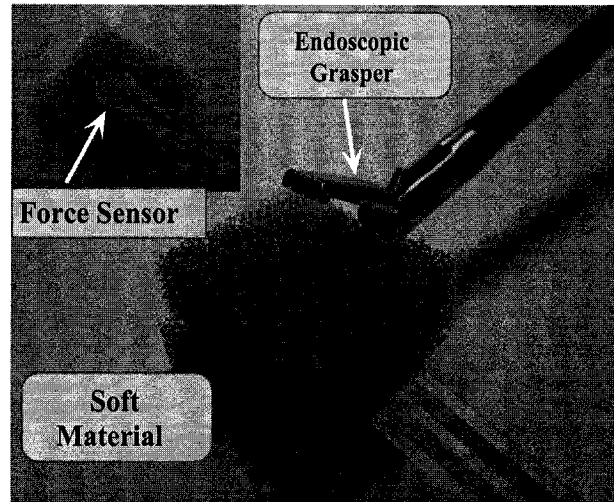


Figure 4.1: The picture of endoscopic grasper, soft object and the sensor used for this experiment.

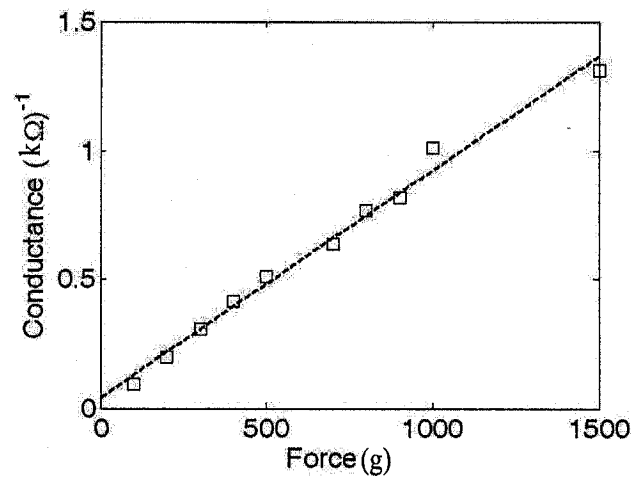


Figure 4.2: The experimental relationship between applied force and conductance of the sensor.

input voltage was required. Therefore, by using another resistor a voltage divider was made. In the later case, an applied load caused a change in the resistance of the sensor and consequently a change in sensor's voltage was observed. From this, force-voltage relation of the FSRs as shown in Figure 4.3 was obtained.

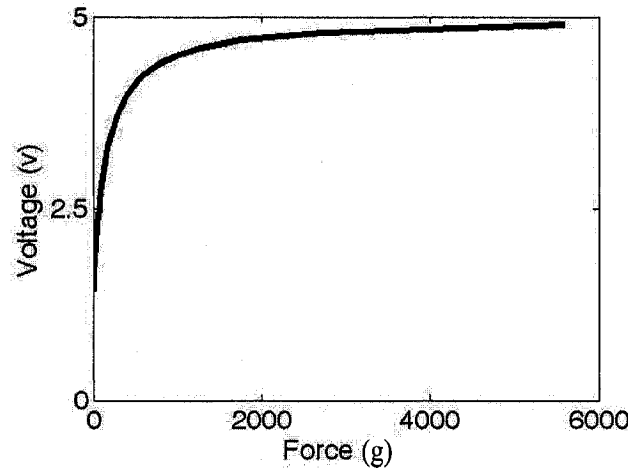


Figure 4.3: The relationship between applied force and sensor's output voltage.

4.2.2 Force Signature

After the sensor was characterized several soft and hard materials were tested. In these tests, materials were grasped several times using a MIS grasper replicating a typical grasping action in MIS surgeries. In order to determine the maximum force that could be experienced by the object, the amplitude of applied force was kept higher than that of normal grasping. Although this force may cause permanent damage to the delicate tissue, it can determine the maximum load under which the smart graspers should be tested. The variation of the voltage for several cycle was recorded. The general force signature for the soft materials were similar. Alternatively, the force profiles for the hard materials were similar together but different from those of soft materials.

Figure 4.4 illustrates the force experienced by a soft material. The frequency content of this force also is shown in the bottom picture. It was observed that the grasping action

creates a force profile which can be approximated by a sinusoidal waveform. Alternatively

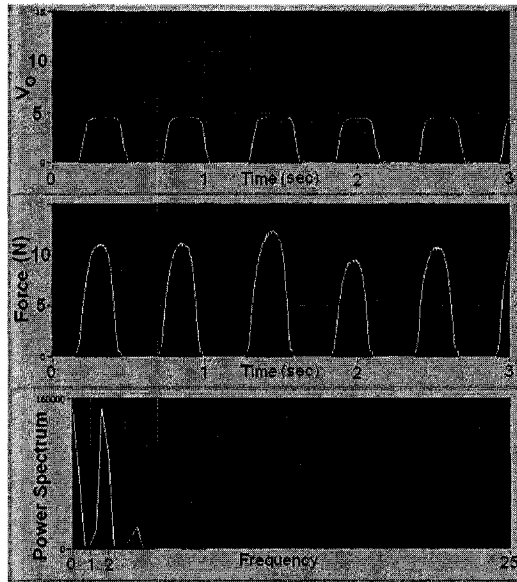


Figure 4.4: The force profile experienced by a grasped soft object. V_0 is the output voltage of the sensor. The corresponding force, sensed by the sensor is also shown in the middle graph. The frequency content (Hz) of the force shows that the force waveform is very similar to sinusoidal or half-sinusoidal waveforms.

the similar tests were performed on the hard materials. Figure 4.5 shows the result of the test on the hard objects. In this case, the measured force can be modeled as a pulse. The results of these tests can be analyzed by the fact that soft objects show a low resistance against the applied load. However, this resistance increases gradually until the strain reaches to high values beyond which object starts resisting against the load. This point is the peak of the force profile. In the releasing phase, the reverse cycle starts. This scenario is different for the hard objects in which the force suddenly jumps to its maximum and maintains until the releasing phase starts. In the releasing phase the grasper suddenly detaches from the hard object and the force drops rapidly. The comparison between frequency content of these two experiments shows that the soft material grasping has a main component in a frequency between 1 and 2 Hz which is similar to the half-wave sinusoidal waveform. Whereas the force profile in hard object grasping can be compared with a pulse.

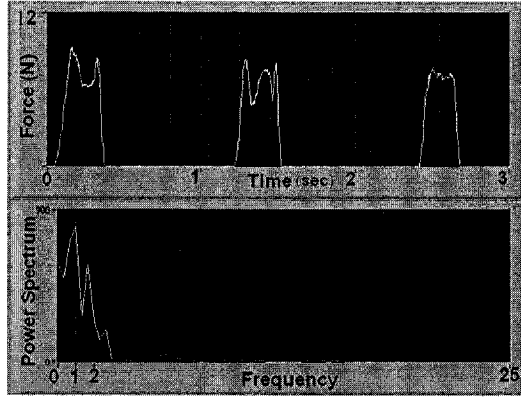


Figure 4.5: The force profile experienced by a grasped hard object.

After understanding the nature of the applied load experienced by the soft object in general, one can look at the force distribution within the grasped object and also at the tissue-grasper interface. As the presence of a lump has a significant contribution in this distribution, the rest of this chapter is devoted to the study of force distribution at grasper surface in the presence of a lump. It was preferred to use hyperelastic formulation to analyze this problem as soft material undergoes large strain under grasping action.

4.3 Hyperelasticity

Conventional theory of elasticity is primarily based on the infinitesimal strains, in which the linear elastic assumptions are applied. For finite deformations, however, these assumptions are not valid and in general the response of the material is different from that of the linear theories. Materials that can experience a recoverable large elastic strain are referred to as hyperelastic materials. For the hyperelastic materials, a Helmholtz free-energy function $\psi = \psi(\mathbf{C}) = \psi_I[I_1(\mathbf{C}), I_2(\mathbf{C}), I_3(\mathbf{C})] = \psi_\lambda(\lambda_1, \lambda_2, \lambda_3)$ exists in such a way that

$$S_{ij} = 2 \frac{\partial \psi}{\partial C_{ij}} \quad (4.1)$$

where I_1 , I_2 and I_3 are the strain invariants of the symmetric right Cauchy-Green tensor \mathbf{C} , and λ_a , $a = 1, 2, 3$ are the principal stretches. The Second Piola-Kirchhoff stress

tensor \mathbf{S} , is related to the Cauchy Stress tensor $\boldsymbol{\sigma}$, by: $\boldsymbol{\sigma} = J^{-1}\mathbf{F}\mathbf{S}\mathbf{F}$, where \mathbf{F} is the deformation gradient of the motion, i.e., $\mathbf{F}(\mathbf{X}, t) = \text{Grad } \mathbf{x}$. It can be shown that the relationship between Cauchy-Green tensor \mathbf{C} and the deformation gradient \mathbf{F} is: $\mathbf{C} = \mathbf{F}^T\mathbf{F}$. The Jacobian of the motion, J , is defined as $J = \det[F_{ij}]$. In this article, to denote scalar, vector and tensor quantities we use uppercase letters when they are evaluated in the reference configuration, and lowercase letters for corresponding quantities in the current configurations. For example, symbols \mathbf{X} and \mathbf{x} represent the positions in the referential(original) and deformed (current) configurations, respectively.

The general form of Cauchy stress tensor $\boldsymbol{\sigma}$ for an isotropic and incompressible material can be derived as [127]:

$$\boldsymbol{\sigma} = -p\mathbf{I} + 2\frac{\partial\psi}{\partial I_1}\mathbf{C} - 2\frac{\partial\psi}{\partial I_2}\mathbf{C}^{-1} \quad (4.2)$$

where I_1, I_2 (and I_3), the invariants of C_{ij} are:

$$\begin{cases} I_1 = \lambda_1^2 + \lambda_2^2 + \lambda_3^2 \\ I_2 = \lambda_1^2\lambda_2^2 + \lambda_2^2\lambda_3^2 + \lambda_3^2\lambda_1^2 \\ I_3 = \lambda_1^2\lambda_2^2\lambda_3^2 = J^2 \end{cases} \quad (4.3)$$

The symbol J is also a measure of compressibility, i.e., the ratio of the deformed elastic volume over the undeformed (reference) volume of material. For incompressible material, therefore, a kinematic constraint, namely $J = \lambda_1\lambda_2\lambda_3 = 1$ can be considered. Hence, as seen in equation 4.2, the two principal invariants I_1 and I_2 are the only independent deformation variables.

4.4 Hyperelastic Relationships in Uniaxial Loading

All strain energy density functions that are introduced for hyperelastic materials contain some unknowns referred as *material constants*. These constants must be accurately computed for the material under the test conditions. The conventional way of deriving these constants is using the experimental stress-strain data. Technically, it is recommended

that these test data should be taken from several modes of deformation over a wide range of strain values. The number of modes of deformation in experimental tests should be at least as many deformation states as will be experienced in the analysis [116].

For the present study, the test data of compression which is the dominant mode in the MIS grasping, was used in order to find the material constants of the strain energy function. For a uniaxial compression, $\lambda_1 = \lambda_{applied} = \lambda$ is the stretch in the direction being loaded. For an incompressible isotropic material in an unconstrained compression test, the stretch in the other two directions are equal, $\lambda_2 = \lambda_3$ and also $\sigma_2 = \sigma_3 = 0$. From the introduced relationships among the principal stretches and the compressibility condition ($J = \lambda_1 \lambda_2 \lambda_3 = 1$) we arrive at:

$$\lambda_2 = \lambda_3 = \lambda^{-1/2} \quad (4.4)$$

For the uniaxial loading the motion χ can be expressed by the explicit equations:

$$\begin{cases} x_1 = \lambda X_1 \\ x_2 = 1/\sqrt{\lambda} X_2 \\ x_3 = 1/\sqrt{\lambda} X_3 \end{cases} \quad (4.5)$$

Therefore, the deformation gradient $F_{aA} = \frac{\partial x_a}{\partial X_A}$; $a, A = 1, 2, 3$ has the form:

$$[\mathbf{F}] = \begin{bmatrix} \lambda & 0 & 0 \\ 0 & \sqrt{\lambda} & 0 \\ 0 & 0 & \sqrt{\lambda} \end{bmatrix} \quad (4.6)$$

The Right Cauchy-Green tensor \mathbf{C} , can be obtained from equation 4.6 as follows:

$$[\mathbf{C}] = [\mathbf{F}]^T [\mathbf{F}] = \begin{bmatrix} \lambda^2 & 0 & 0 \\ 0 & \lambda^{-1} & 0 \\ 0 & 0 & \lambda^{-1} \end{bmatrix} \quad (4.7)$$

The strain invariants, therefore, can be calculated directly from the principal stretches

given by Equation 4.3 or from Cauchy-Green tensor:

$$\begin{cases} I_1 = \text{tr}(\mathbf{C}) = \lambda^2 + 2\lambda^{-1} \\ I_2 = \frac{1}{2}\{[\text{tr}(\mathbf{C})]^2 - \text{tr}(\mathbf{C}^2)\} = 2\lambda + \lambda^{-2} \\ I_3 = \det(\mathbf{C}) = 1 \end{cases} \quad (4.8)$$

Considering relations given in Equation 4.7, the Cauchy stress given by Equation 4.2 will be reduced to the principal stresses:

$$\sigma_{11} = -p + 2\frac{\partial\psi}{\partial I_1}\lambda^2 - 2\frac{\partial\psi}{\partial I_2}\lambda^{-2} \quad (4.9)$$

$$\sigma_{22} = -p + 2\frac{\partial\psi}{\partial I_1}\lambda^{-1} - 2\frac{\partial\psi}{\partial I_2}\lambda = 0 \quad (4.10)$$

Subtracting Equation 4.10 from 4.9, we find that

$$\sigma_{11} = 2(\lambda^2 - \lambda^{-1})\left[\frac{\partial\psi}{\partial I_1} + \frac{\partial\psi}{\partial I_2}\lambda^{-1}\right] \quad (4.11)$$

Therefore, with having a suitable strain energy function, the derivation of ψ respect to the invariants can be obtained and the stresses (here σ_{11}) can be found. For example, consider a strain energy function of the following general form [128],

$$\psi = \sum_{\substack{i=0 \\ j=0}}^{\infty} C_{ij}(I_1 - 3)^i(I_2 - 3)^j \quad (4.12)$$

which can be used for a wide range of applications. For a stress free condition in the reference configuration (undeformed state), ψ should be equal to zero. Since in the reference configuration $\lambda_1 = \lambda_2 = \lambda_3 = 1$, and from Equation 4.8, $I_1 = I_2 = 3$, therefore, I_1 and I_2 are subtracted by 3. In addition, for the same reason the constant C_{00} (when $i = j = 0$) must be zero.

In the above equation when $i = 0$, $j = 1$ and $i = 1$, $j = 0$, the two-term Mooney-Rivlin equation is obtained, i.e., $\psi = C_{10}(I_1 - 3) + C_{01}(I_2 - 3)$. By substitution of partial derivation of ψ respect to I_1 , i.e., $\partial\psi/\partial I_1 = C_{10}$ and I_2 , i.e., $\partial\psi/\partial I_2 = C_{01}$ into Equation 4.11 we find that

$$\sigma_{11} = 2(\lambda^2 - \lambda^{-1})(C_{10} + C_{01}\lambda^{-1}) \quad (4.13)$$

The constants C_{01} and C_{10} in the last equation can be obtained from the stress-strain relations of the material. To develop a more accurate model, more terms can be used. For instance, the 3-term Mooney-Rivlin model for incompressible materials, which was used for the present study is in the form of:

$$\psi = C_{10}(I_1 - 3) + C_{01}(I_2 - 3) + C_{11}(I_1 - 3)(I_2 - 3) \quad (4.14)$$

In the uniaxial stress-strain compression test, a cubic specimen of elastomeric material with the dimension of $17 \text{ mm} \times 17 \text{ mm} \times 19 \text{ mm}$ was cut out of a sheet and was placed between two platens designed for compression tests. Then with a displacement rate of 2 mm/sec the sample was compressed until the force reached to the machine's force limit (40 N) and the test was terminated. The compression tests was done using MCR (Modular Compact Rheometer) 500 from Physica, Anton Paar. In order to reach to a stable and repeatable condition, before recording the test results, three compression tests were done. The output results of the corresponding software was in the form of force and displacement, which was converted to the engineering strain and stress using the area and the initial thickness of the specimens. The dependency of the results to the strain rate, was examined by repeating the test at different strain rates. For the selected rubber-like material, negligible difference between results was observed. Three samples were tested under the same mentioned conditions and the results showed that the maximum error was less than 4% between the samples. The numerical values were averaged and the result is plotted in the Figure 4.6. The shape of the curve is similar to those of compression tests done on the abdominal organs [129] which shows the closeness of the hyperelastic behavior of the elastomeric with the real tissue.

In order to find the constants of the model, the averaged curve was used using least square fitting procedure. The experimental values of engineering stress-strain, then were compared with the curve obtained from the optimization procedure for the 3-term Mooney-Rivlin model as illustrated in Figure 4.6. It should be noted that initially a two-term model was tried. Nevertheless, the three-term model was preferred due to its better approximation. The numerical values of the constants for the two and three terms

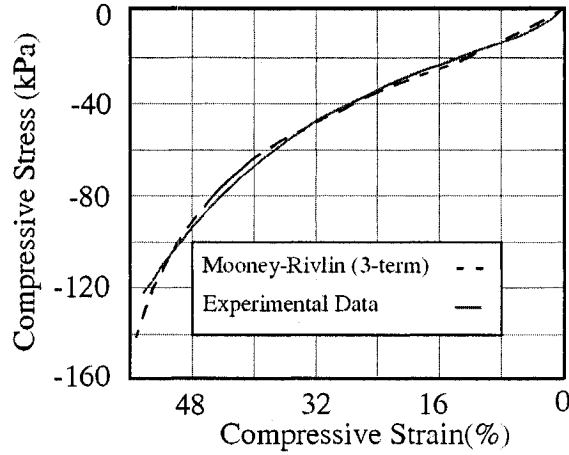


Figure 4.6: Comparison between testing and 3-term Mooney-Rivlin strain energy function. The horizontal and vertical axes are engineering strain and engineering stress, respectively.

Mooney-Rivlin model are summarized in Table 1.

Table 4.1: The constants of 2 and 3 terms Mooney-Rivlin Model (kPa).

Model	N	C_{10}	C_{01}	C_{11}	Residual
Mooney-Rivlin	2	31.33	-8.92	-	7.34
Mooney-Rivlin	3	68.49	-39.88	5.71	4.7

4.5 Finite Element Modeling

A nonlinear three dimensional finite element model using Ansys commercial software was developed. The *mixed u-p formulation* was used to solve the problem because of its superior results in solving the hyperelastic incompressible problems compared with the *pure displacement formulation* [130]. Although the displacement formulation is computationally efficient, its accuracy is dependent on Poisson's ratio or bulk modulus. In this formulation, volumetric strain is determined from derivatives of displacements, which are not as accurately predicted as the displacements themselves. For nearly incompressible materials, in which the Poisson's ratio is close to 0.5 or bulk modulus approaches infin-

ity, any small error in the predicted volumetric strain will appear as a large error in the hydrostatic pressure and subsequently in the stresses. This error, in turn will also affect the displacement prediction, as external loads are balanced by the stresses. This may results in smaller displacements than they should be for a given mesh (which is called *Locking*) or, in some case, it will result in no convergence at all. The mentioned problem also are encountered in fully incompressible deformation, such as fully incompressible hyperelastic materials. In the mixed u-p formulation in which the hydrostatic pressure \bar{P} is interpolated on the element level and solved on the global level independently in the same way as displacement, these difficulties are eliminated. In this method, the contribution of hydrostatic pressure referred to as *volumetric response* is separated from the *deviatoric response*. Therefore, the stress, for instance has to be updated by:

$$\sigma'_{ij} = \sigma_{ij} - \delta_{ij}\bar{P} \quad (4.15)$$

where the prime in σ'_{ij} shows the deviatoric component of Cauchy stress tensor. Alternatively, the deviatoric component of deformation tensor e_{ij} can be expressed as:

$$\epsilon'_{ij} = \epsilon_{ij} - \frac{1}{3}\delta_{ij}e_v \quad (4.16)$$

where $e_v = \delta_{ij}e_{ij} = e_{ii}$ and

$$e_{ij} = \frac{1}{2}\left(\frac{\partial u_i}{\partial x_j} + \frac{\partial u_j}{\partial x_i}\right) \quad (4.17)$$

in which u_i and x_i are the displacement and coordinate in the current configuration, respectively. In addition, for a fully incompressible hyperelastic material, the volume constraint is the incompressible condition (Sussman and Bathe [131], Bonet and Wood [132], Crisfield [133]):

$$1 - J = 0 \quad (4.18)$$

where, $J = |F_{ij}| = dv/dV_0$ in which $|F_{ij}|$ is the determinant of deformation gradient tensor and V_0 is the original volume. The constraint Equation 4.18 is introduced to the internal virtual work by the Lagrangian multiplier \bar{P} . Finally differentiating the

augmented internal virtual work, gives the stiffness matrix in the form of:

$$\begin{bmatrix} K_{uu} & K_{up} \\ K_{pu} & K_{pp} \end{bmatrix} \begin{Bmatrix} \Delta u \\ \Delta \bar{P} \end{Bmatrix} = \begin{Bmatrix} R \\ 0 \end{Bmatrix} \quad (4.19)$$

where Δu and $\Delta \bar{P}$ are displacement and hydrostatic pressure increments, respectively.

The stiffness sub-matrices can be obtained from the following equations [134].

$$K_{uu} = \int_V [B_D]^T [\dot{C}] [B_D] dV \quad (4.20)$$

$$K_{up} = K_{up}^T = - \int_V [B_V]^T [N_p] dV \quad (4.21)$$

$$K_{pp} = - \int_V [N_p]^T \frac{1}{\kappa} [N_p] dV \quad (4.22)$$

where $[\dot{C}]$ is the stress-strain matrix for the deviatoric stress and strain components. The matrix $[N_p]$ can be obtained from the additional interpolation introduced for hydrostatic pressure: $p = [N_p]\{\bar{P}\}$. The deviatoric strain-displacement matrix $[B_D]$ is given by: $\{\epsilon\} = [B_D]\{d\}$ in which $\{d\}$ is the vector of nodal displacements. In element formulation, material constitutive law has to be used to create the relation between stress increment and strain increment. The constitutive only reflects the stress increment due to straining. However, the Cauchy stress can not be used, because it is affected by the rigid body rotation and is not objective (not frame invariant). Therefore, an objective stress is needed to be able to be applied in constitutive law. The Jaumann-Zaremba rate of Cauchy stress expressed by McMeeking and Rice [135] is one of them [127] which is defined as follows:

$$\dot{\sigma}_{ij}^J = \dot{\sigma}_{ij} - \sigma_{ik}\dot{\omega}_{jk} - \sigma_{jk}\dot{\omega}_{ik} \quad (4.23)$$

where $\dot{\sigma}_{ij}^J$ is the Jaumann-Zaremba rate of Cauchy stress, $\dot{\omega} = \frac{1}{2}(\frac{\partial v_i}{\partial x_j} - \frac{\partial v_j}{\partial x_i})$ is the spin tensor and $\dot{\sigma}_{ij}$ is the time rate of Cauchy stress. On the other hand, using the constitutive law, the stress change due to straining can be expressed as:

$$\dot{\sigma}_{ij}^J = C_{ijkl}d_{kl} \quad (4.24)$$

where C_{ijkl} is the material constitutive tensor and d_{kl} is known as rate of deformation tensor and given by:

$$d_{ij} = \frac{1}{2}(\frac{\partial v_i}{\partial x_j} + \frac{\partial v_j}{\partial x_i}) = d_{ji} \quad (4.25)$$

in which v_i is the velocity. By substituting Equation 4.24 into Equation 4.23, the Cauchy stress tensor can be obtained as:

$$\sigma_{ij} = C_{ijkl}d_{kl} + \sigma_{ik}\dot{\omega}_{jk} + \sigma_{jk}\dot{\omega}_{ik} \quad (4.26)$$

In the present study, in order to model the portion of tissue that is grasped by MIS grasper a cube contained a stiffer object is considered for the geometry under study. The bulk soft tissue as well as tumor were modeled using 10-node tetrahedral Solid187 element which has a quadratic displacement behavior and is well suited to modeling irregular meshes. Each node has three degrees of freedom, translations in the nodal x, y and z directions. This element has mixed formulation capability for simulating deformation of nearly incompressible elastoplastic materials, and fully incompressible hyperelastic materials. Although, soft tissue assumed to be hyperelastic, tumor was considered to be isotropic. The strain energy function ψ for soft material was selected to be the 3-term Mooney-Rivlin model [136] due to its satisfactory performance in compression state of stress. As elaborated below the three coefficients of the model for incompressible isotropic hyperelastic materials, were obtained from the implemented experimental stress-strain data using least squares optimization method.

4.5.1 The Parametric Study

As mentioned in Section 4.1, a number of parameters have significant effect on the output, e.g., the voltage output of the sensors positioned on the contact surface. In general, some combinations of the mentioned parameters produce similar stress distribution on the contact surface. Therefore, some restrictive assumptions and relationships are required to formulate the response of the system with respect to the variation of inputs. This is particularly important to facilitate the construction of an inverse model in which the information about the lump could be extracted from the tactile image or stress distribution at the contact surface. Therefore, introducing substitutive parameters obtained by combining several parameters is preferred.

As an example of parameter reduction, consider the parameters that are required to determine the size of a lump. In general, at least three parameters are required to determine the size of a lump. Since tumors can largely be approximated as spherical features, the number of parameters to characterize the size of the tumors or lumps can be reduced to one value, i.e., the lump radius.

The cross section of the finite element model of the hidden mass embedded in the soft tissue is shown in Figure 4.7. In the following, the impact of variation of each involved parameter is presented. To demonstrate the variations of tactile image, the stress distribution recorded on a path defined by a straight line that passes from the middle of the bottom surface, for each case study is recorded and plotted. This was found to be a clearer way than 3-D graphs. The variation of pressure is represented by pressure ratio P/P_{in} , in which P is the pressure distribution across the contact surface caused by the lump and P_{in} is the applied pressure. This ratio, therefore, defines that how much the pressure distribution is influenced by the lump and other associated parameters.

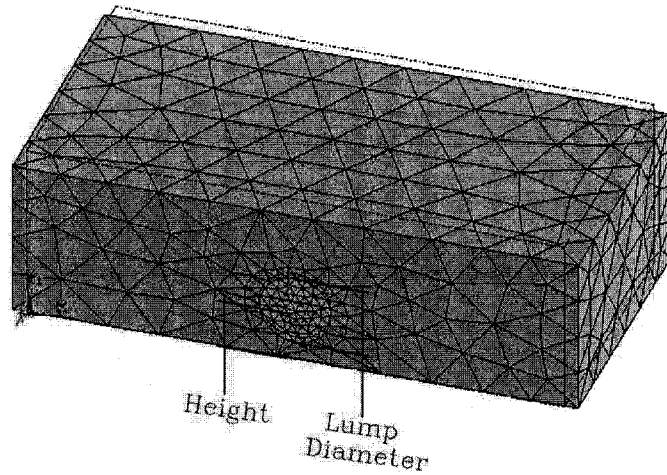


Figure 4.7: A half-model of soft tissue which contains a lump

The Effect of Lump Size

The size of a tumor is normally significant in diagnostic phase of a disease. In addition, early detection of tumors, followed by appropriate treatment can increase the cure rates radically. To show the effect of the tumor size on the pressure distribution and consequently on the system output, a spherical lump was considered inside a bulk soft tissue. In this set of simulations, the diameter of the lump was changed from 2 mm to 8 mm corresponding to the $D/t \approx 0.2$ to $D/t \approx 0.8$ in which D and t are diameter of the lump and thickness of tissue, respectively. For each ratio, the pressure distribution at the contact surface was predicted and is shown in Figure 4.8. In these simulations, the load was applied in the form of displacement(strain). The surface nodes were coupled together and a known displacement (e.g., $U_y = 1$ mm or 4 mm) was applied at top surface of the tissue.

The center of lump was considered to be in the middle of the tissue. From the demonstrated results in Figure 4.9, it can be deduced that with the increase of lump size, the maximum pressure value increases almost linearly for relatively small and medium size lumps, while the peak pressure is elevated nonlinearly for large size lumps. In Figure 4.8, the curve corresponding to the tumor size of $R = 1$ mm, with a low peak value, indicates that the small size lumps are very difficult to be detected. As shown in the next simulation, the maximum pressure ratio is also highly sensitive to the depth of the hidden lump. A lump with a large diameter has two features. It covers larger parts of sensing area. In addition, the outer surface of the lump is closer to the sensing area. The effect of lump depth is discussed in the next section.

The Effect of Depth

The depth of the lump namely H , i.e., the distance of the lump from the bottom contact(sensitive) surface, plays an important role in the amplitude as well as the shape of the pressure contour. Figure 4.10 shows how the stress distribution at the contact surface varies with the depth of the lump. In this test, the diameter of the lump was kept

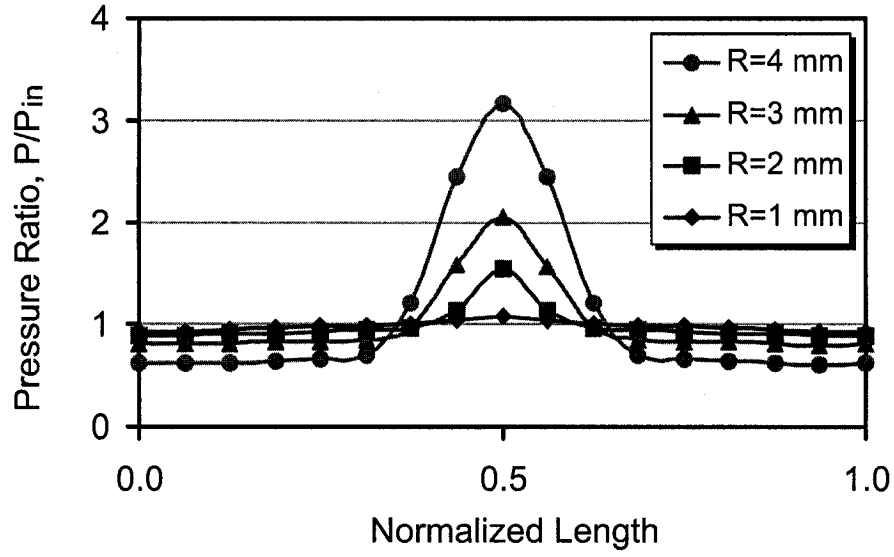


Figure 4.8: The pressure distribution at the contact surface when the lump radius was increased from $R = 1 \text{ mm}$ to $R = 4 \text{ mm}$ and $P_{in} = 5 \text{ kPa}$.

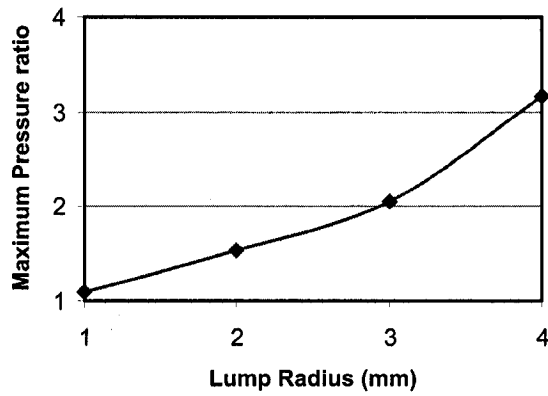


Figure 4.9: The pressure distribution at the contact surface when the lump radius was increased from $R = 1 \text{ mm}$ to $R = 4 \text{ mm}$.

constant, i.e. $D = 4 \text{ mm}$, while the lump height was changed from 2 mm to 8 mm from the contact surface, in 2 mm steps, while a 10% compressive strain ($P_{in} \approx 10 \text{ kPa}$) was applied through the top surface. As seen from this figure, the maximum pressure dramatically drops when the lump distance increases. This trend is shown in Figure 4.11 in which the maximums of each pressure distribution are plotted against the depth of lump. For the cases with distance of 6 mm and 8 mm , the peak pressures are almost identical. However, for farther lumps the pressure curve covers a larger area. For the lump at height $H = 2 \text{ mm}$ a slight undershoot was observed which could be a distinctive sign for marginal lumps. By using this information in design stage, it is possible to calculate the minimum spatial resolution for sensing elements in order to have a good approximation of lump depth. The difficulty in detecting deep lumps suggests that several attempts from different orientation might be required to localize the lump. Furthermore, it can be shown that smart graspers with two sensorized surfaces could perform better in detecting marginal lumps.

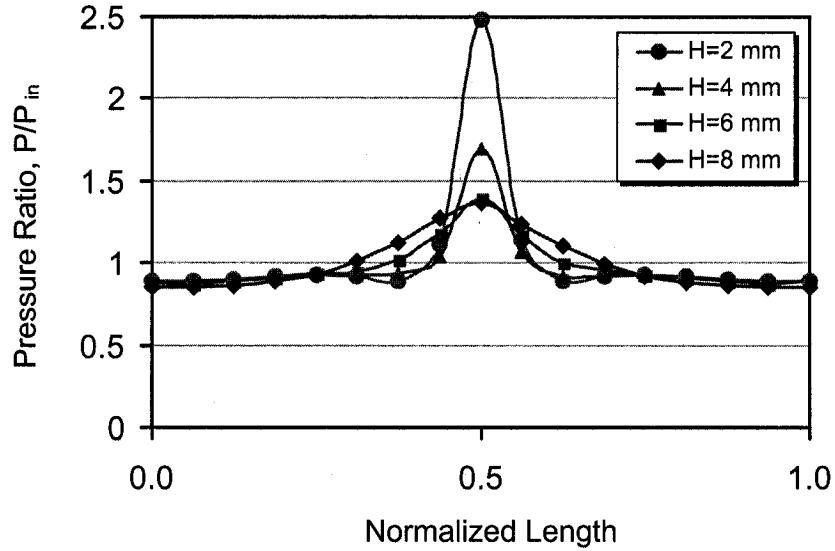


Figure 4.10: The effect of lump depth on the stress distribution when $P_{in} \approx 10 \text{ kPa}$, $R = 2 \text{ mm}$ and the center of the lump is changed from 2 mm to 8 mm from the contact (bottom) surface.

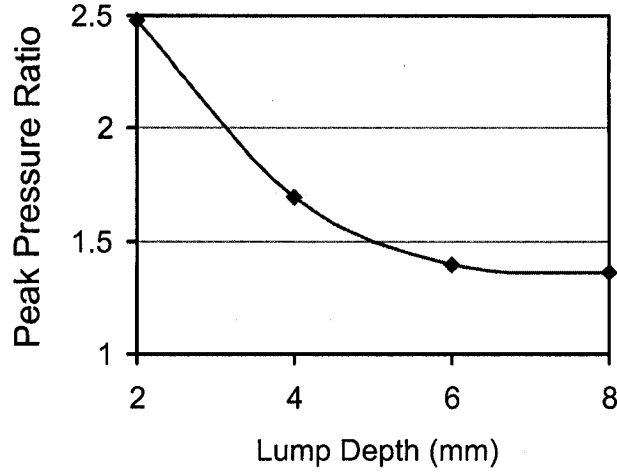


Figure 4.11: Peak pressures for different lump depths when $P_{in} \approx 10 \text{ kPa}$, $R = 2 \text{ mm}$ and the center of the lump is changed from 2 mm to 8 mm from the contact surface.

The Effect of Applied Load

The magnitude of the applied load also affects the pressure distribution. The results of the simulations when the applied load is changed from $U_y = 1 \text{ mm}$ to 4 mm are shown in Figure 4.12. The maximum pressure is proportionally increased with the magnitude of the applied load. This graph also demonstrates that an increase in applied load does not remarkably affect the area under the bell-shaped pressure contour. However, this dependency shows that for softness sensing or lump detection in addition to the stress profile, the magnitude of the total applied load must also be measured.

To exemplify the difference between the results obtained from the linear analysis and those of linearized relationships, we have compared the maximum pressure values computed for various applied displacements with those that are obtained from linear analysis. This comparison which is depicted in Figure 4.13, reveals that first, linear analysis shows higher values and second, this difference has grown for higher deformation loads. This result is in agreement with the nonlinear behavior of the tested elastomeric material illustrated in Figure 4.6. This figure demonstrates that for infinitesimal deformations a straight line could be fit to the experimental data, however for larger deformations this

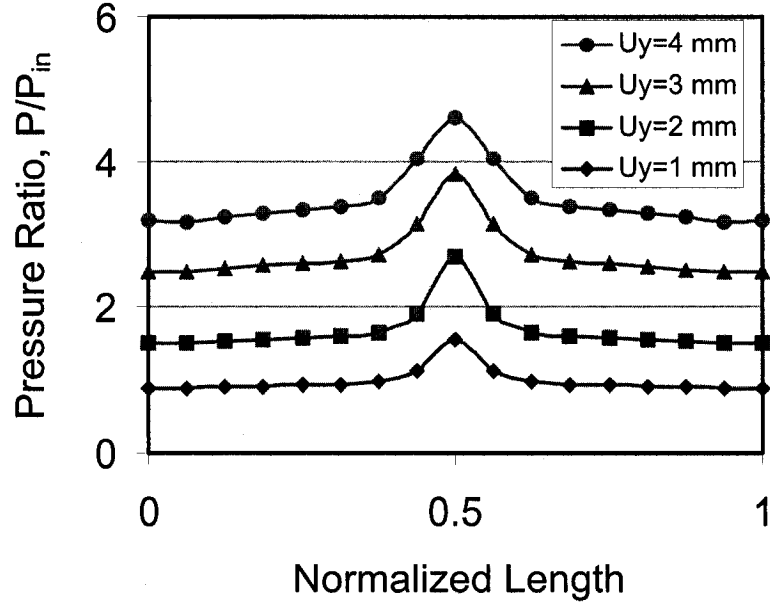


Figure 4.12: The variation of stress profile due to the variations of applied load. The values are normalized based on the background pressure for $U = 1mm$. In these simulations the lump with the radius of $R = 2 mm$ was located in the middle of the tissue.

linear fitting leads to remarkable errors.

The Effect of Lump Stiffness

The stiffness of the lump and tissue are also effective parameters in the studied case. Several researchers [137, 138] have used the ratio of Young's modulus of the lump to that of the soft tissue, (E_L/E_T) , to analyze the relative variations of stiffness of lump respect to that of tissue.

In the present analysis, considering material nonlinearities of tissue from one hand and assuming linear elastic isotropic property for the lump, the comparison between the stiffness of the lump and tissue could be complicated. Therefore, for this part of the analysis, the linear elastic modulus of the tissue was considered to be $E_T = 15 kPa$, close to the values reported for typical soft tissues [139]. Then, the Young's modulus of the lump, (E_L) was changed from $15 kPa$ to $15 MPa$. The results as shown in Figure 4.14, indicate that for the large lump's Young modulus, e.g., $1.5 MPa$ and $15 MPa$ there

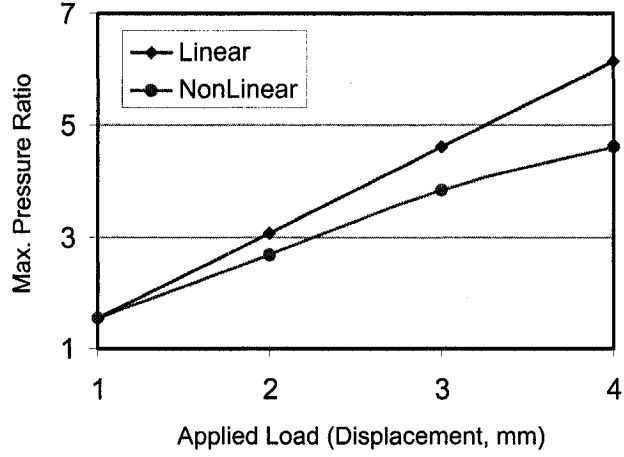


Figure 4.13: The maximum pressures obtained from nonlinear analysis against those of linear analysis. Simulation conditions are similar to that of Figure 4.12.

is no notable difference in stress profile. Indeed, the difference between the maximum pressures for $E_L = 150 \text{ kPa}$ and $E_L = 15 \text{ MPa}$ is less than 7%. In other words, the system output is not much sensitive to E_L for $E_L > 10E_T$. This is useful in reducing the number of unknowns for this problem. Since the reported Young's modulus for the lumps, for instance, in breast cancer, is normally ten times higher than that of the tissue [138], this variable can be regarded as a constant.

4.6 Experimental Validation

Validation is an important step to ensure that the numerical analysis were performed appropriately and the correct results were obtained. Nevertheless, performing experiments are not always easy. For instance, preparation of spherical lumps with the exact dimensions and exact Young's modulus on one hand and carving out their exact shape from the bulk soft tissue on the other hand is difficult. Any gap between lumps and bulk tissue due to inaccurate carving of the tissue yield erroneous results and pressure distribution. It is also challenging to accurately adjust the center of the lump at the intended positions.

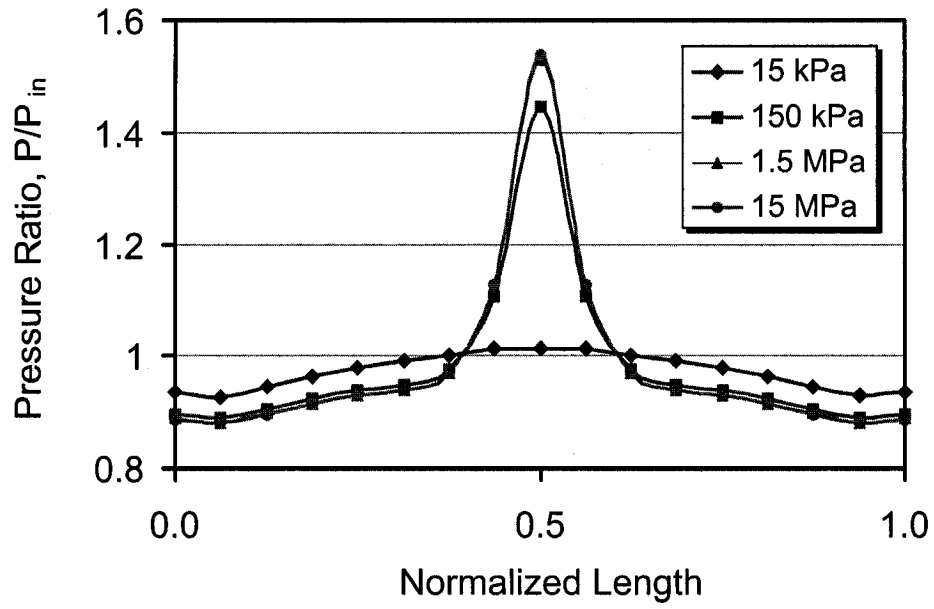


Figure 4.14: The stress distribution for different E_L , the Young's modulus of the lump while the Young's modulus of tissue was kept constant at $E_T = 15 \text{ kPa}$. The applied load was $U_y = 1 \text{ mm}$ and the lump was considered to be in the middle of the tissue.

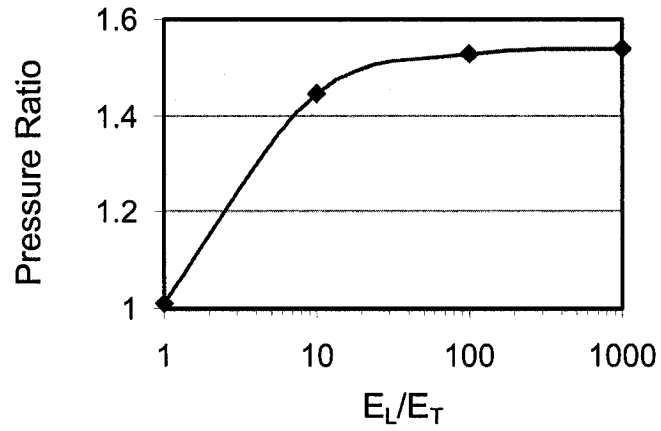


Figure 4.15: The pressure ratio for different E_L/E_T . The similar values for the parameters that of Figure 4.14.

Creating the same boundary condition in experiments and in finite element model is another challenging task. In addition, friction forces could play an important role in many experiments and very difficult to measure and implement, both in the experiments and finite element analysis. The dimensional and geometrical differences between the FEM and experiments are highly probable and could potentially be a source of error. The utilized sensing element are also important in the final result. In this study, an array of the piezoelectric PVDF (Polyvinylidene Fluoride) sensing elements were used to register the stress distribution over the contact area. Therefore, extreme care was applied in making a series of identical sensing elements in the prototyped device. However, after manufacturing some discrepancies among the sensing elements were observed. Therefore, in the initial stage the elastomeric without any lump was placed on the sensing array and the outputs of the sensors were tested and calibrated. Due to mentioned difficulties, at the present study only two different combinations of the parameters were tested. The elastomeric material that was primarily used in the compression tests, was also used in the experimental work as soft tissue. The acrylic balls with two different sizes (3 *mm* and 4 *mm*), simulating the lumps, were inserted into the hollow spaces that were carefully carved out of the bulk elastomeric. To change the depth of the lumps, several layers of the elastomeric material were cut into same dimensions but different thicknesses. The lumps were placed in one of the layers, so that the other elastomeric layers could be used as spacers to increase or decrease the distance of the lump layer from the top or bottom surfaces while the total thickness was kept constant. A dynamic load was applied by the shaker which was driven by a power amplifier and a signal generator. To register the pressure distribution on the contact surface, an array of 1.5 *mm*-wide, 28- μ m thick PVDF film, were positioned 0.5 *mm* apart. The picture of the sensor with seven sensing elements is shown in Figure 4.16. To apply uniform distributed load a flat plate was attached to the probe as shown in Figure 4.17. In order to change the depth of lump, multiple layers of elastomeric material were used. The experimental setup was similar to the previous experiments and is shown in Figure 2.20. The outputs of the sensors were

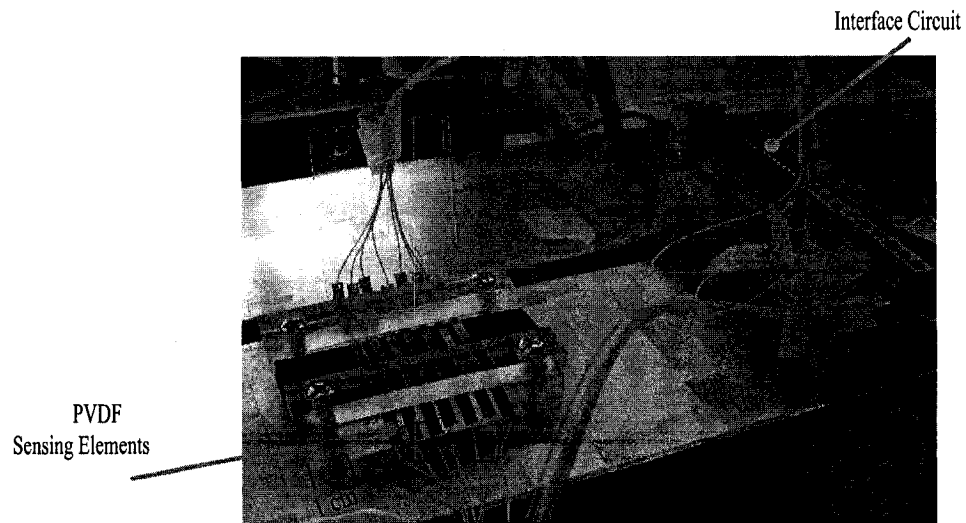


Figure 4.16: The sensor with seven sensing elements is connected to DAQ.



Figure 4.17: Soft object with embedded lumps under the test. Top plate was to replicate the upper jaw of grasper to apply compressive loads.

fed into the connector box through the interface circuit. The data was then transferred to the computer using the DAQ (NI PCI-6225, National Instrument). To reduce the noise effect, in each experiment the average of peak values of at least 20 cycles are recorded and arithmetically averaged. In the first test (i.e. Test1), the parameters were as follows: applied displacement $U_y = 2.5 \text{ mm}$; diameter and depth of the lump were 6 mm and 5 mm , respectively. While in the second test, the applied displacement was $U_y = 1 \text{ mm}$ and diameter and depth of the lump were 4 mm and 4 mm , respectively. The experimental results are compared with finite element results and shown in Figure 4.18.

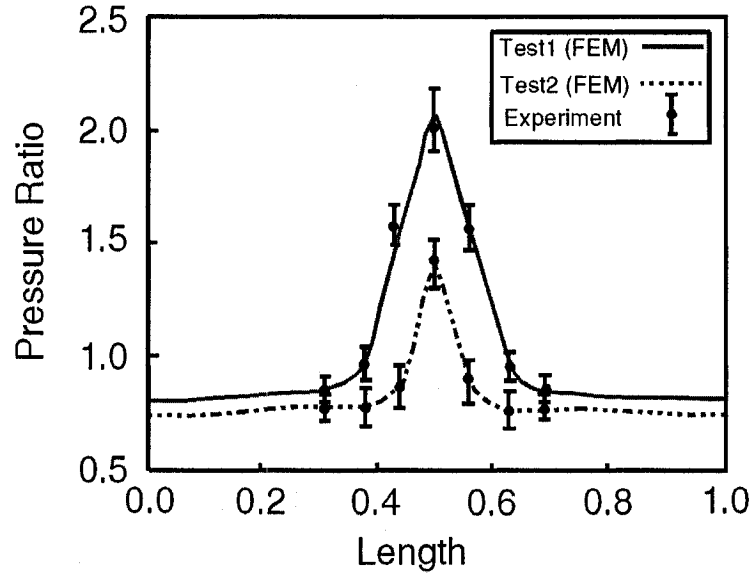


Figure 4.18: The experimental data versus finite element results (error bar indicates the range of readings). The simulation conditions for Test1: $U_y = 2.5 \text{ mm}$, $R = 3 \text{ mm}$, Depth=5 mm and for Test2 : $U_y = 1 \text{ mm}$, $R = 2 \text{ mm}$, Depth=4 mm.

4.7 Discussion and Conclusions

The results obtained from the finite element analysis of a mass embedded in soft tissue are presented in Section 4.5.1 and they show that the pressure distribution at the contact surface is influenced by several parameters such as size, depth and stiffness of the lump as well as the applied force. The nonlinearity of the response respect to these parameters are shown. This nonlinearity can be attributed to both *material nonlinearity* of soft tissue and *geometrical nonlinearity* which happens for large strains. The response to variation in applied load, as depicted in Figure 4.12, shows that although an increase in grasping load causes an increase in the maximum pressure, the shape of curve remains unchanged. In addition, the amount of area that each curve covers remains almost constant. This could be an distinctive sign that differentiates the effect of variations in load from the variations in the size and depth of the lump.

It is shown that although the ratio of Young's modulus of the lump to that of tissue is an effective factor, the stress profile remains almost unaltered for the ratios higher than 10. On the other hand, the pressure ratio is highly sensitive to the variation of stiffness of the lump for $E_L < 10E_T$ which potentially is helpful in detecting lumps in their early stages.

The thickness of tissue clearly affects the stress profile, however, for a specific arrangement of lump and tissue, the increase in tissue thickness is equal to the decrease in lump size. Therefore, it is possible to combine both parameters into one variable in order to reduce the number of involved parameters, by introducing the dimensionless ratio D/t , i.e., the lump diameter to the tissue thickness.

The soft tissue shows very complex behavior including hysteresis and viscoelasticity which have not been considered in this study. Nevertheless, special attention was paid in order to model accurately the nonlinearity of the tissue. To do this, an elastomeric was mechanically tested and the experimental data was used for simulations. Initially several strain energy functions, such as, Ogden, Neo–Hookean and Mooney–Rivlin were considered and finally it was found that 3-term Mooney–Rivlin demonstrated satisfactory

agreement with the experimental data. The geometry and boundary conditions in the simulations were assumed in such a way that replicate the state of a tissue grasped by a typical MIS tool. The existence of the lump within the grasped tissue affects the pressure distribution on the contact surface. Therefore, close inspection of the pressure distribution reveals valuable information about the lump which is useful particularly in developing inverse models of the problem as well as designing the smart endoscopic graspers. The findings of this study can be used to calculate the required sensitivity and resolution of the sensing elements located at the contact surface as well as spatial resolution of any proposed array or matrix of the sensors for this purpose. In addition, the tactile image can be used for the visualization and enhancement of the existing 2-D video images.

Chapter 5

Graphical Rendering of Localized Lumps for MIS Applications

5.1 Introduction

Despite numerous advantages of MIS procedures, there are some shortcomings that have been the subjects of studies in the last decade. Numerous research works on restoring the sense of touch (e.g., force, softness and pulse sensing) to surgeon, have been performed [1, 61, 140]. However, there is just a handful of work conducted on finding hidden anatomical features [25, 67, 102, 141, 142], which are mostly performed for locating breast lumps. Detecting masses or stiffened tissue is a routine practice performed by surgeons commonly in open surgeries. The biological tissue composition and consistency are often changed from one tissue to another by various diseases [65]. For example, malignant tumours are generally harder than the surrounding tissue, and this is the reason why tumours can often be detected by palpation. To the best knowledge of the authors, no comprehensive research work has been reported on the characterizing and rendering hidden masses for MIS or robotic MIS applications. In addition to locating an embedded lump, conveying the extracted information to the surgeon is another challenge. The solution of this problem will also be useful for the development of sophisticated remote palpation device. Some of the earliest tactile sensor designs using piezoresistive and capacitive transduction

principles were reported in the early 1990s [143]. A majority of research works with tactile applications are dedicated to the force and pressure sensors [144, 145, 146, 147]. However, some researchers have introduced tactile sensors capable of softness sensing or lump detection. For instance, a tactile sensor that was able to detect the hardness/softness of an object impressed upon was developed by Omata *et al.* [148]. The sensor works on the principle that contact with an object will cause a change in the resonance frequency of a piezoelectric element. Barmana *et al.* [69] developed a deformable force-stretch array, called DFSA, for lump detection. Their complex sensor combines an array of linearly deformable tactile sensing element (tactels) with length change transducing stretch elements connecting the tactel tips. The force transducers (tactels) are deformable but more rigid than the tissue of the body part to be palpated. The second major components of the DFSA are elastic stretch elements, which bridge the tips of the tactels and conform to the body surface contour. Although the sensor shows satisfactory results in detecting nodules, there is no report that it can be microfabricated and is suitable for MIS applications. Wellman and Howe [67] reported the development of a model along with an inversion algorithm for extracting breast lump features from the distributed contact pressure between a scan head and the tissue. They utilized a matrix of piezoelectric pressure sensors placed at hand held probe which scans the target region. By comparing the response of the system to the places without and with hidden mass, a tactile map was developed. Their parametric study showed the influence of the lump and surrounding parameters on the output response. The techniques such as scanning and signal processing methods used in their study were tailored for the detection of breast tumors. Howe *et al.* [42] also reported investigation on a remote palpation system in which an 8x8 tactile sensor array was used to register the pressure distribution at the contact surface of sensor and object. Then using shape memory alloys, a 6 x 4 pin elements designed as shape display to render the desired shape to the human finger. Another work in the domain of breast lumps was reported [149] in which, a tactile mapping device for characterizing and documenting breast lumps was developed. This device measures three key variables during palpation:

the examiner's search patterns, the applied forces, and the small-scale pressure variations at the skin due to lumps. In a work reported by Yan *et al.* [150] finding an inclusion in a medium was considered as a signal detection problem. All useful information in an observed vector valued function was summarized into a single statistical scalar-value, whose probability distribution under different conditions is known. Comparison of this statistical value to a threshold value permits the detection of the inclusion. A biological sensor for detecting foreign bodies is presented by Shimizu [151]. It consists of a balloon probe, which is constructed with a thin rubber membrane inflated with compressed air, and an optical deformation analyzing system. Although this system can detect the presence of small balls embedded within a sponge, due to its complexity, it cannot easily be applied to MIS graspers. Shikida *et al.* [62] reported a tactile sensor that can detect both force and hardness of an object. It consists of a diaphragm with a mesa structure, a piezo-resistive displacement sensor on the diaphragm, and a chamber for pneumatic actuation. Their proposed sensor is complex and difficult to be used in MIS. In addition, it needs effective way of presenting data to the surgeon. A sensor reported by Najarian *et al.* [152] consists of a rigid cylindrical and a deformable rubber-like section which is able to measure the stiffness of the touched objects. Although this sensor is integrated with a typical endoscopic grasper used in minimally invasive surgeries, its microfabrication is a challenge. Wellman *et al.* have used an array of piezoresistive pressure sensors as a scan head to measure the contact pressure [66, 153]. By measuring the position and orientation of the scan head using an electromagnetic tracker, a tactile map of the tissue is prepared that can show the position and size of the tumors. In research conducted by Wellman *et al.* [67, 154] the experiments and computational method were developed to provide the size and elasticity of breast tumors. Using force-displacement data from indentation tests on a synthetic breast model, embedded tumors could be differentiated from the surrounding tissue-like material. Galea and Howe [155], examined the potential for tactile imaging to measure tissue properties and geometric information about subsurface anatomical features such as large blood vessels. While a couple of papers have investigated the tumor detection

in breast cancer [43, 67, 153], almost no comprehensive work has been done to locate, characterize and render lumps in MIS surgery. In addition, displaying the recorded tactile information has been limited to some primary and complex prototyped shape display devices which require special electronics and signal processing. In this paper, a system for characterizing the embedded lumps and its graphical rendering is introduced. In the proposed system, using an MIS multifunctional tactile sensor [78], the masses within the tissue are detected, located, features extracted, and visually displayed. The utilized sensor unit is a comparatively simple piezoelectric Polyvinylidene Fluoride (PVDF) base tactile sensor which is associated with a new approach for the graphical demonstration of lumps embedded in a soft object. The displayed images are readily recognizable by the surgeon and there is no need for extra hardware. When an array of the sensors is placed in one jaw of the endoscopic grasper, the location of the lump along the grasper could be detected and displayed. While, by using two arrays of the sensors in the upper and lower jaws of the grasper, it is possible to find and graphically represent the depth of the lump in the grasped object as well. Therefore, using the proposed system, surgeons can detect the presence or absence of the lump and obtain useful information on its size and location by simply grasping the target organ by the smart endoscopic grasper.

5.2 System Design

The proposed system used for this study consists of a smart endoscopic grasper equipped with an array of tactile sensors, data acquisition interface (DAQ), and the necessary signal processing algorithms that process the tactile information provided the sensors and finally displaying the visual information. The complete system is schematically shown in Figure 5.1. As shown in this figure, when surgeon uses the smart endoscopic grasper to grasp a tissue, the sensor array measures the contact force distribution across each sensing element as well as the total applied force. The electrical outputs of the piezoelectric sensing elements are then conditioned and transmitted to the data acquisition system.

Using the data acquisition card, the signals are amplified, filtered, digitized and processed by a computer. A computer code was developed in LabView (version 7.1) environment for signal conditioning such as filtering out the line noise. In addition, a rendering algorithm also developed in LabView, was used to map the extracted signal's features to a gray scale image. Using the constructed images, surgeon realizes not only the presence or absence of lump, but also the approximate size and location of the detected lump.

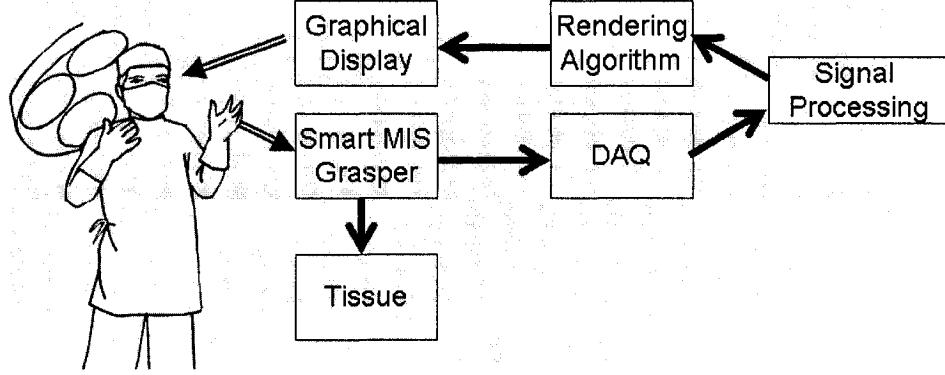


Figure 5.1: Components of the proposed system.

5.3 Sensor Structure

The details of the sensor including its design and working concept have already been presented in [78]. The structure of the sensor integrated with an MIS grasper, as shown in Figure 5.2, is corrugated to ensure a firm grasping of the tissue. Figure 5.2 shows the proposed grasper in which just the lower jaw is equipped with an array of the tactile sensors. The number of the sensors, their length, width and thickness as well as the space between them could be optimized for each particular application. In this study, in order to replicate the human finger spatial resolution, the sensor array was made of seven equally spaced piezoelectric PVDF base sensing elements. The spatial resolution for human finger using the Two-Point Discrimination Threshold (TPDT) is reported to be about 2 mm [156]. Therefore, 1.5 mm wide sensing elements positioned 0.5 mm apart were considered

for this study. Evidently, a finer array will yield into better spatial resolution than that of human finger.

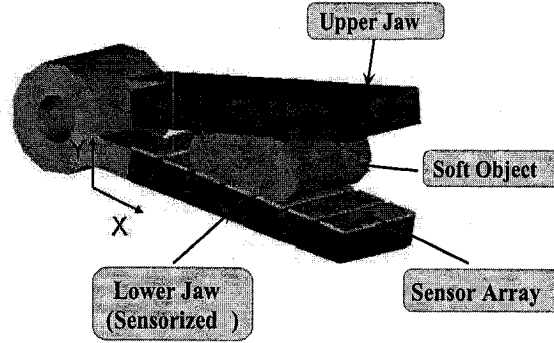


Figure 5.2: A view of the grasper with one active jaw equipped with an array of the seven sensing elements.

5.4 Rendering Algorithm

Two configurations of the sensors on the grasper are examined. The grasper structure shown in Figure 5.2, having one sensorized jaw is capable of locating the lumps in one dimension (x-axis), while the grasper with two sensorized jaws, which will be described in Section 5.4.2, can characterize the lumps in two dimensions, x and y axes (location of the lump in y direction can be considered as lump depth). In both designs, when there is no extraneous feature in soft object, depending on the grasper geometry and design, all sensing elements show either an equal output voltage or exhibit a regular pattern that is assumed as background frame. The presence of the lump causes an uneven voltage distribution through the sensing elements. The deduction of the background frame from the total response yields the net effect of lump and hence will increase the sensitivity. In addition to the lump detection, the softness of the bulk soft object in the sections with no embedded masses can also be measured [154]. The outputs of the sensing elements depend on several factors, such as the ratio of the Young's modulus of the lump E_L to that of the tissue E_T , the size and depth of the lump and the magnitude of the applied

load. Extracting all features of lump from the minimal sensor used in this study is a formidable task, as some combinations of lump stiffness, size, depth and the applied force create similar output pattern. This complexity is also reported by other researchers [67]. However, there are some constraints that can be used to reduce the number of variables or at least to control their range. For instance, our analysis [157] shows that for $\frac{EL}{E_T} > 10$, the variation of this ratio has negligible effect on the output. Fortunately, absolute majority of the reported stiffness for the tumors are greater than this ratio [67]. Therefore, in the practical range, the output response is not much influenced by the variation of the Young's modulus of the lump. Another influential factor is the magnitude of the applied load. The contact force between the grasper and the tissue depends on the load exerted by grasper jaws to the tissue. Therefore, it is necessary to measure the total applied load besides the pressure distribution. The applied load can be measured in different ways. For instance, a strain gauge attached to the jaw can provide data on the magnitude of the applied load. Another approach to measure the applied load was presented in a previous work, in which an extra PVDF film is used at the supports of each sensing element [78]. In the experiments conducted in this study, the load was measured using a reference load cell. Furthermore, to reduce the number of contributing parameters, throughout this article, the force was kept constant. The other remaining factors are the size of tumor, its location in x and y directions. Since the majority of masses can be approximated as spherical features, the number of parameters to characterize the size of the sensor can be reduced to one value, i.e., the lump radius. The first design (see Figure 5.2) overlooks the depth of lump and locates lump merely in x direction. While, by using two sets of arrays of sensing elements in the second design described in Section 5.4.2, it is possible to determine the depth of lump as well.

5.4.1 Graphical Representation of Localized Lump in One Dimension

As shown in Figure 5.2, in the first design the lower jaw is equipped with the sensor array while the upper jaw applies only compressive load to the object containing lumps. To graphically represent the location of the lump, initially an image with seven vertical parallel bands corresponding to the seven sensing elements was considered (see Figure 5.3-b). The intensity of each band was considered to be proportional to the output of the corresponding sensing element. The voltage distribution along the sensor array can be considered as a vector $\{V\}_{1 \times 7}$ that is related to the intensity vector $\{I\}_{1 \times 7}$ by:

$$\begin{cases} I_i = \frac{V_i}{\alpha}(K - 1) & , \quad V_i \leq \alpha \\ I_i = K - 1 & , \quad V_i > \alpha \end{cases} \quad (5.1)$$

where $i = 1, \dots, 7$ and α is the normalizing factor that determines the working range (very soft, soft, medium, etc.), and K is the number of gray scales that are used in construction of graphical image (here $K=256$). It is seen from Equation 5.1 that for a given α , when $V_i \leq \alpha$, the scaling factor α maps the input voltage domain into interval $[0, 1]$, then this value, using $(K-1)$ factor, would be mapped into the corresponding gray level, between 0 to 255. Once $V_i > \alpha$, all the values of V_i would be mapped to the maximum intensity (i.e., $I_i = 255$). For instance, Figure 5.3-b shows the graphical display for the case that two lumps were detected in the grasped tissue. In this case, one of the lumps had been positioned above the sensing element No. 6 and the other one had been placed above and between the sensing elements 2 and 3 (see Figure 5.3-a for the configuration). However, due to the limited number of the sensing elements, the quality of image shown in Figure 5.3-b was not satisfactory. Therefore, by using an interpolation technique the quality of the image as shown in Figure 5.3-c was enhanced. Prior to implementation of interpolation, the number of elements had to be increased from 7 to any desired number (N). To do this, $(N-7)$ extra elements were required. Therefore, $\frac{N-7}{6}$ elements were inserted between each two original elements. The resulted $(1 \times N)$ vector $\{G\}$, is in the following

form:

$$\{G\} = \underbrace{\{G_1, G_2, \dots, G_{N-1}, G_N\}}_{\text{Nelements}} \quad (5.2)$$

in which

$$\begin{aligned} G_1 &= V_1, \quad G_{\frac{N+5}{6}} = V_2, \quad G_{\frac{2N+4}{6}} = V_3, \\ G_{\frac{3N+3}{6}} &= V_4, \quad G_{\frac{4N+2}{6}} = V_5, \quad G_{\frac{5N+1}{6}} = V_6, \quad G_N = V_7 \end{aligned}$$

The intensity values assigned to the inserted elements were calculated using linear interpolation relationship expressed in Equation (3).

$$G_i = V_j \left\{ i - 1 - (j - 1) \left(\frac{N + 5}{6} \right) \right\} \cdot \frac{V_{j+1} - V_j}{(N - 1)/6}, \quad (5.3)$$

where $1 + (j - 1) \frac{N-1}{6} < i < 1 + j \frac{N-1}{6}$.

The indices j ($1 \leq j \leq 6$) and i ($1 \leq i \leq N$) are associated with the original vector $\{V\}$ and the augmented vector $\{G\}$, respectively. The numerical example for $N = 60$, is illustrated in Figure 5.3-c.

5.4.2 Graphical Representation of Localized Lumps in Two Dimensions

Figure 5.4, illustrates the second prototyped grasper in which both upper and lower jaws are equipped with the arrays of sensors. Using this grasper, it is possible to locate lumps in two directions, along the jaw (x-axis) as well as its depth (y-axis). The steps used for the construction of 2D tactile images, are demonstrated in Flowchart 5.5.

For better clarification of the algorithm used in this study, consider the case illustrated in Figure 5.6-a. This figure demonstrates a grasped tissue which contains a lump that is aligned with the sensing elements 2_U and 2_L , where the subscript U and L refer to the Upper and Lower sensing arrays, respectively. The distance of the lump from the upper and lower sensing elements are shown by **a** and **b**, respectively. Figure 5.6-b shows the 2D intensity graph which was built using one dimensional algorithm as explained in Section 5.4.1. This graph consists of two rows of color bands, which are corresponding with two

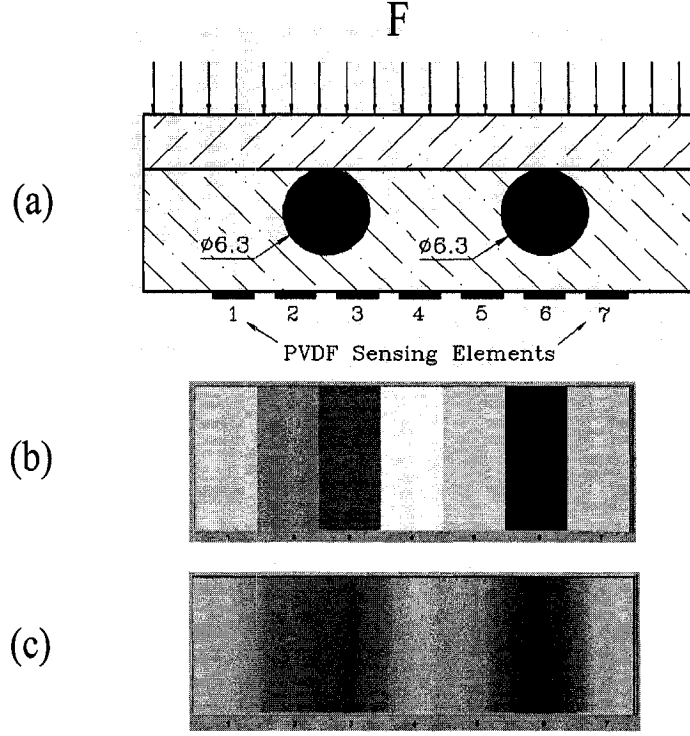


Figure 5.3: Locating the lump in one direction and its graphical rendering.

arrays of the sensors, one on the top and the other at the bottom. Therefore, this graph can be considered as a matrix with 2 rows (color bands) and 7 columns (sensors), i.e. 2x7 cells. The corresponding matrix in which each element represents a voltage amplitude is in the following form:

$$[V] = \begin{bmatrix} V_{U_1} & V_{U_2} & V_{U_3} & V_{U_4} & V_{U_5} & V_{U_6} & V_{U_7} \\ V_{L_1} & V_{L_2} & V_{L_3} & V_{L_4} & V_{L_5} & V_{L_6} & V_{L_7} \end{bmatrix} \quad (5.4)$$

As it can be seen, Figure 5.6-b cannot clearly demonstrate the valuable information about the location of the lump. To show the precise location of the lump, the dimensions of the matrix and consequently the number of matrix elements were increased. The graphical enhancement in x-direction was explained in Section 5.4.1, hence in this section the row operations (y-direction) are emphasized. As shown in Flowchart 5.5 step 5, the number of rows was increased to M by inserting $(M - 2)$ rows of zeros between the first and second rows of matrix $[V]$ which led to an $M \times 7$ matrix. Furthermore using the technique

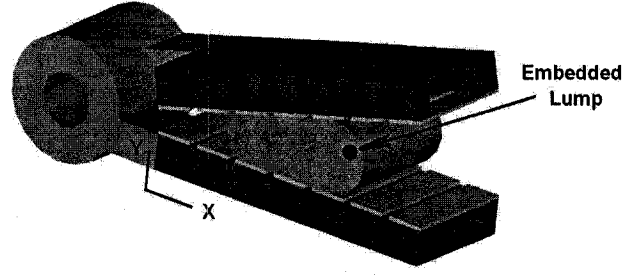


Figure 5.4: The second design of grasper in which both upper and lower jaws are equipped with sensing elements.

explained in Section 5.4.1, the number of columns was also increased to N . The resulted $M \times N$ matrix $[G_0]$ would be in the form of:

$$[G_0] = \underbrace{\begin{bmatrix} G_{U_1} & G_{U_2} & \cdots & G_{U_{(N-1)}} & G_{U_N} \\ 0 & 0 & \cdots & 0 & 0 \\ \vdots & \vdots & \vdots & \vdots & \vdots \\ 0 & 0 & \cdots & 0 & 0 \\ G_{L_1} & G_{L_2} & \cdots & G_{L_{(N-1)}} & G_{L_N} \end{bmatrix}}_{N \text{ Columns}} \quad (5.5)$$

For the graphical representation of the lump, two parameters had to be determined, the location of the center of lump in each column and its corresponding intensity value. In order to designate the vertical location of the center of lump in each column (step 6, flowchart 5.5) a relationship between the thickness of the tissue and the rows of matrix $[G_0]$ was used. If a lump is located in the tissue at a distance of a from the upper sensor array, it will be mapped into the row r , where r can be found from relationship:

$$\frac{r}{M} = \frac{a}{a+b} = \frac{G_U}{G_U + G_L} \quad (5.6)$$

in which $(a+b)$ that is equal to the tissue thickness, was considered to be proportional to the number of rows (M). Regardless of existence of lump, the above equation was applied to all columns (see Figure 5.7). If a lump exists in a column, then a and b are the distances of the center of the lump from the upper and lower sensor arrays,

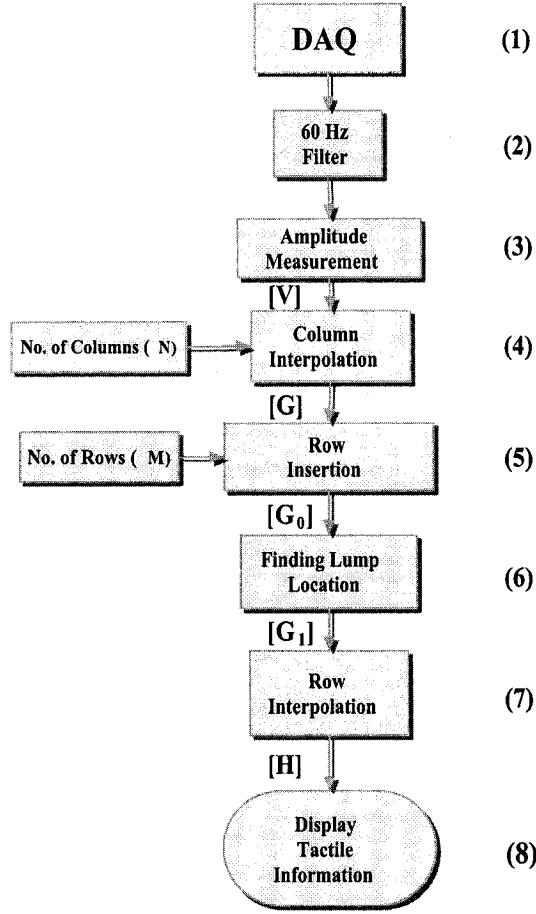


Figure 5.5: The flowchart of the algorithm implemented in LabView and used for the graphical rendering.

respectively. For the columns with no lump, the associated sensor outputs are equal and $G_L = G_U$, thus $r = M/2$. These cells are indicated in Figure 5.7 with gray color. In other words, the algorithm assigns a non-zero value to the middle row of the columns with no lump. Although this value is not significant, it can be considered as a shortcoming of the algorithm. In order to determine the intensity values of these locations in each column, the following relation was used:

$$G_{rj} = GUj + GLj \quad (5.7)$$

where G_{rj} specifies the intensity value of the cell located in the row r and column j , showing the center of lump in that column. The result of this operation is matrix $[G_1]$,

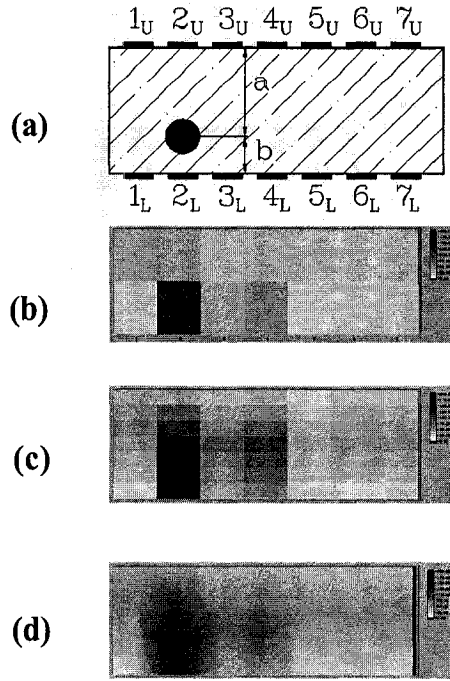


Figure 5.6: The graphical rendering of the characterized lump in two dimensions. (a) A lump located in a soft material with the upper and lower sensor arrays, (b) 2D intensity graph associated with the sensor array outputs, (c) A 7x7 matrix showing the location of the lump, (d) A 60x100 matrix that gives a better information on location and size of the lump.

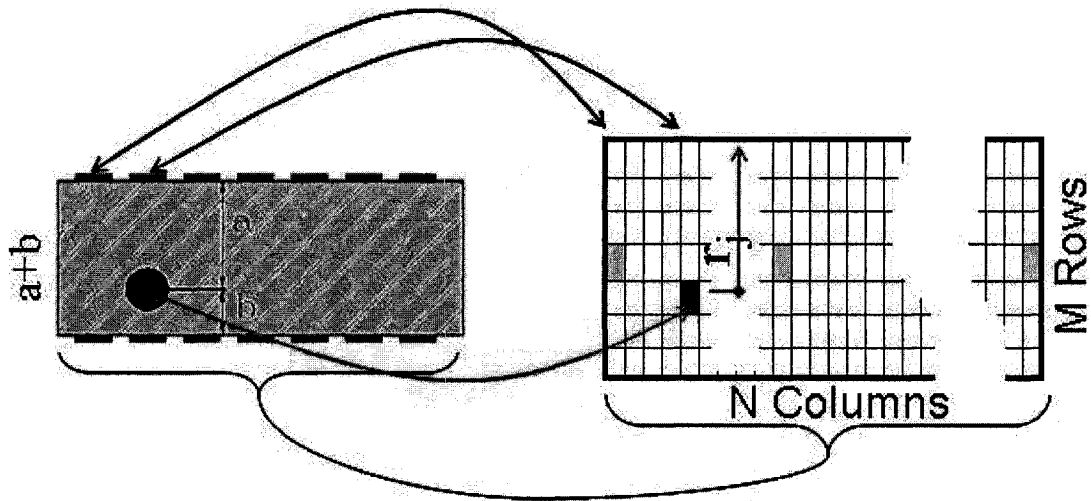


Figure 5.7: The relationship between grasped object and intensity matrix.

in which the centers of detected lumps are specified.

$$[G_1] = \begin{bmatrix} G_{U_1} & G_{U_2} & \cdots & G_{U_N} \\ 0 & 0 & \cdots & 0 \\ \vdots & \vdots & \vdots & \vdots \\ 0 & 0 & \cdots & 0 \\ G_{r_{11}} & G_{r_{22}} & \cdots & G_{r_{NN}} \\ 0 & 0 & \cdots & 0 \\ \vdots & \vdots & \vdots & \vdots \\ 0 & 0 & \cdots & 0 \\ G_{L_1} & G_{L_2} & \cdots & G_{L_N} \end{bmatrix} \quad (5.8)$$

It should be noted that in case of having multiple lumps, the center of each lump will be mapped to a row that corresponds to the lump's original depth in the tissue. Therefore, for instance, $G_{r_{11}}$ and $G_{r_{22}}$ are not necessarily in the same row. As depicted in step 7 of Flowchart 5.5, then a row interpolation procedure was implemented. At this step, in each column three values were known; G_{U_i} , $G_{r_{ij}}$ and G_{L_i} . Therefore, using these values and through a linear interpolation, new intensity distribution was assigned to all zeros. The final intensity matrix $[H]$ can be represented as:

$$[H] = \begin{bmatrix} H_{11} & H_{12} & \cdots & H_{1N} \\ H_{21} & H_{22} & \cdots & H_{2N} \\ \vdots & \vdots & \vdots & \vdots \\ H_{(M-1)1} & H_{(M-1)2} & \cdots & H_{(M-1)N} \\ H_{M1} & H_{M2} & \cdots & H_{MN} \end{bmatrix} \quad (5.9)$$

where, the intensity of each cell was calculated from relationship 5.10.

$$\begin{cases} H_{ij} = G_{U_j} + (i - 1) \frac{G_{r_{jj}} - G_{U_j}}{r_j - 1}, & 1 \leq i \leq r_j, \quad 1 \leq j \leq N \\ H_{ij} = G_{r_{jj}} + (i - r_j) \frac{G_{L_j} - G_{r_{jj}}}{M - r_j}, & r_j \leq i \leq M, \quad 1 \leq j \leq N \end{cases} \quad (5.10)$$

Figure 5.6-c shows the lump position and its approximate size after implementing the mentioned algorithm when $M=N=7$. Evidently, increasing the number of cells in both

directions will enhance the quality of image. Figure 5.6-d, for instance, is the constructed graphical image based on the same sensor's output and enhancement of associated matrix to $M = 60$ and $N = 100$.

5.5 Finite Element Simulations

Two finite element models were developed to analyze the prototyped graspers, using Ansys software. The bulk soft tissue and the lumps were considered to be isotropic. In absence of soft tissue, an elastomeric material supplied by 3M-Profom, was used and the mechanical tests on the samples of the elastomeric, were carried out. Three identical samples were cut out of a sheet (1/2 inch thickness) and using MCR 500 (Modular Compact Rheometer) from Physica, Anton Paar; strain rate controlled (2 mm/sec) compression tests, were performed on each sample. Using the area and the initial thickness of the specimens, the data were converted to engineering stress and strain. The results of nine experiments (three compression tests on each sample) were compared and a maximum error of 6% was observed. In order to find the linear elastic Young's modulus for the elastomeric, the numerical values were averaged and the linear Young's modulus was calculated and used in the finite element models. The Young's modulus of elastomeric was found to be 25 kPa which is in the range of the values reported by Krouskop *et. al* [43] for the typical soft tissues. The Young's modulus of the lump was considered ten times more than that of the tissue. However, as mentioned earlier, increasing the Young's modulus of the lump did not affect the results significantly. Consistent with the experiments, the piezoelectric coefficients of the uniaxial, 28 μm PVDF films that were used in these simulations were selected to be $d_{31}=20$ pC/N, $d_{32}=2$ pC/N and $d_{33}=-18$ pC/N as reported by the manufacturer [112]. The output charges of the sensing elements for different cases in which lumps with different diameters were positioned in different places were computed and plotted. Figure 5.8 shows the finite element model in which one lump is embedded in the soft material. For the first design, a distributed load was applied through the upper

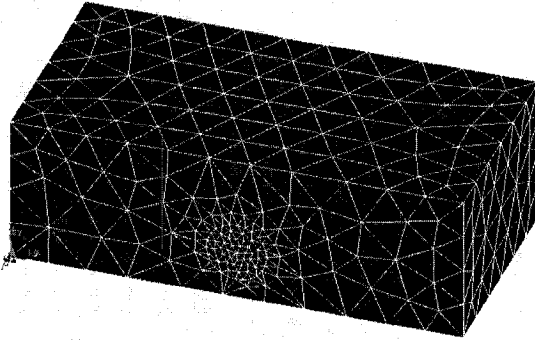


Figure 5.8: A view of the sectioned and meshed finite element model of soft object and the embedded lump.

jaw and soft material was pressed against the lower sensing elements, whereas for the second design two arrays of the sensing elements were considered at the top and bottom surfaces of the object. The *mixed u-p formulation* was used for the problem in which the soft material was meshed using Solid187, a 3-D, 10-node element which has three degrees of freedom U_x , U_y and U_z at each node and is suitable for hyperelastic and large deformations problems. In order to model the piezoelectric PVDF, the Solid98 element was used. This element is also a 10-node tetrahedral element with the capabilities of piezoelectricity (and large deflections). When used in piezoelectric analysis, each node has four degrees of freedom, U_x , U_y and U_z and Volt.

5.6 Experiments

An experimental set up was used to generate tactile information by the application of known loads through the fabricated graspers to the soft object containing lump. The graspers positioned under a probe which was equipped with a reference load cell, while the soft object and lump were sandwiched between two jaws. The photographs of both prototyped graspers, with one and two active jaws are shown in Figures 5.9-a, and 5.9-b, respectively. Because the PVDF base sensing elements were prepared manually, initially

the discrepancy between the output voltages for equal load was observed. To compensate this disparity, a controllable coefficient for each sensing element was defined. Then using homogenous elastomeric materials (without any inclusion) the output of the sensors were identically adjusted. The output voltages of the sensing elements in both designs were processed and according to the explained algorithm, graphically demonstrated. The soft elastomeric material with known Young's modulus was used as the bulk soft object and metallic balls simulating the lumps with different sizes (3.9, 6.3 and 7 mm) were inserted into the hollow spaces carved out of the bulk elastomeric. To change the depth of the lumps, several layers of the elastomeric material were cut into same dimensions but different thicknesses. The lumps were placed in one of the layers, so that the other elastomeric layers were used as spacers to increase or decrease the distance of lump layer from the top and bottom surfaces. A dynamic load was applied by the shaker that was driven by a power amplifier and a signal generator, as shown in Figure 5.10. The outputs of the sensors were fed into the connector box through the buffer electronics. The piezoelectric PVDF can be considered as a voltage source with very high output impedance. Since the DAQ needs the input impedance to be less than $100\text{ k}\Omega$, a buffer was necessary to match the impedance. The data was transferred to the computer, using the DAQ (NI PCI-6225). The DAQ main amplifier was used in RSE (reference single ended) mode [158]. A low pass filter with a cut-off frequency of 40 Hz was used to remove the 60 Hz line noise. In accordance with the explanation in Section 5.4, the processing algorithm was developed in LabView environment for the graphical demonstration of the forces sensed by the sensor elements.

5.7 Results and Discussion

The results of the finite element analysis as well as the graphical representations of tactile information obtained from experimental cases are shown in Figures 5.11 and 5.12 for one and two dimensional procedures, respectively.

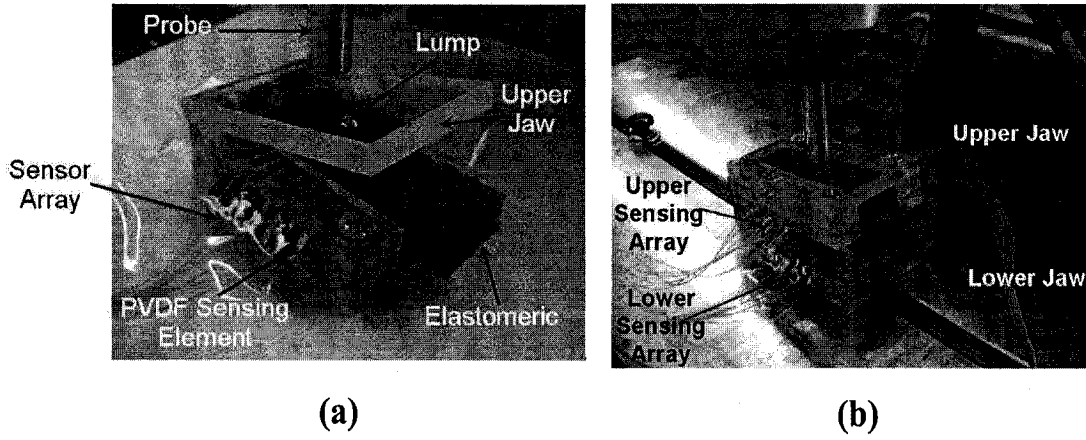


Figure 5.9: Photographs of the sensors under the test. (a) The sensor with one active jaw used for construction of one dimension graphical images. (b) The sensor with two active jaws used for two-dimension graphical rendering of detected lumps.

Each row in Figure 5.11 shows a scenario in which multiple lumps with different sizes were inserted into the elastomeric bulk material. The left column in this figure illustrates the geometrical information about the locations and size of the lumps that were placed in the soft object. The middle column in Figure 5.11, is the one dimensional graphical representation of the sensor's outputs obtained from the experiments. The right column is the normalized voltage response of the sensing elements obtained from the finite element analysis. In the graphical representation in Figure 5.11-a (middle column), the dark column 2 has the highest intensity, showing that the lump is located above this sensing element. This can be compared with the intensity of the sensing elements 4 and 5 that share a lump. For the latter elements, the maximum contact stress value occurs in a place between the sensing elements 4 and 5. Therefore, each sensing element senses part of the load and in comparison with the sensing element 2, shows lower amplitude. These two elements also provide information about the size of the lump. If the middle lump was large enough to cover both sensing elements, the result would be two completely dark bands. Therefore, from the shown gray levels the approximate size of the middle lump can be deduced. The difference observed between the outputs of the sensing elements 2

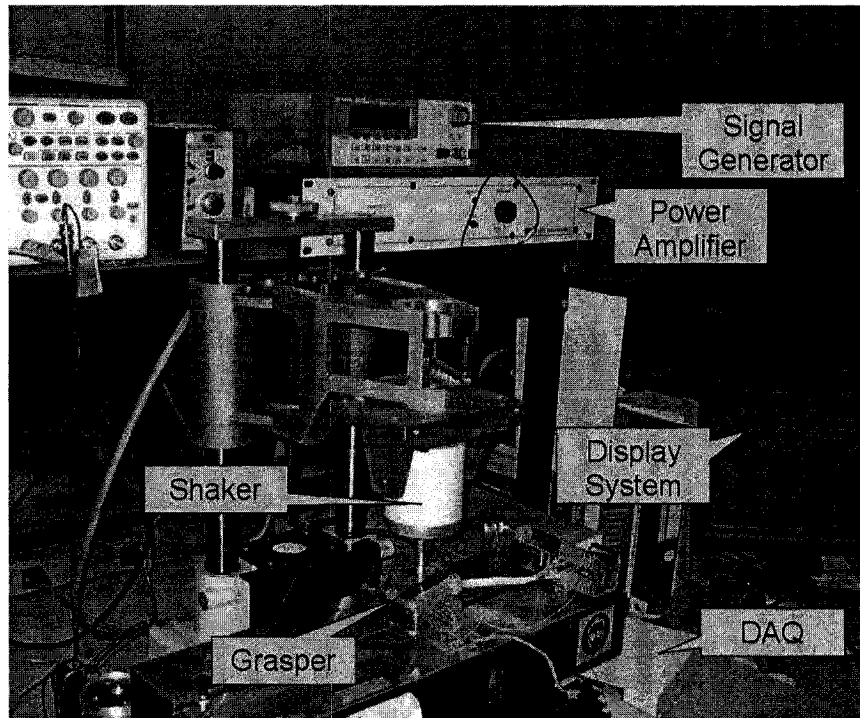


Figure 5.10: Photograph of the experimental setup.

and 7 can be attributed to the edge effect on the latter element. The second case (Figure 5.11-b) shows two identical lumps embedded above the sensing elements 2 and 5. The similar output voltage and intensity can be seen in the graphical representation as well as finite element analysis. In the third case (Figure 5.11-c) a larger lump is placed between two smaller lumps. It is shown that the system is capable of detecting all three masses. However the darker band associated with the sensing element 4, gives information on the relative size of middle lump respect to the other ones. In the last case, (Figure 5.11-d), a small lump had been positioned between two larger lumps. As can be seen from the results, the sensor has not been able to detect the smaller mass. A closer examination of finite element stress distribution shows that two larger lumps created a stress profile between themselves in such a way that the effect of the small mass has been suppressed. This figure demonstrates that for multiple lumps with different sizes and locations, to obtain an accurate result more than one attempt and in different orientations might be needed.

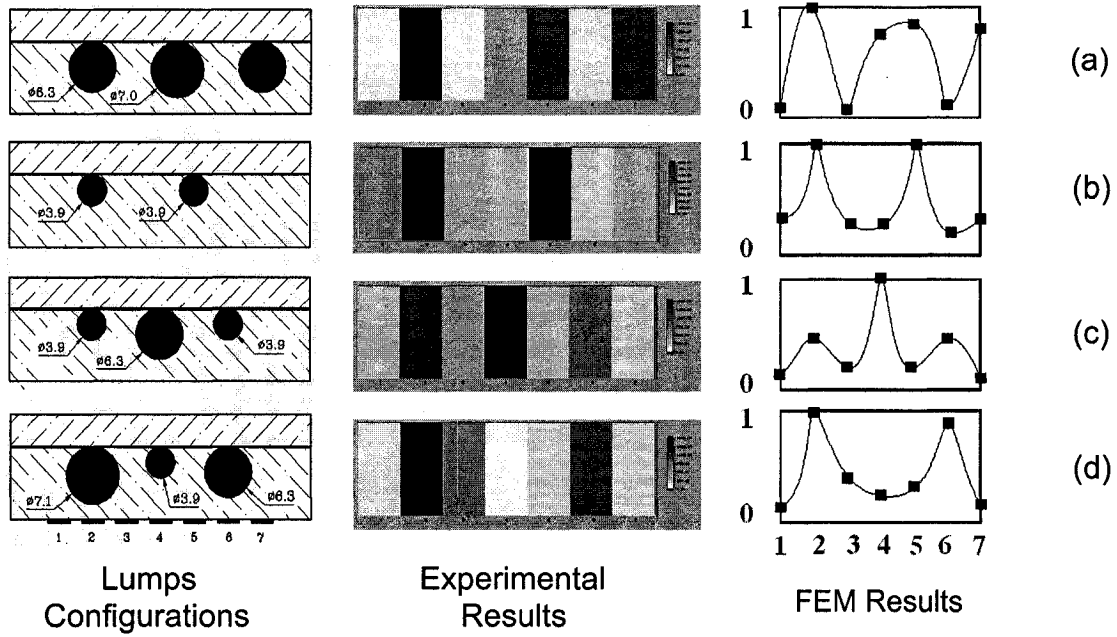


Figure 5.11: The experimental and analytical results of four case study.

Alternatively, Figure 5.12, shows the results of three case studies in which both jaws of the graspers were equipped with arrays of the sensing elements. Figure 5.12-a, demonstrates a case in which two identical lumps were positioned close to the sensing elements 1 and 4 of upper jaw (1U and 4U), respectively. The corresponding graphical image shows clearly the place of the lumps. In addition, the gray level of image gives some information about the size of the lumps. In the next configuration (Figure 11-b), lumps are positioned apart in such a way that one lump is put beneath the sensing element 4U and the second lump is placed above the sensing element 1L (slightly overlapped with sensing element 2L). The graphical image constructed based on the experimental sensor's output is shown in middle column of Figure 5.12-b, in which the place (in x and y directions) is clearly extractable. The gray levels in this case can be compared with those of Figure 5.12-c, in which the lumps positioned far from the sensing elements. Again the position and size of lumps can be clearly perceived from the experimental data shown in the middle column. The finite element results shown in the right column are consistent with the experimental

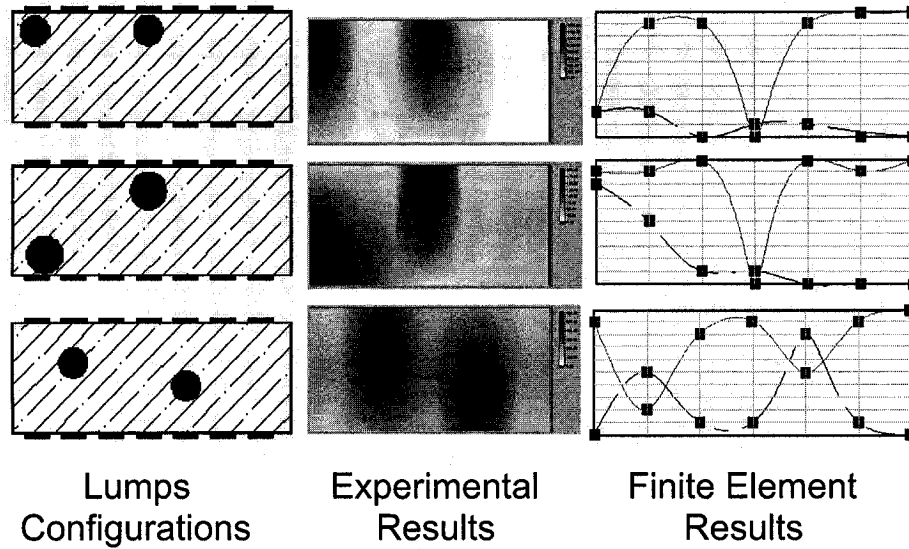


Figure 5.12: The experimental and analytical results for two dimensional localization. Each row illustrates the information of the studied case. In the right column, the dashed line represents the output voltages of the lower array of the sensors, while the solid line is associated with the upper jaw.

data in all three cases. However, implementation of this algorithm may produce gray areas in the middle of image in absence of any lump. To rectify this problem, an enhanced algorithm is under process. , alternatively shows the results of four case studies in which both jaws of the graspers were equipped with arrays of the sensing elements. Figure 5.12-a, demonstrates a case in which two identical lumps were positioned close to the sensing elements 1 and 4 of upper jaw (1U and 4U), respectively. The corresponding graphical image shows clearly the place of the lumps. In addition, the gray level of image gives some information about the size of the lumps. In the next configuration (Figure 5.12-b), lumps are positioned apart in such a way that one lump is put beneath the sensing element 4U and the second lump is placed above the sensing element 1L (slightly overlapped with sensing element 2L). The graphical image constructed based on the experimental sensor's output is shown in middle column of Figure 5.12-b, in which the place (in x and y directions) is clearly extractable. The gray levels in this case can be compared with those of

Figure 5.12-c, in which the lumps positioned far from the sensing elements. Again the position and size of lumps can be clearly perceived from the experimental data shown in the middle column. The finite element results shown in the right column are consistent with the experimental data in all three cases. However, implementation of this algorithm may produce gray areas in the middle of image in absence of any lump.

5.8 Conclusions

Despite an influential shortcoming of Minimally Invasive Sugary (MIS), which is the lack of tactile feedback, it has increasingly been used in different surgical routines. Restoring the missing tactile information, especially the tissue palpation, will be a significant enhancement in MIS capabilities. Tissue palpation is particularly important and commonly used in locating the embedded lumps. The present study is inspired by this essential limitation in MIS procedure and is aimed at developing a system to reconstruct the lost palpation capability of surgeons in an effective way. Having collected necessary information on the size and location of the hidden features using MIS graspers equipped with tactile sensors, the information can be processed and graphically rendered to the surgeon. Therefore, using the proposed system, surgeons can identify presence or absence, location and approximate size of hidden lumps simply by grasping the target organ by smart endoscopic grasper. The results of the conducted experiments on the prototyped MIS graspers represented by graphical images are compared with those of the finite element models.

A system for characterizing and rendering the hidden lumps in soft bulk objects is presented. The proposed system is comprised of an endoscopic grasper equipped with array(s) of tactile sensors, a signal processing unit, graphical rendering algorithm and a graphical display. This setting potentially could be used for lump detection in laparoscopic surgery. Initially the required information has to be collected from the grasped object. This task has been performed by using a multifunctional tactile sensor that had already been developed. A unit of the utilized sensor is capable of measuring the ap-

plied contact force as well as the softness of the grasped object. An array of this sensor which is used in this study, is capable of reporting the location and size of the lump as well. The output voltages of the sensing elements are buffered, digitized, filtered and transmitted to a computer. Then through a rendering algorithm developed in LabView environment, the tactile data were transformed to gray scale image and was displayed on a monitor. The linear elastic modulus of an elastomeric material calculated from the mechanical compression test and used in the finite element analysis. The results of finite element analysis were compared with those of the corresponding conducted experiments. It is shown that using one array of the sensing elements; it is possible to extract lump information including size and longitudinal location. Whereas, using two sets of array of sensors, the information on size, longitudinal position as well as depth of the lump in two dimensions were obtained. The experiments on the prototyped graspers were conducted and the data were graphically rendered on a display. Hard objects were inserted into pre-determined positions in elastomeric and were grasped by the device and the experimental results were compared with the known values. Graphical rendering of localized objects is a feasible technique with great potential for use in MIS. Using this method a part of lost tactile information which is the palpation, can be restored. This capability is useful not only for MIS, but also for MIS robotic surgery and, in general, for robotic surgery. Other anatomical features such as beating arteries potentially could be detected and graphically rendered.

Chapter 6

Design, Analysis, Fabrication and Testing of MEMS Tactile Sensor

6.1 Introduction

MEMS devices are able to offer competitive advantages due to their batch fabrication capabilities, small size, and improved functionality. They also have a reputation for being low cost due to their IC roots. The incorporation of MEMS devices on surgical tools represents one of the greatest growth area. The MEMS technology can improve surgical outcomes, lower risk, and help control costs by providing surgeons with real-time data about instrument force, performance, tissue density, temperature, as well as provide better and faster methods of tissue preparation, grasping, cutting, and extraction[9].

In the previous chapters different subjects associated with the multifunctional tactile sensor were described. In Chapter 2, the working principle and characterization of the piezoelectric PVDF films as transducers were elaborated. Chapter 3 reported the basic scheme of tactile sensor, design criteria and dynamic analysis of the proposed sensor. A macro-size sensor using a metallic support and a flexible polystyrene beam were developed and experiments were conducted. Chapter 4 discussed the tissue-Grasper interaction and the effect of non-linear modeling of the tissue on the responses. In addition, the effect of presence of a lump embedded in the bulky soft tissue on the stress distribution

at the tissue-grasper interface was explained. Using the information of the developed sensor in Chapter 4, a new method of presentation of tactile data was also reported in Chapter 5. However, the ultimate objective is the integration of the proposed sensor with the existing MIS graspers. To do this, the sensor must be miniaturized. Therefore, in order to study the feasibility of miniaturizing the proposed sensor, this chapter describes the microfabrication and testing of micro tactile sensor. In the following sections, the sensor design and its geometry are explained. A finite element model of the designed and microfabricated sensor is developed. To check the accuracy of the numerical model, deflection profile for a given load is compared with that of closed form relationship. The microfabrication steps are also explained and then the experimental results for softness sensing are compared with the results of finite element model.

6.2 Sensor Design

The design and working concept of the sensor were described in Section 3.2 and shown in Figure 3.2. The sensor consists of top and bottom parts. The bottom part, forms the supports and is the base for the top part which consists of hanging beams. The top part encompasses the clamped-clamped hanging beams which are used for softness measurements. For softness sensing, the applied force as well as the resultant deformation need to be recorded. The magnitude of applied load can be measured by piezoelectric films that are sandwiched between the top and bottom parts. However, to measure the resulted deflection, PVDF films are attached to the beams. Figure 6.1 shows how this sensor can be integrated with the MIS graspers.

A unit of the sensor, for instance, with 2, 3 or more beams can be considered as a module. In the remaining of this chapter, to avoid unnecessary complexity, a design with three teeth as shown in Figure 6.2, is considered. This module can then be repeated in an array to cover the whole length (or width) of grasper. Figure 6.2 shows the backside view of the top part of a sensing module with three sensing elements.

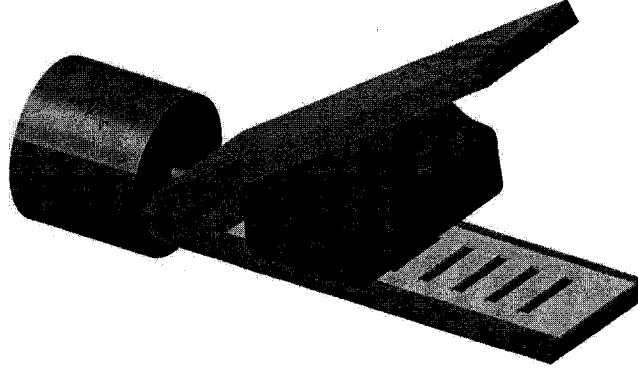


Figure 6.1: A proposed design of the smart grasper in which the incorporation of microfabricated sensor is presented.

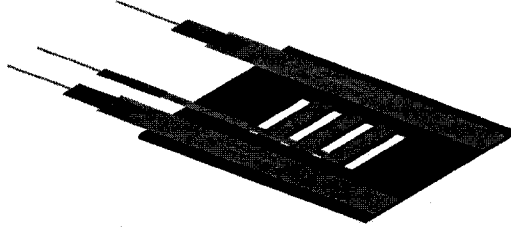


Figure 6.2: Backside view of the sensor's top part. The positions of the PVDF films and the electrodes configurations are illustrated in this view.

Three PVDF films working in extensional mode (d_{31}), were hybrid attached to the beams in order to measure the deflection of the beam. Two end support PVDF films, working in the thickness mode (d_{33}), were sandwiched between top and bottom parts in order to measure the total applied load.

To ensure a firm grasping, an ideal sensor should be corrugated which has been taken into consideration for the current design. As mentioned in Chapter 5, it is possible to have one sensorized jaw or to have both jaws sensorized. In the latter case the capability of the sensor in locating hidden lumps will be increased. For the present study one jaw was considered for sensor integration.

The dimensions of the sensor and particularly beams, should be determined for a given

range of force and softness for any specific application. Using a couple of parameters, the desired working range or sensitivity of the sensor can be achieved. For instance, the length, width and thickness of the beam can influence the load capacity of the sensor as well as its sensitivity. The short and thick beams withstand higher loads but show less flexibility. As a result, lower piezoelectric output would be obtained. Thin and long beams show opposite behavior and are appropriate for delicate applications such as pulse detection. Therefore, dimensions are application dependent and should be determined for each class of applications. Another influential factor on determining the overall dimension of the sensor is the dimensions of original grasper in which the sensor should be integrated. The number of the hanging beams or sensing unit should also be determined in order to satisfy the required spatial resolution.

In order to miniaturize the sensor suitable for integration with the existing MIS graspers the manual techniques should be minimized and batch processing techniques should be used. For instance, PVDF films must be deposited directly on the target areas. However, since this technology was not available for the microfabrication of the sensor, we had to choose the dimensions in such a way that pre-fabricated PVDF films could be cut and placed on the designated areas. Figure 6.3 shows the dimensions that were considered for this work. The length and width of each beam are 7 mm and 2 mm, respectively. Although a sensor with these dimensions can not be integrated into current MIS graspers, the feasibility of sensor microfabrication, its difficulties and capabilities were studied in this work. To have the maximum sensitivity and yet avoiding difficulties of working with very thin silicon wafers, the thickness of silicon considered was 180 μm .

The main advantage of using an array of the sensing module is to register the stress distribution. The profile of stress distribution is specially meaningful when a disruptive object is embedded in bulky soft tissue. As an important case, the impact of existence of a lump on the stress distribution over the unit sensor was studied in Chapter 4.

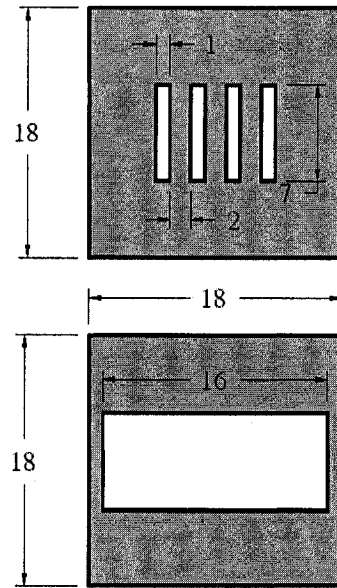


Figure 6.3: The scheme of top and bottom parts,(dimensions are in mm).

6.3 3D Finite Element Modeling

Before performing experiments on the sensor, a finite element modeling of MEMS sensor was carried out. The results of the simulation helped understanding the behavior of sensor under given loads and also the PVDF film response to the loadings. Figure 6.4 shows the meshed model of the sensor. In order to reduce the number of elements, the bottom plate

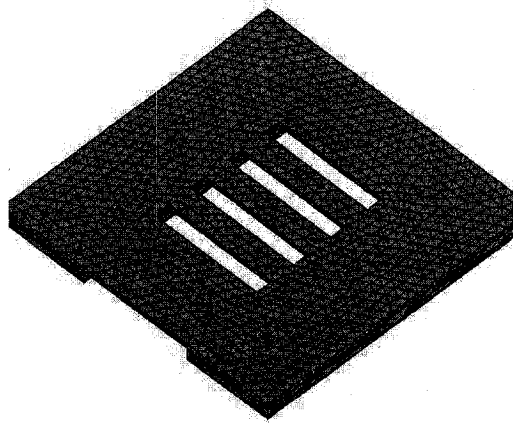


Figure 6.4: The meshed FEM model of the MEMS tactile sensor.

was substituted with only two supports. Since the bottom surface of the bottom part was mechanically constrained, this simplification did not affect the results. This model consisted of two end supports, top plate with three hanging beams and PVDF films which were sandwiched between supports and top plate and also attached to the beams as shown in Figure 6.2. The material properties of 180- μm -thick silicon was considered to be $E=130$ GPa and $\nu = 0.28$ for the supports and top plate. The material properties of the 28- μm -thick PVDF films used in this model are taken from Goodfellow [112] and summarized in Table 2.1 in Section 2.3. The SOLID92 and SOLID98 elements were used for the structural (silicon) parts and the piezoelectric films, respectively. SOLID92 is a 3-D 10 node tetrahedral element which has three degrees of freedom at each node: translations in the nodal x, y, and z directions. On the other hand SOLID98 is a tetrahedral element with a quadratic displacement behavior and is defined by ten nodes with up to six degrees of freedom at each node. When KEYOPT(1) = 3¹ the degrees of freedom are U_X , U_Y , U_Z and VOLT. The governing constitutive equations for piezoelectric materials have already been described in Chapter 2. Additional details are given in Appendix A.

¹Some Ansys elements have additional options, known as KEYOPTs and are referred to as KEYOPT(1), KEYOPT(2), etc. For instance, here KEYOPT(1)=3 sets the type and number of degrees of freedom of the element. KEYOPTs can be specified using the ET command or the KEYOPT command.

6.3.1 Simulation Results

To assess the accuracy of the finite element model, the response of the FEM was compared to that of existing closed form relationship for clamped-clamped beams. As illustrated in Figure 6.5, a distributed load was applied to the first beam and its two supports. The deflection curve due to the distributed load of 111 kPa, is shown in Figure 6.6. This

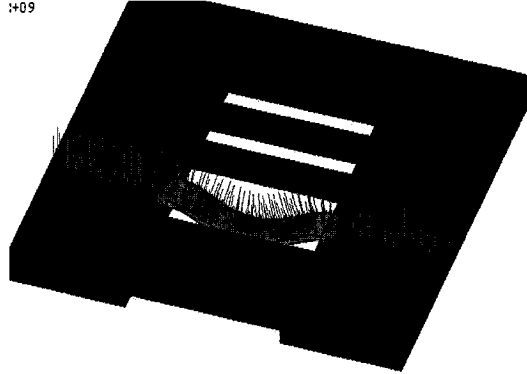


Figure 6.5: The deflected structure when a distributed load of 111 kPa was applied to the first beam and its two supports.

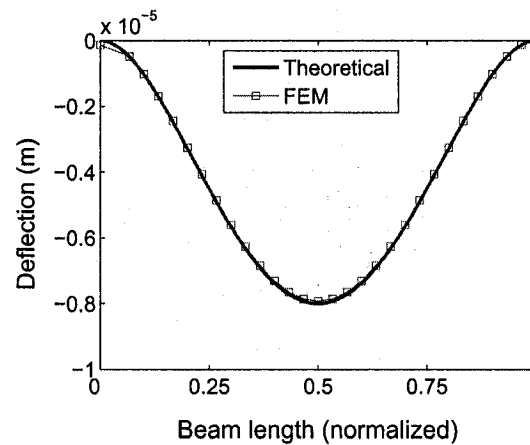


Figure 6.6: The deflection curve of first beam when a distributed load of 111 kPa is applied to the beam and its two end supports. Solid line illustrates the result obtained from Equation 6.1, while the squares indicate the FEM results.

figure also illustrates the result of theoretical analysis for a clamped-clamped beam under

a distributed load which was obtained from the known formula :

$$y = \frac{1}{24} \frac{Wx^2}{EIL} (2Lx - L^2 - x^2) \quad (6.1)$$

in which,

L : Beam length (m)

W : Total applied load (N)

E : Young's modulus of the beam (N/m^2)

I : Area moment of Inertia (m^4)

x : Distance of point on the beam from the origin (here the left support)

It is worth to note that the cross section of the beams after microfabrication using anisotropic wet etching were trapezoid. In order to compare the experimental results with those of the closed form and FEM, the equivalent rectangular cross section was modeled. It was found that the moment of inertia of a rectangular cross section with a width of 2.12 mm and a thickness of 180 μm is equal to the moment of inertia of the etched cross section. This is shown in Figure 6.7. This equivalent moment of inertia and cross section were used in closed form relationship and finite element model. For a

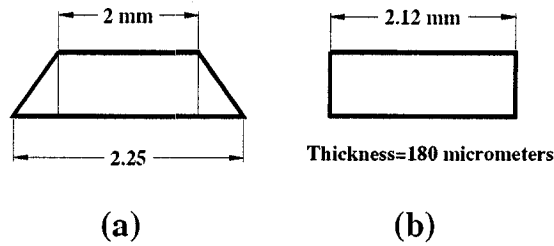


Figure 6.7: (a) The actual cross section after anisotropic etching, (b) the equivalent rectangular cross section used in closed form formula and finite element analysis. In both cases the thickness was 180 μm .

distributed load of 111 kPa, the output voltage of PVDF films associated with the first beam were calculated. The output voltage of the middle PVDF film which is attached to the beam was 680 mV. The calculated voltage for two supports were 85 mV. The equality

of voltages of two supports confirms that the applied load was uniform. For this loading condition, no output voltage from the middle PVDF films associated with the second or third beam was observed. In other words, simulation results show no cross talk between sensor units due to mechanical load transferring. In the next simulation a soft material was considered on top of the first beam and distributed load was applied to the object. The Young's modulus of the object then was varied between 10 kPa and 1 MPa. Figure 6.8 shows the modeling geometry and Table 6.1 summarizes the obtained results.



Figure 6.8: The finite element model of the sensor when a soft material is placed on the first tooth and a uniform compressive load is applied.

Table 6.1 shows that the maximum deflection varies from 1 to 20 micrometer for a range of Young's modulus between 10 kPa to 1 MPa. The maximum σ_x and corresponding PVDF output is also shown in this table.

The relationship between Young's modulus of soft objects and the PVDF output is depicted in Figure 6.9.

6.4 Sensor Fabrication

In order to fabricate the sensor, several process steps were used. The silicon parts, i.e. the top and bottom parts, have to be micromachined. The PVDF films were cut into designed dimensions and attached at their positions. This section describes different steps used in the manufacturing of the sensor.

Table 6.1: The maximum beam deflection at the center, Y_{max} , corresponding stress in x-direction, σ_x , and the output voltage of the middle PVDF film, V_{mid} when Young's modulus of the contact object, E_{obj} is varied between 0.01 MPa to 1 MPa.

E_{Obj} (MPa)	$Y_{max}(\mu m)$	σ_x (MPa)	V_{mid} (mV)
0.01	-20.4	78.6	170
0.05	-11.2	39.6	95.2
0.1	-7.2	22.8	61.2
0.5	-1.8	4.6	15.3
1	-1.0	2.4	8.5

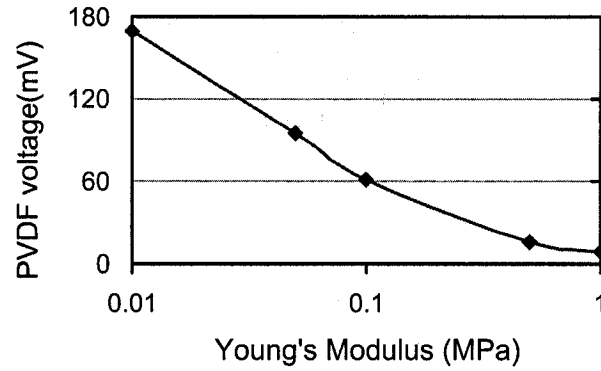


Figure 6.9: The output of the middle PVDF film at constant pressure 111 kPa when the Young's modulus of the contact object is varied between 0.01 MPa and 1 MPa.

Both silicon parts of the sensor were micromachined using anisotropic wet etching. In order to increase the sensitivity of the sensor, thickness of the beams was considered to be less than 200 micrometers. As conventional 500 μm silicon wafer would require an extra 300 μm back etching, a 180 μm -thick, 4-inch(100) silicon wafer was used for the fabrication. Several designs with different number of beams were considered. The bottom part, however, was the same for all designs. Figure 6.10 shows the steps of fabrication procedure. A brief explanation of each step of silicon fabrication is schematically shown in Figure 6.11. For simplicity, cross section of only one beam is shown. The same procedure

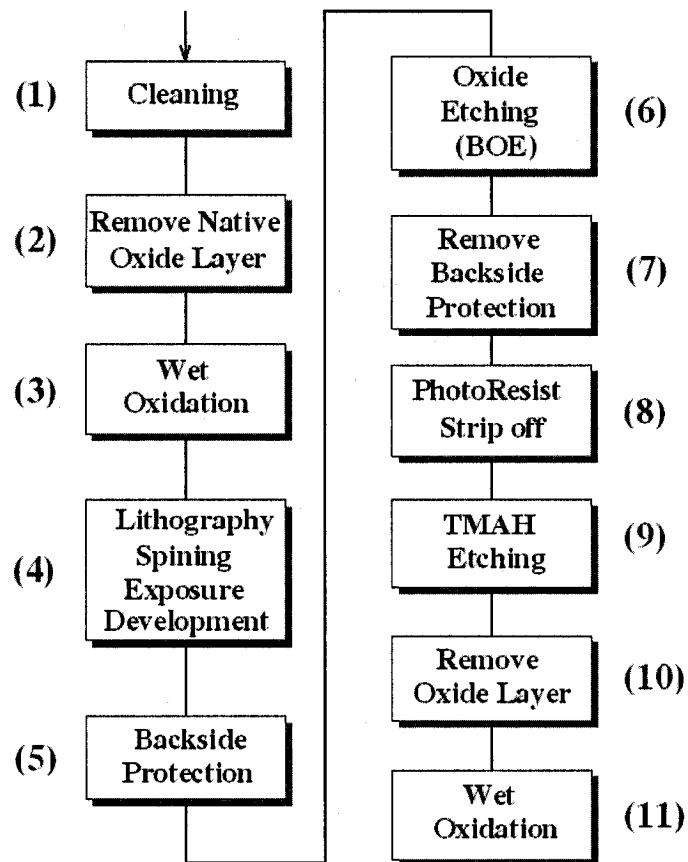


Figure 6.10: Process flow of micromachining process used for top and bottom parts.

was used for both silicon parts, however, only the TMAH etching (step 9) time was different for bottom and top parts. More explanation on each step is given below. As the first step, the silicon wafer was diced into required dimensions (18 mm x 18 mm).

6.4.1 Cleaning

As the first step of the fabrication process, silicon parts were cleaned in order to ensure formation of a homogenous oxide layer. To remove any contamination from the silicon parts, first a primary cleaning was performed. This was mainly for degreasing and dusts removing.

<div> Legend <div> <div>■</div> Silicon Oxide <div>■</div> Photo Resist <div>▨</div> Protection Layer </div> </div>			
Step	Description	Specification	Schematic
1	Pre-Cleaning	$\begin{cases} 10 \text{ min in acetone} \\ 10 \text{ min in iso-propanol} \end{cases}$ in ultrasonic bath	
1	Cleaning	10 min @ Piranah	
2	Removing Oxide Layer	20 Second @ HF, 1 %	
3	Wet Oxidation	20 min for 1000 Å	
4.1	Spin Coating of Photoresist	30 Sec @ 4000 rpm	
4.2	Soft Baking	1 min @ 115 °C	
4.3	Exposure	5 second, a 270 Watts mercury lamp	
4.4	Developing	1 min	
4.5	Hard Baking	30 min @ 105 °C	
5	Backside protection	Using special scotch tape	
6	Oxide Layer Etching	2 min in BOE, 7:1	
7	Remove Backside protection		
8	Photoresist Strip off	$\begin{cases} 10 \text{ min in acetone} \\ 10 \text{ min in iso-propanol} \end{cases}$ in ultrasonic bath	
9	TMAH etching	TMAH 25 % @90 °C $\begin{cases} 1.5 \text{ hr for bottom part} \\ 4.5 \text{ hr for top part} \end{cases}$	
10	Removing Oxide Layer	3 min in buffered HF @ room temperature	
11	Wet Oxidation	20 min for 1000 Å	

Figure 6.11: The sequence of micromachining process summarized.

Precleaning

The samples are placed in a sample holder and immersed in Aceton ($(CH_3)_2CO$) for 10 minutes and then cleaned with Iso-propanol ($CH_3CHOH - CH_3$) for 10 minutes. To accelerate the cleaning process, ultrasonic cleaning was applied at 20 kHz. The samples were then rinsed with DI (Deionized) water and afterward were dried using compressed nitrogen gas.

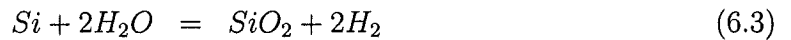
Cleaning

To remove any contamination that could still have remained on the surface of the samples, a commonly used Piranah solution(also known as Caro's acid or Sulfuric Peroxide) [159] was used. Piranah is a solution of Sulfuric Acid (H_2SO_4)-2 vol and Hydrogen Peroxide 30% (H_2O_2)- 1 vol. This solution is exothermic and besides using safety equipments, extra caution in working with hot containers must be exercised. Using a sample holder, samples were put into the solution for 10 minutes.

Due to lightness of the samples, this process needed extra attention. This was because of the bubbles that were produced in the reaction. The bubbles that ere stuck to the surface of the samples, made them float. Therefore, a special cage-type sample holder had to be used. After this step, the samples were rinsed in DI water and then dried in nitrogen. Cleaning in Piranah solution creates a thin layer of oxide on the surface of silicon which should be removed. The formation of oxide layer at this step can visually be inspected. Using 1% Hydrofluoric acid (HF) the oxide layer can be removed. 20 seconds dip in solution of HF was enough to remove the silicon oxide layer.

6.4.2 Oxidation

After the cleaning process, a layer of thermal silicon oxide (SiO_2) was grown on the surface of the (100) single crystal silicon samples. The oxide layer serves as the mask for the subsequent anisotropic etching of the silicon. Thermal oxidation is a high temperature process that can be accelerated using water vapor. The following reactions take place at the silicon surface.



Thermally grown SiO_2 adheres firmly to the silicon substrate without crack or pores. The furnace (Model RCA from Thermco) was used for this wet oxidation process. Although the main oxidation was wet, at the beginning and end of the process, short periods of

dry oxidation were used. The furnaces were a stack of 3 horizontal furnaces used for annealing and oxidation of 4" silicon wafers, as well as smaller silicon samples. First of all, the furnace set point was increased to the desired temperature, 1100 °C. While the temperature rose, the bubbler was prepared. The bubbler was rinsed three times with DI water. It was then filled about 2/3 full with DI water and 10% Vol HCL was added in order to accelerate the oxidation process. Ten to fifteen minutes before loading the samples into the furnace, the heater for the bubbler was switched on. The temperature of bubbler was set to 95°C. The samples were put in a glass rack and kept inside the furnace tube. The first sample normally is a dummy sample as it faces the stream flow and the obtained silicon oxide might not be as uniform as it is desired. In the warm up period, N_2 was connected to the chamber in order to prevent any unwanted reaction during the warm up. This flow also cleans the chamber and helps create a uniform heat distribution by creating a circulation. After reaching the set temperature, the oxidation process was started by disconnecting the N_2 and connecting dry O_2 . The dry oxygen flow was continued for 5 minutes. This was because, dry oxidation creates a uniform and very adhesive sublayer. Then the Oxygen flow was redirected through the bubbler which had reached to the boiling point and began to evaporate. To achieve 1000 Å oxide thickness, 20 minute wet oxidation was enough. The bubbler was then bypassed and dry Oxygen was again connected directly to the chamber. After 5 minutes dry oxidation, the furnace was turned off. In the cooling down phase, oxygen flow was replaced with N_2 . In order to prevent any thermal shock, samples were gradually removed from the furnace at about 400 °C.

6.4.3 Lithography

Patterning silicon oxide layer was carried out through a standard lithography procedure, including photoresist spinning, soft baking, exposurer with ultraviolet light, development and finally hard baking. The designed layout of the mask that was used for the patterning is shown in Figure 6.12.

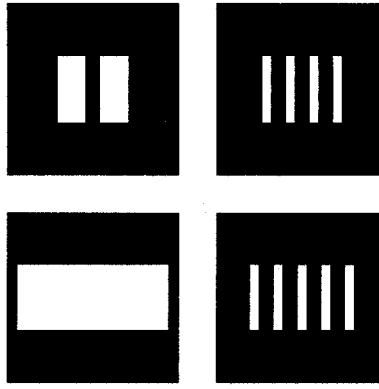


Figure 6.12: The mask patterns used for the lithography process. While the bottom left pattern is the the one that was used for bottom part (supports), the other three patterns were used to fabricate top parts with 1,3 and 4 hanging beams.

Spin Coating

In order to apply a positive photoresist(S 1813 from Shipley) a conventional spinner was used. The duration of 30 seconds at 4000 rpm (acceleration 450 rpm/sec) was selected for this work. This combination was suitable to produce a uniform photoresist layer with a thickness of about $1.6 \mu m$.

Soft Baking

Immediately after the samples were spin coated, they were placed on a hotplate. Using a vacuum line, hard contact between samples and hotplate was created. The temperature of hotplate was set at $115^{\circ}C$ and samples were baked for 1 min.

Exposure

To transfer the mask pattern to the photoresist, a conventional mask aligner (Karl Suss MA6) was used. The exposure time was selected to be 5 seconds while a 270 Watts Mercury lamp (in soft contact mode) was used.

Developing

For the developing step, the samples were developed with photoresist developer (MF-319 from Shipley) for about 1 minute at room temperature while agitated. After developing, samples were inspected under a microscope to detect any probable defects. The picture of some of the samples after developing step is shown in Figure 6.13.

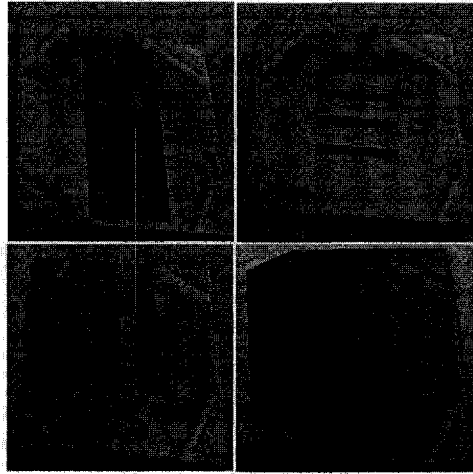


Figure 6.13: The samples after development process.

Hard Bake

In order to reinforce the photoresist for subsequent etching process a hard baking step is required. For hard baking, samples were heated in an oven for 30 min at a temperature of 105 °C.

6.4.4 Oxide layer etching

The conventional etchant for SiO_2 is BOE (Buffered Oxide Etch). BOE is a mixture of hydrofluoric acid, HF (one volume part)² and ammonium fluoride, NH_4F (six or seven volume parts). BOE with an etch rate of approximately 1000 Å min⁻¹ at room temper-

²HF with PH=1 is extremely dangerous and must be treated cautiously. Before working with the chemicals, reading the associated MSDS is highly recommended.

ature is a selective etchant for oxide. It would not etch silicon, so the removal of oxide layer from a silicon crystal is self-limiting. Nevertheless, HF attacks photoresist to some extent, although the addition of ammonium fluoride reduces this effect. When end-point detection is required over silicon, we can make use of the wetting properties of silicon and of oxide. Oxide is *hydrophilic* and is easily wetted by water. Silicon, on the other hand, is *hydrophobic* and repels water. Therefore, a completely etched silicon substrate, dipped in water, will shed the water instantly when removed. By contrast, a substrate with even a very thin layer of oxide on the surface will remain wet.

In order to protect the back side of the samples, a special tape was used. Using a solution of BOE (7:1), two minutes was enough for etching the oxide layer. After rinsing in DI water another inspection by microscope was done. In case of observing residuals of SiO_2 the BOE etching can be repeated. The photoresist layer as well as the protective tapes then were removed in acetone.

6.4.5 Tetramethylammonium Hydroxide, TMAH Etching

One of the conventional anisotropic wet etchant for silicon is tetramethylammonium hydroxide (TMAH). The solution used for this work was TMAH 25 % from Moses Lake Industries. As shown in Figure 6.14, a water bath (from VWR Scientific, Model 1235 PC) was used to control the temperature of TMAH. To maintain the temperature of TMAH at 90 °C, the temperature of the water was set on 95 °C. A condenser at the top of container prevented evaporation of TMAH at this temperature. The condenser was kept cool by circulating water at a flow rate of about 1 lit/min. The samples were put on a sample holder and inserted into the container. The previous characterization tests showed that, etch rates of silicon and thermal oxide are equal to 0.670 $\mu\text{m}/\text{min}$ and 1.15 $\text{\AA}/\text{min}$. Therefore, to etch 180 micrometer of silicon (<100> direction), four and half hours was required. As mentioned before, the sensor consists of two parts. One part which serves as support, was etched for 1.5 hour to obtain an etch depth of 60 μm while the top parts were maintained in TMAH for four and half hours to etch through and

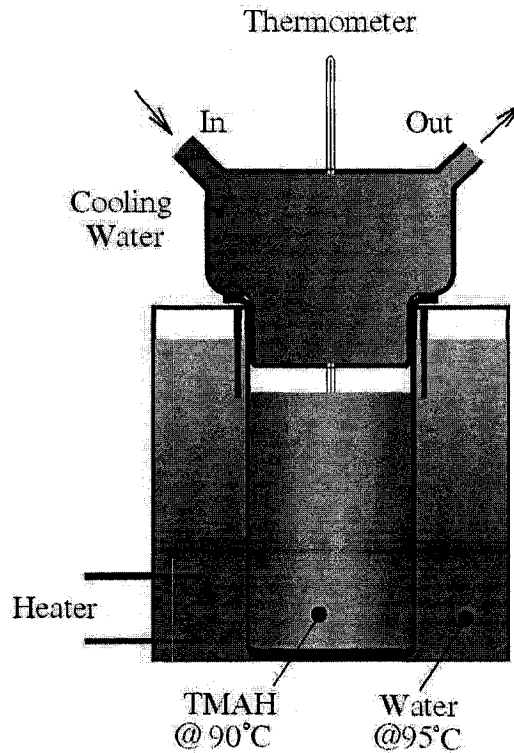


Figure 6.14: The TMAH etching setup used for micromachining.

release the hanging beams. Figure 6.15 shows samples of the etched parts in which (a) is the top part with three beams and (b) is the support.

Due to silicon under etch in TMAH etching, the existing oxide layer in the edges showed some irregularities. To achieve a uniform surface it was decided to remove all existing oxide layer and repeat the oxidation step at the end. In this way a uniform and smooth surface of oxide layer was grown on the wafers.

To remove the oxide layer the samples were treated as stated in Section 6.4.4, then the process of wet oxidation as explained in Section 6.4.2 was repeated. Figures 6.16 and 6.17 show the SEM (Scanning Electron Micrograph) of the fabricated parts. Figure 6.16 shows the void between two beams while Figure 6.17 illustrates a beam and its support. The $\{111\}$ planes which are at the angle 54.7° with (100) plane can also be seen in Figure 6.16.

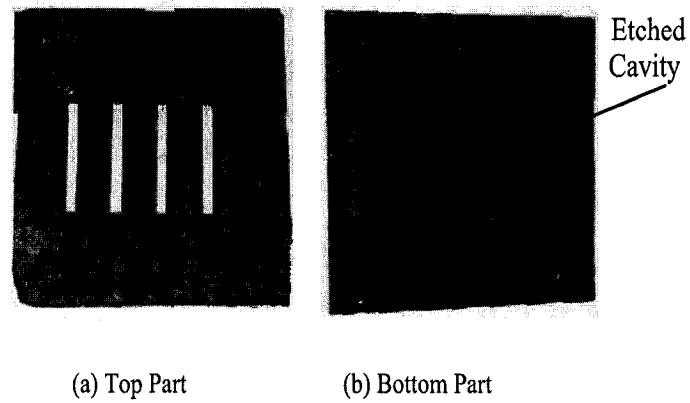


Figure 6.15: Some samples of micromachined silicones are shown.

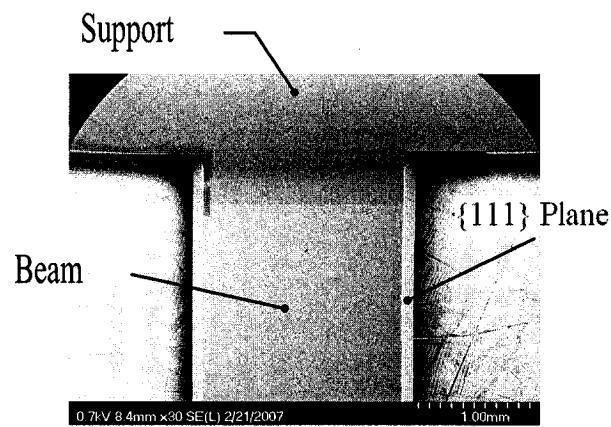


Figure 6.16: A micromachined beam and a support. (The (100) plane, which is parallel to the paper is shown. The {111} planes which make two sides of the beam are also illustrated).

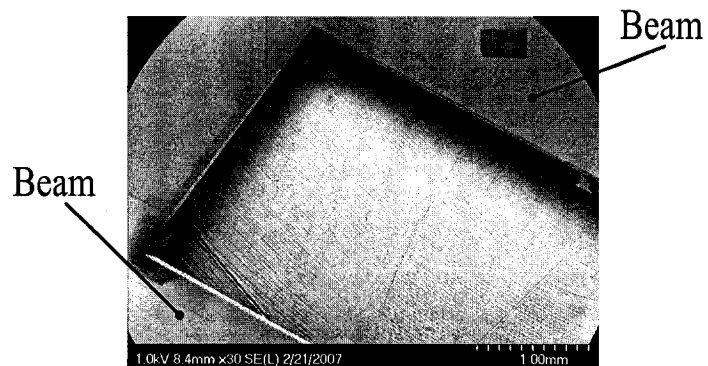


Figure 6.17: The void space between two adjacent beams.

6.4.6 Sensor Assembly

Using the silicon micromachined parts a complete sensing module was hybrid assembled using PVDF films. As mentioned earlier, five PVDF films were used, two of which for supports and the other three for the beams. A $28\text{ }\mu\text{m}$ thick, uniaxial and metalised PVDF film was used from which two $22 \times 4\text{ mm}$ film was cut in such a way that the drawn direction of the film was parallel to the film length. (refer to Figure 6.2 in which arrows show the drawn direction). This was done to minimize the output of the PVDF films at the supports due to any unwanted load and maximize the sensitivity of the output to the compressive load only as explained in Section 3.3. These two films were glued to the top of the supports. From 22 mm length, 18 mm was the active area and 4 mm was used to connect the electrodes. Electrodes were cut from a thin copper foil and adhered to the PVDF films using conductive glue. For the suspended beams three $2 \times 12\text{ mm}$ PVDF films were used. The films were cut in such a way that the drawn direction was in line with the PVDF film length. A picture from the backside of the top part is shown in Figure 6.18. After connecting electrodes to the films, they were glued to the top silicon

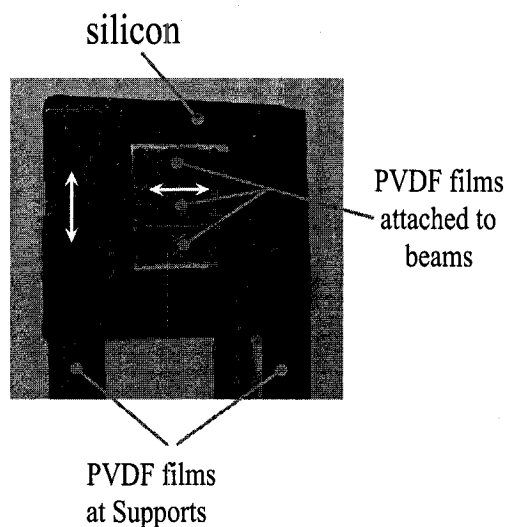


Figure 6.18: The top part of the sensor. PVDF film at the supports and attached to the beams are shown. The direction of the PVDF films are also shown.

part. The wiring of these three films were passed through the empty space between the

top and bottom parts. Finally there were 10 wires each pair belonged to one sensing element. Then the top part on which all the PVDF films were adhered was glued to the bottom silicon part and then for subsequent testing, the assembled sensor system was placed in a plexiglass block. The hybrid assembled MEMS sensor is shown in Figure 6.19.

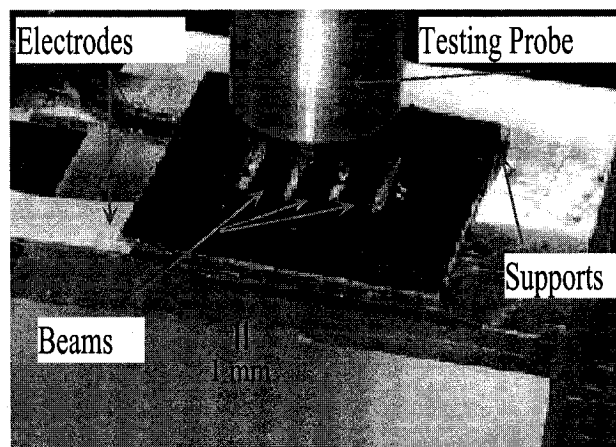


Figure 6.19: The macromachined tactile sensor.

6.5 Testing & Validation: Softness Characterization

In order to validate the simulation results, a softness sensing experiment was conducted on the microfabricated sensor. Prior to conducting the softness tests it was required to estimate the softness of test objects. In addition, to have an accurate method compared to conventional qualitative and heuristic approach which the test objects are labeled in terms very soft, soft, etc an additional quantification technique is used. Durometer (Shore) softness is one of the most commonly used hardness/softness tests for elastomeric materials. The successful application of durometers in mechanical property evaluation of soft tissue such as skin is reported by Falanga *et al.* [160]. The measurement of elasticity of tumors surrounded by soft tissue is reported in [161] and the range of elasticity of breast tumors was found to be between 150-990 kPa. Durometer gauge measures the depth of surface penetration of an indenter of a given geometry. Since both force and deflection

are measured, durometer is typically used as a stiffness indicator. Figure 6.20 shows the working concept of a typical durometer. When durometer is pressed against a soft object, depends on the softness of the object, the calibrated spring is compressed. The softness number then can be read from a dial connected to the spring. The shape of indenter tip is different and it depends on the type of durometer. The durometer hardness test is defined

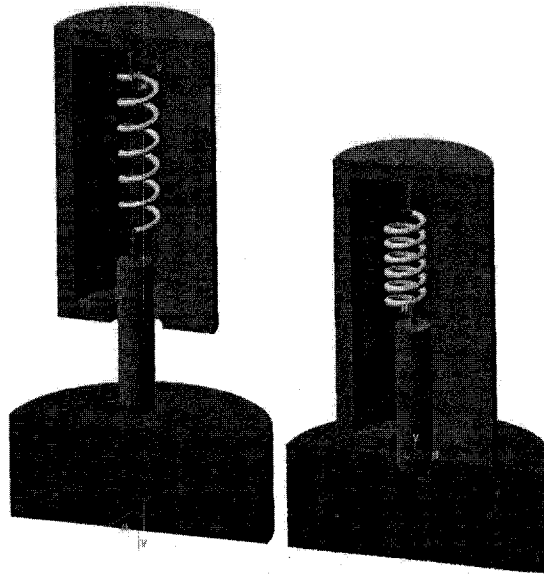


Figure 6.20: A picture of durometer used in this study.

by ASTM D 2240 which covers seven types of durometers: A,B, C, D, DO, O and OO [162]. Table 6.2 summarizes the overall information about durometers A and OO types that are used in this study. In this group, type OO is considered for the measurement of very

Table 6.2: General specifications of durometers type A and OO.

Scale of Durometer	Material To be used	Main Spring	Indenter Shape
A	Soft elastomeric materials, rubber and rubber-like	822 gr	Flat cone point, 35°
OO	Light Foams, sponge rubber and animal tissue	113 gr	Sphere 3/32"

soft materials. As shown in Figure 6.21 commercially available durometer test consists of

four components according to ASTM D 2240: Presser foot, indenter extension indicating device (e.g. dial), and calibrated spring. The scale reading is proportional to the indenter movement. The soft material samples were measured using standard durometers type



Figure 6.21: Durometer type OO.

OO and A. In addition, the compressive Young's modulus of the objects for small strains ($< 10\%$) were measured using a conventional compression test. The relationship between durometer dial reading and Young's modulus of the objects is shown in Figure 6.22. The Young's modulus of the harder object was measured as 6MPa . The objects were then used to test microfabricated sensor for softness sensing. The experimental setup used for this testing has already been described in 3.5. Figure 6.23 shows the MEMS sensor under test with electrodynamic shaker for applying dynamic loads. The soft objects were placed on the first beam. Then a compressive load was applied on to the top surface of the objects using a rigid plate at the end of probe in order to mimic the grasping condition. Then the output of the PVDF films attached to all the three beams were recorded and compared. Four samples were tested. Three of them were considered as soft objects and the last one was considered as medium-hard object. In contrast to the finite element results a moderate cross-talk between 3 channels were observed. This cross-talk can be attributed to both mechanical and electrical phenomena. The dynamic force applied to

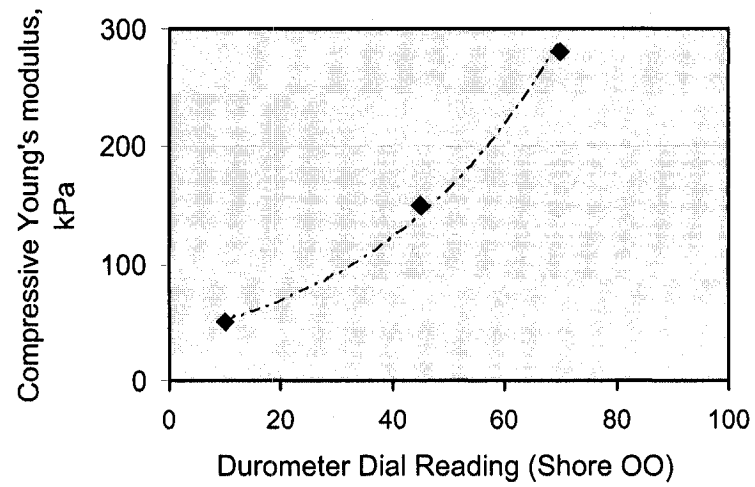


Figure 6.22: Durometer dial reading scale OO versus Young's modulus of soft objects are plotted.

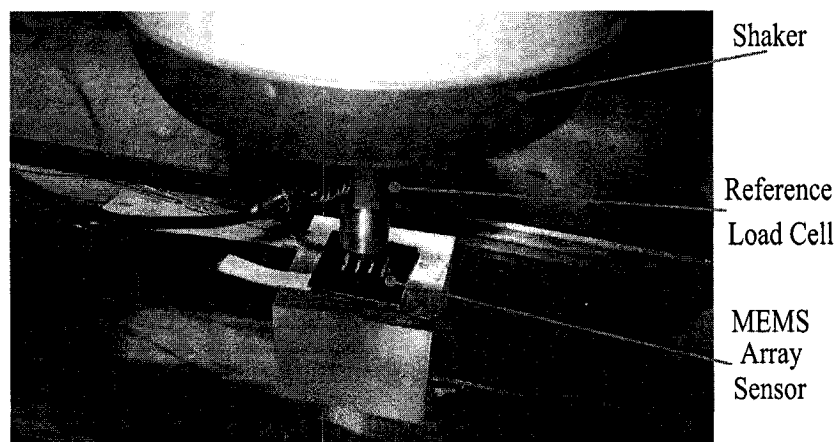


Figure 6.23: MEMS sensor being tested using a electrodynamic shaker.

a beam can induce some vibration into adjacent beams which causes some output from other channels. On the other hand, each sensing element had two electrodes and their associated wires, therefore 10 wires had to be used that could potentially affect the other channels. Figure 6.24 shows the output of the middle PVDF films for three different soft objects with softness number 10, 43 and 70 in Shore OO scale when a distributed load of 111 kPa was applied at 20 Hz. The results of finite element model solved for these material properties are also added to the figure for comparison. As mentioned earlier, some level of cross-talk was observed, recorded and shown in Figure 6.25. Similar to the previous test a sinusoidal distributed load at 20 Hz was applied to the first beam and this time the output of all beams were recorded. The results show that even when no load is applied to the second and third beams, there exist output voltage in the other two channels. The existence of a lump within the soft object would cause a point load. Chapter 5 demonstrates the capabilities of millimeter-size sensor in detecting point loads and their locations. Similarly, the micromachined sensor array potentially is capable of lump detection.

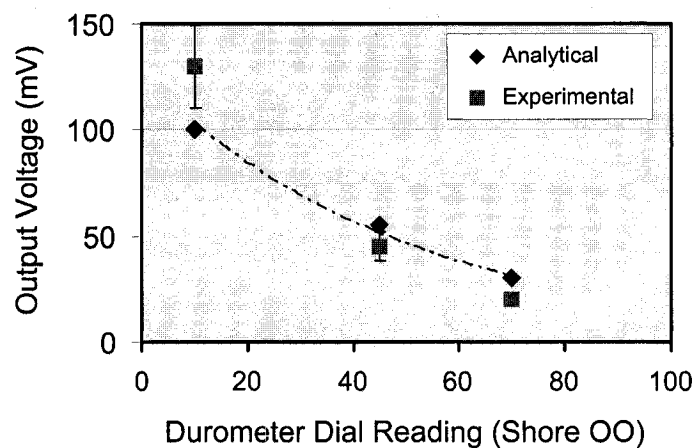


Figure 6.24: Durometer dial reading scale OO versus Young's modulus of soft objects are plotted.

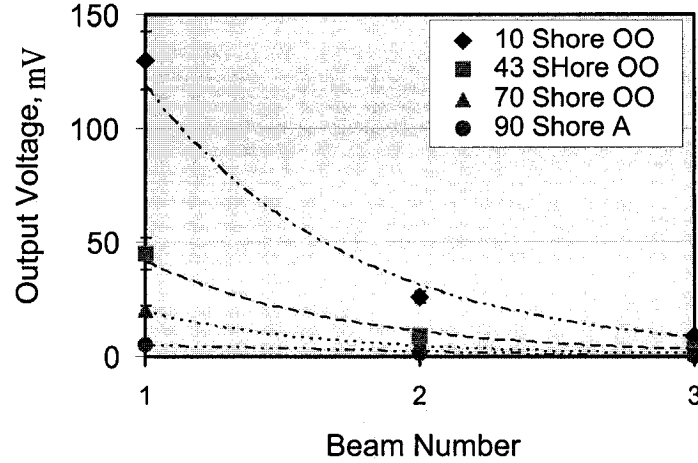


Figure 6.25: Durometer dial reading scale OO versus Young's modulus of soft objects are plotted.

6.6 Discussion and Conclusions

The feasibility of microfabrication of the proposed sensor is demonstrated. Using anisotropic wet etching the silicon parts of the sensor were fabricated. Although, the thinness of the wafer created some difficulties, it was shown that the fabrication procedure is workable. Even though the sensor has been fabricated with hybrid integration of commercial PVDF films, developing specific methods for deposition of PVDF through monolithic integration is crucial in further miniaturization of the sensor. The developed 3D finite element model was shown to be accurate. The sensor voltage output for materials with Young's modulus between 10 kPa and 1 MPa were also presented. Even though, no cross talk between sensing units was observed in theoretical analysis, some cross talk was observed in testing due to vibration transmission and also electrical cross talk. Using durometer Shore OO, several elastomeric materials were characterized and then were tested with the MEMS sensor. The PVDF output voltages obtained from the experiments were in good agreement with those of finite element model. The range of Young's modulus used for this study was between 50 and 280 kPa corresponding to the softness number of 10 to 70 in Shore OO. A single material with Young's modulus 6 MPa and corresponding

softness number 90 in Shore A was also used in the experiments. It is shown that the fabricated MEMS sensor is capable of measuring the softness. As explained in Chapter 4, any hidden lump in bulky soft tissue would cause a concentrated load superimposed with the background distributed load. This point load affects the output voltage of middle PVDF film. In addition, in the presence of a lump the output of PVDF at supports would be different. In a sensor array, the the outputs that are influenced by the lump can be compared with the outputs of a sensing unit with no lump. This comparison gives us valuable information about the size and position of the lump.

Chapter 7

Summary, Conclusions, Contributions and Proposed Future Work

7.1 Summary and Conclusions

Minimally invasive surgery has grown rapidly over the past two decades. Its promising results have encouraged many researchers to work towards enhancement of this technology. Among several shortcomings, severe restrictions on surgeon's tactile capabilities has been the focus of the present study. History of medical devices shows that retrofitting existing surgical tools is the preferred method in enhancement of an existing medical device, as it is a faster path to market and also more acceptable for doctors who are familiar with their applications and use. As a result, the approach would be to add the tactile sensing capability to existing MIS tools. Consequently, several tactile sensors have been developed to restore the tactile capabilities of the surgeons. However, a multifunctional sensor capable of replicating all of the capabilities of human finger has not been devised and prototyped. A good candidate would be a sensor with the following specifications: biocompatibility, firm grasping, force sensing, softness sensing, force position detection,

good working range, miniaturization capability, less expensive, sterilizable or disposable, simple structure, durable and less wiring.

This thesis has tried to take one step forward to address the above mentioned requirements of MIS technique by introducing a novel method for softness sensing and devising a multifunctional tactile sensor which addresses many of the requirements of an ideal MIS endoscopic tactile sensor. The materials used in this design, such as silicon and piezoelectric PVDF films have already been used in biomedical applications. The sensor is designed in such a way that its geometry is a corrugate shape to enhance grasping. In Chapter 3, it is shown that the proposed sensor is capable of measuring the applied load. In addition, it was shown that the sensor differentiates grasped objects based on their softnesses. Another useful feature is the capability to find position of a concentrated load. The later capability is important particularly in finding the hidden anatomical objects, such as lumps or arteries. Presence of a lump within a bulky soft tissue influences the stress distribution within the grasped object and at the tissue-grasper interface which is described in Chapter 4. This chapter also demonstrates the capability of a sensor in extracting some useful information about the embedded lump from the stress profile that appears at the sensor surface. The sensor design also has the ability to change the working range of sensor in terms of force or softness. By changing the dimensions of beams, such as, thickness and length, as well as the thickness of the PVDF films the working range of sensor can be optimized further for any specific application. Chapter 6 of this dissertation is dedicated to microfabrication of sensor using MEMS technology. This chapter shows that MEMS technology is quite feasible for developing the sensor. The microfabrication of the sensor was achieved using anisotropic wet etching of silicon, which is a standard procedure in MEMS technology. Although this study does not address the sterilization problems, sensor can be sterilized using ETO (ethylene oxide), which is very common for sterilization of similar products. On the other hand the idea of disposable grasper tip is also workable. In this application, sensorized tip can be designed in such a way that after each surgery it can be detached from MIS tool and disposed. Using of piezoelectric

PVDF has made the sensor suitable for medical applications, as it does not need any driving unit. The piezoelectric PVDF produces charge when it is strained and this charge can be detected by an embedded charge amplifier. Chapter 2 of this document is dedicated to characterization of piezoelectric PVDF which later has been used throughout this research work. In addition, for completeness, a new method to feedback the extracted tactile information to a surgeon is presented in Chapter 5. This chapter particularly is dedicated to graphical representation of localized lumps.

On summary, a novel technique for softness sensing is introduced in this thesis. The piezoelectric PVDF as a sensing element is also tested and characterized. The uniaxial and biaxial PVDF films are selected for design and the influence of orthotropic property of uniaxial PVDF is investigated. In addition, the effect of friction on the PVDF output is also investigated. The latter investigation was found to be potentially useful in finding the friction coefficient of surfaces. It is shown that the proposed method is specially suitable for low friction coefficients. A macro size sensor was fabricated and the feasibility of the working concept was demonstrated. Since experiment on human or animal soft tissue was not possible, elastomeric materials which exhibit many characteristics of soft tissue were used in this study. The theoretical approach including closed form dynamic formulation and finite element method were shown to be in good agreement with the outcome of the experiments. The nonlinear properties of soft objects which affect the output of the sensor are discussed in Chapter 4. A graphical representation method to display the information of a localized lump is presented in Chapter 5. The microfabrication of the sensor as well as its finite element model and experimental tests are presented in Chapter 6. Summary of the thesis, contributions and suggestions for future work are discussed in Chapter 7.

7.2 Contributions

This thesis presents studies regarding the tactile sensing for minimally invasive surgery. To the best knowledge of the author the followings are several novel and original contributions to the field:

1. The orthotropic properties of uniaxial and biaxial films are characterized.
2. The performance of PVDF films in sandwich configurations in presence of friction is characterized. The outcome of this study also opens a new avenue for a novel technique to measure the coefficient of friction of a surface.
3. A novel method for softness sensing is introduced.
4. It is shown that the proposed sensor is a multifunctional tactile sensor capable of measuring force, force position, softness and lump detection.
5. A nonlinear hyperelastic model of the grasped tissue with an embedded lump is developed and the influence of the lump parameters, such as, size, depth and stiffness is studied.
6. A novel technique of representing tactile information to the surgeon is devised. In this graphical approach, the sensor gathers the tactile information and then feeds back to the surgeon using the developed algorithm.
7. The proposed sensor is miniaturized through micromachining. In addition to the micromachining, the finite element analysis and testing of MEMS sensor are also presented.

Some of the original contributions of this thesis are published [78, 124, 119], accepted [163, 164, 165] or is submitted for publication as follows:

- Sokhanvar S, Dargahi J and Packirisamy M,” Nonlinear Modeling and Experimental Evaluation of Soft Tissue Embedded Lumps for MIS Applications”, submitted to the Journal of Biomechanical Engineering, ASME (Ref: BIO-07-1079, Mar 2007).

7.3 Proposed Future Work

As explained earlier, this thesis presented a novel method of softness sensing and feasibility of the proposed method both in macro and micro sizes. However, the ultimate objective of this work would be prototyping a commercializable smart grasper for MIS applications. In order to achieve this goal, a couple of improvements are suggested. It should start from operating room where the exact needs of surgeons, limitations, concerns and expectations should be recorded and transformed into engineering format. These include designating the target MIS tools, and the types of tissues and range of applied forces. The properties of the target tissues for each specific operation, should be characterized. On the other hand the dimensions of selected MIS tools must be used in the sign of sensor modules. Using monolithic techniques, PVDF could be deposited onto micro-sized areas. This method ensures that all sensing elements in an array would perform identically. The electrodes can also be connected to the PVDF films using microfabrication techniques. One of important issues in developing such a grasper is testing and calibration. The grasper should be tested in *in-vivo* conditions as well as *ex-vivo* setup. Signal processing is a key part of the device. The responses of the device to different tissues and to exitance of a lump must be recorded and analyzed. Using the information gathered at this stage a database (or knowledge base) can be provided. Then, in real applications, the sensor's output would be interpreted using the stored database. Eventually, this information should be introduced to the surgeon in an effective way. One such way, namely graphical rendering of tactile information, is presented in this thesis. The other important issues in the continuation of this work are sterilization and packaging. The grasper should be design in a way that can be easily sterilized, for instance using ethylene oxide. Any kind of packaging would probably change the performance of the smart grasper, and must be considered in design and testing stages. An interesting and challenging continuation would be monolithic integration of piezoelectric layer with silicon for further miniaturization.

Bibliography

- [1] Bicchi A, Canepa G, Rossi D D, Iaconi P, and Scilingo E P. A sensorized minimally invasive surgery tool for detecting tissue elastic properties. *Proceedings of the 1999 IEEE, Int. Conf. on Rob. And Auto., Minneapolis, Minnesota*, pages 884–888, 1996.
- [2] Lujan J A, Parrilla P, Robles R, Marín P, Torralba J A, and Garcia-Ayllon J. Laparoscopic cholecystectomy vs open cholecystectomy in the treatment of acute cholecystitis. *Arch. Surg.*, 133:173–175, 1998.
- [3] Fager PJ. The use of haptic in medical applications. *Int J Medical Robotics and Computer Assisted Surgery*, 1(1):36.42, 2004.
- [4] Gaspari A and Di Lorenzo N. State of the art of robotics in general surgery. *Business Briefing: Global Healthcare*, pages 1–6, 2002.
- [5] Sastry S S, Cohn M, and Tendick F. Millirobotics for remote, minimally invasive surgery. *Robotics and Autonomous Systems*, 21(3):305–316, 1997.
- [6] Uchio Y, Ochi M, Adachi N, Kawasaki K, and Iwasa J. Arthroscopic assessment of human cartilage stiffness of the femoral condyles and the patella with a new tactile sensor. *Medical Engineering and Physics*, 24(6):431–435, 2002.
- [7] Zamorano L, Li Q, Jain S, and Kaur G. Robotics in neurosurgery: state of the art and future technological challenges. *Int J Medical Robotics and Computer Assisted Surgery*, 1(1):7–22, 2004.

- [8] Cleary K and Charles N. State of the art in surgical robotics, clinical applications and technological challenges. *computer assisted surgery*, 6:312–328, 2001.
- [9] Rebello K J. Applications of mems in surgery. *Proceedings of the IEEE*, 92(1):43–55, January 2004.
- [10] MAck M. Minimally invasive and robotic surgery. *J. Amer. Med. Assoc.*, 285(5):568–572, Feb 2001.
- [11] Dargahi J. An endoscopic and robotic tooth-like compliance and roughness tactile sensor. *the Journal of Mechanical Engineering Design (ASME)*, 124:576–582, Sept. 2002.
- [12] Son J S, Cutkosky M R, and Howe R D. Comparison of contact sensor localization abilities during manipulation. *Robotics and Autonomous Systems*, 17(4):217–233, 1996.
- [13] Miyaji K, Sugiura S, Inaba H, Takamoto S, and Omata S. Myocardial tactile stiffness during acute reduction of coronary blood flow. *The Annals of Thoracic Surgery*, 69(1):151–155, 2000.
- [14] Wen Z, Wu Y, Zhang Z, Xu S, Huang S, and Li Y. Development of an integrated vacuum microelectronic tactile sensor array. *Sensors and Actuators A: Physical*, 103(3):301–306, 2003.
- [15] Leineweber M, Pelz G, Schmidt M, Kappert H, and Zimmer G. New tactile sensor chip with silicone rubber cover. *Sensors and Actuators A: Physical*, 84(3):236–245, 2000.
- [16] Mei T, Li W J, Ge Y, Chen Y, Ni L, and Chan M H. An integrated mems three-dimensional tactile sensor with large force range. *Sensors and Actuators A:Physical*, 80(2):155–162, 2000.

- [17] Omata S and Terunuma Y. New tactile sensor like the human hand and its applications. *Sensors and Actuators A: Physical*, 35(1):9–15, 1992.
- [18] Lee M H and Nicholls H R. Tactile sensing for mechatronics-a state of the art survey: A review article. *Mechatronics*, 9(1):1–31, Feb 1999.
- [19] Kolesar E S, Reston P R, Ford D G, and Fitch R C. Mutiplexed piezoelectric polymer tactile sensor. *Journal of Robotic Systems*, 9(1):37–63, 1992.
- [20] Johansson R S and Vallbo A B. Tactile sensitivity in the human hand: relative and absolute densities fo four types of mechanoreceptive units in glabrous skin. *J. of Physiol.*, 286:283–300, 1979.
- [21] Dargahi J and Najarian S. Human tactile perception as a atandard for artificial tactile sensing- a review. *Int J Medical Robotics and Computer Assisted Surgery*, 1:23–35, 2004.
- [22] Dario P. Tactile sensing: Technology and applications. *Sensors and actuators A:Physical*, 25:251–256, 1991.
- [23] Lee M H. Tactile sensing: New directions, new challenges. *The international Journal of Robotics Research*, 19:636–643, July 2000.
- [24] Lederman S J. *The perception of texture by touch, Tactual perception: A sourcebook*. Cambridge University Press, New York, 1982.
- [25] Fearing RS, Moy G, and Tan E. Some basic issues in teletaction. *IEEE International Conference on Robotics and Automation*, pages 3093–3099, 1997. USA, Albuquerque.
- [26] Fisch A, Mavroidis C, Melli-Huber J, and Bar-Cohen Y. *Haptic devices for virtual reality, telepresence, and human-assistive robotics, in Biologically-inspired intelligent robots*. SPIE Press, 2003.

- [27] Bicchi A, Scillingo E P, and De Rossi D. Haptic discrimination of softness in teleoperation: The role of the contact area spread rate. *IEEE Transactions On Robotics and Automsation*, 16(5):496–504, 2000.
- [28] Clark F J and Horch K W. Handbook of perception and human perfomance, volume 1: Sensory processes and perception. *John Wiley and Sons*, Chapter 13, 1986.
- [29] Vallbo A B and Johansson R S. Properties of cutaneous mechanoreceptors in the human hand related to touch sensation. *Human Neurobiology*, 3:3–14, 1984.
- [30] Kandel E R, Schwartz J H, and Jessell T M. *Principles of Neural Science*. McGraw-Hill Companies Inc., 4th edition edition, 2000.
- [31] Elsner P, Berardesca E, Wilhelm KP, and Maibach HI. *Bioengineering of the skin: Skin biomechanics*, volume V. CRC Press, 1st edition, 2001.
- [32] Russell R A. *Robotic tactile sensing*. Printice Hall Publishing Co., 1991.
- [33] Banks J L. Design and control of an anthropomorphic robotic finger with multi-point tactile sensation. M.sc. thesis, Massachusetts Institute of Technology, 2001.
- [34] Gentilucci M, Toni I, Daprati E, and Gangitano M. Tactile input of the hand and the control of reaching to grasp movements. *Experimental Brain Research*, 114:130–137, 1997.
- [35] Lederman S J. *Active Touch*. Pergamon Press, 1978.
- [36] Srinivasan M A and LaMotte R H. Tactual discrimination of softness. *Journal of Neurophysiology*, 73(1):88–101, 1995.
- [37] Krueger L E. *Historical Perspective in Tactual Perception*. Cambridge University Press, 1982.
- [38] Howe R D and Matsuoka Y. Robotics for surgery. *Annual Review of Biomedical Engineering*, 1:211–240, 1999.

- [39] Tendick F, Mori T, and Way L. The future of laparoscopic surgery. *Fundamentals of Laparoscopic surgery*, 1995.
- [40] Rininsland H H. Basics of robotics and manipulators in endoscopic surgery. *Journal of Endoscopic Surgery*, 1:154–159, 1993.
- [41] Dario P, Carrozza MC, Lencioni L, Magnani B, and D’Attanasio S. A micro robotic system for colonoscopy. *Proceedings of the IEEE International Conference on Robotics and Automation, IEEE Robotics and Automation Society*, pages 1567–1572, 1997.
- [42] Howe R D, Peine W J, Kontarinis D A, and Son J S. Remote palpation technology. *Proceedings of IEEE Engineering in Medicine and Biology Magazine*, 14(3):318–323, 1994.
- [43] Krouskop T A, Wheeler T M, Kallel F, Garra B S, and Hall T. Elastic moduli of breast and prostate tissues under compression. *Ultrasound Imaging*, 20(4):260–274, 1998.
- [44] Riva G and Gamberini L. *Virtual reality in telemedicine, Communications Through Virtual Technology*. ISO Press Amsterdam, 2003.
- [45] Bashshur R L, Mandil S, and Shannon G W. State-of-the-art telemedicine/telehealth symposium, an international perspective. *Telemedicine Journal and e-Health*, 8(2):13–35, 2002.
- [46] De Martines N, Mutter D, Vix M, Leroy J, Glatz D, Rosel F, Harder F, and Marescaux J. Assessment of telemedicine in surgical education and patient care. *Annals of Surgery*, 232:282–291, 2000.
- [47] McDaris D. *Telesurgery: the medical wave of the future*. University of Southern California Publications, 2003.

- [48] Kwon D S and Woo K Y. Microsurgical telerobot system. *Proceedings of the IEEE/RSJ International Conference on Intelligent Robotics and Systems*, pages 945–950, 1998.
- [49] Peine W. J. *Remote Palpation Instruments for Minimally Invasive Surgery*. PhD thesis, Harvard University, Oct. 1998.
- [50] Gerling G J, Weissman A M, Thomas G W, and Dove E L. Effectiveness of a dynamic breast examination training model to improve clinical breast examination (cbe) skills. *Cancer Detection and Prevention*, 27:451–456, 2003.
- [51] Rao N P, Dargahi J, Kahrizi M, and Sokhanvar S. Design and microfabrication of a hybrid piezoelectric - capacitive tactile sensor. *Sensor Review*, 26(3):186–192, 2006.
- [52] Qi HJ, Joyce K, and Boyce M C. Durometer hardness and the stress-strain behavior of elastomeric materials. *Rubber Chemistry and Technology*, 76(2):419–435, May/Jun 2003.
- [53] Hertz DL Jr and Farinella AC. Shore a durometer and engineering properties. *Presented at the Fall Technical Meeting of The New York Rubber Group*, pages 1–13, Sep. 1998.
- [54] Sadao Omata and Yoshikazu Terunuma. Development of new type tactile sensor for detecting hardness and/or softness of an object like human hands. *IEEE*, 1991.
- [55] Yamamoto Y and Kawai K. Development of measuring method for softness of epidermis using rotational step response. *IEEE*, 1999.
- [56] Bajcy R. Shape from touch, advances in automation and robotics ed g n saridise. 1999. London: JAI.
- [57] Bardelli R, Dario P, De Rossi D, and Pinotti P C. Piezoelectric polymer : new sensor materials for robotic application. *Proc. 13th Int. Sym. Industrial Robotics*, pages 18–45–56, 1983.

- [58] De Rossi D, Domenici C, and Nannini A. Artificial sensing skin mimicking electromechanical transduction properties of human dermis. *IEEE Trans. Biomed. Eng.*, 35:83–92, 1988.
- [59] Thomas V J and Patil K M. Three dimensional stress analysis for the mechanics of plantar ulcers in diabetic neuropathy. *Medical and Biological Engineering and Computing*, 42:230–235, 2004.
- [60] Tanaka M and Furubayashi M. Development of an active palpation sensor for detecting prostatic cancer and hypertrophy. *Smart Mater. Struct.*, 9:878–884, 2000.
- [61] Dargahi J, Parameswaran M, and Payandeh S. A micromachined piezoelectric tactile sensor for endoscopic grasper: theory, fabrication and experiments. *Journal of Micro-Electromechanical Systems*, 9(3):329–336, Sept. 2000.
- [62] Shikida M, Shimizu T, Sato K, and Itoigawa K. Active tactile sensor for detecting contact force and hardness of an object. *Sensors and Actators: A*, 103:213–218, 2003.
- [63] Beebe D, Denton DD, Radwin RG, and Webster JG. A silicon-based tactile sensor for finger-mounted applications. *IEEE Trans. On Biomed. Eng.*, 45(2):151–159, 1998.
- [64] Lindahl OA, Omata S, and Angquist KA. A tactile sensor for detection of physical properties of human skin *in vivo*. *J of Medical Eng & Technology*, 22(4):147–153, July/Aug 1998.
- [65] Miyaji AK, Furuse A, Nakajima J, Kohno T, Ohtsuka T, Yagyu K, Oka T, and Omata S. The stiffness of lymph nodes containing lung carcinoma metastases a new diagnostic parameter measured by a tactile sensor. *Cancer*, 80(10):1920–1925, 1997.
- [66] Wellman PS, Howe RD, Dewagan N, Cundari MA, Dalton E, and Kern KA. Tactile imaging: a method for documenting breast masses. *Proceedings of the First Joint*

BMES/EMBS Conference, IEEE Computer Society Press, pages 1131–1132, 1999.
Piscataway, NJ.

- [67] Wellman PS and Howe RD. Extracting features from tactile maps. *Proceedings of the Second International Conference on Medical Image Computing and Computer-Assisted Intervention*, pages 1133–1142, 1999.
- [68] Wellman P S, Dalton E P, Krag D, Kern K, and Howe R D. Tactile imaging of breast masses. *Arch. Surg*, 136:204–208, 2001.
- [69] Barman I G and Sujoy K. Analysis of a new combined stretch and pressure sensor for internal nodule palpation. *Sensors & Actuators A: Physical*, 125(2):210–216, Jan 2006.
- [70] Hosseini M, Najarian S, Motaghinasab S, and Dargahi J. Detection of tumours using a computational tactile sensing approach. *Int. J. Med Robotics Assist Surg*, 2:333–340, 2006.
- [71] Kattavenos N, Lawrenson B, Frank T G, Pridham M S, Keatch R P, and Cuschieri A. Force-sensitive tactile sensor for minimal access surgery. *Minimally Invasive Therapy & Allied Technologies*, 13(1):42–46, Feb 2004.
- [72] Kawai H. The piezoelectricity of polyvinylidene fluoride. *Jpn J Applied Physics*, 8:975–6, 1969.
- [73] Pereira D, Shankar V N, Sathiyanaarayan S, Lakshmana Rao C, and Sivakumar S M. Vibration control of a cantilever beam using distributed pvdf actuator. *Proceedings of SPIE - The International Society for Optical Engineering*, 5062(2):598–604, 2002.
- [74] De Abreu G, Jose F R, and Valder S. Digital optimal vibration control of a flexible structure containing piezoelectric elements. *Proceeding of the ASME Design Engineering Technical Conferences and Computers and Information in Engineering Conference. Volume 5: 19th Biennial Conference on Mechanical Vibration and Noise*, pages 1739–1748, 2003.

- [75] Wang D H and Huang S L. Health monitoring and diagnosis for flexible structures with pvdf piezoelectric film sensor array. *Journal of Intelligent Material Systems and Structures*, 11(6):482–491, 2000.
- [76] Hurlebaus S and Lothar G. Smart layer for damage diagnostics. *Journal of Intelligent Material Systems and Structures*, 15(9-10):729–736, 2004.
- [77] Lee Y S, Elliott S J, and Ganrdonio P. Distributed four-layer pvdf actuator/sensor arrangement for the control of beam motion. *Proceedings of SPIE - The International Society for Optical Engineering*, 4326:284–294, 2001.
- [78] Sokhanvar S, Packirisamy M, and Dargahi J. A novel pvdf based softness and pulse sensor for minimally invasive surgery. *The Third IEEE International Conference on Sensors, Austria,,* pages 24–27, 2004.
- [79] Laroche G, Merios Y, Schwarz E, Guidoin R, King M W, Paris E, and Douville Y. Polyvinylidene fluoride monofilament sutures: Can they be used safely for long term anastomoses in the thoracic aorta? *Artif. Organs.*, 19(11):1190–9, 1995.
- [80] Tasaka S and Miyata S. The origin of piezoelectricity in poly (vinylidene fluoride). *Ferroelectrics*, 32:17–23, 1981.
- [81] Lue H and Hanagud S. Pvdv film sensor and its applications in damage detection. *Journal of Aerospace Engineering*, pages 23–30, 1999.
- [82] Bloomfield P E. Production of ferroelectric oriented pvdf films. *J. Plastic Film and Sheeting*, 4(2):123–129, 1988.
- [83] Xu Y. *Ferroelectric Materials and their applications*, North-Holand, 1991.
- [84] Sakata J and Mochizuki M. Preparation of organic thin films by an electrospray technique i. crystal forms and their orientation in poly(vinylidene fluoride) films. *Thin Solid Films*, 195:175–184, 1991.

- [85] Asahi J and Sakata J. Integrated pyroelectric infrared sensor using pvdf thin film deposited by electro-spry method. *Mat. Res. Soc. Symp. Proc.*, 310:v, 1993.
- [86] Binnie T D, Weller H J, He Z, and Setiadi D. An integrated 16*16 pvdf pyroelectric sensor array. *IEEE Transactions on Ultrasonics, and Frequency Control*, 47(6):1413–1420, 2000.
- [87] Weller H J, Setiadi D, and Binnie T D. Low-noise charge sensitive readout for pyroelectric sensor arrays using pvdf thin film. *Sensors and Actuators*, 85:267–274, 2000.
- [88] Spearritt D J and Asokanthan S F. Torsional vibration control of a flexible beam using laminated pvdf actuators. *Journal of Sound and Vibration*, 193(5):941–956, 1996.
- [89] Nye J F. *Physical properties of crystals*. Oxford, 1960.
- [90] Thompson M L. On the material properties and constitutive equations of piezoelectric poly vinylidene fluoride (pvdf). *PhD thesis*, Nov 2002. Drexel University.
- [91] Blazer E, Koh W, and Yon E. A miniature digital pressure transducer. *Proc. 24th Annu. Conf. Engineering Medicine and Biology*, page 211, 1971.
- [92] Roy S. Biomems for minimally invasive medical procedures. *BioMEMS 2002 Conference*, 2002.
- [93] Kovacs G T A. *Mircomachined Transducers Sourcebook*. McGraw-Hill, 2002.
- [94] Hsu T R. *MEMS and Microsystems Design and Manufacture*. McGraw Hill, 2002.
- [95] Von Munch W. A 3*3 pyroelectric detector array with improved sensor technology. *Sensors and Actuators A*, (41-42):156–160, 1994.
- [96] Fujitsuka N, Sakata J, Miyachi Y, Mizuo K, Ohtsuka K, and Taga Y. Monolithic pyroelectric infrared image sensor using pvdf thin film. *Sensors and Actuators A*, (66):237–243, 1998.

- [97] Schellin R, Hess G, Kuehnel W, Sessler G M, and Fukada E. Silicon subminiature microphone with organic piezoelectric layers: Fabrication and acoustical behavior. *IEEE*, pages 929–934, 1991.
- [98] Hoon D. Pyroelectric properties of the b-polyvinylidene fluoride (pvdf) thin film prepared by vacuum deposition with electric field application. *Jpn. J. Appl. Phys.*, 41:7234–7238, 2002.
- [99] Park S H. The dielectric properties of functional pvdf thin films by physical vapor deposition method. In *Proc. of the 5th Int. Conf. On Prop. And appl. Of dielectric mat.*, korea, 1997.
- [100] Choy K L and Wei Bai. Preparation of oriented poly(vinylidene fluoride) thin films by a cost-effective electrostatic spary-assisted vapor deposition-based method. *Thin Solid Films*, 372(1-2):6–9, 2000.
- [101] Chatrathi K.K. *Microfabrication and Characterization of PVDF Copolymer Thin Films Suitable for Integrating with Optical Microsystems*. Master thesis, Concordia University, Montreal, Canada, Spring 2007.
- [102] Howe R D, Peine W J, Kontarinis D A, and Son J S. Remote palpation technology. *IEEE Engineering in Medicine and Biology*, 14(3):318–323, May/June 1995.
- [103] Minoru T and Soitiro T. Theory of curved, clamped, piezoelectric film, air-born transducers. *IEEE Transactions on Ultrasonics, Ferroelectrics, and Frequency Control*, 47(6), Nov. 2000.
- [104] Roh Y, Varadan V V, and Varadan V K. Characterization of all the elastic, dielectric, and piezoelectric constants of uniaxially oriented poled pvdf films. *IEEE Transactions on Ultrasonics, Ferroelectrics, and Frequency Control*, 49(6):836–847, June 2002.
- [105] Birlikseven C, Altinta E, and Durusoy H Z. A low-temperature pyroelectric study of pvdf thick films. *Journal of Material Science in Electronics*, 12:601–603, 2001.

- [106] Dargahi J. Piezoelectric and pyroelectric transient signal analysis for detection of the temperature of a contact object for robotic tactile sensing. *Sensors and Actuators A*, 71:89–97, 1998.
- [107] Guy I L and Zheng Z. Piezoelectricity and electrostriction in ferroelectric polymers. *Ferroelectrics*, 264(1-4):1691–1696, 2001.
- [108] Zhenj Z, Guy I L, and Trevor L T. Piezoelectric coefficient of thin polymer films measured by interferometry. *Journal of Intelligent Material Systems and Structures*, 9:69–73, 1998.
- [109] Royer D and Kmetik V. measurment of piezoelectric constants using an optical heterodyne interfrometer. *Electronics letters*, 28(19):1828–1830, 1992.
- [110] Klaase P T A and Van Turnhout J. Dielectric, pieso- and pyroelectric properties of the three crystalline forms of pvdf. *Third International Conf. On Dielectric Materials, Measurments and Applications, IEE Conf Publication*, (177):411–414, 10-13 Sep. 1979.
- [111] Kepler R G and Anderson R A. Piezoelectricity and pyroelectricity in polyvinylidene fluoride. *J. Appl. Phys.*, 49(8):4490–4494, Aug. 1978.
- [112] Goodfellow. 237 lancaster avenue, suite 252, devon pa, 19333-1594, usa,. page www.goodfellow.com.
- [113] Airmar Technology Corporation. New hampshire 03055-4613, usa,. page <http://www.airmar.com>.
- [114] Ueberschlag P. Pvdv piezoelectric polymer. *Sensor Review*, 21(2):118–125, 2001.
- [115] Simo JC and Laursen TA. An augmented lagrangian treatment of contact contact problems involving friction. *Computers and Structures*, 42(1):97–116, 1992.
- [116] Ansys Inc. Theory reference. *Ansys Release 9.0.002114*.

- [117] Yen P L. Palpation sensitivity analysis of exploring hard objects under soft tissue. *Proceedings of the 2003 IEEE/ASME International Conference on Advanced Intelligent Mechatronics, AIM 2003*, pages 1102–1106, 2003.
- [118] Jungnickel BJ. *Polymeric Materials Ebcyclopedia*, volume 8- 7115. CRC Press, 1996.
- [119] Dargahi J, Sokhanvar S, and Packirisamy M. Theoretical and experimental techniques in using polyvinylidene fluoride (pvdf) films as a transducer in sensor systems. *Trans. of the Canadian Society of Mech. Eng.*, 28(2B):291–307, 2004.
- [120] Wang T T and Herbert J M. The applications of ferroelectric polymers (london: Blackie. *Journal of Intelligent Material Systems and Structures*, pages 69–70, 1988.
- [121] The Institute of Electrical and Electronic Engineers Inc. Ieee standards on piezoelectricity, ansi/ieee std. 176-1987.
- [122] James ML, Smith GM, and Wolford JC. *Vibration of mechanical and structural systems, with microcomputer applications*. Harper and Row, Publication Inc., 1989.
- [123] Newland DE. *Mechanical vibration analysis and computation*. Longman Scientific and Technical., 1989.
- [124] Sokhanvar S, Packirisamy M., and Dargahi J. A multifunctional pvdf based tactile sensor for minimally invasive surgery. *J. of Smart Mat. and Structures*, 16:989–998, 2007. Considered for IoP Select, a special collection of superior articles, <http://Select.iop.org>.
- [125] Sokhanvar S, Packirisamy M, and Dargahi J. Tactile sensor acts as a human finger in minimally invasive surgery. *PhysOrg.com*, 2007. Published: 09:39 EST, June 27.
- [126] Instron Industrial Products. 900 liberty street grove city, pa 16127.
- [127] Holzapfel GA. *Nonlinear Solid Mechanics: A continuum approach for engineering*. John Wiley & Sons Ltd., 2000.

- [128] Williams J G. *Stress Analysis of Polymers*. Longman, London, 1973.
- [129] Miller k. Constitutive modeling of abdominal organs. *J Biomechanics*, 33:367–373, 2000.
- [130] Ansys Inc. Documentation for ansys, modeling material nonlinearities/ mixed u-p formulation. *Ansys, Release 10*.
- [131] Sussman T and Bathe K J. A finite element formulation of nonlinear incompressible elastic and inelastic analysis. *Computers & Structures*, 26(1/2):357–409, 1987.
- [132] Bonet J and Wood R D. *Nonlinear Continuum Mechanics for Finite Element Analysis*. Cambridge University Press, 1997.
- [133] Crisfield M A. *Non-linear Finite Element Analysis of Solids and Structures*, volume 2-Advanced Topics. John Wiley & Sons, 1997.
- [134] Bathe K J. *Finite Element Procedures*. Printice-Hall, 1996.
- [135] McMeeking R M and Rice J R. Finite element formulations for problems of large elastic-plastic deformations. *Int. J. of Solids and Structures*, 121:601–616, 1975.
- [136] Rivlin RS. *Large Elastic Deformations, Rheology : Theory and applications*. Academic press, New York, 1956.
- [137] Hosseini M, Najarian S, Motaghinasab S, and Dargahi J. Detection of tumours using a computational tactile sensing approach. *Int. J. Med Robotics Assist Surg*, 2:333–340, 2006.
- [138] Wellman PS and Howe RD. Extracting features from tactile maps. *Proceedings of the Second International Conference on Medical Image Computing and Computer-Assisted Intervention*, pages 1133–1142, 1999.
- [139] Yu W, Li Y, Zheng Y P, Lim N Y, Lu M H, and Fan J. Softness measurements for open-cell foam materials and human soft tissue. *Meas. Sci. Technol*, 17:1785–1791, 2006.

- [140] Dargahi J and Najarian S. Advances in tactile sensors design/manufacturing and its impact on robotics applications- a review. *Industrial Robot: An International Journal*, 32(3):268–281, 2005.
- [141] Eklund A, Bergh A, and Lindahl OA. A catheter tactile sensor for measuring hardness of soft tissue: measurement in a silicone model and in an in vitro human prostate model. *Medical and Biological Engineering and Computing*, 37:618–624, 1999.
- [142] Hannaford B, Trujillo J, Sinanan M, Moreyra M, Rosen J, Brown J, Leuschke R, and MacFarlane M. *Computerized endoscopic surgical grasper, in Studies in Health Technology Informatics - Medicine Meets Virtual Reality*. ISO Press, Amsterdam, 1998.
- [143] Wolfenbittel R F and Regtien P P L. Polysilicon bridges for the realization of tactile sensors. *Sens. and Actuators A: Phys*, 26(1-3):257–264, 1991.
- [144] Kane B J, Cutkosky M R, and Kovacs G T A. Cmos-compatible traction stress sensor for use in high-resolution tactile imaging. *Sensors and Actuators A: Physical*, 54(1-3):511–516, 1996.
- [145] Gray B L and Fearing R S. A surface micromachined microtactile sensor array. *Proceedings of the IEEE International Conference on Robotics and Automation*, 22-28 April 1996. Minneapolis, MN, USA.
- [146] Beebe D J, Hsieh A S, Radwin R G, and Denton D D. A silicon force sensor for robotics and medicine. *Sensor and Actuators A: Phys.*, 50(1-2):55–65, 1995.
- [147] Wang L and Beebe D J. A silicon-based shear force sensor: development and characterization. *Sens. Actuators A: Phys.*, 84(1-2):33–44, 2000.
- [148] Omata S, Murayama Y, and Constantinou CE. Real time robotic tactile sensor system for the determination of the physical properties of biomaterials. *Sensors and Actuators A: Physical*, 112:278–285, 2004.

- [149] Wang Y, Nguyen C, Srikanbana Gengt R, and Freedmantt M T. Tactile mapping of palpable abnormalities for breast cancer diagnosis. *Proceedings of the 1999 IEEE International Conference on Robotics & Automation*, May 1999. Detroit, Michigan.
- [150] Yan J, Scott PK, and Fearing RS. Inclusion probing: Signal detection and haptic playback of 2d fem and experimental data. *1999 ASME International Mechanical Engineering Congress and Exposition*, November 14-19, 1999.
- [151] Shimizu H, Kiyono S, Gao W, and Shioji H. A biological sensor for detecting foreign bodies using a balloon-probe. *Key Engineering Materials Vols.*, 295-296:133–138, October 2005.
- [152] Najarian S, Dargahi J, and Zheng XZ. A novel method in measuring the stiffness of sensed objects with applications for biomedical robotic systems. *Key Engineering Materials*, 295-296:133–138, October 2005.
- [153] Lau CKL, Wagner CR, and Howe RD. Algorithms for tactile rendering in compliant environments. *2004 Haptics Symposium*, pages 32–39, 2004.
- [154] Wellman PS, Dalton EP, Krag D, Kern K, and Howe R. Tactile imaging of breast masses. *Arch. Surg.*, 136:204–208, Feb 2001.
- [155] Galea A M and Howe R D. Liver vessel parameter estimation from tactile imaging information. *Proceedings of Medical Simulation: International Symposium-ISMS 2004*, June 17-18 2004. Cambridge, MA.
- [156] Geiger SR. Handbook of physiology section 1: The nervous system. *American Physiological Society*, 29, 1984.
- [157] Sokhanvar S, Dargahi J, and Packirisamy M. Nonlinear modeling and testing of soft tissue embedded lump for mis applications. *Submitted to the Int. J. of Medical Robotics and Computer Assisted Surgery.*, 2007.

- [158] National Instruments DAQ SCB-68, 68-Pin Shielded Connector Block User Manual. December 2002 Ed.
- [159] He J H, Sun S, Ye J, and Lim T M. Self -assembly carbon nanotubes on cantilever biosensor for sensitivity enhancement. *Journal of Physics:Conference Series*, 34:423–428, 2006.
- [160] Falanga V and Bucalo B. Use of a durometer to assess skin hardness. *Journal of the American Academy of Dermatology*, 29(1):47–51, July 1993.
- [161] Ladeji-Osias JO and Langrana NA. Analytical evaluation of tumors surrounded by soft tissue. *Engineering in Medicine and Biology Society, 2000. Proceedings of the 22nd Annual International Conference of the IEEE*, 3:2114–2117, 2000. Chicago, IL, USA.
- [162] QI HJ, Joyce K, and Boyce MC. Durometer hardness and the stress-strain behavior of elastomeric materials. *Rubber Chemistry and Technology*, 76(2):419–435, May/Jun 2003.
- [163] Sokhanvar S, Ramezanifard M R, Packirisamy M, and Dargahi J. Computer aided minimally invasive surgery: A reality-based soft tissue modeling approach. *Int. J. Computer Applications in Technology*, 2007. Accepted for publication.
- [164] Dargahi J Sokhanvar S, Ramezanifard M R and Packirisamy M. Graphical rendering of localized lumps for mis applications. *J of Medical Devices, ASME, Accepted*, 2007.
- [165] Dargahi J Sokhanvar S and Packirisamy M. Influence of friction on piezoelectric sensors. *J. of Sensors and Actuators, A: Physical, Accepted*, doi:10.1016/j.sna.2007.07.035, 2007.
- [166] Roh Y and Varadan V V. Characterization of all the elastic, dielectric and piezoelectric constants of uniaxially oriented poled pvdF films,. *IEEE Trans Ultrason Ferroelectr Freq Control*, 49(6):836–47, 2002.

- [167] Cuhat D R. Multi-point measurement using pvdf piezoelectric film with application to direct sensing of modes in structures. *PhD Thesis, Purdue University*, 1999.
- [168] Taber L A. *Nonlinear Theory of Elasticity: Applications in Biomechanics*. World Scientific, 2004.
- [169] Ogden R W. *Nonlinear Elastic Deformations*. Dover, New York, 1997.
- [170] Beatty M F. Topics in finite elasticity: Hyperelasticity of rubber, elastomers, and biological tissues-with examples. *Applied Mechanics Review*, 40(12):1699–1734, Dec. 1987.
- [171] Gurtin ME. *An Introduction to Continuum Mechanics*. Academic Press, New York, 1981.
- [172] Gadala M S and Wang J. Simulation of metal forming processes with finite element methods. *Int. J. for Numerical Methods in Eng.*, 44:1397–1428, 1999.
- [173] Cisloiu R. *A stablized mixed finite element formulation for finite strain deformation*. Phd dissertaion, University of Pittsburgh, 2006.
- [174] EerNisse EP. Variational method for electroelastic vibration analysis. *IEEE Trans. Sonics Ultrasonics*, SU-14:153–160, 1967.
- [175] Holland R and EerNisse EP. Variational evaluation of admittances of multielectroded three-dimensionsl piezoelectric structures. *IEEE Trans. Sonics Ultrasonics*, SU-15:119–132, 1968.
- [176] Holland R. Resonant properties of piezoelectric ceramic rectangular parallelepipeds. *J. Acoust. Soc. Am.*, 43:988–997, 1968.
- [177] Allik H and Hughes J R. Finite element method for piezoelectric vibration. *Int. J. for Numerical Methods in Engineering*, 2:151–157, 1970.

Appendix A

Piezoelectric governing equations

The constitutive equations of PVDF is taken from the constitutive equations governing the crystals in general. Therefore, first the constitutive equations of crystals are discussed and then the equations are tailored for the PVDF and also for the sensing applications which is the concern of this study.

Constitutive Equations of the Crystals

The constitutive equations for a crystal encompass the mechanical, electrical and thermal properties of a crystal. The relations between these properties are illustrated by the diagram in Figures A.1 and A.2 [89]. In the three outer corners, stress σ_{ij} , electric field E_i , and temperature T are normally chosen as independent variables and all may be thought of as "forces" applied to the crystal. Alternatively, in the three corresponding inner corners, appear entropy per unit volume S , electric displacement D_i and strain ϵ_{ij} , which are the direct results of theses "forces" can be considered as dependent variables. The relations between these pairs of corners (shown by thick lines) are sometimes called *principal effects*:

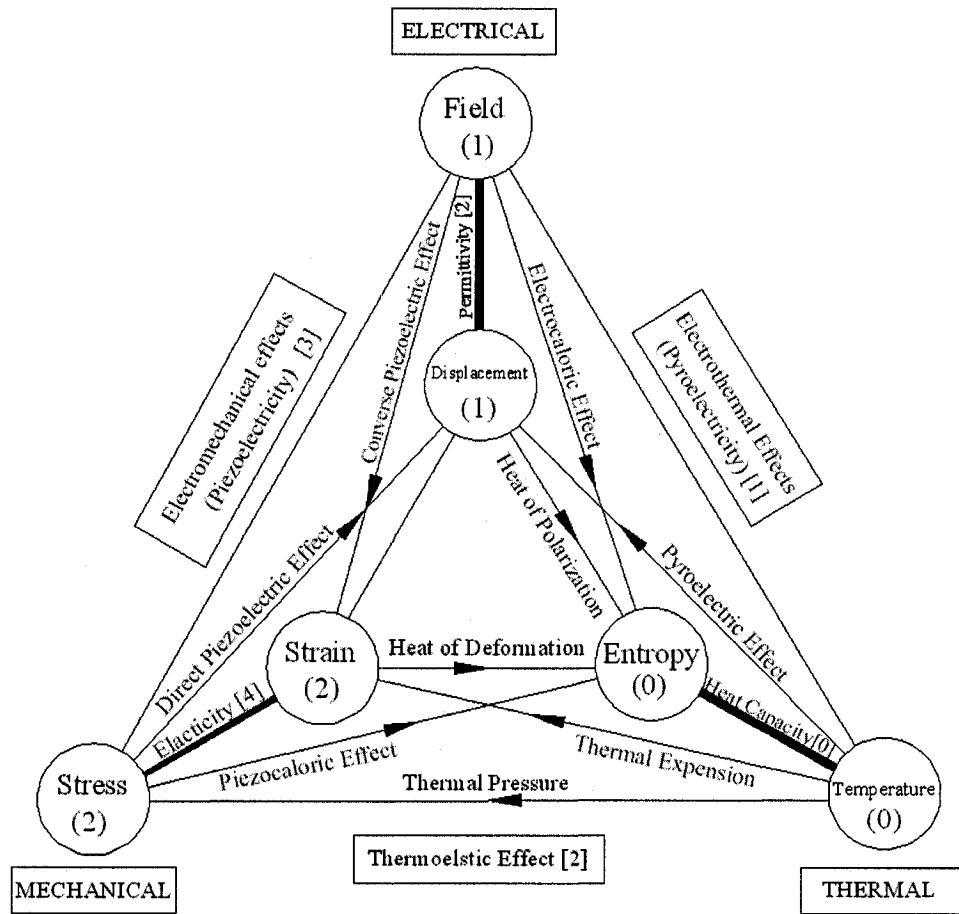


Figure A.1: The relations between mechanical, electrical and thermal properties of a crystal. The names of the effects are shown. The tensor rank of each variable is shown in round brackets and the rank of the properties in square brackets [89].

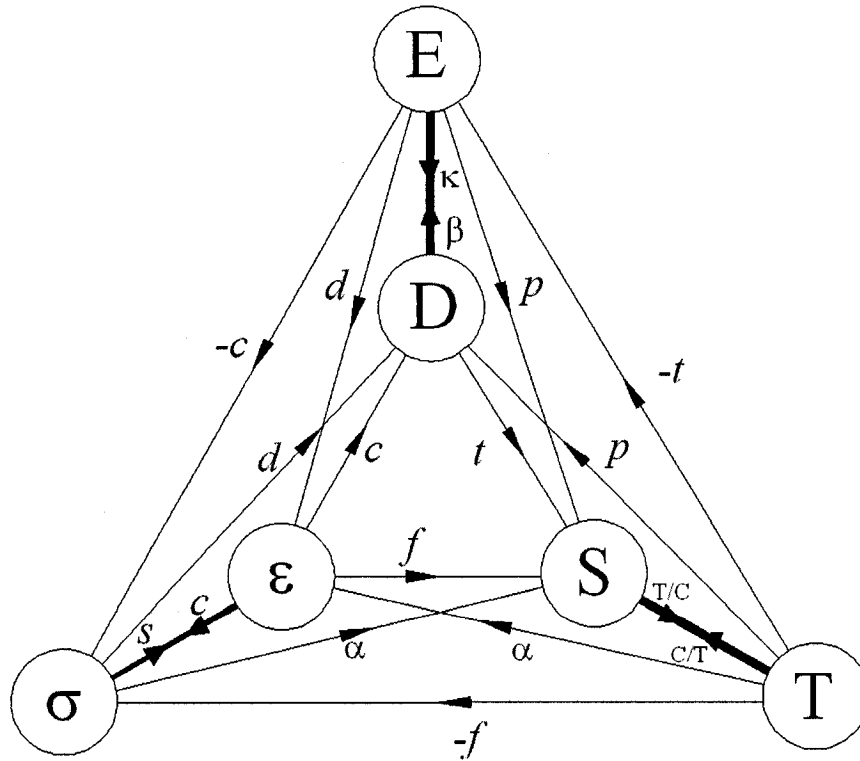


Figure A.2: The relations between mechanical, electrical and thermal properties of a crystal. The symbols corresponding to each variable and properties are illustrated [89].

1. An increase of temperature produces a change of entropy thus considering a unit volume:

$$dS = (C/T)dT \quad (\text{A-1})$$

where C (a scalar) is the heat capacity per unit volume, and T is the absolute temperature.

2. A small change of Electric field dE_i produces a change of electric displacement dD_i according to the equation:

$$dD_i = \kappa_{ij} dE_j \quad (\text{A-2})$$

where κ_{ij} is the permittivity tensor.

3. A small change of stress $d\sigma_{kl}$ produces a change of strain $d\epsilon_{ij}$ according to the equation:

$$d\epsilon_{ij} = s_{ijkl} d\sigma_{kl} \quad (\text{A-3})$$

where s_{ijkl} are the elastic compliances.

Figures A.1 and A.2 also illustrate the relations that are called *coupled effects*. These are denoted by the lines joining pairs of points which are not both at the same corner. Consider for instance, the two diagonal lines at the bottom of the diagram. One shows *thermal expansion*, the strain produced by a change of temperature, while the other shows the *piezocaloric effect*, that is, the entropy (heat) produced by a stress. These coupled effects connect scalars with second-rank tensors, and are therefore themselves to be specified by second-rank tensors. For instance, for thermal expansion, the relation is:

$$d\epsilon_{ij} = \alpha_{ij} dT \quad (\text{A-4})$$

The piezoelectric coupled effects are shown on the left of the diagram. The direct piezoelectric effect is given in differential form by:

$$dP_i = d_{ijk} d\sigma_{jk} \quad (\text{A-5})$$

since $D_i = \kappa_0 E_i + P_i$ then $dP_i = dD_i - \kappa_0 dE_i$. Therefore, if the electric field in the crystal is held constant, $dP_i = dD_i$ and we may write A-5 as:

$$dD_i = d_{ijk} d\sigma_{jk} \quad (E \text{ constant}) \quad (\text{A-6})$$

The converse piezoelectric effect is the relation between electric field and strain (see Figures A.1 and A.2). Since these coupled fields relate a first-rank tensor (E_i or D_i) with a second-rank tensor (σ_{ij} or ϵ_{ij}), they are themselves given by third-rank tensors. The coupled effects on the right of the diagram are concerned with *pyroelectricity*. They all connect a vector (D_i or E_i) with a scalar (S or T), and therefore expressed by first-rank tensors. The equation for the pyroelectric effect may be written as:

$$dP_i = p_i dT \quad (\text{A-7})$$

where p_i are the pyroelectric coefficient of the crystal. With the assumption of constant electric field, we have:

$$dD_i = p_i dT \quad (E \text{ Constant}) \quad (\text{A-8})$$

The pyroelectricity effect sometimes is categorized into *primary* and *secondary pyroelectricity*. If during the heating a crystal, its shape and size are held fixed (Crystal clamped), it is called primary effect. On the contrary, the crystal may be released so that thermal expansion can occur quite freely. In this case an extra effect can be observed that is referred to as secondary pyroelectricity. The magnitude of the effects observed in the two experiments would be different. Indeed what is observed in the later condition is the primary effect plus the additional component of secondary effects. This phenomena is not limited to the pyroelectricity and similar discussion could equally well be given of secondary thermal expansion, or secondary piezoelectricity, if the magnitude of these effects warranted it. Normally the set of σ (stress), E (electric field) and T (temperature) are considered as independent variable, while ϵ (strain), D (electric displacement) and S (entropy) are dependent variables. However other alternatives are also possible. Therefore, the general form of linear (first-order effects) constitutive equations for a piezoelectric crystal are in

the following form:

$$\epsilon_{ij} = s_{ijkl}^{E,T} \sigma_{kl} + d_{kij}^T E_k + \alpha_{ij}^E \Delta T \quad (\text{A-9})$$

$$D_i = d_{ijk}^T \sigma_{jk} + \kappa_{ij}^{\sigma,T} E_j + p_i^\sigma \Delta T \quad (\text{A-10})$$

$$\Delta S = \alpha_{ij}^E \sigma_{ij} + p_i^\sigma E_i + (C^{\sigma,E}/T) \Delta T \quad (\text{A-11})$$

where :

ϵ_{ij} : Second rank strain tensor

s_{ijkl} : Forth rank elastic compliance tensor

σ_{ij} : Second rank stress tensor

d_{ijk} : Third rank piezoelectric coefficient tensor (direct and converse effects)

E_k : First rank electric field tensor

α : Second rank thermal coefficients tensor

(thermal expansion and piezocaloric effects)

ΔT : Zero rank temperature tensor

D_i : First rank electrical displacement

κ_{ij} : Second rank permittivity tensor

p_i : First rank pyroelectric coefficients tensor

(pyroelectricity and electrocaloric effects)

(C/T) : Zero rank heat capacity tensor.

The subscript i, j, k, l take values between 1 and 3. The superscript E means that the material property, for instance the elastic compliance is measured under the constant electric field (short-circuit condition), and T means the material property, for instance the dielectric constant is measured under the constant stress. In general, there are 3^n independent components for each tensor of rank n . For instance, piezoelectric coefficient matrix (rank 3) and elastic compliance matrix (rank 4) have 27 and 81 independent components, respectively. However, since d_{ijk} are symmetric in j and k , s_{ijkl} are symmetric in i and j , k and l respectively, independent components can be reduced. For a given piezoelectric material, the number of independent parameters can be further reduced,

using symmetry relations in the material. For instance, the piezoelectric PVDF which is the focus of this section, is classified under Orthorhombic system, class $mm2$ (or C_{2v}) among 32 defined crystal classes. The number of independent variables which are required for this class is depicted in Figure A.3. To avoid unnecessary complexity of dealing with

	σ	E	ΔT	
ϵ				9
				5
				3
D				3
				1
ΔS				1
				<hr/> 22

Figure A.3: The number of independent variables for $mm2$ class. The darker circles show non-zero components.

temperature change and its effects, normally the experiments are done in a constant temperature. In this case the third terms of Equations A-9 through A-11 are zero. In many applications the changes of entropy is negligible and can be ignored. For instance, in majority of sensing and actuating problems only the first two equations are used:

$$\epsilon_{ij} = s_{ijkl}^{E,T} \sigma_{kl} + d_{kij}^T E_k \quad (A-12)$$

$$D_i = d_{ijk}^T \sigma_{jk} + \kappa_{ij}^{\sigma,T} E_j \quad (A-13)$$

For the sensing applications and in the absence of electric field these relations are even further reduced to:

$$\epsilon_{ij} = s_{ijkl}^{E,T} \sigma_{kl} \quad (A-14)$$

$$D_i = d_{ijk}^T \sigma_{jk} \quad (A-15)$$

For the *Uniaxially drawn PVDF*¹, the d_{ij} and s_{ij} and ε matrices have the following form [120]

$$[s] = \begin{bmatrix} s_{11} & s_{12} & s_{13} & 0 & 0 & 0 \\ s_{12} & s_{22} & s_{23} & 0 & 0 & 0 \\ s_{13} & s_{23} & s_{33} & 0 & 0 & 0 \\ 0 & 0 & 0 & s_{44} & 0 & 0 \\ 0 & 0 & 0 & 0 & s_{55} & 0 \\ 0 & 0 & 0 & 0 & 0 & s_{66} \end{bmatrix} \quad (\text{A-16})$$

$$[d] = \begin{bmatrix} 0 & 0 & 0 & 0 & d_{15} & 0 \\ 0 & 0 & 0 & d_{24} & 0 & 0 \\ d_{31} & d_{32} & d_{33} & 0 & 0 & 0 \end{bmatrix} \quad (\text{A-17})$$

$$[\varepsilon] = \begin{bmatrix} \varepsilon_{11} & 0 & 0 \\ 0 & \varepsilon_{22} & 0 \\ 0 & 0 & \varepsilon_{33} \end{bmatrix}$$

The integral of electrical displacement over the body surface gives the charge. For a piezoelectric film (including PVDF), the only practical surface that charge Q can be collected is the surface of the film (Thickness direction). Therefore for a PVDF film in sensing applications (electrical field is negligible), considering A-17, expansion of A-15 arrives at:

$$Q_3 = d_{31}\sigma_1 + d_{32}\sigma_2 + d_{33}\sigma_3 \quad (\text{A-18})$$

A-1 The IEEE Notations

Another popular alternative form of Equations A-9 and A-10 (when change in temperature ≈ 0) is suggested by IEEE which is also adopted by Ansys:

$$\begin{cases} T_{ij} = c_{ijkl}^E S_{kl} - e_{kij} E_k \\ D_i = e_{ikl} S_{kl} + \varepsilon_{ij}^S E_k \end{cases} \quad (\text{A-19})$$

¹For definition see Section 1.6

where

T_{ij} : stress components, (σ_{ij} is adopted in this document)

c_{ijkl} : strain components

e_{kij} : piezoelectric coefficients

E_k : electric field components

D_i : electric displacement components

ϵ_{ij} : permittivity components

Implementing a compressed matrix notation, the above equation can be expressed in a more familiar form. This matrix notation consists of replacing ij or kl by p or q , where i, j, k and l take the values 1, 2, 3 and p, q take the values 1, 2, ..., 6 according to the Table A.1 . Then c_{ijkl} , e_{ikl} and T_{ij} can be replaced by c_{pq} , e_{ip} and T_p respectively. The

Table A.1: Conversion table for replacing tensor indices with matrix indices.

ij or kl	p or q
11	1
22	2
33	3
23 or 32	4
31 or 13	5
12 or 21	6

constitutive equations A-19 can be written as:

$$\begin{cases} T_p = c_{pq}^E S_q - e_{kp} E_k \\ D_i = e_{iq} S_q + \epsilon_{ik}^S E_k \end{cases} \quad (\text{A-20})$$

where $S_{ij} = S_p$ when $i = j$, $p = 1, 2, 3$ and

$2S_{ij} = S_p$ when $i \neq j$, $p = 4, 5, 6$.

In the matrix format it can be written [130]:

$$\{T\}_{6 \times 1} = [c]_{6 \times 6} \{S\}_{6 \times 1} - [e]_{6 \times 3} \{E\}_{3 \times 1} \quad (\text{A-21})$$

$$\{D\}_{6 \times 1} = [e]_{6 \times 6}^T \{S\}_{6 \times 1} + [\epsilon]_{6 \times 3} \{E\}_{3 \times 1} \quad (\text{A-22})$$

Normally the units are: $[e] : pC/m^2$, $[c] : N/m^2$ and $[d] : pC/N^2$.

Typical set of data for the piezoelectric analysis is the set of $[e]$, $[c]$ and $[\epsilon^S]$ or the set of $[d]$, $[s]$ and $[\epsilon^T]$ where $[\epsilon^S]$ is the dielectric permittivity matrix at constant strain while $[\epsilon^T]$ is the dielectric permittivity matrix at constant stress and the following relationships can be found between them:

$$[\epsilon^S] = [\epsilon^T] - [e]^T [d] \quad (\text{A-23})$$

The orthotropic dielectric matrix $[\epsilon]$ uses the electrical permittivity and the following values for the dielectric permittivity matrix at constant stress are used in this study [166, 167]:

$$[\epsilon^T] = \begin{bmatrix} 7.35 & 0 & 0 \\ 0 & 9.27 & 0 \\ 0 & 0 & 8.05 \end{bmatrix}$$

The following values are used in this study [166, 167]:

The piezoelectric strain matrix $[d](pC/N)$

$$[d] = \begin{bmatrix} 0 & 0 & 0 & 0 & d_{15} & 0 \\ 0 & 0 & 0 & d_{24} & 0 & 0 \\ 20 & 2 & -18 & 0 & 0 & 0 \end{bmatrix}$$

²Recall from Section 1.6 that $D = d \sigma$ and $\epsilon = d^T E$ (relationship 1.1), where d is the piezoelectric coefficient, σ is the stress, D the electric displacement and E electric field. On the other hand the stress strain are related by: $\sigma = c \epsilon$ or alternatively $\epsilon = s \sigma$ where c and s are the elastic stiffness and compliance matrices, respectively. The matrix d is called *piezoelectric strain matrix* as it initially relates mechanical strain to the electric field. In addition, from $\epsilon = d^T E$ we can write $c\epsilon = cd^T E$ and then using the Hook's relation: $\sigma = c\epsilon$. Therefore, the piezoelectric matrix can also be defined in $[e]$ form (*piezoelectric stress matrix*, since it relates the electrical field with stress) where the relationship between them can be defined as: $[e] = [c][d]$

The stiffness matrix $[c](Gpa)$ are used as:

$$[c] = \begin{bmatrix} 4.7 & 2.92 & 2.14 & 0 & 0 & 0 \\ 2.43 & 4.83 & 1.99 & 0 & 0 & 0 \\ 2.20 & 2.38 & 4.60 & 0 & 0 & 0 \\ 0 & 0 & 0 & 0.106 & 0 & 0 \\ 0 & 0 & 0 & 0 & 0.104 & 0 \\ 0 & 0 & 0 & 0 & 0 & 2.66 \end{bmatrix}$$

Throughout this document, for two dimensional analysis, unless otherwise stated, the data provided by the manufacturer, Goodfellow, for the uniaxial and biaxial PVDF film (see table 2.1 in Section 2.3) were used.

Appendix B

Transverse Vibration of Beams

Transverse vibration of a prismatic beam in the x - y plane is shown in Figure B.1-a, in which symbol y represent the transverse displacement of a typical segment of the beam, located at the distance x from the left-hand end. Figure B.1-b, shows a free-body diagram of an element of length dx with internal and inertial actions upon it.

When the beam is vibration transversely, the dynamic equilibrium for forces in the y

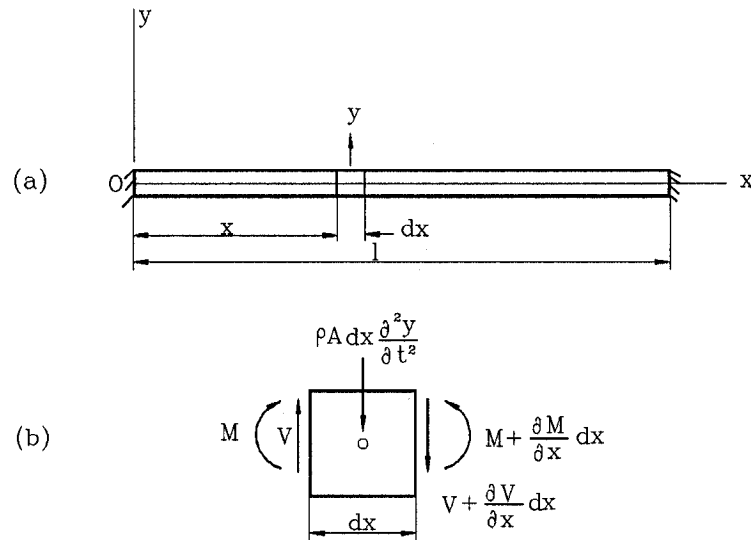


Figure B.1: Schematic of the prismatic bar and its free body diagram.

direction is:

$$V - (V + \partial V / \partial x) dx - \rho A dx \partial^2 y / \partial t^2 = 0 \quad (\text{B-1})$$

and the moment equilibrium conditions gives :

$$-Vdx + (\partial M/\partial x)dx \approx 0 \quad (\text{B-2})$$

substitution of V from Equation B-2 into Equation B-1 produces :

$$(\partial^2 M/\partial x^2)dx = -\rho A dx (\partial^2 y/\partial t^2) \quad (\text{B-3})$$

From elementary flexural theory we have :

$$M = EI(\partial^2 y/\partial x^2) \quad (\text{B-4})$$

use this expression in Equation B-3, we obtain :

$$\frac{\partial^2}{\partial x^2}(EI \frac{\partial^2 y}{\partial x^2})dx = -\rho A dx (\frac{\partial^2 y}{\partial t^2}) \quad (\text{B-5})$$

In the particular case of a prismatic beam the flexural rigidity EI does not vary with x , and we have :

$$EI(\partial^4 y/\partial x^4)dx = -\rho A dx (\partial^2 y/\partial t^2) \quad (\text{B-6})$$

or

$$\partial^4 y/\partial x^4 = -1/a^2 (\partial^2 y/\partial t^2) \quad (\text{B-7})$$

where $a = \sqrt{EI/\rho A}$ when a beam vibrates transversely in one of its natural modes, the deflection at any location varies harmonically with time, as follows:

$$y = X(A \cos \omega t + B \sin \omega t) \quad (\text{B-8})$$

where subscript i for the i^{th} mode has been omitted.

Substitution of Equation B-8 into Equation B-7 results in

$$d^4 X/dx^4 - (\omega^2/a^2)X = 0 \quad (\text{B-9})$$

This equation is the equation of the motion for transverse free vibration of a prismatic beam. For the case of forced vibration the force $Q(x, t)$ will appear in the right side of equation. By introducing the symbol $\omega^2/a^2 = K^4$ Equation B-9 can be written as:

$$d^4 X/dx^4 - K^4 X = 0 \quad (\text{B-10})$$

To satisfy Equation B-10, we let $X = e^{nx}$ and obtain : $e^{nx}(n^4 - K^4) = 0$. The roots of the later equation are found to be: $n_1 = K, n_2 = -K, n_3 = jK, n_4 = -jK$. The general form of the solution for Equation B-10 becomes: $X = Ce^{Kx} + De^{-Kx} + Ee^{jKx} + Fe^{-jKx}$ or in the equivalent form:

$$X = C_1 \sin Kx + C_2 \cos Kx + C_3 \sinh Kx + C_4 \cosh Kx \quad (\text{B-11})$$

or in the following equivalent:

$$X = C_1(\cos Kx + \cosh Kx) + C_2(\cos Kx - \cosh Kx) + C_3(\sin Kx + \sinh Kx) + C_4(\sin Kx - \sinh Kx) \quad (\text{B-12})$$

the constants C_1, C_2, C_3 and C_4 in the Equation B-11 must be determined in each particular case from the boundary conditions at the ends of the beam.

For example at a fixed end, the deflection and the slop are equal to zero, so that

$$(X)_{x=0} = 0, (dX/dx)_{x=0} = 0, (X)_{x=l} = 0, (dX/dx)_{x=l} = 0 \quad (\text{B-13})$$

From the first two boundary conditions and Equation B-12 we take $C_1 = C_3 = 0$, so that $X = C_2(\cos Kx - \cosh Kx) + C_4(\sin Kx - \sinh Kx)$ and from the other two boundary conditions:

$$C_2(\cos Kl - \cosh Kl) + C_4(\sin Kl - \sinh Kl) = 0 \quad (\text{B-14})$$

$$C_2(\sin Kl + \sinh Kl) + C_4(-\cos Kl + \cosh Kl) = 0 \quad (\text{B-15})$$

from which the following frequency equation can be deduced.

$$\cos Kl \cosh Kl = 1 \quad (\text{B-16})$$

A few of the lowest consecutive roots of this equation are:

K_0l	K_1l	K_2l	K_3l	K_4l
0	4.730	7.853	10.996	14.137

The normal modes can be superimposed to produce the total response as :

$$y = \sum_{i=1}^{\infty} X_i(A_i \cos \omega_i t + B_i \sin \omega_i t) \quad (\text{B-17})$$

we shall now re-examine equation B-10 as an eigenvalue problem of the form

$$X_i'''' = \lambda_i X_i \text{ where } \lambda_i = K_i^4 = (\omega_i/a)^2$$

Orthogonality properties of the eigenfunctions will be studied by considering modes i, j as follows:

$$X_i'''' = \lambda_i X_i$$

$$X_j'''' = \lambda_j X_j$$

Multiplying the first equation by X_j and the second one with X_i and integrating the products over the length of the beam, we obtain:

$$\int_0^l X_i'''' X_j dx = \lambda_i \int_0^l X_i X_j dx \quad (\text{B-18})$$

$$\int_0^l X_j'''' X_i dx = \lambda_j \int_0^l X_i X_j dx \quad (\text{B-19})$$

Integration of the left hand side of these equations by parts yields:

$$[X_i''' X_j]_0^l - [X_i'' X_j']_0^l + \int_0^l X_i'' X_j'' dx = \lambda_i \int_0^l X_i X_j dx \quad (\text{B-20})$$

$$[X_j''' X_i]_0^l - [X_j'' X_i']_0^l + \int_0^l X_i'' X_j'' dx = \lambda_j \int_0^l X_i X_j dx \quad (\text{B-21})$$

The end conditions B-13 require that the integrand terms in the above equations vanish.

Therefore, subtraction of Equation B-21 from B-20 produces:

$$(\lambda_i - \lambda_j) \int_0^l X_i X_j dx = 0 \quad (\text{B-22})$$

This expression is zero when $i = j$. To satisfy Equation B-22 when $i \neq j$ and for distinct eigenvalues ($\lambda_i \neq \lambda_j$), we must have

$$\int_0^l X_i X_j dx = 0, \quad (i \neq j) \quad (\text{B-23})$$

Substituting this expression into equation B-20, we find

$$\int_0^l X_i'' X_j'' dx = 0, \quad (i \neq j) \quad (\text{B-24})$$

and from equation B-21 it is also seen that

$$\int_0^l X_i'''' X_j = 0, \quad (i \neq j) \quad (\text{B-25})$$

Equations B-23, B-24 and B-25 constitute the orthogonality relationships for transverse vibrations of a prismatic beam. For the case of $i = j$, the integral in Equation B-22 may be any constant α_i , as follows

$$\int_0^l X_i^2 dx = \alpha_i, \quad (i \neq j) \quad (\text{B-26})$$

When the eigenfunctions are normalized in this manner, Equations B-36 and B-20 yield

$$\int_0^l X_i'''' X_i dx = \int_0^l (X_i'')^2 dx = \lambda_i \alpha_i = K_i^4 \alpha_i = (\omega_i/a)^2 \alpha_i \quad (\text{B-27})$$

For the purpose of transferring the equation of motion B-7 to principal coordinates, we rewrite it as:

$$m\ddot{y}dx + ry'''' dx = 0 \quad (\text{B-28})$$

in which $m = \rho A$ is the mass per unit length of the beam, and $r = EI$ is the flexural rigidity. Expansion of the transverse motion in terms of time functions ϕ_i and displacement X_i gives:

$$y = \sum_i \phi_i X_i (i = 1, 2, 3, \dots, \infty) \quad (\text{B-29})$$

Substituting Equation B-29 into equation of motion B-28, we obtain:

$$\sum_{i=1}^{\infty} (m\ddot{\phi}_i X_i + r\phi_i X_i'''' dx) = 0 \quad (\text{B-30})$$

Multiplication of Equation B-30 by the normal function X_j , followed by integration over length, produces:

$$\sum_{i=1}^{\infty} (m\ddot{\phi}_i \int_0^l X_i X_j dx + r\phi_i \int_0^l X_i'''' X_j dx) = 0 \quad (\text{B-31})$$

From the orthogonality relationship given by Equations B-23 and B-25 through B-27, we see that (for $i = j$) the equation of motion in principal coordinates becomes:

$$m_{\omega_i} \ddot{\phi}_i + r_{\omega_i} \phi_i = 0, \quad (i = 1, 2, 3, \dots, \infty) \quad (\text{B-32})$$

in which $m_{\omega_i} = m \int_0^l X^2 dx = m\alpha_i$ and $r_{\omega_i} = r \int_0^l X_i'''' X_i dx = r \int_0^l (X_i'')^2 dx = m\omega_i^2 \alpha_i$. We may set the normalization constant equal to unity, so that Equations B-26 and B-27 give:

$$\int_0^l X_i^2 dx = 1, \quad \int_0^l X_i'''' X_i dx = \int_0^l (X_i'')^2 dx = K_i^4 = (\omega_i/a)^2 \quad (\text{B-33})$$

Then Equation B-32, divided by m , takes the form :

$$\ddot{\phi}_i + \omega_i^2 \phi_i = 0 \quad , (i = 1, 2, 3, \dots, \infty) \quad (\text{B-34})$$

This equation is now said to be expressed in "normal coordinates". In this way, the differential equation of motion B-6 has been transformed to normal coordinates by substituting Equation B-29 for y . In a general case the transverse response of a beam to initial conditions of displacement and velocity, using normal-mode approach can be found as follows: At $t = 0$ initial displacements are expressed as $y_0 = f_1(x)$ and that the initial velocity are given by $\dot{y}_0 = f_2(x)$, from Equation B-29 we can write

$$\sum_{i=1}^{\infty} \phi_{0i} X_i = f_1(x) \quad (\text{B-35})$$

$$\sum_{i=1}^{\infty} \dot{\phi}_{0i} X_i = f_2(x) \quad (\text{B-36})$$

Multiplying the last two equations by X_j and then integration over the length gives:

$$\sum_{i=1}^{\infty} \phi_{0i} \int_0^l X_i X_j dx = \int_0^l f_1(x) X_j dx \quad (\text{B-37})$$

$$\sum_{i=1}^{\infty} \dot{\phi}_{0i} \int_0^l X_i X_j dx = \int_0^l f_2(x) X_j dx \quad (\text{B-38})$$

From orthogonality and normalization relationships (for $i = j$) we obtain:

$$\phi_{0i} = \int_0^l f_1(x) X_i dx \quad (\text{B-39})$$

$$\dot{\phi}_{0i} = \int_0^l f_2(x) X_i dx \quad (\text{B-40})$$

Therefore, the free-vibration responses of the normal modes are:

$$\phi_i = \phi_{0i} \cos \omega_i t + (\dot{\phi}_{0i}/\omega_i) \sin \omega_i t, \quad (i = 1, 2, 3, \dots, \infty) \quad (\text{B-41})$$

Substitution of this expression into Equation B-29 produces the combined response of all modes as:

$$y = \sum_{i=1}^{\infty} X_i \left(\phi_{0i} \cos \omega_i t + (\dot{\phi}_{0i}/\omega_i) \sin \omega_i t \right) \quad (\text{B-42})$$

B-1 Distributed load

To calculate the *forced* transverse response of prismatic beam, we assume the beam is subjected to a distributed force per unit length, $Q(x, t)$. In this case the differential equation of motion for a typical element of the beam becomes:

$$m\ddot{y}dx - ry''''dx = Q(x, t)dx \quad (\text{B-43})$$

by dividing both sides of this equation by $m = \rho A$ (the mass per unit length), we obtain:

$$\ddot{y}dx - a^2y''''dx = q(x, t) \quad (\text{B-44})$$

where $a^2 = r/m$ and $q(x, t) = Q(x, t)/m$. Equation B-44 will be transformed to normal coordinate by substituting Expression B-29 for y , multiplying by X_j , and integration over the length as follows:

$$\sum_{i=1}^{\infty} \left(\ddot{\phi}_i \int_0^l X_i X_j dx - a^2 \phi_i \int_0^l X_i'''' X_j dx \right) = \int_0^l X_j q(x, t) dx \quad (\text{B-45})$$

Using the condition of orthogonality and normalization (for $i = j$) we obtain

$$\ddot{\phi}_i + \omega_i^2 \phi_i = \int_0^l X_i q(x, t) dx, \quad (i = 1, 2, 3, \dots, \infty) \quad (\text{B-46})$$

The integral on the right side is the i^{th} normal mode load. The response of the i^{th} vibrational mode is found by the Duhamel integral to be:

$$\phi_i = (1/\omega_i) \int_0^l X_i \int_0^t q(x, \acute{t}) \sin \omega_i(t - \acute{t}) d\acute{t} dx \quad (\text{B-47})$$

Substitution of this time function into Equation B-29 gives the total vibrational response as:

$$y = \sum_{i=1}^{\infty} (X_i/\omega_i) \int_0^l X_i \int_0^t q(x, \acute{t}) \sin \omega_i(t - \acute{t}) d\acute{t} dx \quad (\text{B-48})$$

If the loading $Q(x, t)$ can be expressed as the product $Q(x, t) = f(x)Q(t)$ the Equation B-48 may be written in the simpler form :

$$y = \sum_{i=1}^{\infty} (X_i/\omega_i) \int_0^l f(x) X_i dx \int_0^t q(\acute{t}) \sin \omega_i(t - \acute{t}) d\acute{t} \quad (\text{B-49})$$

B-2 Concentrated Force

If a load $P_1(t)$ is concentrated at point x_1 , no integral over length is required, so that the response will be:

$$y = \sum_{i=1}^{\infty} (X_i X_{i1} / \omega_i) \int_0^t q_1(\hat{t}) \sin \omega_i(t - \hat{t}) d\hat{t} \quad (\text{B-50})$$

in which the symbol X_{i1} represents the normal function X_i evaluated at point x_1 and $q_1(t) = P_1(t)/m$. For a pulsating force $P_1(t) = P \sin \omega t$, applied at the distance $x = x_1$ from the left end we have:

$$y = (2P/ml) \sum_{i=1}^{\infty} (X_i X_{i1} / \omega_i) \int_0^t \sin \omega \hat{t} \sin \omega_i(t - \hat{t}) d\hat{t} \quad (\text{B-51})$$

or

$$y = \frac{2P}{ml} \sum_{i=1}^{\infty} \frac{X_i X_{i1}}{\omega_i^2} \left(\sin \omega t - \frac{\omega}{\omega_i} \sin \omega_i t \right) \beta_i \quad (\text{B-52})$$

where $\beta_i = \frac{1}{(1 - \frac{\omega^2}{\omega_i^2})}$ is the magnification factor.

Appendix C

Large Deformation Mechanics

This appendix provides an overview of concepts and equations used in large deformation mechanics. The Lagrangian (or material) description in which each particle is permanently labelled with its original Coordinates, is chosen for the listed equations. Additional information can be sought in [127, 168, 169, 170, 133, 171].

C-1 Measures of deformation in 1-D

Different measures of deformation are defined for both linear and nonlinear mechanics. As

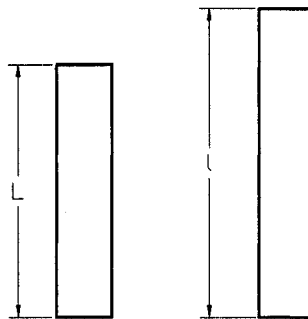


Figure C.1: The undeformed and deformed length of a bar.

shown in Figure C.1, if L is the original (undeformed) length of a bar and l is the current

(deformed) length, the deformation of the bar can be described by the *stretch ratio*, λ , as

$$\lambda = \frac{l}{L} \quad (\text{C-1})$$

In an undeformed state ($l=L$), the stretch ratio, $\lambda = 1$. A number of strain measures has been defined in terms of stretch ratio, λ in general form: $\epsilon = f(\lambda)$. For instance, for very small length changes (linear region), the definition $\epsilon = \frac{\Delta L}{L}$ where $\Delta L = l - L$ is commonly used. For large deformations, however, some other measures have been found useful, such as:

$$\epsilon^{ln} = \int_L^l \frac{dl}{l} = \ln \lambda, \quad \text{true(Logarithmic)strain} \quad (\text{C-2})$$

$$\epsilon^g = 1/2(\lambda^2 - 1), \quad \text{Green's strain} \quad (\text{C-3})$$

C-2 Kinematics: Continuum Mechanics Approach

A body in which both *mass* and *volume* are continuous functions of continuum particles is called *continuum body* which determined by macroscopic quantities.

C-2.1 Configuration

An *initial configuration* of a body \mathfrak{B} at some time $t = t_0$, is often the natural choice of the *reference configuration*, occupying the region Ω_0 . The *current configuration* of the body, occupying the region Ω , is the configuration of \mathfrak{B} at time t . When \mathfrak{B} is in its reference configuration, let the position vector of a material point $P \in \mathfrak{B}$ relative to some prescribed origin O be denoted by $\mathbf{X}(P)$ which is referred as the *reference position* of P . Then, the region Ω_0 occupied by \mathfrak{B} when it is in its reference configuration can be considered as a set of reference positions:

$$\Omega_0 = \{\mathbf{X}(P), P \in \mathfrak{B}\}$$

Alternatively the position vector of a material point $P \in \mathfrak{B}$, when \mathfrak{B} is in its current configuration at time t , relative to the same origin O is denoted by $\mathbf{x}(P, t)$ and referred

to as the *current position* of P (See Figure 3.1). The region Ω occupied by \mathfrak{B} at time t can be thought as a set of current positions:

$$\Omega = \{\mathbf{x}(P, t), P \in \mathfrak{B}\}$$

The reference Cartesian coordinates of a material point will be denoted by (X_1, X_2, X_3) and the current Cartesian coordinates will be denoted by (x_1, x_2, x_3) , so that $\mathbf{X} = X_A \hat{\mathbf{e}}_A$ and $\mathbf{x} = x_a \hat{\mathbf{e}}_a$. For every reference position \mathbf{X} corresponding to a material point in the reference configuration Ω_0 , $\mathbf{x} = \mathcal{X}(\mathbf{X}, t)$, $x_a = \mathcal{X}_a(X_1, X_2, X_3, t)$, where vector operator $\mathcal{X}(\cdot, t) : \Omega_0 \longrightarrow \Omega$. This mapping is invertible and there is a vector operator $\mathcal{X}^{-1}(\cdot, t) : \Omega \longrightarrow \Omega_0$. Thus for every current position \mathbf{x} corresponding to a material point in the current configuration Ω ,

$$X = \mathcal{X}^{-1}(\mathbf{x}, t), \quad X_A = \mathcal{X}_A^{-1}(x_1, x_2, x_3, t)$$

These mappings define the *motion* of the body which can be a combination of *rigid-body motion* and a *deformation*.

C-2.2 Material and Spatial Descriptions

If tensor $\mathbf{T}(P, t)$ represents some physical quantity associated with the material point P of a body at time t , it can be given either in terms of the material points' positions in the reference configuration $\mathbf{X}(P)$, which is called the *material description* of the tensor field \mathbf{T} and is shown by $\mathbf{T} = \Psi(\mathbf{X}, t) = \tilde{\Psi}(X_1, X_2, X_3, t)$ or in terms of the material points' positions in the current configuration $\mathbf{x}(P, t)$ which is called the *spatial description* of the tensor field \mathbf{T} and is defined by $\mathbf{T} = \psi(\mathbf{x}, t) = \tilde{\psi}(x_1, x_2, x_3, t)$. The first definition is often referred to as Lagrangian description while the latter one is referred to as Eulerian description and related to each other by $\Psi(\mathbf{X}, t) = \psi[\mathcal{X}(\mathbf{X}, t), t]$. The value of the tensor quantity \mathbf{T} is the same at any given material point, regardless of whether a material or spatial description is used for the position of that material point.

C-2.3 Displacement

The vector field $\mathbf{U}(\mathbf{X}, t) = \mathbf{x}(\mathbf{X}, t) - \mathbf{X}$ is a function of the referential position \mathbf{X} and time t , and characterizes the *material description* of the displacement field. According to the

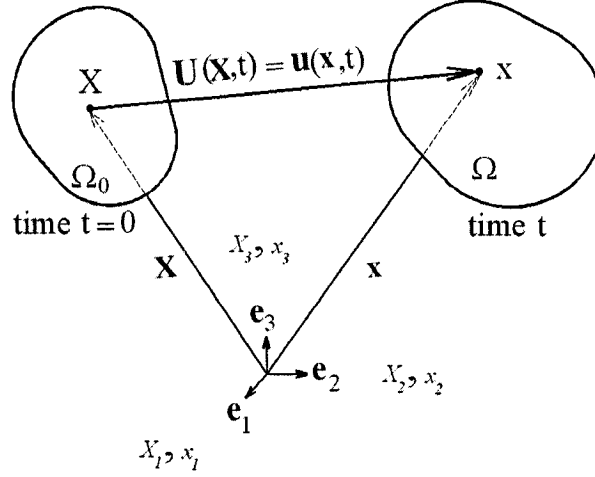


Figure C.2: Displacement field of a typical particle.

Figure C.2, the relationship between material and spatial descriptions are:

$$\mathbf{U}(\mathbf{X}, t) = \mathbf{U}[\mathcal{X}^{-1}(\mathbf{x}, t), t] = \mathbf{u}(\mathbf{x}, t) \quad (\text{C-4})$$

For a *rigid-body motion* any particle moves an identical distance, with the same magnitude and same direction at time t . Therefore, the displacement field is independent of \mathbf{X} , however, though it can be a function of time t .

C-2.4 Deformation Gradient Tensor and Jacobian of the motion

The second order tensor \mathbf{F} is called the *deformation gradient tensor* and is given by $\mathbf{F}(\mathbf{X}, t) \equiv \text{Grad } \mathbf{x}$, $F_{aA} \equiv \frac{\partial x_a}{\partial X_A}$ (such that $d\mathbf{x} = \mathbf{F} \cdot d\mathbf{X}$), where X_A is the reference Cartesian coordinates. It can be shown that the deformation gradient tensor $\mathbf{F} = F_{aA} \hat{\mathbf{e}}_a \hat{\mathbf{e}}_A$ is related to both the reference and current configurations, as indicated by the combination of the lowercase and uppercase indices. Tensors of this kind are known as *two-point tensors*. The deformation gradient tensor \mathbf{F} , contains both rigid body rotation and distortion

(stretching). \mathbf{F} is generally not symmetric and cannot be diagonalized. The *Jacobian of the motion* is defined as $J(\mathcal{X}, t) \equiv \det \mathbf{F}(\mathbf{X}, t)$. The necessary and sufficient conditions for an isomorphic motion are that J exists and $J \neq 0$ at every material point in the body.

C-2.5 Polar Decomposition Theorem

The deformation gradient tensor can be uniquely decomposed as either $\mathbf{F} = \mathbf{R} \cdot \mathbf{U}$, stretching followed by rigid body rotation, or $\mathbf{F} = \mathbf{V} \cdot \mathbf{R}$, rigid body rotation followed by stretching, where \mathbf{R} is an orthogonal two-point tensor and \mathbf{U} and \mathbf{V} are symmetric, positive definite tensors. The *right Cauchy stretch tensor* \mathbf{U} is given by $\mathbf{U} \equiv (\mathbf{F}^T \cdot \mathbf{F})^{1/2}$. The *left Cauchy stretch tensor* \mathbf{V} is given by $\mathbf{V} \equiv (\mathbf{F} \cdot \mathbf{F}^T)^{1/2}$. Finally the *rotation tensor* \mathbf{R} is given by $\mathbf{R} = \mathbf{F} \cdot \mathbf{U}^{-1} = \mathbf{V}^{-1} \cdot \mathbf{F}$.

The matrices \mathbf{U} and \mathbf{V} each completely characterize the deformation of the body and \mathbf{R} characterizes a separate rigid-body motion.

C-3 Strain Tensor: Referential formulation

The deformation of a body, independent of both translation and rotation can be described by several second order tensors. The *right Cauchy-Green deformation tensor* \mathbf{C} is defined as $\mathbf{C} \equiv \mathbf{F}^T \cdot \mathbf{F} = \mathbf{U}^2 = \mathbf{C}^T$. The right Cauchy-Green tensor \mathbf{C} (also referred to as the *Green deformation tensor*) is an important strain measure in material coordinates.

For every material point that experiences a rigid-body motion, the right Cauchy-Green deformation tensor $\mathbf{C} = \mathbf{U} = \mathbf{I}$ and $\mathbf{F} = \mathbf{R}$. The *Green-Lagrange strain tensor*, is defined as $\mathbf{E} \equiv \frac{1}{2}(\mathbf{C} - \mathbf{I})$, and vanishes the rigid-body motions.

C-3.1 Dilation

For a material volume \mathfrak{B} that occupies the region Ω_0 in the reference configuration and region Ω in the current configuration, the size of material volume in the reference and current configuration are $V = \int_{\Omega_0} dV$ and $v = \int_{\Omega} dv$, respectively.

The differential volumes in the reference and current configurations are $dV = d\mathbf{X}_1 \times d\mathbf{X}_2 \times d\mathbf{X}_3$, and $dv = d\mathbf{x}_1 \times d\mathbf{x}_2 \times d\mathbf{x}_3$, respectively. Recalling that $J \equiv \det \mathbf{F}$ it can be seen that, $dv = JdV$. The change in size of the material volume is

$$v - V = \int_{\Omega} (J - 1)dV \quad (\text{C-5})$$

The integrand in C-5, is known as the *dilation*, $e = J - 1$, and represents the change in volume per unit reference volume at a material point. The dilation is sometimes referred to as volume strain. The dilation is related to the right Cauchy-Green deformation tensor, Green-Lagrange strain tensor, and right Cauchy stretch tensor as follows:

$$e = \det \mathbf{U} - 1 = \sqrt{\det \mathbf{C}} - 1 = \sqrt{\det(\mathbf{I} + 2\mathbf{E})} - 1 \quad (\text{C-6})$$

The motion is *isochoric* (Volume is conserved) at a material point if and only if $e = 0$ at that material point. There is a local reduction in the volume if $-1 < e < 0$ and there is a local increase in volume if $e > 0$.

C-3.2 Strain-Displacement Relations

Recall that the displacement vector field relates the positions of material points in the reference and current configurations such that $\mathbf{x} = \mathbf{X} + \mathbf{u}$ (see Figure C.2). Therefore the deformation gradient tensor $\mathbf{F} \equiv \text{Grad} \mathbf{x}$ can be given as

$$\mathbf{F} = \mathbf{I} + \text{Grad} \mathbf{u}, \quad F_{iA} = \delta_{iA} + \frac{\partial u_i}{\partial X_A} \quad (\text{C-7})$$

The Green-Lagrange strain tensor can be thus written as

$$\mathbf{E} = \frac{1}{2}(\mathbf{F}^T \cdot \mathbf{F} - \mathbf{I}) = \frac{1}{2}[(\mathbf{I} + \text{Grad} \mathbf{u})^T \cdot (\mathbf{I} + \text{Grad} \mathbf{u}) - \mathbf{I}] \quad (\text{C-8})$$

which simplifies to :

$$\mathbf{E} = \frac{1}{2}[\text{Grad} \mathbf{u} + (\text{Grad} \mathbf{u})^T + (\text{Grad} \mathbf{u})^T \cdot (\text{Grad} \mathbf{u})], \quad E_{AB} = \frac{1}{2}\left(\frac{\partial u_A}{\partial X_B} + \frac{\partial u_B}{\partial X_A} + \frac{\partial u_C}{\partial X_A} \frac{\partial u_C}{\partial X_B}\right) \quad (\text{C-9})$$

which is expressed in terms of the material description of the displacement field.

C-4 Stress Tensor: Referential formulation

Consider a deformable continuum body \mathfrak{B} occupying an arbitrary region Ω of physical space with boundary surface $\partial\Omega$ at time t . If the body be cut by a plane which passes any given point $x \in \Omega$ with spatial coordinate x_a at time t , the resultant force acting on a surface element ds is called $d\mathbf{f}$ and the following relationship can be obtained.

$$d\mathbf{f} = \mathbf{t}ds = \mathbf{T}dS \quad (\text{C-10})$$

where, $\mathbf{t} = \mathbf{t}(\mathbf{x}, t, \mathbf{n})$ and $\mathbf{T} = \mathbf{T}(\mathbf{X}, t, \mathbf{N})$. Here, \mathbf{t} represents the *Cauchy(true) traction vector* (force measured per unit surface area defined in the current configuration), exerted on ds with outward normal \mathbf{n} . Alternatively, vector \mathbf{T} represents the *first piola-Kirchhoff (nominal) traction vector* (force measured per unit surface area defined in the reference configuration) and points in the same direction as the Cauchy traction vector \mathbf{t} .

The vectors \mathbf{t} and \mathbf{T} that act across the surface elements ds and dS with respective normals \mathbf{n} and \mathbf{N} are referred to as *surface tractions* or *contact forces* or just *loads*. Typical surface tractions are contact and friction forces.

Cauchy's Stress Theorem: There exist unique second-order tensor fields σ and \mathbf{P} so that:

$$\mathbf{t}(\mathbf{x}, t, \mathbf{n}) = \sigma(\mathbf{x}, t)\mathbf{n} \quad (\text{C-11})$$

$$\mathbf{T}(\mathbf{X}, t, \mathbf{N}) = \mathbf{P}(\mathbf{X}, t)\mathbf{N} \quad (\text{C-12})$$

where σ denotes a symmetric spatial tensor field called the *Cauchy(true) stress tensor*, while \mathbf{P} characterizes a tensor field called *first piola-Kirchhoff (nominal) stress tensor*. Relation C-11 which combines the surface traction with the stress tensor, is one of the most important axioms in continuum mechanics. Finally the relationship between the Cauchy stress tensor σ and the first Piola-Kirchhoff stress tensor \mathbf{P} can be obtained from equations C-10 and C-11 as follows:

$$\mathbf{t}(\mathbf{x}, t, \mathbf{n})ds = \mathbf{T}(\mathbf{X}, t, \mathbf{N})dS, \quad (\text{C-13})$$

$$\sigma(\mathbf{x}, t)\mathbf{n}ds = \mathbf{P}(\mathbf{X}, t)\mathbf{N}dS \quad (\text{C-14})$$

and substituting from Nanson's formula¹, i.e. $ds = JF^{-T}dS$, \mathbf{P} can be written in the form

$$\mathbf{P} = J\sigma\mathbf{F}^{-T} \quad (\text{C-15})$$

C-4.1 Alternative Stress Tensors

Often it is convenient to work with the so-called *Kirchhoff stress tensor* τ , which differs from the Cauchy stress tensor by the volume ration J and is defined by:

$$\tau = J\sigma \quad (\text{C-16})$$

Another useful stress tensor is *second Piola-Kirchhoff stress tensor* which does not admit a physical interpretation in terms of surface tractions. The relationship between the first Piola-Kirchhoff stress tensor \mathbf{P} and the symmetric second Piola-Kirchhoff stress tensor \mathbf{S} is

$$\mathbf{P} = \mathbf{F}\mathbf{S} \quad (\text{C-17})$$

C-5 Constitutive Equation

A constitutive equation represents the intrinsic physical properties of a continuum body. It determines generally the state of stress at any point of the body to any arbitrary motion at time t . The constitutive equation of an isothermal elastic body relates the Cauchy stress tensor $\sigma = \sigma(\mathbf{x}, t)$ at each place $\mathbf{x} = \mathcal{X}(\mathbf{X}, t)$ with deformation gradient $\mathbf{F} = \mathbf{F}(\mathbf{X}, t)$. For homogeneous bodies in which the Cauchy stress tensor and reference

¹In order to compute the relationship between the unit vectors \mathbf{n} and \mathbf{N} consider an arbitrary material line element $d\mathbf{X}$, which maps to $d\mathbf{x}$ during a certain motion \mathcal{X} . The infinitesimal volume in the current configuration dv can be shown as a dot product. Therefore starting from relationship $dv = J(\mathbf{X}, t)dV$, we have $dv = ds \cdot d\mathbf{x} = Jd\mathbf{S} \cdot d\mathbf{X} = JdV$ with $ds = ds\mathbf{n}$ and $d\mathbf{S} = d\mathbf{S}\mathbf{N}$ denoting vector elements of infinitesimally small areas defined in the current and reference configurations, respectively.

Recalling that $d\mathbf{x} = \mathbf{F}d\mathbf{X}$, the later relationship may be written as:

$\underbrace{(\mathbf{F}^T ds - Jd\mathbf{S})}_0 \cdot d\mathbf{X} = 0$ Since the latter relation hold for arbitrary material line element $d\mathbf{X}$, it can be concluded that $ds = J\mathbf{F}^{-T}d\mathbf{S}$. This relation is known as Nanson's formula.

mass density ρ_0 are independent of the position \mathbf{X} , the constitution equation may be expressed as:

$$\sigma = \mathfrak{g}(\mathbf{F}) \quad (\text{C-18})$$

which determines the stress σ from the given deformation gradient \mathbf{F} . Another alternative form of constitutive equation which turns out to be very useful in the theory of elasticity is the relationship between Cauchy-Green tensor \mathbf{C} and the second Piola-Kirchhoff stress tensor \mathbf{S} in the form of

$$\mathbf{S} = \mathfrak{h}(\mathbf{C}) \quad (\text{C-19})$$

A so-called hyperelastic material (or Green-elastic material) postulates the existence of a Helmholtz free-energy function Ψ , which is defined per unit reference *volume* rather than per unit *mass*. The following reduced form of constitutive equation for hyperelastic materials at finite strains can be derived:

$$\mathbf{S} = 2 \frac{\partial \Psi(\mathbf{C})}{\partial \mathbf{C}} = \frac{\partial \Psi(\mathbf{E})}{\partial \mathbf{E}} \quad (\text{C-20})$$

in which $\mathbf{E} = 1/2(\mathbf{C} - \mathbf{I})$ is the Green-Lagrange strain tensor. It can also be shown that for isotropic materials, the strain energy may be expressed by the identity :

$$\Psi(\mathbf{C}) = \Psi(\mathbf{b}) \quad (\text{C-21})$$

C-5.1 Constitutive Equations in terms of Invariants

The strain energies, may be expressed as a set of independent strain invariants of the symmetric Cauchy-Green tensors \mathbf{C} and \mathbf{b} , namely, through $I_a = I_a(\mathbf{C})$ and $I_b = I_b(\mathbf{b})$, $a=1,2,3$, respectively. With reference to C-21, the constitutive equation can be expressed equivalently in the form of :

$$\Psi = \Psi[I_1(\mathbf{C}), I_2(\mathbf{C}), I_3(\mathbf{C})] = \Psi[I_1(\mathbf{b}), I_2(\mathbf{b}), I_3(\mathbf{b})] \quad (\text{C-22})$$

Since \mathbf{C} and \mathbf{b} have the same eigenvalues, which are the squares of principal stretches λ_a^2 , $a=1,2,3$, we conclude that

$$I_1(\mathbf{C}) = I_1(\mathbf{b}), \quad I_2(\mathbf{C}) = I_2(\mathbf{b}), \quad I_3(\mathbf{C}) = I_3(\mathbf{b}) \quad (\text{C-23})$$

where the three principal invariants are explicitly given by:

$$I_1(\mathbf{C}) = \text{tr} \mathbf{C} = \lambda_1^2 + \lambda_2^2 + \lambda_3^2 \quad (\text{C-24})$$

$$I_2(\mathbf{C}) = 1/2[(\text{tr} \mathbf{C})^2 - \text{tr}(\mathbf{C}^2)] = \lambda_1^2 \lambda_2^2 + \lambda_2^2 \lambda_3^2 + \lambda_3^2 \lambda_1^2 \quad (\text{C-25})$$

$$I_3(\mathbf{C}) = \det \mathbf{C} = J^2 = \lambda_1^2 \lambda_2^2 \lambda_3^2 \quad (\text{C-26})$$

For the stress-free reference configuration, the strain-energy functions C-22, with (5.89)-(5.91). must satisfy the normalization condition, i.e. $\Psi = 0$, for $I_1 = I_2 = 3$ and $I_3 = 1$. Assuming that $\Psi(\mathbf{C}) = \Psi(I_1, I_2, I_3)$ has continuous derivatives with respect to the principal invariants I_a , $a=1,2,3$, from chain rule of differentiation we find,

$$\frac{\partial \Psi(\mathbf{C})}{\partial \mathbf{C}} = \frac{\partial \Psi}{\partial I_1} \cdot \frac{\partial I_1}{\partial \mathbf{C}} + \frac{\partial \Psi}{\partial I_2} \cdot \frac{\partial I_2}{\partial \mathbf{C}} + \frac{\partial \Psi}{\partial I_3} \cdot \frac{\partial I_3}{\partial \mathbf{C}} \quad (\text{C-27})$$

After derivatives of first, second and third invariants with respect to \mathbf{C} are derived and substituted we arrive at:

$$\mathbf{S} = 2 \frac{\partial \Psi(\mathbf{C})}{\partial \mathbf{C}} = 2 \left[\left(\frac{\partial \Psi}{\partial I_1} + I_1 \frac{\partial \Psi}{\partial I_2} \right) \mathbf{I} - \frac{\partial \Psi}{\partial I_2} \mathbf{C} + I_3 \frac{\partial \Psi}{\partial I_3} \mathbf{C}^{-1} \right] \quad (\text{C-28})$$

The spatial counterpart of constitutive equation C-28 can be found using :

- The relation between the Cauchy stress σ and the second Piola-Kirchhoff stress \mathbf{S} defined by $\sigma = J^{-1} \mathbf{F} \mathbf{S} \mathbf{F}^T$
- by multiplying the tensor variables $\mathbf{I}, \mathbf{C}, \mathbf{C}^{-1}$ with \mathbf{F} from the left-hand side and with \mathbf{F}^T from the right hand side, we may write by means of the left Cauchy-Green tensor $\mathbf{b} = \mathbf{F} \mathbf{F}^T$, that $\mathbf{F} \mathbf{I} \mathbf{F}^T = \mathbf{F} \mathbf{F}^T = \mathbf{b}$, $\mathbf{F} \mathbf{C} \mathbf{F}^T = (\mathbf{F} \mathbf{F}^T)^2 = \mathbf{b}^2$, $\mathbf{F} \mathbf{C}^{-1} \mathbf{F}^T = (\mathbf{F} \mathbf{F}^{-1})(\mathbf{F}^{-T} \mathbf{F}^T) = \mathbf{I}$.

Therefore, with C-28 we deduce that

$$\sigma = 2J^{-1} \left[\left(I_2 \frac{\partial \Psi}{\partial I_2} + I_3 \frac{\partial \Psi}{\partial I_3} \right) \mathbf{I} + \frac{\partial \Psi}{\partial I_1} \mathbf{b} - I_3 \frac{\partial \Psi}{\partial I_2} \mathbf{b}^{-1} \right] \quad (\text{C-29})$$

C-5.2 Incompressible isotropic hyperelasticity

In general for isotropic materials, Ψ is dependent to three strain invariants of Cauchy-Green tensors \mathbf{C} or \mathbf{b} . However, for the incompressible materials a kinematic constraint

$I_3 = \det \mathbf{C} = \det \mathbf{b} = 1$ should be taken into consideration. Therefore, the two principal invariants I_1 and I_2 are the only independent deformation variables. Further details can be found, for example in [Ogden 1982, 1986]. A suitable strain-energy function for incompressible isotropic hyperelastic materials, in view of C-22, is given by

$$\Psi = \Psi[I_1(\mathbf{C}), I_2(\mathbf{C})] - \frac{1}{2}p(I_3 - 1) = \Psi[I_1(\mathbf{b}), I_2(\mathbf{b})] - \frac{1}{2}p(I_3 - 1) \quad (\text{C-30})$$

where $p/2$ serves as an indeterminate *Lagrange multiplier*. Differentiating Equation C-30 with respect to \mathbf{C} and performing some mathematical operations, the constitutive equation of incompressible isotropic hyperelastic materials in terms of Cauchy stress tensor σ can be derived as

$$\sigma = -p\mathbf{I} + 2\frac{\partial \Psi}{\partial I_1}\mathbf{b} - 2\frac{\partial \Psi}{\partial I_2}\mathbf{b}^{-1} \quad (\text{C-31})$$

Appendix D

Finite Element Formulations

This appendix provides a concise overview of concepts and equations used in finite element modeling in the present research work.

D-1 Nonlinear Finite Element formulation

For shortness reasons, only some aspects of nonlinear finite element techniques are described here. Normally three different sources of nonlinearity are known; material, geometry and nonlinear boundary conditions. Nonlinear stress-strain relationship referred to as material nonlinearity. The nonlinear relationship between strains and displacements or between stresses and forces are called geometric nonlinearity. Boundary conditions or loads, for instance in contact and friction problems, may introduce nonlinearities due to instantaneous changes in stiffness occur over time. The nonlinear problems of finite strain deformations, generally are solved by three approaches: Lagrangian Formulation, Eulerian Formulation and Arbitrary Lagrangian-Eulerian Formulation (ALE)[134]. In the Lagrangian approach, which normally is used for deformations of structural elements, the finite element mesh is attached to the material and moves through space along with it. Lagrangian formulations can further be classified into two categories: the Total Lagrangian method (TL), in which the equilibrium is expressed with respect to the reference (undeformed) configuration and the Updated Lagrangian method (UL), in which the current

configuration acts as reference state.

D-1.1 Fundamental Equations

In the finite strain deformation [130],

- Geometry changes during deformation. The deformed domain at a particular time is generally different from the undeformed domain and domain at any other time.
- Strain is no longer infinitesimal so that a large strain definition has to be employed.
- Cauchy stress can not be updated simply by adding its increment. It has to be updated by a particular algorithm in order to take into account the finite deformation.
- Incremental analysis is necessary to simulate the nonlinear behaviors.

Based on the principle of *virtual work* a set of linearized simultaneous equations are derived. Assuming all variables, such as coordinates x_i , displacements u_i , strains ϵ_{ij} , stresses σ_{ij} and other material variables have been solved for and are known at time t ; it is possible to solve a set of linearized simultaneous equations having displacements (and hydrostatic pressures in the mixed u-p formulation) as primary unknowns to obtain the solution at time $t + \Delta t$. The simultaneous equations are derived from the element formulations based on the principle of virtual work¹ (see for instance [172]). Let V be the volume occupied by a part of body B in the current configuration and S the surface of deformed body on which tractions are prescribed. Assume, the surface traction at any point on S be the force \mathbf{f}^S per unit of current area and let the body force at any point in the volume be \mathbf{f}^B per unit current volume, then

$$\int_V \sigma_{ij} \delta e_{ij} dV = \int_V f_i^B \delta u_i dV + \int_S f_i^S \delta u_i dS \quad (\text{D-1})$$

¹The principle of virtual work simply states that the work done by the external force subjected to any virtual displacement field is equal to the work done by the equilibrating stresses on the deformation of the same displacement field.

where σ_{ij} are the Cauchy stress components, and $e_{ij} = \frac{1}{2}(\frac{\partial u_i}{\partial x_j} + \frac{\partial u_j}{\partial x_i})$. The right side of Equation D-1 denotes the internal virtual work, W . A linear set of equations are obtained by differentiating the virtual work, keeping linear terms and ignoring all higher order ones. (see for example [132, 172]). In element formulation, material constitutive law has to be used to create the relation between stress increment and strain increment. Since the Cauchy stress rate $\dot{\sigma}$ is affected by the rigid body rotation, it is not objective (not frame indifference), an objective stress rate is required. *Jaumann rate of Cauchy stress* [135] is the one that conventionally is used [127]².

$$\dot{\sigma}_{ij}^J = \dot{\sigma}_{ij} - \sigma_{ik}\omega_{jk} - \sigma_{jk}\omega_{ik} \quad (D-2)$$

where $\dot{\sigma}_{ij}^J$ is the Jaumann rate of Cauchy stress, $\omega = \frac{1}{2}(\frac{\partial v_i}{\partial x_j} - \frac{\partial v_j}{\partial x_i})$ is the spin tensor³ and σ_{ij} is the time rate of Cauchy stress. On the other hand, using the constitutive law, the stress change due to straining can be expressed as:

$$\dot{\sigma}_{ij}^J = C_{ijkl}d_{kl} \quad (D-3)$$

where C_{ijkl} is the material constitutive tensor and d_{kl} is known as rate of deformation tensor and given by:

$$d_{ij} = \frac{1}{2}(\frac{\partial v_i}{\partial x_j} + \frac{\partial v_j}{\partial x_i}) = d_{ji} \quad (D-4)$$

in which v_i is the velocity. By substituting Equation D-4 into Equation 4.23, the Cauchy stress tensor can be obtained as:

$$\sigma_{ij} = C_{ijkl}d_{kl} + \sigma_{ik}\omega_{jk} + \sigma_{jk}\omega_{ik} \quad (D-5)$$

²Objective stress tensor is not limited to only Jauman stress rate. In deed, there are many objective stress tensors such as Oldroyd stress rate and Green-Naghdi stress rate.

³The spin tensor (or rate of rotation tensor) ω indeed is the skew part of the spatial velocity gradient tensor \mathbf{l} in which $\mathbf{l}(\mathbf{x}, t) = \mathbf{d}(\mathbf{x}, t) + \omega(\mathbf{x}, t)$,

where

$$\begin{aligned} \mathbf{d} &= \frac{1}{2}(\mathbf{l} + \mathbf{l}^T) = \frac{1}{2}(\text{grad} \mathbf{v} + \text{grad}^T \mathbf{v}) = \frac{1}{2}(\frac{\partial v_i}{\partial x_j} + \frac{\partial v_j}{\partial x_i}) = \mathbf{d}^T \\ \mathbf{w} &= \frac{1}{2}(\mathbf{l} - \mathbf{l}^T) = \frac{1}{2}(\text{grad} \mathbf{v} - \text{grad}^T \mathbf{v}) = \frac{1}{2}(\frac{\partial v_i}{\partial x_j} - \frac{\partial v_j}{\partial x_i}) = \mathbf{w}^T \end{aligned}$$

The spin tensor \mathbf{l} itself relates the material time derivatives of \mathbf{F}^{-1} and \mathbf{F}^{-T} as follows:

$$\dot{\mathbf{F}}^{-1} = -\mathbf{F}^{-1}\mathbf{l}$$

D-1.2 Mixed Formulation Methods

In some circumstances the standard displacement based finite elements show dissatisfactory performance. *Locking*⁴, which can be attributed to the over-constrained systems, specifically is a major shortcoming of this approach. Although the *shear locking* (bending) severity can be alleviated by mesh refinement or using higher order elements, *volumetric locking* (incompressible or near incompressible materials) cannot be solved by refining the mesh. For nearly incompressible (Poisson's ratio close to 0.5 or bulk modulus approaches infinity) or incompressible materials, displacements are not accurately predicted. Using derivations of displacements to calculate the volumetric strains causes erroneous results. Since the external loads are at any moment balanced by stresses through the principle of virtual work, any small error in volumetric strain will transform into a larger error in the stresses and hydrostatic pressures, which in turn will have a detrimental effect on the displacements [134]. There are two methods for eliminating volumetric locking, namely *reduced integration procedures* and using *multi-field elements*, both have their own shortcomings [173]. In multi-field elements, pressure or stress and strain fields are considered as independent variables, and therefore they are interpolated independently of the displacements. When the hydrostatic pressure is used as an additional independent field, the formulation is called *mixed u-p formulation*.

Mixed u-p Formulation

In the mixed u-p formulation (u and p, stand for displacement and pressure, respectively) pressure is obtained at global level instead of being calculated from volumetric strain. Therefore, the solution accuracy is independent of Poisson's ratio or bulk modulus. The final stiffness matrix has the format of:

$$\begin{bmatrix} K_{uu} & K_{up} \\ K_{pu} & K_{pp} \end{bmatrix} \begin{Bmatrix} \Delta u \\ \Delta \bar{P} \end{Bmatrix} = \begin{Bmatrix} \Delta F \\ 0 \end{Bmatrix} \quad (\text{D-6})$$

⁴Locking can generally be considered as the tendency for the finite element solution to approach zero due to restrictions in the body being modeled.

where:

Δu : displacement increment

$\Delta \bar{P}$: hydrostatic pressure increment

D-2 Piezoelectric formulation

The finite element formulation (used by Ansys) is taken from the work done by Holland and EerNisse [174, 175, 176] which is presented in a useful format by [177]. Using variational principle, the derivation starts from the definition of virtual work density

$$\delta W = \{\delta \mathbf{u}\}^T \{\mathbf{F}\} - \delta \phi \sigma \quad (\text{D-7})$$

where

$\{\mathbf{u}\}$: displacement,

ϕ : electric field,

$\{\mathbf{F}\}$: mechanical force density,

σ : charge density, and

δ : a virtual quantity.

The electric flux density $\{\mathbf{D}\}$, stress $\{\mathbf{T}\}$, electric field $\{\mathbf{E}\}$ and mechanical strain $\{\mathbf{S}\}$, for linear material behavior are related through the matrix form of the constitutive equations (see A-21 and A-22)

$$\begin{aligned} \{\mathbf{T}\} &= [\mathbf{c}]\{\mathbf{S}\} - [\mathbf{e}]\{\mathbf{E}\} \\ \{\mathbf{D}\} &= [\mathbf{e}]^T \{\mathbf{S}\} + [\epsilon]\{\mathbf{E}\} \end{aligned} \quad (\text{D-8})$$

Assuming V as the volume of the body, S_1 the part of boundary where traction is prescribed, S_2 that part of boundary where the charge is prescribed and ρ the density, the result of applying virtual work principle may be stated in the following form:

$$\int_V \left\{ \{\delta \mathbf{S}\}^T [\mathbf{c}] \{\mathbf{S}\} - \{\delta \mathbf{S}\}^T [\mathbf{e}] \{\mathbf{E}\} - \{\delta \mathbf{E}\}^T [\mathbf{e}]^T \{\mathbf{S}\} - \right.$$

$$\left\{ \delta \mathbf{E} \right\}^T [\epsilon] \{ \mathbf{E} \} - \{ \delta \mathbf{u} \}^T \{ \bar{\mathbf{F}} \} + \rho \{ \delta \mathbf{u} \}^T \{ \ddot{\mathbf{u}} \} + \delta \phi \bar{\sigma} \Big\} dV - \int_{S_1} \{ \delta \mathbf{u} \}^T \{ \bar{\mathbf{T}} \} dS + \int_{S_2} \delta \phi \bar{\sigma}' dS - \{ \delta \mathbf{u} \} \{ \mathbf{P} \} + \delta \phi \{ \mathbf{Q} \} = 0 \quad (\text{D-9})$$

where

$\{ \bar{\mathbf{F}} \}$: body force,

$\{ \bar{\mathbf{T}} \}$: surface traction,

$\{ \mathbf{P} \}$: point force,

$\bar{\sigma}$: body charge,

$\bar{\sigma}'$: surface charge,

\mathbf{Q} : point charge

In order to generate the matrix relations for a finite element, the continuous displacements and potential are expressed in terms of i nodal values through interpolation functions \mathbf{N}_u and \mathbf{N}_ϕ

$$\begin{aligned} \{ \mathbf{u} \} &= [\mathbf{N}_u] \{ \mathbf{u}_i \} \\ \phi &= \{ \mathbf{N}_\phi \} \{ \phi_i \} \end{aligned} \quad (\text{D-10})$$

where

$\{ \mathbf{u} \}$: displacements within element domain in the x, y, z directions

ϕ : electrical potential within element

$[\mathbf{N}_u]$: matrix of displacement shape functions

$\{ \mathbf{N}_\phi \}$: vector of electrical potential shape function

$\{ \mathbf{u}_i \}$: vector of nodal displacement

$\{ \phi_i \}$: vector of nodal electrical potential

The expanded forms of $[\mathbf{N}_u]$ and $\{ \mathbf{N}_\phi \}$ is in the form of:

$$[\mathbf{N}_u] = \begin{bmatrix} N_1 & 0 & 0 & \cdots & N_n & 0 & 0 \\ 0 & N_1 & 0 & \cdots & 0 & N_n & 0 \\ 0 & 0 & N_1 & \cdots & 0 & 0 & N_n \end{bmatrix}$$

$$\{\mathbf{N}_\phi\} = (N_1 \ N_2 \ \cdots \ N_n)$$

where N_i is the shape function for the node i . In a similar manner, the prescribed body and surface force (charge) distributions are expressed through interpolation functions and nodal values as

$$\begin{aligned}\{\bar{\mathbf{F}}\} &= [\mathbf{N}_{\bar{\mathbf{F}}}] \{\bar{\mathbf{F}}_i\} \\ \{\bar{\mathbf{T}}\} &= [\mathbf{N}_{\bar{\mathbf{T}}}] \{\bar{\mathbf{T}}_i\} \\ \bar{\sigma} &= \{\mathbf{N}_{\bar{\sigma}}\} \{\bar{\sigma}_i\} \\ \bar{\sigma}' &= \{\mathbf{N}_{\bar{\sigma}'}\} \{\bar{\sigma}'_i\}\end{aligned}\tag{D-11}$$

Differentiating Equations D-10 yields expressions for the strains and electric field

$$\begin{aligned}\{\mathbf{S}\} &= [\mathbf{B}_u] \{\mathbf{u}_i\} \\ \{\mathbf{E}\} &= -[\mathbf{B}_\phi] \{\phi_i\}\end{aligned}\tag{D-12}$$

The following two equilibrium equations are the result of substitution of relations D-10, D-11 and D-12 into Equation D-9:

$$\begin{aligned}[\mathbf{m}] \{\ddot{\mathbf{u}}_i\} + [\mathbf{k}_{uu}] \{\mathbf{u}_i\} + [\mathbf{k}_{u\phi}] \{\phi_i\} &= \{\mathbf{F}_B\} + \{\mathbf{F}_S\} + \{\mathbf{F}_P\} \\ [\mathbf{k}_{\phi u}] \{\mathbf{u}_i\} + [\mathbf{k}_{\phi\phi}] \{\phi_i\} &= \{\mathbf{Q}_B\} + \{\mathbf{Q}_S\} + \{\mathbf{Q}_P\}\end{aligned}\tag{D-13}$$

where the terms in Equation D-13 are defined in Table D.1. Once nodal values of displacement and electric potential for an element have been determined, stress and electric flux density at any point in the element can be found by substituting Equations D-12 into Equations D-8

$$\begin{aligned}\{\mathbf{T}\} &= [\mathbf{c}][\mathbf{B}_u] \{\mathbf{u}_i\} + [\mathbf{e}][\mathbf{B}_\phi] \{\phi_i\} \\ \{\mathbf{D}\} &= [\mathbf{e}]^T [\mathbf{B}_u] \{\mathbf{u}_i\} - [\epsilon][\mathbf{B}_\phi] \{\phi_i\}\end{aligned}\tag{D-14}$$

Table D.1: Description of terms in equations D-13

$[\mathbf{k}_{uu}] = \int_V [\mathbf{B}_u]^T [\mathbf{c}] [\mathbf{B}_u] d(Vol)$	Structural Stiffness matrix
$[\mathbf{k}_{u\phi}] = \int_V [\mathbf{B}_u]^T [\mathbf{e}] [\mathbf{B}_\phi] dV$	Piezoelectric Coupling matrix
$[\mathbf{k}_{\phi u}] = \int_V [\mathbf{B}_\phi]^T [\mathbf{e}]^T [\mathbf{B}_u] dV$	
$[\mathbf{k}_{\phi\phi}] = - \int_V [\mathbf{B}_\phi]^T [\epsilon] [\mathbf{B}_\phi] dV$	Dielectric Conductivity matrix
$[\mathbf{m}] = \rho \int_V [\mathbf{N}_u]^T [\mathbf{N}_u] dV$	Structural Mass matrix
$\{\mathbf{F}_B\} = \int_V [\mathbf{N}_u]^T [\mathbf{N}_{\bar{F}}] dV [\bar{\mathbf{F}}_i]$	Body force vector
$\{\mathbf{F}_S\} = \int_{S_1} [\mathbf{N}_u]^T [\mathbf{N}_{\bar{T}}] dS [\bar{\mathbf{T}}_i]$	Surface force vector
$\{\mathbf{F}_P\} = [\mathbf{N}_u]^T \{\mathbf{P}\}$	Concentrated force vector
$\{\mathbf{Q}_B\} = - \int_V \{\mathbf{N}_\phi\} \mathbf{N}_{\bar{\sigma}} dV \{\bar{\sigma}_i\}$	Body charge vector
$\{\mathbf{Q}_S\} = - \int_{S_2} \{\mathbf{N}_\phi\} \mathbf{N}_{\bar{\sigma}'} dS \{\bar{\sigma}'_i\}$	Surface charge vector
$\{\mathbf{Q}_P\} = -\{\mathbf{N}_\phi\} \mathbf{Q}$	Point charge vector